DOCTORAL THESIS IN JOINT SUPERVISION

Università degli Studi di Milano

Doctoral Program in Industrial Chemistry (XXXVI cycle)

Department of Chemistry

Universidad de Cádiz

Doctoral program in Nanoscience and Technology of Materials

Department of Materials Science and Metallurgical Engineering and Inorganic Chemistry

Selective oxidation of cyclohexane to KA oil using heterogeneous catalysts

Ph.D. Student: ALESSANDRO VOMERI
Matr. R12837

Supervisor: Prof. LAURA PRATI

Co-Supervisor: Prof. ANA HUNGRÍA

Ph.D. Coordinator: Prof. DOMINIQUE MARIE ROBERTO'

A.A. 2023/2024

Table of contents

1. Introduction

1.1. The importance of KA oil

The selective oxidation of cyclohexane (Cy) to cyclohexanol (CyOH) and cyclohexanone (Cy=O), collectively known as KA oil or K-A oil, is a pivotal reaction in industrial chemistry due to its significance in the production of adipic acid and ε-caprolactam [1]. These latter are in turn primarily utilized for the industrial synthesis of nylon-6,6 and nylon-6, respectively [2,3]. Adipic acid holds paramount importance in the industrial sector as it is the most vital dicarboxylic acid, owing to the substantial demand for nylon fibres [4]. Furthermore, projections indicate that ε-caprolactam's global production was anticipated to reach approximately 6.5 million tons per year by 2023 [5]. Additionally, a combined annual growth rate of 6.1% for the global market of both nylon varieties is expected from 2017 to 2025 [3]. However, the oxidation of cyclohexane to KA oil presents significant challenges due to thermodynamic and kinetic constraints in conflict with each other, as the reactivity of KA oil (overoxidation) contrasts with the initial difficulty in activating the C-H bond [6,7]. This disparity necessitates the use of mild reaction conditions, particularly temperature and pressure, to mitigate the formation of undesired over-oxidation by-products. In fact, currently the greatest challenge faced in commercial processes is the difficulty of effectively controlling selectivity [8]. Employing mild conditions helps minimize the likelihood of over-oxidation but limits the progress of the reaction's initial step, resulting in low conversion rates. To address these challenges, researchers have investigated various strategies and catalysts to enhance the selective oxidation of cyclohexane. The primary aim of this doctoral thesis is to tackle the aforementioned challenges by focusing on the design of suitable catalysts and investigating optimal reaction conditions, while simultaneously considering their industrial applicability.

1.1.1. What is KA oil: Cyclohexanol and cyclohexanone as industrial feedstock

The mixture of cyclohexanone (K) and cyclohexanol (A) is referred to as KA oil and finds it highest employment in the production of polyamides, in particular of nylon-6 (polycaprolactam) and of nylon-6,6 (poly-hexamethylene adipamide) [9]. Other uses of the KA oil mixture are found in the fields of polyurethanes and polyester production.

Cyclohexanone has been produced on the industrial scale for more than 80 years [1]. Nowadays, its production is obtained by one of three ways: 1) the oxidation of cyclohexane, 2) the reduction of phenol or 3) the hydration of cyclohexene to cyclohexanol with subsequent dehydrogenation [9]. Being the main application of cyclohexanone the production of caprolactam, it finds other minor applications as solvent due to its non-corrosive properties [10]. Cyclohexanol can be produced by the same three pathways (avoiding the dehydrogenation step in (3)), being the hydration of cyclohexene the most promising method in terms of costs, product selectivity and safety, but maintaining low conversion and slow reaction rates [11]. Beyond nylon, cyclohexanol is used as an intermediate in the chemical synthesis of many goods, such as solvents resins and fragrances, but also as solvent in antibiotics, anti-inflammatory medicines and analgesics fabrication [12].

1.1.2. Adipic acid and ε-Caprolactam

Adipic acid (AA) serves as a significant chemical feedstock in various industrial applications, with its primary use lying in the production of nylon-6,6. The industrial production of adipic acid with a one-step process was first commercialized by Du Pont in 1937 [13], and now consists in the oxidation of KA oil using excess HNO_3 in the presence of Cu(II) and ammonium metavanadate catalysts [14]. The reaction diagram illustrated in Figure 1.1 depicts the production process for adipic acid starting from the KA oil mixture.

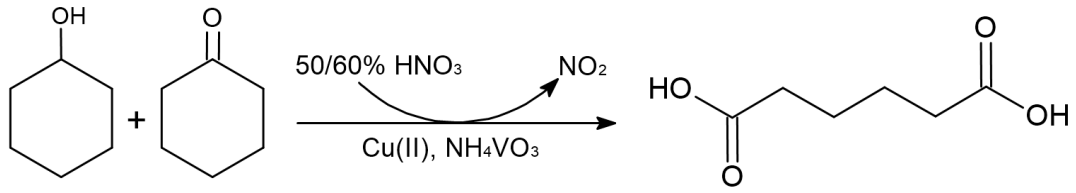

Figure 1.1. Industrial transformation of KA oil into adipic acid.

While the primary use of adipic acid is nylon-6,6 production, there are other ways in which adipic acid can be employed [15], as the manufacture of polyurethanes, adipate esters, plasticizers and other miscellaneous applications. In 2022, the global market size for adipic acid reached USD 4,887.59 million, and it is anticipated to exhibit a compound annual growth rate (CAGR) of 3.8% during the forecast period of 2023 to 2030. The increasing demand for adipic acid is driven by the growing utilization of nylon-6,6, which is extensively employed in

the automotive and electrical & electronics industries worldwide to produce lightweight and durable plastics. Adipic acid finds widespread application in various end-use sectors, including electrical & electronics, automotive, building & construction, packaging & consumer goods, textile, and others. The rising demand for nylon-6,6 fibre and polyurethane across a diverse range of industries is expected to positively impact the market's growth in the forthcoming years [16].

ε-caprolactam, or caprolactam, is a vital chemical compound widely used in the production of nylon-6, a versatile polyamide polymer. This cyclic amide, with a chemical formula of $C_6H_{11}NO$, serves as the precursor for the synthesis of nylon-6 through a ring-opening polymerization process. Caprolactam is characterized by its distinct six-membered lactam ring structure, which imparts unique properties to the resulting polymer. It is predominantly employed in the manufacture of fibres and filaments (90%), and the rest in engineering plastics (10%) due to its exceptional mechanical strength, thermal stability, and chemical resistance [17]. The industrial-scale manufacturing of ε-caprolactam continues to rely on conventional methodologies. In this process, cyclohexanone oxime is synthesized by reacting cyclohexanone with hydroxylamine sulphate in the presence of ammonia [18]. Subsequently, the Beckmann rearrangement is performed in fuming sulfuric acid, followed by neutralization to release the desired lactam [19](Figure 1.2). However, this classical approach suffers from drawbacks, including intricate reaction pathways and the generation of a significant quantity of ammonium sulphate as a by-product [20].

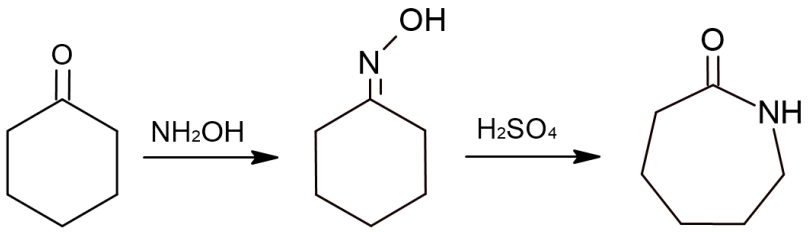

Figure 1.2. Reaction scheme of the industrial transformation of cyclohexanone into caprolactam.

The demand for caprolactam has witnessed substantial growth over the years, driven by its extensive applications in industries such as textiles, automotive, electronics, and consumer goods. The global caprolactam market is expected to experience further expansion, spurred by increasing population, urbanization, and evolving consumer preferences. The caprolactam market is projected to exhibit a compound annual growth rate (CAGR) of 5.79% during the

period from 2022 to 2027. Additionally, the market size is anticipated to witness a substantial increase, estimated at USD 5,184.34 million. The growth trajectory of the market is influenced by various factors, such as the significant industrial significance of nylon, the increasing adoption of bio-refineries, and the substantial volumes of waste generated from ammonium sulphate [21].

1.1.3. Nylon-6 and nylon-6,6

Nylon-6 and nylon-6,6 belong to a category of polymers called polyamides, playing significant roles in the synthetic fibre industry. The remarkable success of nylon-6,6 fuelled substantial growth in this sector. This particular polymer was first synthesized by Wallace Hume Carothers in 1935 at DuPont's laboratories, and three years later, DuPont obtained a patent for the manufacturing process [22]. Later, in 1939, Paul Schlack in Germany discovered nylon-6, which was produced using a different method. These two fibres have since become prominent in the realm of commodity fibres, exerting a profound influence on the global fibre industry [23]. The two nylon varieties are considered among the most important polymers in industry and are experiencing significant growth in the global market. With a projected compound annual growth rate (CAGR) of 6.4% from 2023 to 2030, the demand for nylon in the automobile industry is a key driver of this growth [24]. In the automobile industry, nylon is used in engine components, offering lightweight design flexibility without compromising safety. It finds demand in the premium carpet industry and clothing sector due to its smooth texture and low maintenance requirements. Nylon composites are also used to manufacture automotive parts, reducing weight and improving fuel efficiency. Overall, nylon's applications span across automotive, textiles, and apparel industries, driven by its versatility and environmental advantages. The reaction schemes of nylon-6 and -6,6 production from caprolactam and adipic acid is reported in Figure 1.3.

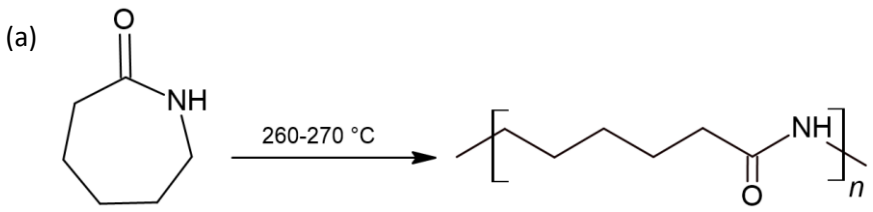

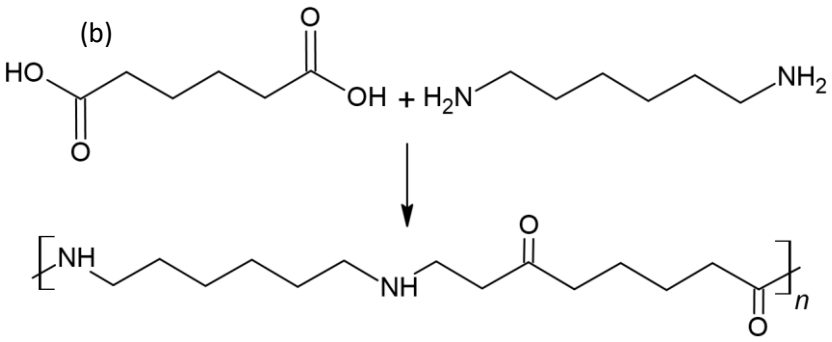

Figure 1.3. Schematic representation of a) nylon-6 production from caprolactam and b) nylon-6,6 production from adipic acid.

Novel routes for the production of nylon intermediates are being researched in the last decades, with the intent of avoiding the energy and cost inefficient processes currently adopted, by keeping particular interest in the bio-based [25] and recycled [26] nylon obtainments.

1.2. KA oil production: Oxidation of cyclohexane

Since the production of nylon was commercialized and scaled up in the late 30's of the XX century, the oxidation of cyclohexane exploded as a hot topic of investigation by many research groups and enterprises. Given the importance of the reaction, both homogeneous and heterogeneous catalytic processes have been developed through the years. In this section, the revolutionary discoveries made in the field are reported and compared in a walkthrough of the most relevant applications, reaction conditions and manifold catalytic systems explored.

1.2.1. Industrial process and related concerns

There are two main current industrial processes that require optimization. In fact, in the classical process developed in the 1940s [27], the oxidation is carried out at 140-180°C and 8-20 bars of air in the presence of soluble cobalt(II) naphthenate salt as homogeneous catalyst (Figure 1.4). In fact, in homogeneous processes transition metals such as Co^{2+}, Mn^{2+}, and Cr^{2+}, can undergo a one-electron switch and catalyse this initiation through the Haber-Weiss cycle [28]. A selectivity of 70-80% at conversion below 6% is obtained with a K/A ratio of 0.3-0.6 [1,28].

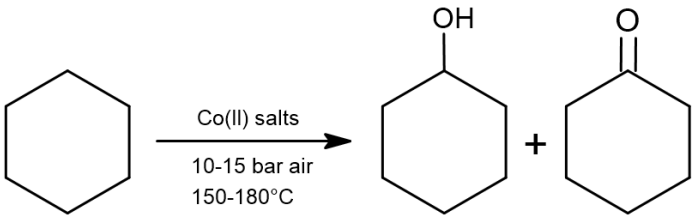

Figure 1.4. Industrial process for the oxidation of cyclohexane.

The addition of Cr(III) salts can lead to dehydration of cyclohexyl hydroperoxide to cyclohexanone and water, therefore increasing the K/A up to 2.5 [29]. A recent two-steps process which non-catalytically oxidizes cyclohexane to cyclohexyl hydroperoxide using air in the same conditions of T and P of the industrial practice and in a reactor possessing inert inner walls (avoiding the addition of substances which can decompose the hydroperoxide), subsequently converts it catalytically into KA oil with a K/A ratio of ~1.5 in the presence of a phthalocyanine or porphyrin complex immobilized on a carrier material [28,30]. It was found that higher conversion (10%) and one of the lowest K/A ratios (1:9) can be obtained modifying the industrial process with the addition of boric acid into the initial mixture, as the boric acid can form precipitates with cyclohexanol and cyclohexyl hydroperoxide, preventing their overoxidation [31].

However, the drawbacks related to the classical process are multiple: the difficulty of separation and reutilization of the homogeneous cobalt salts, the relatively high temperature and pressure conditions and the limitation of the conversion to maintain a high (but still improvable) selectivity to KA oil. These difficulties make the process unattractive in this period of transition towards a greener and more sustainable chemistry, and the development of catalysts which can actually obtain higher conversion while maintaining high selectivity to KA oil at milder reaction conditions is extremely desirable. Despite the long commercial history of the cyclohexane oxidation process, the continued issuance of numerous patents and publications indicates ongoing research and development efforts. These works primarily focus on enhancing selectivity and carbon efficiency during the oxidation and decomposition steps. Additionally, other areas of interest include improving energy efficiency, treating and upgrading by-product streams, and implementing specialized equipment within the process [9].

1.2.2. Heterogeneous catalysis

At present, nearly 90% of the processes in the industry of chemicals employ catalysts, and almost 80% of the manufactured products make use of catalysis during their production [32]. The role of the catalyst is that of lowering the activation energy barrier of a reaction that would not occur otherwise at the same conditions, allowing for the obtainment of the desired products at milder conditions or in shorter time. This way, the kinetics of the reaction is greatly affected, while the thermodynamics remains unaffected. The utilization of catalysis has consistently been a crucial instrument in the development of more environmentally friendly procedures. Presently, we are witnessing the significant role catalysis plays in transforming biomass into fuels and chemistry [33].

Catalysis is a wide discipline that can be divided in three main groups: heterogeneous, homogeneous, and enzymatic catalysis. However, the scope of this thesis is the development of suitable heterogeneous catalysts for the selective oxidation of cyclohexane and entering in detail on homogeneous and enzymatic catalysis would go beyond that scope. While enzymatic catalysis is based on the employment of a biological molecule (the enzyme) as the catalytic material, homogeneous catalysis employs catalytic systems that are in the same phase of the reagents. Homogeneous catalysts represent some advantages over heterogeneous catalysts, such as a higher contact with the reagents, lower operating temperatures, high selectivity and tunability of the catalytic sites due to their nature of metal-organic complexes featuring coordinating ligands which can be selected appropriately. However, homogeneous catalysis represents only for the 25% of the industrial processes employing catalysts [34], since the drawbacks represented by their separation and recycling turn into an important economic disadvantage. Moreover, they generally produce a great amount of waste materials, cause corrosion of the industrial materials or deposit on the reactor walls, thus creating environmental hazards that are to be avoided [35].

Heterogeneous catalysts are in a different phase (usually solid) with respect to the reactants and are preferrable to industries because of their ease of recovery and reutilization, thermal stability and absence of organic moieties. Due to the absence of specific localized active sites where the reactants can coordinate to, the adsorption of the reactants on the surface of the material is the first step taking place. The adsorption and desorption of the reactants and

products are the rate determining steps for the heterogeneous process [36], and tuning the properties of the material is key to their acceleration and in brief the performance of the catalyst.

Heterogeneous catalysts continue being widely employed in oxidation reactions, being the selective oxidation of organic compounds one of the greater fields of application [37]. In this frame, metal oxide catalysts play a crucial role in the majority of acid-base and selective- and total-oxidation catalytic processes carried out in industry [38]. Metal oxides possess distinct characteristics, including acidity and/or basicity (Lewis and/or Brønsted) as well as redox behaviour (in the presence of transition metal ions), which confer specific catalytic properties [39]. Moreover, metal oxides can feature a variety of defects and active sites, such as the presence of anionic or cationic vacancies, steps and terraces [40], which can play an important role in the oxidation reactions. Among the pioneers in the field of oxidation catalysis, the renowned Prof. Robert K. Grasselli coined a series of principles which can guide researchers to a deeper understanding of metal oxide catalysts behaviour for optimizing their design, known as the "seven pillars of oxidation catalysis" [41]. These principles can be resumed as follows:

1) The lattice oxygen of a reducible metal oxide behaves as a more versatile and selective oxidizing agent than O_2. Investigation of the reducibility of the material is key.
2) Metal-oxygen bond strength should be of intermediate strength under reaction conditions, to avoid the absence of reaction (too strong) or overoxidation (too weak).
3) The host structure must be flexible, able to contain O and anion vacancies and favouring their diffusion and migration.
4) The material should possess redox properties, and rapidly re-oxidize in the presence of O_2.
5) The multifunctionality of the active sites is crucial in the promotion of each single step of the catalytic cycle.
6) Site isolation. The surface lattice oxygens must be spatially isolated from each other in defined groupings on the catalyst surface to achieve selectivity.
7) The cooperation of phases. When a single host structure is not enough for the catalytic functions required, two active phases can be put in intimate proximity obtaining a positive effect.

With the aim of providing an improvement to the current industrial process of cyclohexane oxidation for the reasons already explained, many heterogeneous catalysts have been developed in the past decades such as metal (Au, Ag, Co, V, Fe, Cr, Ti, etc.) supported on oxides, carbons, mesoporous materials and metalorganic structures [42,43]. Among the cited metals, tested using air or O_2 as oxidant, gold resulted one of the most employed despite the elevated cost, particularly due to its great performance in selective oxidation reactions [44,45] and considering its efficiency in activating the C-H bond [46]. Several studies have also suggested the use of metal/metal oxide-based catalysts and many mixed oxides are being reported with good results in a recent 2022 review on cyclohexane oxidation [47]. It is nowadays most important to find inexpensive systems featuring abundant metals, with high T and P stability and possessing interesting redox capabilities helpful for facilitating the single electron exchanges of the radical reaction mechanism. Many heterogeneous systems featuring transition metals have been researched for this reaction due to their low cost, availability and interesting electronic properties, as mixed metals oxides [48–50] or supported on a variety of supports such as zeolites [51], aluminophosphates [52,53], mesoporous silica [54,55], and carbons [56].

In the present work, different heterogeneous systems have been prepared focusing on maintaining a high selectivity to KA oil through control on the preparation, with thorough catalyst characterization and exploring metal-support interaction with novel combinations of metals (see chapter 1.4. Project aims and objectives).

1.2.3. Autoxidation and reaction mechanism

Another challenge of the oxidation of cyclohexane is represented by the reaction mechanism. Both the autoxidation and the catalysed reaction proceed via a complex radical-chain mechanism, reported and simplified in Scheme 1.1.

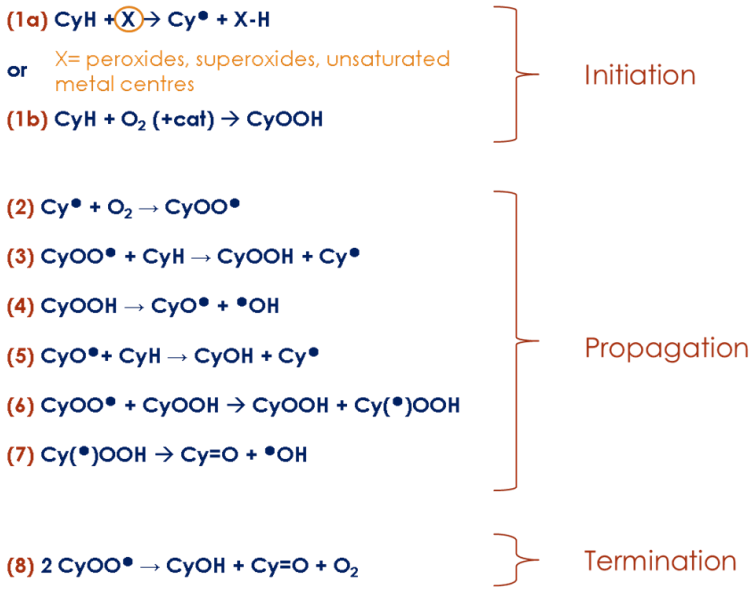

Scheme 1.1. Radical-chain mechanism for the oxidation of cyclohexane.

The chain initiation can proceed through the activation of the C–H bond by abstraction of an H atom due to the cleavage by an unsaturated metal centre, a peroxide or a superoxide species bound to metal centres or metal oxides [57]. For this reason, the use of a suitable radical initiator would be able to favour the initiation of the cycle and improve the kinetics of the reaction. Alternatively, the chain initiation can be started by the catalytic insertion of an O_2 molecule in the C-H bond of cyclohexane yielding the cyclohexyl hydroperoxide (CyOOH) intermediate [29,58], where the formation of the CyOOH is the rate determining step of the reaction [59,60]. The formation of cyclohexanol (CyOH) and cyclohexanone (Cy=O) takes place from the mutual destruction of two peroxyl radicals according to reaction (8) but can also occur during the steps (5–7).

However, more in-depth look at cyclohexanol and cyclohexanol formation can be discussed looking at the works of Hermans et al. An initial important source of cyclohexanol is attributed to a Franck–Rabinowitch cage reaction between the formed CyOOH and cyclohexyl radical (Cy•), according to what was observed also by Berezin [61]. In a Franck–Rabinowitch cage [62], the molecules in a solvent are more accurately described by encapsulated particles, called cage pairs, than individual particles. In order to interact with other molecules, the caged molecules must diffuse from their solvent cage.

Hermans research group found that the high-speed reaction between CyOO• and CyOOH proceeds by involving the unstable Cy-αH•OOH radical, which spontaneously breaks down to form the ketone (Cy=O) and the •OH radical [63]. It has been discovered that the majority of the alcohol is produced by the "hot" •OH radical through a secondary reaction known as the "activated cage" reaction, similar to the one described earlier. This demonstrates that the highly reactive CyOOH intermediate is the main contributor to the production of ketone and alcohol, although it also generates some by-products [64]. Additionally, the rapid decomposition of the α-hydroxy-cyclohexylperoxyl radical into HO_2• and cyclohexanone, observed during the relatively fast oxidation of CyOH, acts as another source for ketone formation. This reaction occurs through a swiftly equilibrated process [64].

The research group employed a model calculation to confirm that experimentally the main source of by-products is not the overoxidation of cyclohexanone, which is a secondary source, but the CyOOH species, which decompose leading to the formation of ring-opened reactive ω-formyl radicals (•CH_2-$(CH_2)_4$-CHO) [65]. A resume of CyOOH possible reaction patterns proposed in [65] is described in Scheme 1.2 from Hermans et al.

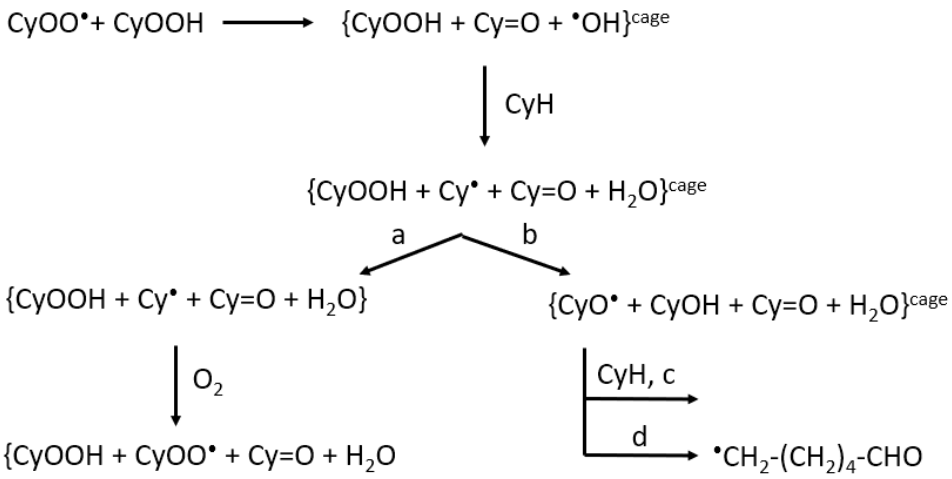

Scheme 1.2. Possible reaction pathways involving CyOOH.

In conclusion, numerous by-products can be obtained from this reaction. A variety of C6 and C5 by-products can be obtained by ring-opening in long reaction runs or under harsh conditions. In particular, for the industrial process (80% selectivity to KA oil) the remaining 20% selectivity is counting for the obtainment of n-butyric, n-valeric, succinic, glutaric and adipic acids [31]. The formation of adipic acid, the most important byproduct, by radical chain oxidation reactions of 6-hydroxyhexanoic and 6-oxohexanoic acids remains unclear. In both

the cobalt salt-catalysed and uncatalysed reactions, longer oxidation time simultaneously causes a decrease of 6-hydroxyhexanoic concentration while increasing adipic acid relative concentration. Nevertheless, this was not established to be the main route of adipic acid formation, since the major amount was demonstrated to be formed through cyclohexanone and then 2-hydroxycyclohexanone oxidation, even at low conversion values of cyclohexane. Considering this route, adipic acid is considered more as a final product of cyclohexane oxidation rather than an intermediate, and most of its formation (86-95%) proceeds via cyclohexanone [66].

1.2.4. Air/oxygen as oxidant

The utilization of both pure molecular oxygen and oxygen in air is extensively employed in oxidation catalysis, and the selection of the oxygen source is typically determined by economic factors. In low-conversion-high-selectivity processes where the reactant is recycled, the inclusion of nitrogen gas incurs additional costs, making pure oxygen more economically favourable. Moreover, the solubility of oxygen in the solvent is a crucial consideration in liquid systems, often leading to the preference for pure oxygen from an economic standpoint. On the other hand, air is generally employed when the process operates in the gas phase with a high conversion of the reactant (>80%) [67].

In classical industrial processes, the oxidation of cyclohexane is commonly carried out in stirred tank reactors or staged bubble reactors, using air or a mixture of oxygen and nitrogen with an oxygen concentration below 21%. Understanding the role and impact of oxygen on reaction rates and selectivity is crucial for the improvement of the process. In general, it is expected that incorporating oxygen-enriched air or pure oxygen should enhance the rates of hydrocarbon oxidation. However, the potential risk of deflagration has posed a significant challenge when evaluating the effect of oxygen, not only in pilot-scale setups but also in laboratory reactors [68]. Therefore, the use of pure oxygen or oxygen-enriched air has the potential to improve the productivity of cyclohexane oxidation, but safety concerns must be addressed before implementation.

Greene et al. [69] successfully oxidized cyclohexane using pure oxygen for the first time. They conducted a comparison between this new process and the traditional method, revealing

notable improvements. The mean reaction residence time was reduced, operating temperature was slightly lowered, and both selectivity and productivity increased, all while maintaining the same cyclohexane conversion of 4%. However, since the reactor used was different than the industrial one, one could still argue if the improvement is due to the increased oxygen partial pressure or to the different transport effects in the two reactors [68]. Furthermore, in the same work a set of experimental studies conducted by Jevtic et al. revealed that increasing the initial oxygen concentration in the vapor phase from 20% to 50% has a beneficial impact on reaction rates and yield and established that the rate of oxygen consumption follows a first-order relationship with respect to oxygen, as the decay of oxygen partial pressure over time remained unaffected by the initial partial pressure of oxygen.

However, this is in contrast with the findings of Suresh et al. [70], according to whom the oxidation of cyclohexane exhibits zero-order kinetics with respect to oxygen when the conversion of cyclohexane is relatively low. Therefore, within the conversion range considered (4-5% in the industrial process), the concentration of oxygen does not significantly affect the rate of cyclohexane oxidation. In the batch mode of operation for the uncatalyzed reaction system, the initial quantity of oxygen supplied to the system is finite and eventually gets depleted. Consequently, the oxygen partial pressure and concentration in the liquid phase progressively decrease over time until they reach negligible levels. Mechanistic studies are to be carried out in order to solve this debate present in the literature. Considering the high use of hydroperoxides as oxidants for this reaction as alternatives, it is good to recall that molecular oxygen stands out as an ideal green oxidant due to its affordability, abundant availability, and complete environmental safety [71].

1.2.5. TBHP and H_2O_2 as oxidants

Hydroperoxides are very reactive molecules containing the hydroperoxyl functional group (-OOH). Their general formula is ROOH, where R represents an organic group in the case of organic hydroperoxides. Hydroperoxides can react with or without cleavage of the oxygen–oxygen bond. Reactions that lead to the cleavage of the oxygen-oxygen bond can occur through heterolytic, homolytic, or metal-promoted oxidation-reduction reactions [72].

In order to understand the reactivity of hydroperoxides, one must consider the electronic structure of O_2. In fact, O_2 is a paramagnetic molecule with two unpaired electrons in a pair of π* orbitals of identical energy, such as presented in Figure 1.5.

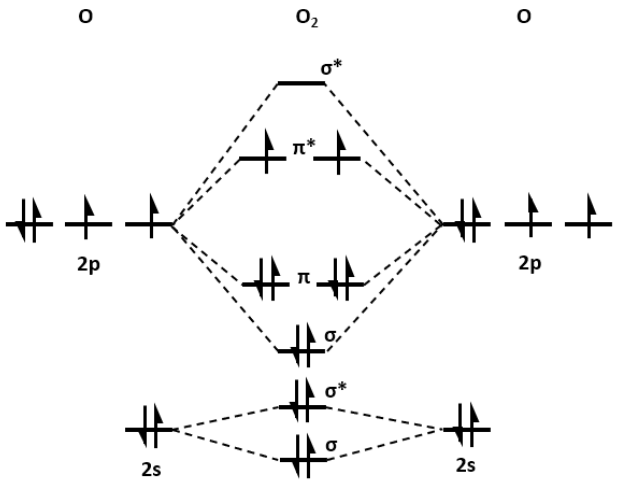

Figure 1.5. Representation of the molecular orbitals in O_2.

Therefore, the addition of electrons to the O_2 molecule leads to the occupancy of antibonding (π*) orbitals, resulting in the weakening of the O-O bond. This weakening is reflected in both the length of the O-O bond and its dissociation energy. As a result, the resulting superoxo* (O2•−) and peroxo* (O_2^{2-}) species are much more reactive. Stable hydroperoxides that have been extensively used in catalytic oxidations are hydrogen peroxide (H_2O_2), tert-butyl hydroperoxide (TBHP), cumyl (or cumene) hydroperoxide ($C_6H_5C(CH_3)_2OOH$), and ethylbenzene hydroperoxide [73] (Figure 1.6a,b,c and d).

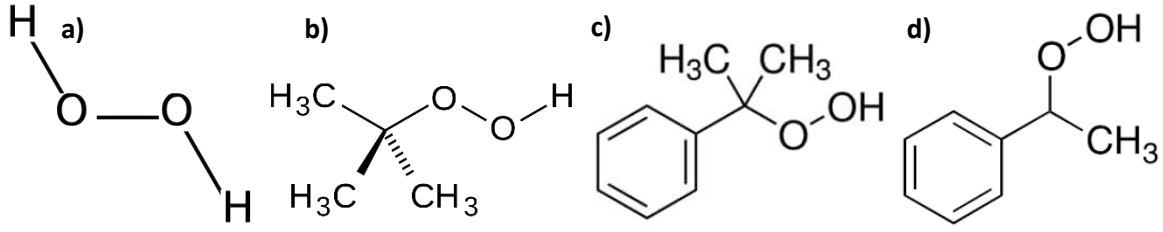

Figure 1.6. Hydroperoxides typically employed in oxidation catalysis, namely a) hydrogen peroxide, b) tert-butyl hydroperoxide, c) cumyl hydroperoxide and d) ethylbenzene hydroperoxide.

Among these oxidants, tert-butyl hydroperoxide (TBHP) is the most commonly employed radical initiator in the oxidation of cyclohexane with heterogeneous systems, and its successful use can be found in many works [74–77]. TBHP is also one of the most stable hydroperoxides, and a study was conducted observing its decomposition at different

temperatures [78]. In the same study, the group detected that at 50-75°C it is stable, at 95-100°C it decomposes yielding only tert-butyl alcohol and oxygen, while at higher temperatures (e.g. 250°C) it decomposes violently through a radical mechanism that yields acetone, methanol, t-butyl alcohol, formaldehyde and water plus some residue. Furthermore, the formation of tert-butoxyl radicals ($tBuO^{\bullet}$) initiates a chain decomposition of the hydroperoxide, which is accompanied by free-radical processes related to the specific substrate [79].

Hydrogen peroxide exhibits a higher oxidation potential compared to molecular oxygen, making it effective in various reaction conditions including both acidic and basic environments [80]. It also possesses the highest active oxygen content (47%) among the typical oxidants compared to O_2 (100%), and greater than TBHP (17.8%) [81]. Hydrogen peroxide has been deeply studied in the oxidation of cyclohexane too, and its applications at low temperature are numerous in literature, mostly with homogeneous catalysts [82,83] working in a Fenton-like regime and/or with the employment of acids as co-catalyst [84,85].

Developing an efficient catalyst presents significant challenges due to the opposing polarity of the two reactants involved – hydrogen peroxide being strongly hydrophilic and cyclohexane being highly hydrophobic [86]. According to Sato's principle, for the catalyst to function effectively, it needs to facilitate the adsorption of both hydrogen peroxide and cyclohexane. Therefore, an effective heterogeneous catalyst should possess a carefully balanced hydrophobic surface, meeting the necessary criteria [86,87].

Cumene hydroperoxide (CHP) is generated through the oxidative reaction of cumene using air as the oxidizing agent in the presence of aqueous sodium carbonate serving as a catalyst, and approximately 94.5% of its use is dedicated to the manufacture of phenol and acetone [88]. Despite being less expensive than TBHP, cumene hydroperoxide is also quite toxic, corrosive and flammable [89]. On the other hand, the utilization of ethylbenzene hydroperoxide, as opposed to cumene hydroperoxide or tert-butyl hydroperoxide, provides the advantage of simultaneously generating styrene, even though the synthesis of styrene via the autoxidation of ethylbenzene is more intricate compared to a hydrocarbon containing a tertiary C-atom [90]. Generally, cumene hydroperoxide and ethylbenzene hydroperoxide are not employed in the oxidation of cyclohexane due to these limitations.

From the perspective of their degradation products, H_2O_2 and TBHP fall under the environmentally friendly category as they produce only H_2O, O_2, and tert-butanol. However, when evaluating the sustainability of an oxidizing agent, it is crucial to consider not only the degradation products but also the environmental impact associated with its production. The industrial production of H_2O_2 is typically carried out through the anthraquinone oxidation (AO) process [91], which is not regarded as a green route due to its high energy requirements and generation of significant waste [92]. Similarly, TBHP is obtained through the reaction of tert-butyl alcohol with H_2O_2 in an acidic solution and faces similar environmental limitations as H_2O_2 [93].

TBHP has been observed to exhibit greater reactivity in liquid-phase oxidation reactions when compared to O_2 due to its singlet state, as opposed to the triplet ground state of O_2. Additionally, TBHP demonstrates greater stability in comparison to H_2O_2, showing reduced decomposition tendencies [94]. Furthermore, when compared to hydrogen peroxide and organic peracids, tert-butyl hydroperoxide displays lower reactivity and higher solubility in organic solvents.

The toxicity of the two oxidants must be considered as well. The National Toxicology Program of the U.S. designed a study on the dangers related to TBHP use [95] and demonstrated that the metabolism of TBHP leads to the generation of free radicals, and its contact can cause skin irritation through dermal exposure. Similarly, hydrogen peroxide can cause severe biological injuries due to its reactivity and generation of free radicals [96]. Therefore, the investigation for a less toxic and possibly cheaper radical initiator for the oxidation of cyclohexane is highly desirable.

1.3. Heterogeneous catalysts preparation and characterization

Heterogeneous catalysts are solids commonly grouped into supported and bulk (unsupported) materials, featuring particles of nanometric size. The preparation of the catalysts is key to the obtainment of the desired structure, tuned for the best performance in a specific reaction. Numerous methodologies of preparation exist nowadays, which can give very different morphological properties to the final material and influence its catalytic properties, changing parameters such as the particles size, distribution, dispersion and composition. In order to

better understand the structure-activity correlation of a heterogeneous catalyst, exhaustive and systematic characterization of the materials through solid-state analytical techniques is essential. In this paragraph, an overlook is given to the supported and bulk catalysts preparation methods utilized within the thesis work, followed by the description of the techniques utilized for the morphological investigation.

1.3.1. Supported metal NPs

Supported metal nanoparticles can be composed of a single metal (monometallic) or two (bimetallic) or more metals, with a diameter ranging between 1 and 100 nm. In the case of the existence of a metallic bond between two or more different metal species in the same particle, the nanoparticle can be referred to as alloy [97].

The role of the support in heterogeneous catalysis is of paramount importance as it influences the generation and stabilization of the active phase, while also regulating the interactions between the adsorbates and the catalyst surface. Furthermore, the effectiveness of a catalyst is directly related to the dispersion of metals, as the active sites are located on the surface atoms. In particles exceeding one micron in size, the population of metal atoms residing on the surface is surpassed by the abundance of atoms located in the bulk region, whereas in nanoscale particles the relative presence of atoms on the surface becomes significant. Indeed, when a particle reaches the nanoscale size (1.5-10 nm) the quantum size effect takes place, which explains particle confinement behaviour through quantum mechanics [98]. At this dimension, the valence and conduction bands cease to exhibit characteristics typical of metals and instead adopt discrete energy levels (Figure 1.7). This results in a variation of the band gap of the material, and of its optical and electronic properties [99].

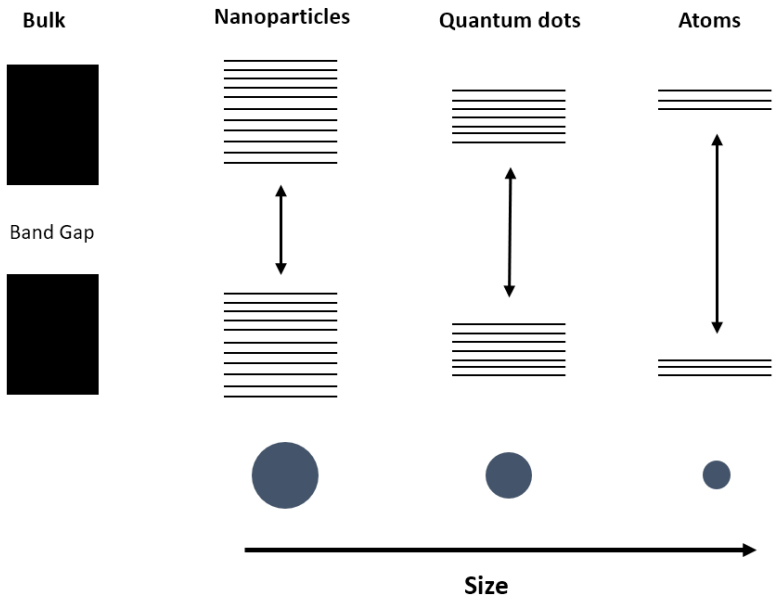

Figure 1.7. Schematic representation of the quantum size effect occurring in nanometric-size particles.

Nanoparticles are thermodynamically unstable. Consequently, a support with a large surface area is one of the most effective solutions for stabilizing them, and for achieving a high degree of metal dispersion and exposing surface atoms. Additionally, the support can either remain inert, actively participate in the reaction process, or form compounds with the species being supported. In the case of metallic species, it is common to employ a non-metallic support or a metal oxide as the supporting material. Beyond its role in the catalytic reaction, the support also facilitates the recovery step by enabling easy separation from the reaction mixture at the conclusion of the process. Lastly, the morphology and pore size of the support are influential factors in enhancing the stability and performance of the supported catalyst [100].

1.3.1.1. Supported metal NPs preparation

The number of applications of metal supported catalysts in heterogeneous catalysis reactions has increased over the past years, despite their demanding characteristics, as they necessitate to couple high selectivity towards the desired product with high stability and productivity [101]. In this regard, the most established techniques for preparation of dispersed metallic phase in terms of size, composition and dispersion of the nanoparticles are liquid phase routes, as sol immobilization, electrochemical deposition, incipient wetness, (co)impregnation and (co)precipitation ("co-" when two metals are present and one of them is forming the supporting material). Other established methodologies involving gas phase

routes are chemical vapour deposition, solvated metal atom dispersion and chemical vapour impregnation.

It is often difficult to control the dimension and structure of the nanoparticles because there are many factors that can influence the resulting structure. For example, in sol immobilization, the nature and concentration of the stabilizer ligand and of the reducing agent, but also experimental parameters as solution pH, temperature and pressure [102]. Moreover, adsorption of the colloidal nanoparticles onto the support surface may cause the nanoparticles to restructure upon deposition and during subsequent heat treatments [103]. However, this preparation methods offer advantages in the control of size, dispersion and/or composition of the obtained particles, and still are among the most widely employed for obtaining supported metal NPs.

Among all techniques, we particularly focus on sol immobilization, incipient wetness and solvated metal atom dispersion, which have been employed for the preparation of supported metal NPs in this work.

1.3.1.1.1. Sol immobilization

The sol immobilization technique allows for the deposition of metal precursors onto supports without the need for subsequent activation steps. This method offers advantages such as preserving the morphology, particle size, and dispersion of the final catalyst. Here, the active phase is first pre-formed in a solution and then deposited onto the support, avoiding undesirable changes. A schematic representation of the sol immobilization technique is reported in Figure 1.8.

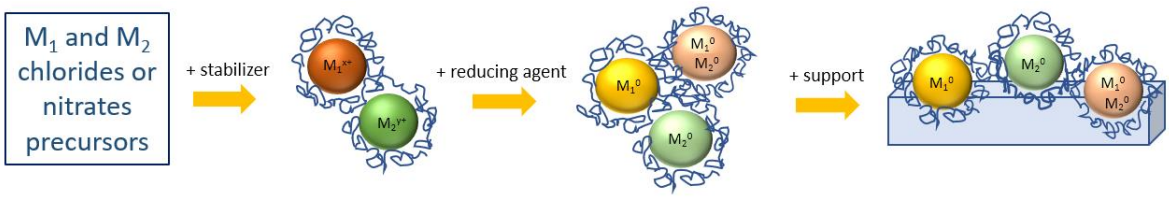

Figure 1.8. Sol immobilization technique for the preparation of supported metal NPs.

Stabilizing agents are employed to prevent the agglomeration of nanoparticles, ensuring control over size and shape. To initiate the formation of metal nanoparticles, reducing agents

are introduced into a solution containing metal salts or complexes and the protecting agent. The reducing agent facilitates the conversion of the metal precursor into zero-valent nuclei. Then, the deposition of the reduced and stabilized particles (active phase) is completed by adding the support and letting the solution under stirring. A final washing step is typically conducted to partially remove the protective agent. This step is necessary to prevent hindrance in the interaction between the substrate and the metal nanoparticles, which could reduce the overall catalyst activity [102,104,105].

Nucleation and growth (Figure 1.9) are fundamental steps in the production of nanocrystals using this technique. Nucleation involves the formation of zero-valent nuclei from metal precursors through processes such as decomposition or reduction. Maintaining reproducibility requires careful control of experimental conditions, including stirring, presence of impurities, and temperature, as nucleation is highly sensitive to these factors [106]. After nucleation, nuclei undergo structural fluctuations until they reach a critical size. Beyond this size, the nuclei maintain well-defined morphologies as seeds. The growth of these seeds occurs through the addition of atoms still present in the solution. The balance between the decrease in bulk energy and the decrease in surface energy determines the continuous growth of nanocrystals. Coalescence and Ostwald ripening are processes that can influence seed growth and particle size distribution if not adequately controlled [107,108].

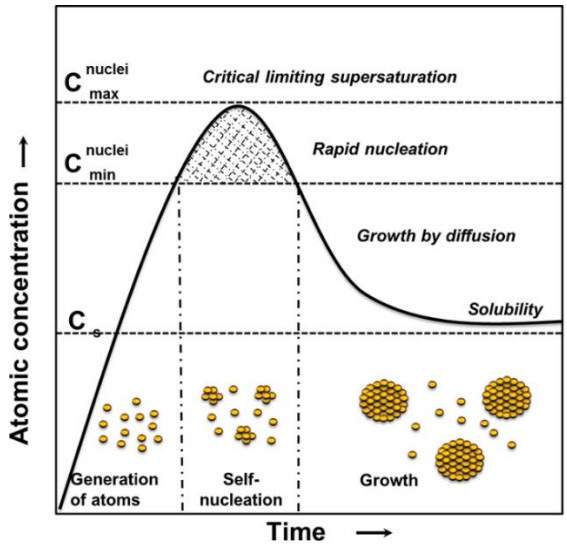

Figure 1.9. Nucleation and growth of metal nanocrystals. Reference taken from Andreescu et al. [109]*, Khan, R.; Rehman, A.; Hayat, A.; Andreescu, S. Magnetochemistry 2019, 5, 63. https://doi.org/10.3390/magnetochemistry5040063.*

Various factors must be carefully considered to control the formation and characteristics of nanoparticles. The choice of reducing and stabilizing agents, temperature, pH, and metal precursor play crucial roles. Several reducing agents have been extensively studied [102,104,110–114], and sodium borohydride resulted to be the most effective choice. The pH of the solution significantly influences redox processes (related to H^+ and OH^- species in water), complexation, and reducing agent performance [115]. Temperature affects reaction potential, solubility, and growth mechanisms, with excessively high temperatures leading to uncontrolled growth and agglomeration [116,117]. Stabilizing agents on their part can employ electrostatic or steric mechanisms to prevent nanoparticle agglomeration [118].

The choice of stabilizing agent is critical as it affects aggregation prevention, particle size determination, and overall catalyst activity. For instance, polyvinyl alcohol, tetrakis(hydroxypropyl)phosphonium chloride, and citrate have been shown to play crucial roles in maintaining particle size and activity in the synthesis of gold nanoparticles [105]. The interaction between the metal and ligand in the stabilizing agent also influences catalyst activity, stability, and selectivity through various processes [119].

In conclusion, the sol immobilization technique offers advantages by allowing the pre-formation of the active phase in solution and precise control over nanoparticle size, shape, and properties. Careful control of parameters such as reducing agents, stabilizing agents, pH, temperature, and metal precursor is essential for successful application. This technique can be applied to various support materials, and provides flexibility in their choice, primarily dependent on the support's isoelectric point (IEP) and the nature of the stabilizing agent. The choice of stabilizing agent and its interaction with the metal nanoparticles can significantly impact the stability, selectivity, and activity of the final catalyst. Therefore, careful consideration and control of these parameters are crucial for the successful application of the sol immobilization technique.

1.3.1.1.2. Solvated metal atom dispersion (SMAD)

Having discussed the problematics related to liquid phase preparation routes, one solution to minimize the influencing factors during catalysts syntheses is proceeding through a gas-phase synthesis, which eliminates the use of solvents, stabilising surfactants and other complications

[101]. Vapour deposition techniques are often employed in industrial and laboratory catalysts preparation in order to obtain thin films of substances on chosen support material. Typically, the most used deposition technique is Chemical Vapor Deposition (CVD), which allows to produce uniform and stable thin films on solid materials, often useful in the semiconductor industry. The CVD technique takes advantage of the reaction between a precursor, in the gas phase, and the surface (wafer) on which the reaction happens. Volatile precursors react and/or decompose on the surface resulting in the deposited product. Nevertheless, the gas-to-particle conversion in the CVD process can lead to a heterogeneous composition of particles due to variations in vapor pressure, nucleation, and growth rates.

Solvated Metal Atom Dispersion (SMAD) represents an interesting approach to generating highly reactive solvated nanoparticles, which presents an intriguing modification of the Chemical Vapour Deposition (CVD) method. In this procedure, a bulk metal (in the form of powder or pellets) is subjected to Joule heating within an alumina holder under conditions of high vacuum (Figure 1.10). Through the co-condensation of metal vapours in the presence of weakly organic ligands serving as stabilizers (e.g., acetone, acetonitrile, or benzene), condensation occurs on the reactor wall, which is fully immersed in liquid nitrogen at a temperature of -196 °C. Upon gradual warming, the frozen matrix melts, initiating the nucleation and subsequent growth of metal nanoparticles. Here, the employment of slow warming together with a large excess of solvent:metal molar ratio, or the use of more strongly coordinating solvents yields smaller particles [120]. Finally, immobilization is achieved by simply inserting the desired support, followed by the necessary evaporation of the solvent.

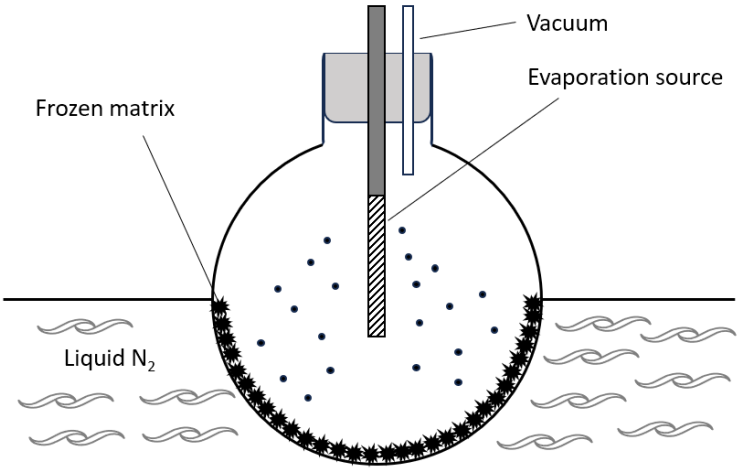

Figure 1.10. Schematic representation of solvated metal atom dispersion reactor vessel.

The significant advantage of this technique lies in its ability to directly synthesize nanoparticles in their metal oxidation state, thereby circumventing the need for subsequent activation steps that may introduce undesired modifications to the catalytic system, as reported in the sol immobilization technique. Furthermore, a notable feature of this variant is its utilization of bulk metal as a precursor, eliminating the requirement for often toxic and/or corrosive metal precursors employed in CVD processes [121].

1.3.1.1.3. Incipient wetness impregnation

Impregnation and drying is a methodology that involves bringing a metal precursor solution (consisting of dissolved metal salts) into contact with a porous support material.

The incipient wetness preparation method is an impregnation technique which is also known by the name of pore volume impregnation (PVI), name deriving from the fact that the amount of precursors solution used during the preparation is calculated to be exactly enough to fill in the pore volume of the support. This differentiates it from wet impregnation (WI), which works with an excess of the precursors' solution. Among the various techniques available, this method is one of the most commonly utilized for the preparation of heterogeneous catalysts, as it allows for the production of a limited amount of waste with a low-cost and straightforward preparation [122].

In the incipient wetness procedure follows this order: a precursor solution is prepared, usually chlorides or nitrates of the metal(s) in water, and the amount of employed water per gram is the one that has to be used to prepare a solution with the appropriate amount of metal precursor(s) that one wants to be supported. To help this process, the BET (Brunauer-Emmett-Teller) area measurement provides an assessment of the exposed surface area per gram of the material and can offer an estimation of the water-holding capacity within the support's pores. Then, the technique wholly revolves around the impregnation of the support with the solution until it reaches a saturation point where it can no longer absorb additional water without appearing visibly wet. Through the controlled, drop-by-drop spilling of the solution into the support, followed by mixing and mortaring the solution enters the pores of the support and is gradually let dry and evaporate. The phenomenon of capillary action takes place and facilitates the movement of the solution into the pores. Upon final calcination, the

nitrates are broken and the metallic species under the form of oxides remain anchored inside the pores, as illustrated in Figure 1.11.

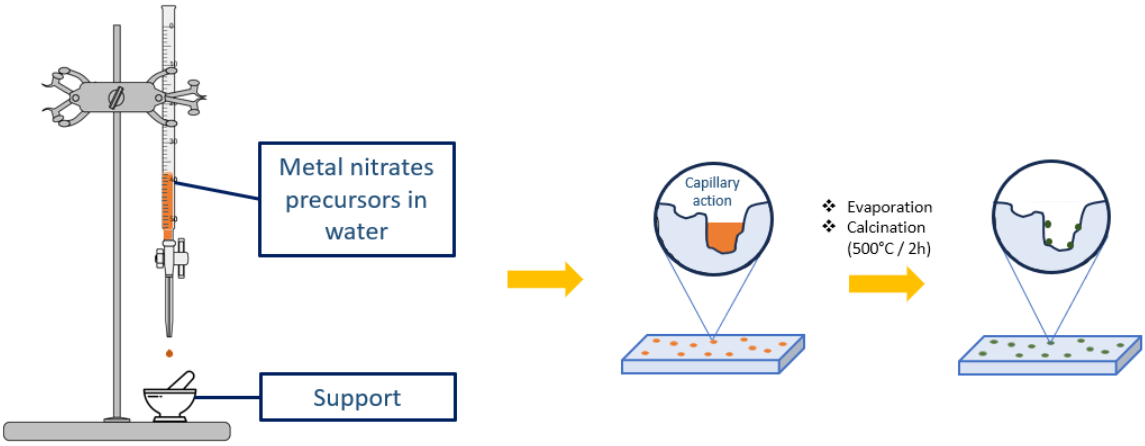

Figure 1.11. Schematic representation of the Incipient wetness preparation method.

Depending on the desired application, the so-obtained catalyst can then be reduced or oxidised in order to activate the metal species and to remove any remaining metal precursor residues.

Again, there are some parameters that can drastically influence the successful outcome of the preparation. As in sol immobilization, the pH of the solution is important for the effective electrostatic adsorption of the metal species on the surface of the support. To achieve that, the pH of the solution must be different than the point of zero charge (PZC) of the support material. This can make a difference when choosing whether to employ the wet impregnation or incipient wetness method [123]. The temperature and concentration of the precursors also affect the preparation. In fact, the temperature influences both the precursor's solubility and the solution viscosity, causing a different wetting time, whereas the concentration can influence the mass transfer conditions during impregnation and evaporation [124].

1.3.1.2. Bimetallic nanoparticles

In the past years, several families of bimetallic catalysts have been commercialised for use in industrial environmental treatment, chemical synthesis and petroleum refining processes. With the term bimetallic catalyst is intended a catalyst formed by two different metal atoms (Figure 1.12), often on a non-metallic support presenting some interaction. Bimetallic

nanomaterials can present various architectures including crown-jewel structure, random-alloyed structure, core-shell structure, heterostructure and hollow structure, among others. Depending on their bimetallic structure, these nanomaterials possess different chemical and physical properties [125].

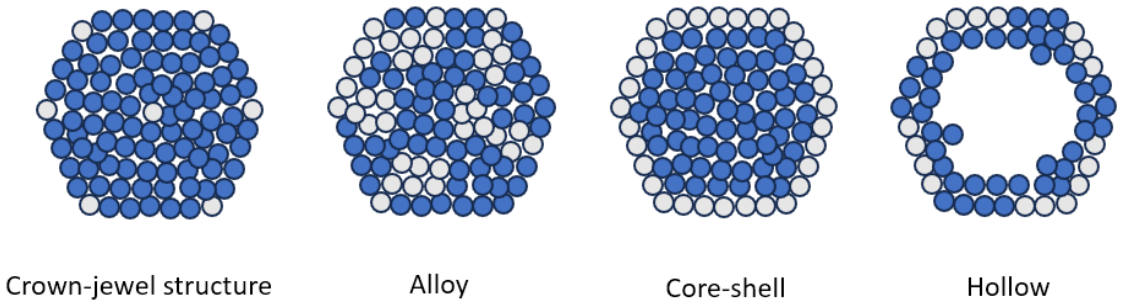

Figure 1.12. Possible structural arrangements of bimetallic alloyed systems.

Pertinently with the scope of this thesis, particular focus is given to random-alloyed bimetallic particles, which are characterised by a homogenous distribution of the two metals across the whole particle. Alloys are generally classified as interstitial or substitutional depending on the atomic arrangement. In substitutional alloys, when atoms are relatively similar in size, some of the atoms composing the original structure are substituted by the other component (e.g. in bronze alloy, some Cu atoms are substituted by Sn atoms). On the other hand, in the case of interstitial alloys, one of the two atoms is much smaller in size than the other, thus it penetrates the bigger atom structure and is trapped in the spaces between the atoms, the interstices [126] (Figure 1.13).

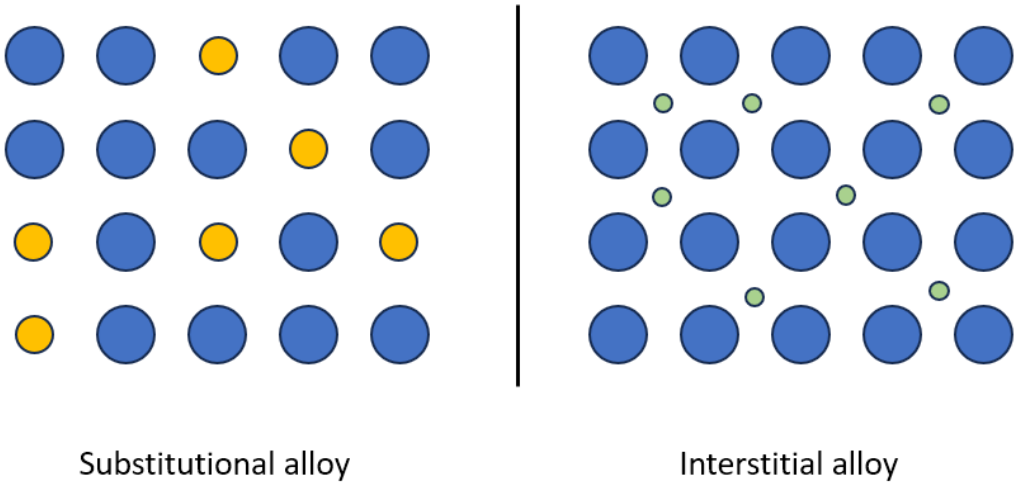

Figure 1.13. Differences between substitutional and interstitial alloys.

In general, control over the structure of bimetallic nanocrystals is achieved during the synthetic procedure by tuning thermodynamic (e.g. temperature, pressure, etc.) and kinetic (diffusion, solubility, etc.) parameters. Varying these parameters results in a different atomic distribution of the two metals, thus leading to different structures [125]. Moreover, if three or more metals are available to form alloys with each other, the resulting amount of each bimetallic alloy will be proportional to a) the molar amount of each metal, b) the ability to form an alloy with the partner and c) the surface contact between each metal couple.

The field of heterogeneous catalysis has recently turned its attention to the study of bimetallic catalysts because they have often been shown to outperform their monometallic counterparts in terms of both activity and selectivity.

There are two main effects resulting from the formation of a bimetallic system. The first is called “ensemble effect” and it involves a structural effect on composition of the active surface sites, that in turn can affect reactivity. This happens because, in monometallic systems, reagent molecules approach metal clusters with a preferential orientation, the one with the lower adsorption barrier. By introducing a second metal, the original surface composition can be disrupted, modifying the previous metal structure. This results in an alteration of the adsorption geometry which in turn can affect both activity and selectivity of the catalyst [127].

The second effect, namely ligand effect, consists in an electronic interaction resulting from the formation of new heteronuclear metal-metal bonds. It involves not only charge transfer from the less electronegative to the most electronegative metal, but also a shift of the d-band centre of the correspondent molecular orbitals compared to the parent metals. As an example, consider a reagent molecule that is experiencing chemisorption with a bimetallic system. Depending on the second metal introduced in the bimetallic system, the resulting d-band MO is at higher or lower energy compared to the single metal. This subsequently involves either the lowering or raising energy level of the antibonding (d-σ)* MO with the substrate. As a consequence, this MO has its electron density increased or decreased, respectively, thus either weakening or strengthening the substrate-metal bond. This phenomenon results in either favoured or unfavoured desorption and affects reaction rate [128]. These ensemble and ligand effects are deeply correlated to each other, and it is difficult to disentangle and study them separately.

1.3.2. Bulk catalysis

Unsupported materials employed in heterogeneous catalysis fall in the category of bulk catalysts. These systems occupy a large section of industrial catalysis and are mainly produced when the active components are cheap. Since the preferential preparation method is precipitation, they are also referred to as precipitated catalysts [129]. However, other methodologies comprise fusion and alloy leaching, sol-gel syntheses and microemulsions, hydrolysis and hydrothermal synthesis.

Bulk systems can be grouped as conductors (metals and alloys), semiconductors (oxides and sulphides) or insulators (metal oxides or solid acid or bases) [36]. Among these categories, metal oxides and mixed metal oxides, which can range from the typical MO_x oxide to clays, zeolites and metal phosphates, are the most employed in industry. These systems are exploited in reactions such as ammonolysis, dehydrogenation, dehydration of alcohols, ammoxidation and many oxidation processes [130].

Already in the 1930s, clays and aluminosilicates were investigated in applications such as crude oil cracking to produce high quality gasoline. No further than ten years later, synthetic alumina-silica catalysts, or zeolites, replaced them due to their higher surface area and are still used today in the fluidized catalytic cracking (FCC) process [131]. On the other hand, metal oxides found applications in the petroleum industry, organic synthesis, fine chemical production and green chemistry [132].

Metal oxides are binary compounds of oxygen with a metal, possessing a surface featuring oxide anions (O^{2-}) bound to a metal cation (M^{x+}). The surface of these materials is important, as its properties differ from the properties of the bulk due to a different coordination symmetry of the metal cations. Moreover, the presence of defects of various types (O vacancies, terraces, kinks) is another fundamental characteristic of these materials, as it can greatly influence the catalytic performance [133]. Particularly for transition metals oxides (TMO), the control of defects for obtaining enhanced or unprecedented functional properties opened a recent investigation field called defect engineering, also due to the great electronic properties of these materials, majorly linked to their partially unoccupied d orbitals [134]. Oxides containing two or more different metal cations are called mixed oxides, and can be binary, ternary or quaternary. In a crystalline mixed oxide, while it is often difficult to

understand which of the metal cations is the active centre of a catalytic site, the presence and prevalence of different crystallographic faces was proven to give rise to different catalytic properties of the final material [132]. On the other hand, amorphous mixed oxides generally exhibit high surface area and frequently feature a microporous pore structure [135]. They possess unique properties, and unlimited possible variation in composition, pore architecture and domain size tuneable with the synthetic procedure, which is why they are meeting research interest [136].

The development of catalysis science regarding bulk mixed oxides has been constrained by the intricate nature of catalyst powders, including variable oxidation states and coordination, the chemical properties of surface sites (such as redox, basic, or acidic properties, either Lewis or Bronsted), involvement of surface and bulk lattice oxygen atoms in oxidation reactions, and the presence of vacancies or defects [137]. Nevertheless, the advantage of using cheap metal systems, with high chemical and physical stability and possessing great redox properties is fuelling the investigation of their applications. Among all the bulk systems presented, this thesis work will focus on mixed oxides, which were prepare and utilized for cyclohexane oxidation.

1.3.2.1. Mixed oxides preparation

Mixed oxides can be obtained with a variety of methodologies. Among them, liquid-phase preparation methods prevail, such as coprecipitation, sol-gel and hydrothermal syntheses [138], and also inverse microemulsion [139].

The coprecipitation process involves creating an aqueous solution that contains the desired cations and combining it with another solution that contains the precipitating agent. The resulting precipitate is then separated from the liquid through filtration, dried, and subjected to thermal decomposition to obtain the desired compound. The method can be carried out at constant or variable pH [140], and other parameters such as mixing rate or temperature control the final result. In this regard, the nature of the metals is key. For example, if two metals possess similar precipitation pH, they can form an intimate solid solution whereas, if their precipitation pHs are very different, eventual segregation of the particles can be achieved.

The sol-gel preparation method involves the creation of an amorphous gel through the combination of solutions, which is subsequently dehydrated at relatively low temperatures [141]. This method offers significant advantages, including high purity and precise control over the composition of the resulting mixed oxide particles. Alkoxides of the metal species are used as precursors, which is advantageous as they readily react with water forming the initial colloidal sol by hydrolysis and polycondensation. However, the use of alkoxides increases the cost of the preparation quite significantly, and the nature of the metal species chosen influences the process as well.

The hydrothermal method has gained significant popularity in the fabrication of nanostructured materials due to its straightforward process, excellent efficiency, and cost-effectiveness [142]. It employs temperature between the boiling point of water and its critical temperature, and pressures up to 15 MPa, and can require a final calcination step. This technique facilitates the growth of crystals at temperatures well below their melting points, offering the possibility of discovering new crystal phases or the production of larger bulk crystals with reduced thermal strain [143], with good control on the crystallinity of the final materials.

The inverse microemulsion method was chosen among all these methods for the preparation of oxides and mixed oxides of this thesis work, due to the advantages of obtaining very homogeneous mixed oxides with high surface area and crystalline structure. Therefore, the preparation is discussed in depth in the next section.

1.3.2.2. Inverse microemulsion

The term microemulsion was defined in 1959 by Schulman et al. [144], and his group worked on optimizing and describing the preparation methods in the following years. From oil recovery to the synthesis of nanoparticles, microemulsions have been investigated in wide range of applications up to this day.

Numerous modifications of the inverse microemulsion methodology have been developed over the years. The one employed in this thesis work consists in preparing two aqueous solutions, one containing the metal precursors (nitrates) and the other a precipitating agent (hydroxide species). At this point, two distinct microemulsions are prepared, stabilizing the

aqueous solutions in an organic phase (from here the term “inverse” or “water-in-oil”) with the help of a suitable surfactant and co-surfactant. Once the two microemulsions are stable, the one containing the base is poured into the other. Upon mixing, the droplets come in contact and the metal precursors precipitate as the corresponding hydroxides and oxides. After, centrifuge washing of the solution with an organic phase (e.g. methanol) is necessary to remove the organic components. Upon drying, the catalyst is calcined in order to break the nitrates, transform the remaining hydroxides into oxides and completely remove any remaining template, thus obtaining the final mixed oxide. A schematic representation of the methodology is reported in Figure 1.14.

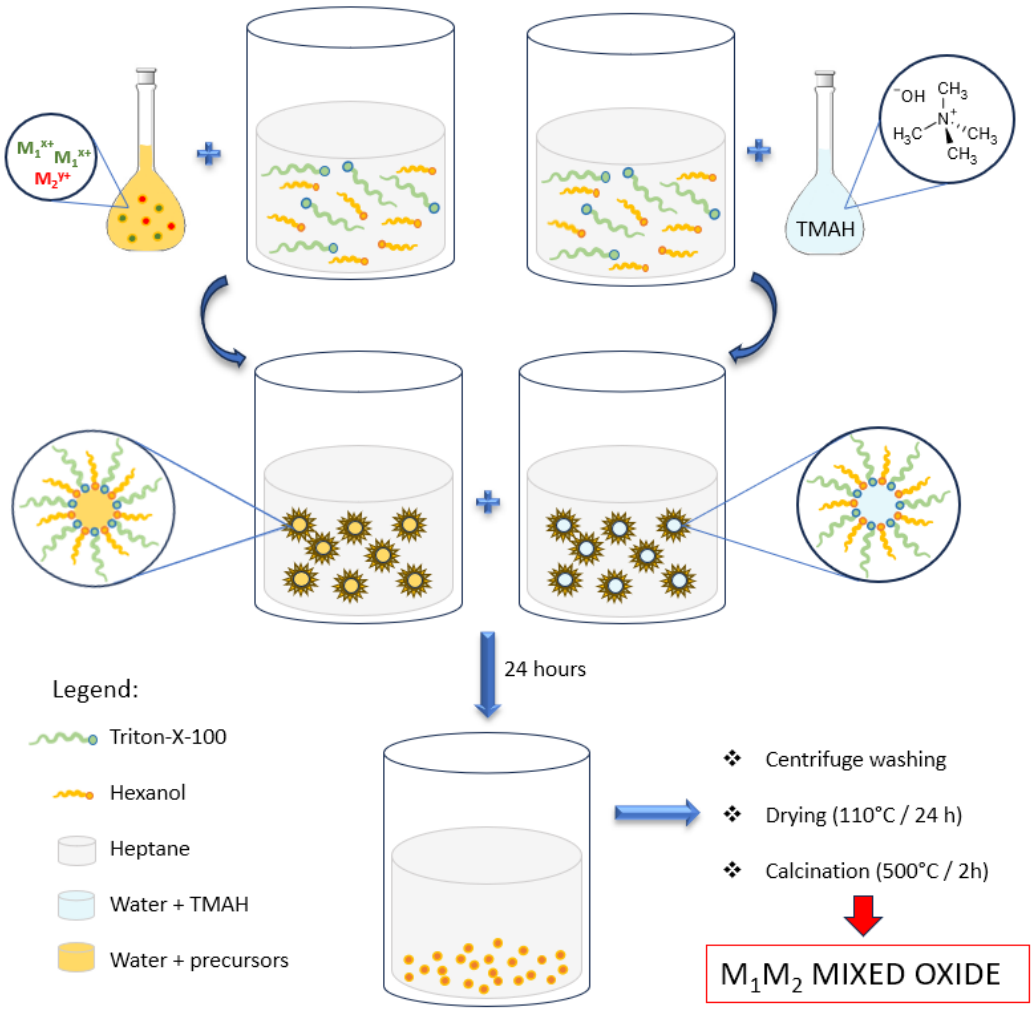

Figure 1.14. Schematic representation of the inverse microemulsion preparation method.

Various parameters can influence the result of the technique. Various research teams have observed distinct patterns regarding the impact of intermicellar exchange rate [145], water-to-surfactant molar ratio and reactant concentration [146].

Microemulsions are in fact complex systems from a thermodynamic perspective due to their composition of at least four components and the presence of an electric double layer encompassing the droplets, where this electric double layer significantly contributes to the system's free energy [147]. Among the components, the co-surfactant, being uncharged, can easily adsorb without being hindered by the electric field, thereby facilitating the reduction of interfacial tension necessary for microemulsion formation. The water content within the system is important as well and it is quantified by the water to surfactant molar ratio, denoted as ω_0. Studies have demonstrated that the initial ω_0 value directly influences the final particle size [148–150], enabling control over synthesis outcomes by adjusting ω_0. Furthermore, if reactant concentration is increased it was demonstrated to correspond to an enlargement in particle size [151].

At the end of the procedure, the inverse microemulsion preparation allows for the obtainment of mixed small sized particles (around 10 nm) of each phase present, possessing crystalline structure. If the preparation is carried out correctly, the two or more phases result very homogeneously mixed and retain a satisfactory correspondence between the theoretical composition (% of the metals) and the actual composition.

1.3.3. Characterization techniques

Characterization of the prepared materials is a key point for the understanding of their properties and behaviour in a specific reaction. On solid materials such as heterogeneous catalysts, characterization can be carried out through a variety of different techniques. Among these, one of the most complete techniques is electron microscopy, which allows for full morphological assessment of the specimens.

Electron microscopy comprises a family of techniques which can mainly be divided into scanning electron microscopy (SEM) and transmission electron microscopy (TEM). SEM uses a focused beam of electrons to scan the surface of a specimen. When the electrons interact with the sample, they produce signals such as secondary electrons, backscattered electrons, and X-rays. These signals are detected and used to create a detailed image of the specimen's surface morphology. On the other hand, TEM utilizes transmitted electrons and the resulting interactions between the electrons and the specimen provide information about the

specimen's composition, crystal structure, and morphology [152]. Electron microscopes (both in SEM and TEM mode) can also be equipped with an Energy Dispersive X-ray (EDX) detector for performing the elemental analyses of the samples. TEM can also include an Electron Energy Loss Spectrometer (EELS). The detailed analysis of the fine structure of the spectra allows for determining, in addition to composition, other properties of the material such as coordination environment, oxidation states, etc..

Among X-ray related techniques, a surface sensitive technique which is also frequently utilized for the characterization of solid materials is X-ray photoelectron spectroscopy (XPS). In XPS, the kinetic energy at which electrons are emitted after the sample is exposed to X-Rays, is specific to the elements present on the material's surface. XPS can provide information about oxidation states and composition. On the other hand, for measurements of crystalline materials, X-ray diffraction is a complementary technique which can deliver priceless information on the crystalline phases of the material. These two techniques combined are very helpful for determining the structural and electronic variation of a catalyst after usage or upon a reduction/oxidation treatment.

For the characterization of other surface properties of solid materials, such as the surface area or pore volume, many adsorption techniques have been developed. BET analysis is one of the most widely employed, as it allows to measure the surface area, the type and volume of the pores and their distribution, and gives information on surface interactions. Another gas adsorption method is diffuse reflective infrared Fourier transform spectroscopy (DRIFTS), which allows for the detection of active surface sites using probe molecules as CO [153].

When structural modifications take place, Raman Spectroscopy offers valuable insights into reaction mechanisms by providing specific information about defects in the catalyst's structure, both within the bulk material and at the surface. Additionally, it allows for the detection of adsorbates and reaction intermediates, further enhancing our understanding of the process [154].

In this thesis, the assessment of structure-activity correlation was investigated studying the prepared catalysts with electron microscopy, X-ray diffraction and photoelectron spectroscopy and BET surface area measurements.

1.3.3.1. High resolution transmission electron microscopy (HRTEM)

High resolution transmission electron microscopy (HRTEM) is a powerful technique that allows for the determination of the atomic structure of a sample [155].

In HRTEM mode, a parallel electron beam interacts with the sample, generating a transmitted beam and several diffracted beams that have slightly changed direction, resulting from the elastic and coherent scattering of the electron beam with the electric potential of the material. As the electron-matter interaction is strong, the intensity of the diffracted beams is high, and they may undergo several consecutive scattering phenomena before leaving the material. This multiple scattering process is called dynamic diffraction and is minimised for very thin samples. This "multiple scattering " [170] effect implies that the amplitude and phase of the diffracted beams depend on the thickness of the material. These beams, after passing through the sample, are focused by using the objective lens, as shown in Figure 1.15.

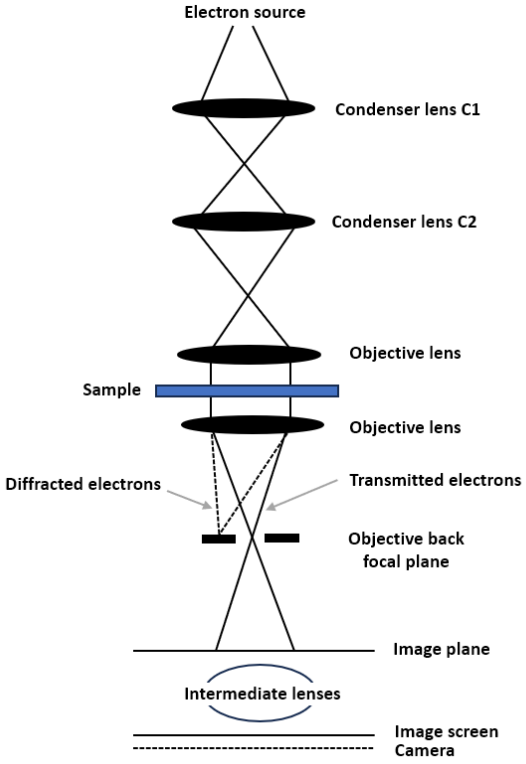

Figure 1.15. Schematic representation of the electron microscope in HRTEM mode.

This lens forms the diffraction pattern of the material at a finite distance (in the back focal plane), which generates the first image by the subsequent interaction of the diffracted beams. The quality of the objective lens is decisive as the intermediate lenses and the projection lens magnify the image formed in the objective lens.

To form a HREM image, the transmitted beam and several diffracted beams are selected with the aperture of the objective lens and interact with each other causing a series of modulations in the intensity of the image in the form of interference fringes. If the observed material is crystalline and correctly oriented, one- and two-dimensional fringe patterns that are related to atomic columns and planes can be observed using this technique. HREM images are not directly interpretable, however, digital diffraction patterns (DDPs), which are simply a representation of the square of the Fourier Transform modulus of the image on a logarithmic scale, can be obtained from them to extract structural information. For this purpose, the angles and spacings between the reflections corresponding to the different crystalline planes in the digital diffraction patterns are measured, and the spacings in the real planes are calculated and compared with those of the crystalline phases under study. An example is reported in Figure 1.16. The phase is attributed through the angles and distances measurements, using a database (here EjeZ software) for finding the correct phase and the indication of the zone axis ([u v w]) from which the phase is hit by the electron beam (in this case [1 0 1]).

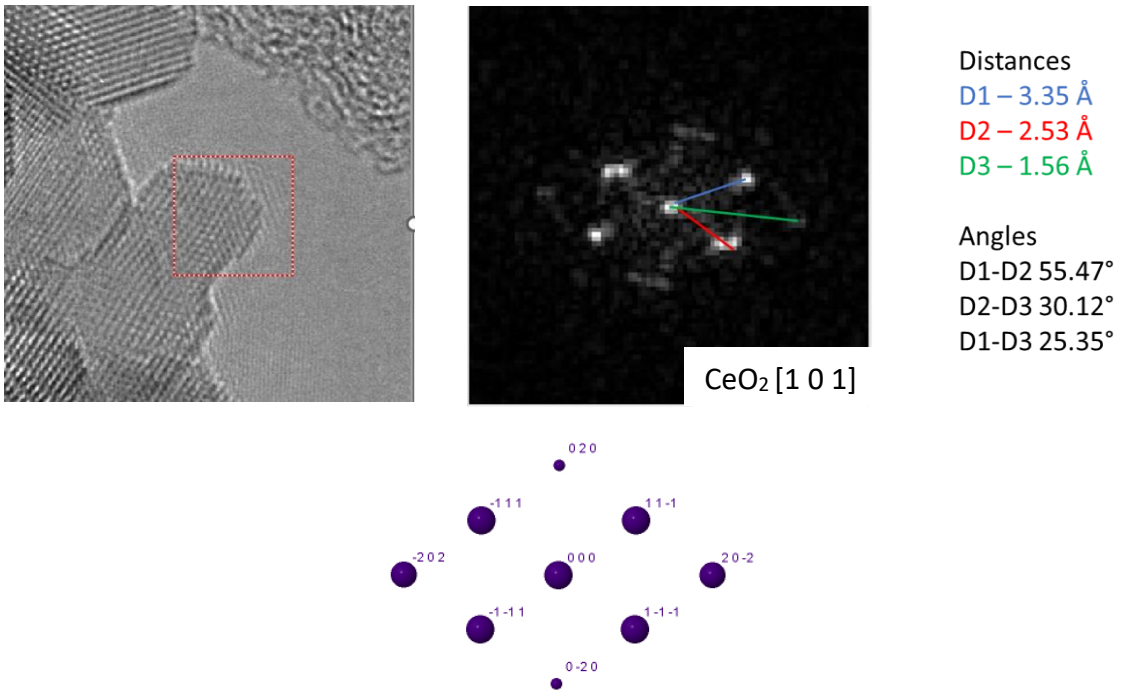

Figure 1.16. Examination of the angles and distances in the digital diffraction pattern obtained from a HRTEM image of a sample containing CeO_2. Image acquired with the Talos F200X microscope at Cádiz University and processed using Digital Micrograph and EjeZ softwares.

In order to obtain structural information with a spatial resolution better than 1 Angstrom, the use of Aberration corrected microscopy (AC-HREM) is necessary. By correcting the aberrations of the objective lens, the delocalisation effects observed on the surface of the catalyst particles when high resolution images are acquired with conventional microscopes are minimised. This feature therefore allows sharp surfaces to be displayed and is essential for a detailed analysis of the metal-support interface.

Spherical aberration is an optical phenomenon in which light rays passing through a lens or mirror with a spherical surface fail to converge at a single focal point, causing oblique rays to focus at a different location than the central rays. Experimentally, the correction of spherical aberration (Cs) in image-corrected microscopes is done by using the Zemlin method [156]. This procedure consists of the iterative correction of the different aberrations of the lenses. For this purpose, the Fourier transform of an amorphous area (usually carbon) at different beam tilt angles, thus creating the so-called Zemlin tableau [157] (Figure 1.17). The software then determines the values of the aberrations and suggests the corrections to be introduced to improve these values. This procedure is carried out as many times as necessary as many times as necessary until the optimal values for image acquisition are obtained.

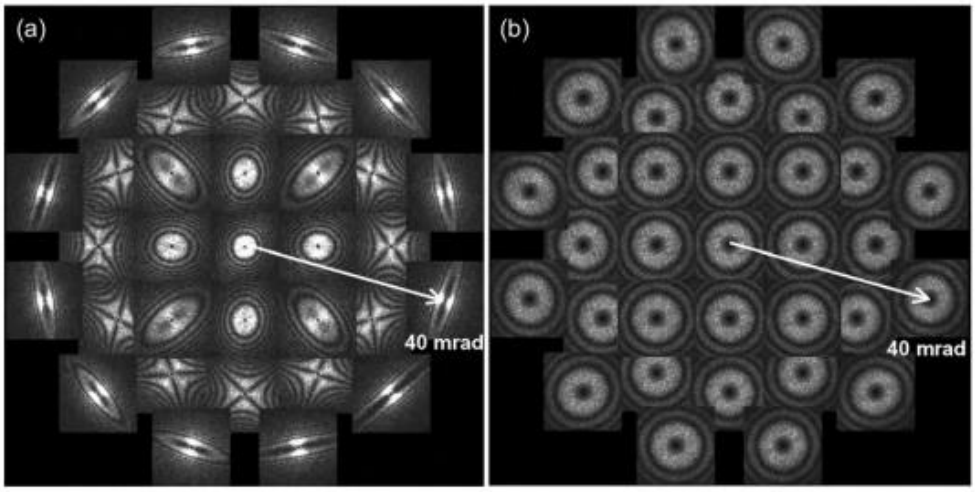

Figure 1.17. Zemlin diffractogram tableau from a series of TEM images of an amorphous carbon film (a) without (Cs = 0.65 mm) and (b) with correction. Image published from Hosokawa et al. [146], DOI:10.1093/jmicro/dfs134.

Modern double corrected microscopes also feature chromatic aberration correction (Cc). Chromatic aberration consists in a spread of electron beams on the focal plane of the objective lens due to the difference in the focal positions for the electron beams with different energies.

Cc correction was achieved later, and one of the most revolutionary consequences of Cc correction is the possibility to perform better in situ real-time techniques [158]. In conclusion, the utilization of Cs and Cc correction enables the attainment of higher levels of image resolution at lower accelerating voltages, thereby offering a means to mitigate or eliminate electron irradiation-induced damage in samples [159].

1.3.3.2. Scanning transmission electron microscopy (STEM)

Scanning Transmission Electron Microscopy allows for high-resolution imaging and provides detailed information about the structure and composition of samples at the nanoscale. [160]. Differently from a conventional TEM, in STEM mode the electron beam is focused to a fine spot that scans the sample, the image obtained being an intensity distribution map of the signal collected by the detector. In this mode there are different signals that can be recorded by different detectors: electrons that pass through the sample without appreciable deflection (bright field signal, BF), electrons which have been deflected at low angles (annular dark field signal, ADF), and electrons scattered at very high angles collected by the high-angle annular dark-field detector (HAADF signal). A schematic representation of the detectors positioning is reported (Figure 1.18).

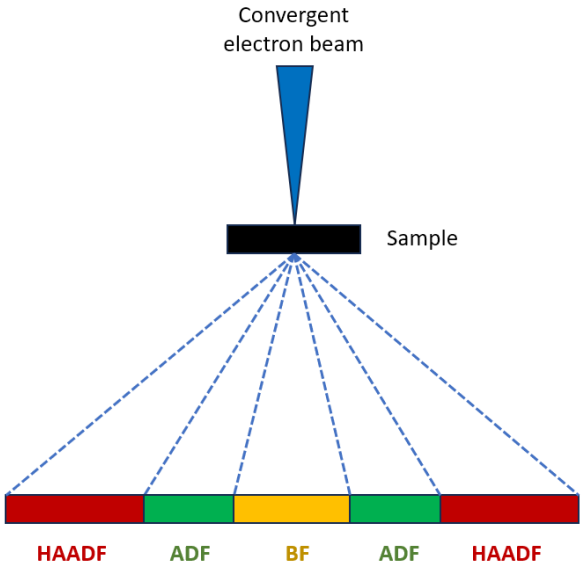

Figure 1.18. Schematic representation of the detectors equipped on a modern electron microscope for STEM mode.

The electrons collected by the HAADF detector are scattered at a high angle as a result of an incoherent elastic interaction, a phenomenon referred to as the Rutherford scattering [161].

The image formed is proportional to the thickness of the sample [162] and to the square of the atomic number (a Z'), hence they are called contrast images. These images of an incoherent nature are formed by the convolution between the convergent beam and an object function which has maxima at the positions of the atomic columns parallel to the beam. Therefore, if the beam size is smaller than the interatomic distances and the orientation of the crystal is appropriate, atomic resolution images can be obtained[1]. The incorporation of probe correctors, which minimise the aberrations of the condenser lens, allow the resolution of these images to be improved to values close to or even below the Angstrom.

The spherical aberration correction mode in STEM mode is very similar to that used in HREM mode, but in this case a Zemlin table is generated which contains a set of images of the deconvoluted (underfocus and overfocus) probe images at different angles of inclination. From here, an iterative process is started to correct the aberration coefficients.

Due to the possibility of studying the composition of materials and particles with nanometric precision, particularly useful when observing nanoparticles dispersed on a support with high surface area, usually the STEM mode is associated with elemental composition analysis of the scanned areas. In order to carry it out, the Energy Dispersive X-ray Analysis (EDX) apparatus is mounted on the electron microscope.

1.3.3.3. Energy dispersive X-ray analysis (EDX)

EDX is a is an analytical technique used for the elemental analysis of a material The technique can be performed a quick and easy way, it allows for coverage for all but the lightest elements, and quantitative data can be obtained as well [163].

By interacting inelastically with the sample, an incident electron can strip an electron from one of the inner layers of the atom. The gap left by this electron can be filled by one of the upper electron shells, emitting the excess energy in the form of X-rays. The emission of energy is characteristic of the electronic jump between the two layers involved in the process, which makes it possible to identify the presence of a certain element [161]. Thus, a detector can collect these X-rays, analyse them for energy and obtain an X-ray energy dispersion spectrum, each signal with a specific chemical element and a specific energy jump. EDX experiments thus allow the identification of the elements present in the sample either in a point or in a selected

area. In addition, it is possible to determine the ratio between these elements from various quantification protocols [164].

1.3.3.4. X-ray photoelectron spectroscopy (XPS)

The XPS technique (X-ray Photoelectron Spectroscopy) is based on the photoelectric effect Figure 1.19, which occurs when a high-energy electromagnetic radiation beam (typically in the X-ray range) interacts with a material, causing the emission of electrons. The kinetic energy at which these electrons are emitted is specific to the elements present on the material surface. Furthermore, by carefully analysing the signals, other parameters such as oxidation states or chemical environment of these elements can be extracted [165].

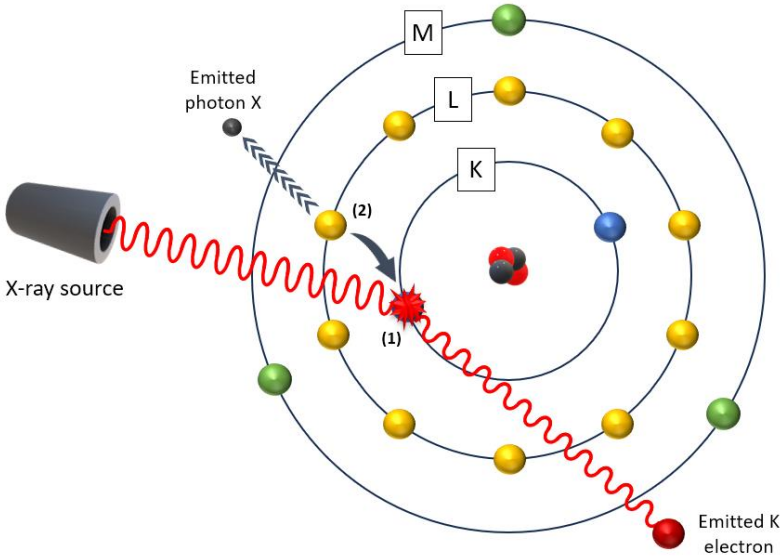

Figure 1.19. Schematic representation of the photoelectric effect.

Typically, the acquired spectrum encompasses both valence band and core-shell electrons. However, given the abundance of information provided by valence band electrons within a limited energy range and the complexities associated with their analysis, it is preferable to focus on the evaluation of core-shell electrons. This approach facilitates the differentiation of various elements present in the sample. The spectrum is characterized by multiple sharp peaks superimposed on a continuous background. These narrow peaks correspond to pure photoelectrons emitted from the sample, satellite peaks, and Auger electrons resulting from the emission of additional electrons. The auger electrons emission is represented in Figure 1.20.

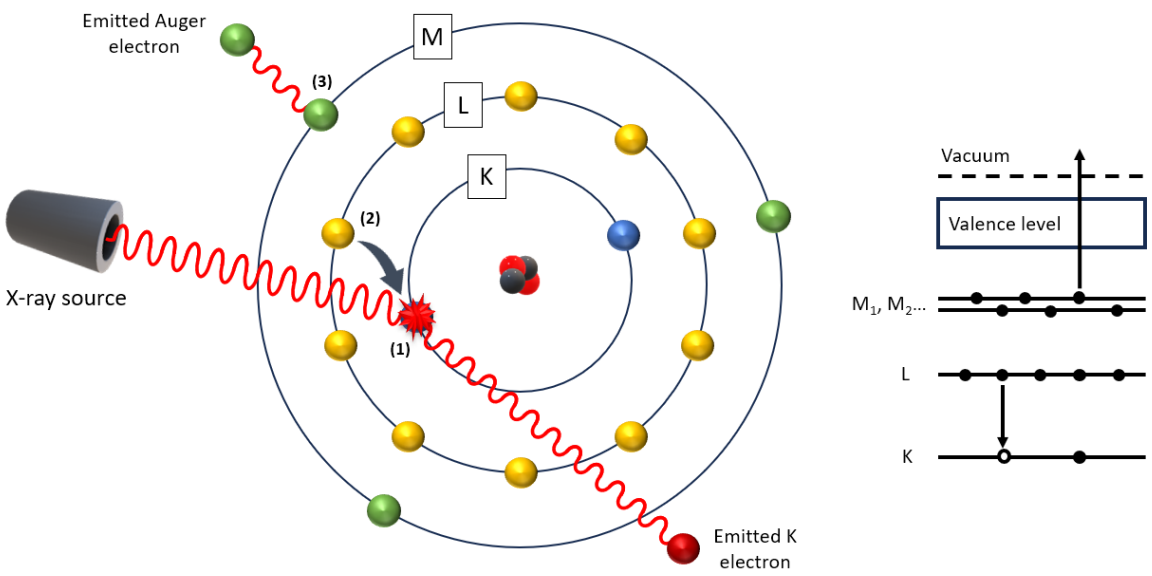

Figure 1.20. Schematic illustration of an Auger electron emission.

The results obtained by the XPS technique focus only on the first few nanometres of the sample surface (1-10 nm, depending on the element being analysed). This limited probing depth arises from the inelastic scattering of low-energy photoelectrons, causing them to lose energy upon penetration into the material and preventing their escape from the sample [166].

In a classical XPS spectrophotometer (Figure 1.21) an excitation source, such as an X-ray tube or synchrotron radiation, generates an X-ray beam, which is focused onto the sample surface using electron lenses. Magnesium (Mg) and aluminum (Al) are commonly employed as X-ray sources due to their intense X-ray emission and narrow energy bandwidth. The experimental setup operates under ultra-high vacuum (UHV) conditions to minimize gas collisions with the emitted photoelectrons. Subsequently, the emitted electrons enter electron lenses that guide them towards the analyzer. Within the analyzer, only photoelectrons with a specific energy can traverse the electrostatic field established between the hemispheres. Finally, the electrons are amplified and detected at the exit slit by the electron detection system [167].

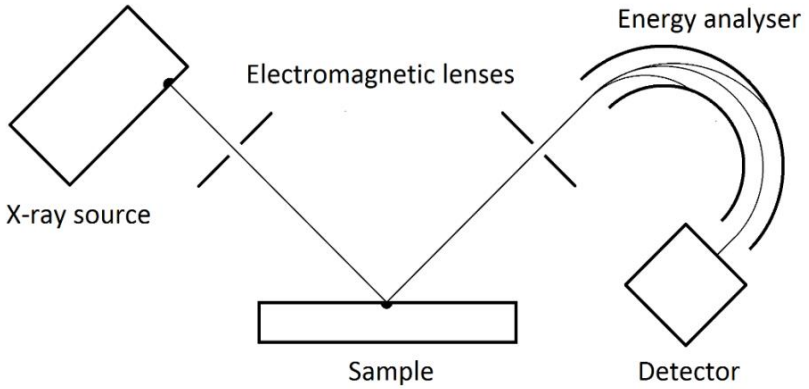

Figure 1.21. Schematic illustration of an XPS spectrophotometer.

In conclusion, the efficacy of XPS as a technique stems from the fact that the chemical surroundings of an atom significantly influence the measured binding energies (BEs) of core-level electrons, a phenomenon known as chemical shift [168]. This feature enables the determination of bonding structures and their variations with respect to processing parameters or surface treatments. The identification of existing bonds is typically accomplished by comparing the measured BE values with those available in literature databases [169].

1.3.3.5. X-ray diffraction (XRD)

When an electromagnetic radiation with an appropriate wavelength (X-rays) interacts with a crystalline solid, a diffraction phenomenon occurs, which is described by Bragg's Law [170].

$\lambda=2d\sin\theta$, where θ is the diffraction angle, λ is the wavelength of the incident radiation, and d is the spacing between atomic planes. Different operating modes exist in X-ray diffraction (XRD), with the most common one being the powder X-ray diffraction mode, used when working with polycrystalline and multiphase samples, such as most heterogeneous catalysts. In this technique, the sample is distributed over a confined surface, and the diffracted beams are collected at various angles (Figure 1.22).

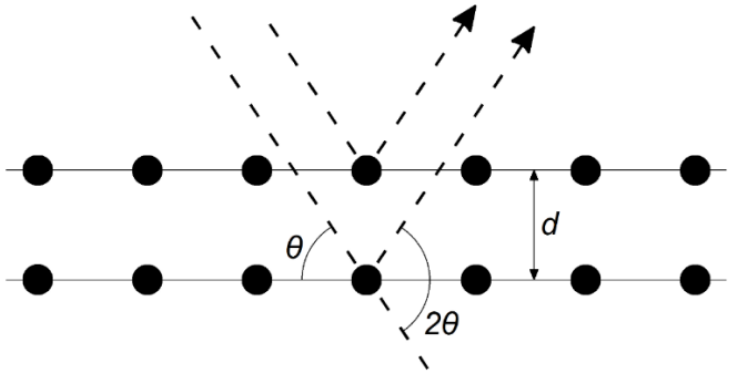

Figure 1.22. Schematic representation of Bragg's parameters.

The obtained powder diffraction patterns are represented as rings, which, when plotted in a unidirectional manner, become diffraction peak patterns. Various information can be extracted from the position, width, and height of the diffraction peaks. The most important ones include the identification of crystalline phases present in the sample, crystal stress, and crystalline domain size.

To measure the volume-weighted average crystalline domain size, the Scherrer Equation was employed (

Equation 1.1):

$$\tau = \frac{K \cdot \lambda}{\beta \cdot \cos\theta}$$

Equation 1.1. Scherrer's Equation for the determination of the average crystalline domain size.

Where θ is the average domain size weighted in volume, K is a dimensionless factor close to 1, λ is the X-ray wavelength, β is the width of the chosen peak (typically the most intense one) at half of its height after subtracting the intrinsic broadening caused by the measurement instrument, and θ is the Bragg angle.

1.3.3.6. Nitrogen physisorption using BET theory

Brunauer-Emmett-Teller (BET) theory, serving as the basis for an important analysis technique, aims to explain the physical adsorption of gas molecules on a solid surface and provides insights into the measurement of the specific surface area, porosity, and pore size distribution of materials. This theory applies to systems of multilayer adsorption and utilizes non-reactive

gases as adsorbates to quantify the specific surface area [171]. Among the gases commonly employed for surface probing in BET methods, nitrogen is the most frequently used.

Most solid materials contain voids within their structure which can be characterized based on their size, type, and shape and are referred to as pores. Porosity is a property that encompasses all the pores present within the material, either in their entirety or as an overall effect. The overall porosity is determined by calculating the ratio of the volume of pores to the total volume of the material [172]. The specific surface area represents the ratio of the total surface area of the porous material to its mass, while the percentage of porosity corresponds to the ratio of the total volume of cavities to the total volume of the material.

The surface area of a material is often associated with various properties like dissolution rates, catalytic activity, moisture retention, and shelf life. Equation 1.2, known as the BET equation, explains the connection between the number of gas molecules adsorbed (X) at a specific relative pressure (P/P_0). Additionally, there is a second parameter, C, which is linked to the heat of adsorption [173].

$$\frac{1}{X\left[\left(\frac{P_0}{P}\right)-1\right]} = \frac{1}{XmC} + \frac{C-1}{XmC}\left(\frac{P}{P_0}\right)$$

Equation 1.2. BET equation describing the relationship between the number of adsorbed molecules and the relative pressure.

For most solids, specifically when nitrogen is used as the adsorbate, the BET equation generates a linear graph of $1/[X(P_0/P)-1]$ versus P/P_0, although this linear relationship is only applicable within a restricted region of the adsorption isotherm. The surface area of the material is calculated from the slope and intercept of this linear plot.

In a typical BET experiment, the sample is degassed for a defined time, and then both the adsorption and subsequent desorption of N_2 take place keeping the sample cooled at -77°C (with liquid N_2). The adsorption and desorption isotherms thus obtained are important to classify the type of pores present in the material. There are six main types of isotherms for porous materials according to IUPAC classification (Figure 1.23).

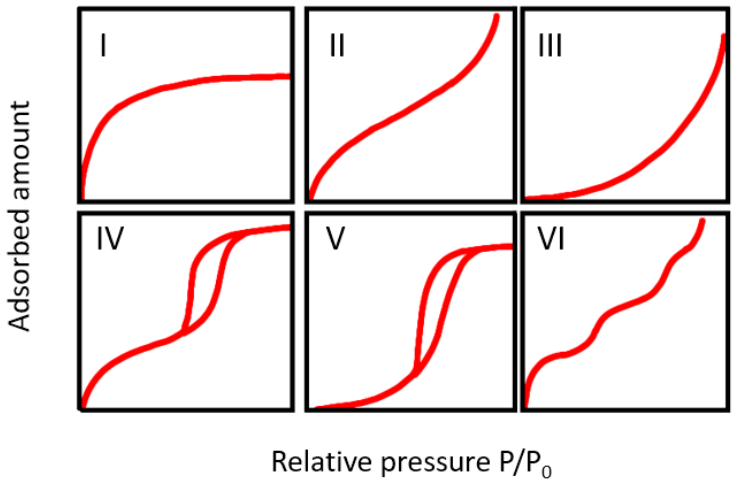

Figure 1.23. IUPAC classification of the possible adsorption and desorption isotherms for porous materials.

Isotherm I is typical of microporous materials, whereas isotherms II, III and VI are typical of nonporous or macroporous materials. Isotherms IV and V are the most common and are related to mesoporous materials, both presenting a hysteresis loop. There is a widely acknowledged relationship between the texture of a mesoporous material, such as pore size distribution, pore geometry, and connectivity, and the shape of its hysteresis loop [174].

The behaviour of numerous adsorption systems is covered by the Brunauer and IUPAC classifications of gas-solid adsorption isotherms. However, there are cases where the isotherms of certain systems do not fit into any of the IUPAC classes and are not classified as intermediate between the existing cases [175]. Nevertheless, the IUPAC classification is still valid in most cases and also in this thesis work, where the materials fit the mesoporous category.

1.3.4. Analytical concerns

It is well established that product analysis for this reaction is complicated due to different reasons such as a) the solubility of the products after cooling down the reactor, b) the thermal stability of some products such as CyOOH, c) gas-phases products that could evaporate while opening and refilling the autoclave and d) evaporation of cyclohexane itself during the work-up [30]. The use of a suitable internal standard is ~~also~~ preferred to minimize the errors related to mixing volumes and the variations due to evaporation and other phenomena happening in the batch withdrawals. However, the choice of a suitable internal standard is not easy, being

the reaction pathway radical-mediated thus generating highly reactive species. Biphenyl and chlorobenzene are among the employed internal standards in the literature [7,29,30,57,74,176–178].

Another concern is represented by the number of liquid-phase by-products possibly obtained from the free radical overoxidation of cyclohexanol and cyclohexanone. Many are the possible oxidized products of cyclohexane deriving from the addition of O to the ring or even ring-opening, and it is often difficult to distinguish between them with GC analyses. Regarding the solubility of by-products in the reaction mixture, one of the most relevant issues is represented by the production of adipic acid. Indeed, adipic acid obtainment is preferrable to KA oil itself, being it a worthy chemical at the root of the polymerization process to obtain nylon-6,6 (see chapter 1.1.2. Adipic acid and ε-Caprolactam). Adipic acid is insoluble in cyclohexane, and only partially soluble in minor amounts in cyclohexanol [179]. Therefore, whenever it is produced, the majority of it remains in the form of white/transparent solid on the bottom of the autoclave. In order to perform an actual quantitative analysis though, a method for recovering also the dissolved part is necessary and will be presented in this thesis work.

1.4. Project aims and objectives

This doctoral thesis framed the co-supervision agreement (co-tutela) between the Universities of Milan and Cádiz. In this frame, the collaboration between the two universities was strengthened through a solid exchange of information, publications and techniques which gave reciprocal advantages, made possible due to my extended stay and participation to the activities in both sites.

My thesis project was aimed at the development of innovative heterogeneous catalysts for the selective oxidation of cyclohexane to KA oil. The prepared materials were tuned through preparation and characterization and selected in terms of selectivity to the desired product, but also productivity of KA oil compared to state-of-the-art competitors. Numerous catalytic tests were performed and were necessary to study the optimal reaction conditions, as the right catalyst:substrate ratio, the influence of the initial concentration of the radical initiator, the stirring and the sampling methodologies. Moreover, the difficulties existing in products

analysis were addressed by the utilization of different techniques. All the new catalysts were tuned and tested to work under much milder reaction conditions (120°C and 4 bar pressure) than the industrial practice and most state-of-the-art works, using O_2 as oxidant.

In Milan, due to the available equipment and thanks to the experience of the group in catalysts preparation, my focus was oriented to the preparation of new materials, catalytic testing, and thorough products analysis. On the other hand, thanks to the advanced characterization techniques present in Cádiz and following the purpose of my co-tutela there, during my stay I have been trained on electron microscopy and other solid-state analytical techniques which I successfully utilized for characterizing the catalysts, with the aim of inferring important structure-activity correlation.

1.5. References

[1] M.T. Musser, Ullmann's Encycl. Ind. Chem. (2005).

[2] K. Ueda, M. Hosoda, T. Matsuda, K. Tai, Polym. J. 30 (1998) 186–191.

[3] Y. Lee, K.Y. Andrew Lin, E.E. Kwon, J. Lee, J. Clean. Prod. 227 (2019) 624–633.

[4] E. Skoog, J.H. Shin, V. Saez-Jimenez, V. Mapelli, L. Olsson, Biotechnol. Adv. 36 (2018) 2248–2263.

[5] WMS Strategy, The Global Caprolactam Market - Research and Markets, n.d.

[6] A.K. Suresh, M.M. Sharma, T. Sridhar, Ind. Eng. Chem. Res. 39 (2000) 3958–3997.

[7] L. Wang, Y. Zhang, H. Yuan, R. Du, J. Yao, H. Li, Catal. Letters 151 (2021) 1663–1669.

[8] M.A. Andrade, L.M.D.R.S. Martins, Catal. 10 (2020).

[9] J.T. Tinge, Liq. Phase Aerob. Oxid. Catal. Ind. Appl. Acad. Perspect. (2016) 33–39.

[10] 2020-2027 Cyclohexanone Market Size | Global Industry Report, Cyclohexanone Market Size | Global Industry Report, 2020-2027, 2023.

[11] M. Hu, H. Tian, Chinese J. Chem. Eng. 40 (2021) 96–105.

[12] 2030 Cyclohexanol Market Size, Share & Growth Report, Cyclohexanol Market Size, Share & Growth Report, 2030, 2023.

[13] A. Castellan, J.C.J. Bart, S. Cavallaro, Catal. Today 9 (1991) 237–254.

[14] S. Van De Vyver, Y. Román-Leshkov, Catal. Sci. Technol. 3 (2013) 1465–1479.

[15] F. Cavani, S. Alini, in: Sustain. Ind. Chem., 2009, pp. 367–425.

[16] www.grandviewresearch.com, Adipic Acid Market Size, Share & Trends Analysis Report, 2030, 2023.

[17] J. Tinge, M. Groothaert, H. op het Veld, J. Ritz, H. Fuchs, H. Kieczka, W.C. Moran, in: Ullmann's Encycl. Ind. Chem., 2018, pp. 1–31.

[18] F. Hao, J. Zhong, P. Le Liu, K.Y. You, C. Wei, H.J. Liu, H.A. Luo, J. Mol. Catal. A Chem. 351 (2011) 210–216.

[19] H.F. U. Brand, R. Schmitz, E. Deuker, US Patent, 1989.

[20] O. Immel, H.H. Schwarz, K. Starke, W. Swodenk, Chemie Ing. Tech. 56 (1984) 612–613.

[21] www.technavio.com, Caprolactam Market by Application, End-User, and Geography - Forecast and Analysis 2023-2027, 2023.

[22] M.T. Musser, in: Ullmann's Encycl. Ind. Chem., 2000.

[23] B.L. Deopura, A.K. Mukherjee, in: V.B. Gupta, V.K. Kothari (Eds.), Springer Netherlands, Dordrecht, 1997, pp. 318–359.

[24] S.& T.R. Global Nylon Market Size, Global Nylon Market Size, Share & Trends Report, 2030, 2023.

[25] J.P. Lange, J.Z. Vestering, R.J. Haan, Chem. Commun. (2007) 3488–3490.

[26] C. Mihut, D.K. Captain, F. Gadala-Maria, M.D. Amiridis, Polym. Eng. Sci. 41 (2001) 1457–1470.

[27] Donald J. Loder - E.I. Du Pont de Nemours & Co., Production of Cyclic Alcohols and Ketones, 2,223,494, 1940.

[28] J.R. Chen, Process Saf. Prog. 23 (2004) 72–81.

[29] A. Ramanathan, M.S. Hamdy, R. Parton, T. Maschmeyer, J.C. Jansen, U. Hanefeld, Appl. Catal. A Gen. 355 (2009) 78–82.

[30] B.P.C. Hereijgers, B.M. Weckhuysen, J. Catal. 270 (2010) 16–25.

[31] U. Schuchardt, W.A. Carvalho, E.V. Spinacé, Synlett 1993 (1993) 713–718.

[32] C.D. Millholland, Industrial Catalysts - Catalyst Analysis - Advancing Materials, 2021.

[33] J.G. De Vries, S.D. Jackson, Catal. Sci. Technol. 2 (2012) 2009.

[34] B. Cornils, W.A. Herrmann, J. Catal. 216 (2003) 23–31.

[35] M.E. Ali, M.M. Rahman, S.M. Sarkar, S.B.A. Hamid, J. Nanomater. 2014 (2014) 192038.

[36] J.C. Védrine, Catalysts 7 (2017).

[37] D. Duprez, F. Cavani, Handbook Of Advanced Methods And Processes In Oxidation Catalysis: From Laboratory To Industry, World Scientific Publishing Company, 2014.

[38] J.L.G. Fierro, CRC Press (1st Ed.) (2006) 808.

[39] J.C. Védrine, ChemSusChem 12 (2019) 577–588.

[40] J.C. Volta, J.L. Portefaix, Appl. Catal. 18 (1985) 1–32.

[41] R.K. Grasselli, ChemInform 34 (2003) 79–88.

[42] P. Khirsariya, R. Mewada, Int. J. Eng. Dev. Res. 2 (2014) 3911–3914.

[43] U. Schuchardt, D. Cardoso, R. Sercheli, R. Pereira, R.S. da Cruz, M.C. Guerreiro, D. Mandelli, E. V Spinacé, E.L. Pires, Appl. Catal. A Gen. 211 (2001) 1–17.

[44] A. Stephen, K. Hashmi, G.J. Hutchings, A.S.K. Hashmi, G.J. Hutchings, (n.d.).

[45] C. Della Pina, E. Falletta, L. Prati, M. Rossi, (2008).

[46] C. Della Pina, E. Falletta, M. Rossi, Chem. Soc. Rev. 41 (2012) 350–369.

[47] A. Abutaleb, M.A. Ali, Rev. Chem. Eng. 38 (2022) 769–797.

[48] L. Sun, J. Liu, W. Luo, Y. Yang, F. Wang, C. Weerakkody, S.L. Suib, Mol. Catal. 460 (2018) 16–26.

[49] I. Graça, S. Al-Shihri, D. Chadwick, Appl. Catal. A Gen. 568 (2018) 95–104.

[50] P. Liu, K. You, R. Deng, Z. Chen, J. Jian, F. Zhao, P. Liu, Q. Ai, H. Luo, Mol. Catal. 466 (2019) 130–137.

[51] C.R. Riley, N.E. Montgomery, N.N. Megally, J.A. Gunn, L.S. Davis, Open Catal. J. 5 (2012) 8–13.

[52] Y. Hong, D. Sun, Y. Fang, Chem. Cent. J. 12 (2018) 36.

[53] Z. Xiao, W. Zhan, Y. Guo, Y. Guo, X. Gong, G. Lu, Chinese J. Catal. 37 (2016) 273–280.

[54] R. Goyal, B. Sarkar, S. Sameer, A. Bag, A. Bordoloi, ACS Appl. Nano Mater. 2 (2019) 5989–5999.

[55] K.J. Betsy, C. Nayak, A. Lazar, A. Krishnan, D. Bhattacharyya, S.N. Jha, C.P. Vinod, ChemCatChem 10 (2018) 3291–3298.

[56] C. Xu, L. Jin, X. Wang, Y. Chen, L. Dai, Carbon N. Y. 160 (2020) 287–297.

[57] M. Conte, X. Liu, D.M. Murphy, K. Whiston, G.J. Hutchings, Phys. Chem. Chem. Phys. 14 (2012) 16279–16285.

[58] P. Wu, P. Bai, K.P. Loh, X.S. Zhao, Catal. Today 158 (2010) 220–227.

[59] M. Sadiq, M. Ali, R. Iqbal, K. Saeed, A. Khan, M.N. Umar, H.U. Rashid, J. Chem. Sci. 127 (2015) 1167–1172.

[60] R. Pohorecki, J. Bałdyga, W. Moniuk, W. Podgórska, A. Zdrójkowski, P.T. Wierzchowski, Chem. Eng. Sci. 56 (2001) 1285–1291.

[61] I.V. BEREZIN, E.T. DENISOV, N.M. EMANUEL', Oxid. Cyclohexane (1966) 163–211.

[62] E. Rabinowitch, W.C. Wood, Trans. Faraday Soc. 32 (1936) 1381–1387.

[63] I. Hermans, P.A. Jacobs, J. Peeters, Chem. - A Eur. J. 12 (2006) 4229–4240.

[64] I. Hermans, T.L. Nguyen, P.A. Jacobs, J. Peeters, ChemPhysChem 6 (2005) 637–645.

[65] I. Hermans, P. Jacobs, J. Peeters, Chem. - A Eur. J. 13 (2007) 754–761.

[66] A.L. Perkel, S.G. Voronina, Russ. Chem. Bull. 68 (2019) 1478–1498.

[67] J. Ebner, D. Riley, in: C.S. Foote, J.S. Valentine, A. Greenberg, J.F. Liebman (Eds.), Springer Netherlands, Dordrecht, 1995, pp. 204–248.

[68] R. Jevtic, P.A. Ramachandran, M.P. Dudukovic, Ind. Eng. Chem. Res. 48 (2009) 7986–7993.

[69] M.I. Greene, C. Sumner, R.J. Gartside, Cyclohexane Oxidation, U.S. Patent 5,780,683, 1998.

[70] A.K. Suresh, T. Sridhar, O.E. Potter, AIChE J. 34 (1988) 69–80.

[71] S.S. Stahl, P.L. Alsters, Liquid Phase Aerobic Oxidation Catalysis: Industrial Applications and Academic Perspectives, Wiley, 2016.

[72] J. Sanchez, T.N. Myers, Van Nostrand's Encycl. Chem. (2005).

[73] A. Scarso, G. Strukul, in: J. Reedijk, K.B.T.-C.I.C.I.I. (Second E. Poeppelmeier (Eds.), Elsevier, Amsterdam, 2013, pp. 177–221.

[74] X. Liu, M. Conte, Q. He, D.W. Knight, D.M. Murphy, S.H. Taylor, K. Whiston, C.J. Kiely, G.J. Hutchings, Chem. - A Eur. J. 23 (2017) 11834–11842.

[75] L. Wang, S. Zhao, C. Liu, C. Li, X. Li, H. Li, Y. Wang, C. Ma, Z. Li, J. Zeng, Nano Lett. 15 (2015) 2875–2880.

[76] Y.J. Xu, P. Landon, D. Enache, A.F. Carley, M.W. Roberts, G.J. Hutchings, Catal. Letters 101 (2005) 175–179.

[77] M. Wu, Y. Fu, W. Zhan, Y. Guo, Y. Guo, Y. Wang, G. Lu, Catalysts 7 (2017).

[78] N.A. Milas, D.M. Surgenor, J. Am. Chem. Soc. 68 (1946) 205–208.

[79] T.G. Traylor, S. Tsuchiya, Y. Byun, C. Kim, (1993) 2775–2781.

[80] B. Puértolas, A.K. Hill, T. García, B. Solsona, L. Torrente-Murciano, Catal. Today 248 (2015) 115–127.

[81] A. Goti, F. Cardona, in: P. Tundo, V. Esposito (Eds.), Springer Netherlands, Dordrecht, 2008, pp. 191–212.

[82] G. de Ruiter, J.S. Costa, K. Lappalainen, O. Roubeau, P. Gamez, J. Reedijk, Inorg. Chem. Commun. 11 (2008) 787–790.

[83] M. Sutradhar, L.M. Martins, T.R. Barman, M.L. Kuznetsov, M.F.C.G. da Silva, A.J.L. Pombeiro, New J. Chem. 43 (2019) 17557–17570.

[84] L.S. Shul'pina, M. V Kirillova, A.J.L. Pombeiro, G.B. Shul'pin, Tetrahedron 65 (2009) 2424–2429.

[85] N.A. Alekar, S.B. Halligudi, R. Rajani, S. Gopinathan, C. Gopinathan, React. Kinet. Catal. Lett. 72 (2001) 169–176.

[86] Y. Du, Y. Xiong, J. Li, X. Yang, J. Mol. Catal. A Chem. 298 (2009) 12–16.

[87] T. Sato, J. Dakka, R.A. Sheldon, J. Chem. Soc. Chem. Commun. (1994) 1887–1888.

[88] H.-Y. Hou, C.-M. Shu, T.-L. Tsai, J. Hazard. Mater. 152 (2008) 1214–1219.

[89] https://pubchem.ncbi.nlm.nih.gov/compound/Cumene-hydroperoxide, (2023).

[90] P.P. Toribio, A. Gimeno-Gargallo, M.C. Capel-Sanchez, M.P. de Frutos, J.M. Campos-Martin, J.L.G. Fierro, Appl. Catal. A Gen. 363 (2009) 32–39.

[91] J.M. Campos-Martin, G. Blanco-Brieva, J.L.G. Fierro, Angew. Chemie - Int. Ed. 45 (2006) 6962–6984.

[92] R. Kosydar, A. Drelinkiewicz, J.P. Ganhy, Catal. Letters 139 (2010) 105–113.

[93] A.P. Meshcheryakov, M.I. Batuev, A.D. Matveeva, Bull. Acad. Sci. USSR, Div. Chem. Sci. 4 (1955) 661–666.

[94] N.M.R. Martins, L.M.D.R.S. Martins, C.O. Amorim, V.S. Amaral, A.J.L. Pombeiro, Catalysts 7 (2017).

[95] M. Behl, M.B. Kadiiska, M.R. Hejtmancik, D. Vasconcelos, R.S. Chhabra, Cutan. Ocul. Toxicol. 31 (2012) 204–213.

[96] C.C. Winterbourn, Toxicol. Lett. 82–83 (1995) 969–974.

[97] H.K. G. Ertl, J. Weitkamp, (2008).

[98] T. Daniels-Race, in: M.B.T.-N. Feldman (Ed.), Woodhead Publishing, 2014, pp. 399–423.

[99] S. V Nair, S. Sinha, K.C. Rustagi, Phys. Rev. B 35 (1987) 4098–4101.

[100] D. Astruc, F. Lu, J.R. Aranzaes, Angew. Chemie Int. Ed. 44 (2005) 7852–7872.

[101] M.M. Forde, L. Kesavan, M.I. bin Saiman, Q. He, N. Dimitratos, J.A. Lopez-Sanchez,

R.L. Jenkins, S.H. Taylor, C.J. Kiely, G.J. Hutchings, ACS Nano 8 (2014) 957–969.

[102] A. Villa, D. Wang, G.M. Veith, F. Vindigni, L. Prati, Catal. Sci. Technol. 3 (2013) 3036–3041.

[103] L. Kesavan, R. Tiruvalam, M.H.A. Rahim, M.I. bin Saiman, D.I. Enache, R.L. Jenkins, N. Dimitratos, J.A. Lopez-Sanchez, S.H. Taylor, D.W. Knight, C.J. Kiely, G.J. Hutchings, Science (80-.). 331 (2011) 195–199.

[104] L. Prati, A. Villa, Catalysts 2 (2011) 24–37.

[105] A. Villa, D. Wang, D.S. Su, L. Prati, ChemCatChem 1 (2009) 510–514.

[106] Y. Wang, J. He, C. Liu, W.H. Chong, H. Chen, Angew. Chemie Int. Ed. 54 (2015) 2022–2051.

[107] H. Zheng, R.K. Smith, Y. Jun, C. Kisielowski, U. Dahmen, A.P. Alivisatos, Science (80-.). 324 (2009) 1309–1312.

[108] P.W. Voorhees, J. Stat. Phys. 38 (1985) 231–252.

[109] R. Khan, A. Rehman, A. Hayat, S. Andreescu, Magnetochemistry 5 (2019).

[110] N. Dimitratos, F. Porta, L. Prati, A. Villa, Catal. Letters 99 (2005) 181–185.

[111] K. Alshammari, Y. Niu, R.E. Palmer, N. Dimitratos, Philos. Trans. R. Soc. A Math. Phys. Eng. Sci. 378 (2020) 20200057.

[112] A. Henglein, J. Phys. Chem. B 104 (2000) 6683–6685.

[113] D. Burshtain, L. Zeiri, S. Efrima, Langmuir 15 (1999) 3050–3055.

[114] N.R. Jana, L. Gearheart, C.J. Murphy, Chem. Mater. 13 (2001) 2313–2322.

[115] A.D. Pomogailo, G.I. Dzhardimalieva, Nanostructured Materials Preparation via Condensation Ways, Springer, 2014.

[116] X. Liu, R. Huang, J. Zhu, Chem. Mater. 20 (2008) 192–197.

[117] J. Zhang, H. Liu, Z. Wang, N. Ming, Adv. Funct. Mater. 17 (2007) 3295–3303.

[118] I. Capek, Noble Metal Nanoparticles: Preparation, Composite Nanostructures, Biodecoration and Collective Properties, Springer, 2017.

[119] S. Campisi, M. Schiavoni, C.E. Chan-Thaw, A. Villa, Catalysts 6 (2016) 185.

[120] U. Schubert, N. Hüsing, Synthesis of Inorganic Materials, Wiley, 2000.

[121] L. Prati, A. Villa, Gold Catalysis: Preparation, Characterization, and Applications, CRC Press, 2016.

[122] J.R.A. Sietsma, A. Jos van Dillen, P.E. de Jongh, K.P. de Jong, Stud. Surf. Sci. Catal. 162 (2006) 95–102.

[123] P. Munnik, P.E. de Jongh, K.P. de Jong, Chem. Rev. 115 (2015) 6687–6718.

[124] N.M. Deraz, J. Ind. Environ. Chem. 2 (2018) 19–21.

[125] X. Liu, D. Wang, Y. Li, Nano Today 7 (2012) 448–466.

[126] https://chem.libretexts.org/, LibreTexts, Chap. 6.7A and 6.7B, 2016.

[127] W.M.H. Sachtler, in: Handb. Heterog. Catal., 2008, pp. 1585–1593.

[128] R. Hou, Catalytic and Process Study of the Selective Hydrogenation of Acetylene and 1,3-Butadiene, 2017.

[129] J. Hagen, in: Ind. Catal., 2015, pp. 211–238.

[130] H.F. Rase, Handbook of Commercial Catalysts: Heterogeneous Catalysts, CRC press, 2000.

[131] W.Y. Teoh, Heterog. Catal. Adv. Des. Charact. Appl. Vol. 1 2 1–2 (2021) 3–19.

[132] M.B. Gawande, R.K. Pandey, R. V. Jayaram, Catal. Sci. Technol. 2 (2012) 1113–1125.

[133] C. Chizallet, G. Costentin, M. Che, F. Delbecq, P. Sautet, J. Phys. Chem. B 110 (2006) 15878–15886.

[134] W. Li, J. Shi, K.H.L. Zhang, J.L. Macmanus-Driscoll, Mater. Horizons 7 (2020) 2832–2859.

[135] M.A.F. Pyman, A.M. Posner, J. Colloid Interface Sci. 66 (1978) 85–94.

[136] G. Frenzer, W.F. Maier, Annu. Rev. Mater. Res. 36 (2006) 281–331.

[137] I.E. Wachs, K. Routray, ACS Catal. 2 (2012) 1235–1246.

[138] P. Cousin, R.A. Ross, Mater. Sci. Eng. A 130 (1990) 119–125.

[139] A. Martínez-Arias, M. Fernández-García, V. Ballesteros, L.N. Salamanca, J.C. Conesa, C. Otero, J. Soria, Langmuir 15 (1999) 4796–4802.

[140] D.M. Bezerra, E.M. Assaf, Sci. Tecnol. Mater. 30 (2018) 166–173.

[141] P.A. Haas, Chem. Eng. Prog. 85 (1989) 44–52.

[142] H. Peng, L. Zhang, Q. Sun, J. Shen, X. Xu, X. Fang, W. Liu, Z. Wang, N. Zhang, X. Wang, ChemistrySelect 2 (2017) 6364–6369.

[143] M. Prakasam, O. Viraphong, O. Cambon, A. Largeteau, in: Adv. Solid Oxide Fuel Cells Electron. Ceram., 2015, pp. 151–156.

[144] J.H. Schulman, W. Stoeckenius, L.M. Prince, J. Phys. Chem. 63 (1959) 1677–1680.

[145] R.P. Bagwe, K.C. Khilar, Langmuir 16 (2000) 905–910.

[146] P. Monnoyer, A. Fonseca, J.B. Nagy, Colloids Surfaces A Physicochem. Eng. Asp. 100 (1995) 233–243.

[147] M.A. Malik, M.Y. Wani, M.A. Hashim, Arab. J. Chem. 5 (2012) 397–417.

[148] A. Nanni, L. Dei, Langmuir 19 (2003) 933–938.

[149] Y. Berkovich, A. Aserin, E. Wachtel, N. Garti, J. Colloid Interface Sci. 245 (2002) 58–67.

[150] J.-L. Lemyre, A.M. Ritcey, Chem. Mater. 17 (2005) 3040–3043.

[151] I. Lisiecki, M.P. Pileni, Langmuir 19 (2003) 9486–9489.

[152] www.thermofisher.com, Transmission Electron Microscopy vs Scanning Electron Microscopy, n.d.

[153] C.C. Zhang, J. Shi, S. Hartlaub, J.P. Palamara, I. Petrovic, B. Yilmaz, Catal. Commun. 150

(2021) 106273.

[154] C. Hess, Chem. Soc. Rev. 50 (2021) 3519–3564.

[155] M. RÜHLE, M. WILKENS, in: R.W. CAHN, P.B.T.-P.M. (Fourth E. HAASEN† (Eds.), North-Holland, Oxford, 1996, pp. 1033–1113.

[156] F. Zemlin, K. Weiss, P. Schiske, W. Kunath, K.H. Herrmann, Ultramicroscopy 3 (1978) 49–60.

[157] F. Hosokawa, H. Sawada, Y. Kondo, K. Takayanagi, K. Suenaga, J. Electron Microsc. (Tokyo). 62 (2013) 23–41.

[158] R. Leary, R. Brydson, Chromatic Aberration Correction: The next Step in Electron Microscopy, Elsevier Inc., 2011.

[159] E.A. Stach, Mater. Today 11 (2008) 50–58.

[160] www.cui.kcl.ac.uk, Scanning Transmission Electron Microscopy, n.d.

[161] D.B.W.C.B. Carter, Transmission Electron Microscopy A Textbook for Materials Science, springer publication, 2009.

[162] S.J. Pennycook, L.A. Boatner, Nature 336 (1988) 565–567.

[163] W.J. Wolfgong, in: A.S.H. Makhlouf, M.B.T.-H. of M.F.A. with C.S. from the A. and A.I. Aliofkhazraei (Eds.), Butterworth-Heinemann, Boston, 2016, pp. 279–307.

[164] A. Parisini, S. Frabboni, G.C. Gazzadi, R. Rosa, A. Armigliato, Microsc. Microanal. 24 (2018) 193–206.

[165] M.P. Seah, D. Briggs, J.T. Grant, Surf. Anal. by Auger X-Ray Photoelectron Spectrosc. (2003) 345–375.

[166] J.F. Watts, J. Wolstenholme, An Introduction to Surface Analysis by XPS and AES, Wiley, 2019.

[167] G. Greczynski, L. Hultman, Prog. Mater. Sci. 107 (2020) 100591.

[168] E. Sokolowski, C. Nordling, K. Siegbahn, Phys. Rev. 110 (1958) 776.

[169] B.V. Crist, J. Electron Spectros. Relat. Phenomena 231 (2019) 75–87.

[170] C. Suryanarayana, M.G. Norton, in: C. Suryanarayana, M.G. Norton (Eds.), Springer US, Boston, MA, 1998, pp. 3–19.

[171] M. Nasrollahzadeh, M. Atarod, M. Sajjadi, S.M. Sajadi, Z. Issaabadi, Plant-Mediated Green Synthesis of Nanostructures: Mechanisms, Characterization, and Applications, 1st ed., Elsevier Ltd., 2019.

[172] P. Pourhakkak, A. Taghizadeh, M. Taghizadeh, M. Ghaedi, S. Haghdoust, in: M.B.T.-I.S. and T. Ghaedi (Ed.), Adsorpt. Fundam. Process. Appl., Elsevier, 2021, pp. 1–70.

[173] www.wiki.anton-paar.com/it-it/teoria-bet/, BET Theory, n.d.

[174] Z.A. ALOthman, Materials (Basel). 5 (2012) 2874–2902.

[175] M.D. Donohue, G.L. Aranovich, Adv. Colloid Interface Sci. 76–77 (1998) 137–152.

[176] L.L. Yicheng Zhang, Weili Dai, Guangjun Wu, Naijia Guan, Chinese J. Catal. 35 (2014) 108–119.

[177] J. Xie, Y. Wang, Y. Li, Y. Wei, React. Kinet. Mech. Catal. 102 (2011) 143–154.

[178] P. Liu, K. You, R. Deng, Z. Chen, J. Jian, F. Zhao, P. Liu, Q. Ai, H. Luo, Mol. Catal. 466 (2019) 130–137.

[179] X. Yu, Z. Shen, Q. Sun, N. Qian, C. Zhou, J. Chen, J. Chem. Eng. Data 61 (2016) 1236–1245.

2. Experimental

This section is divided in three parts: the first regarding the techniques employed for catalysts preparation, the second discussing the experimental setup used for the characterization of the catalysts and of the reaction products, and the third considering the equipment and conditions used for cyclohexane oxidation tests.

2.1. Catalysts preparation

In this part the synthetic steps employed to produce the FeCo series, the AuCu and AuSn series, and the CeZr series discussed in the Results and Discussion Chapters 3.1, 3.2. and 3.3. are reported.

2.1.1. FeCo series: Fe, Co and Fe_1Co_1 supported on γ-Al_2O_3

This group is composed of three series of three catalysts: Fe/Al_2O_3, Co/Al_2O_3 and bimetallic Fe_1Co_1/Al_2O_3, each one at 2 wt% loading and obtained with different preparation methods, namely sol immobilization, inverse microemulsion and (modified) incipient wetness.

2.1.1.1. Fe, Co and Fe_1Co_1 on γ-Al_2O_3 by sol immobilization

This series of three catalyst was prepared in Milan by the sol immobilization technique [1,2]. A schematic representation of the procedure is reported (Figure 2.1).

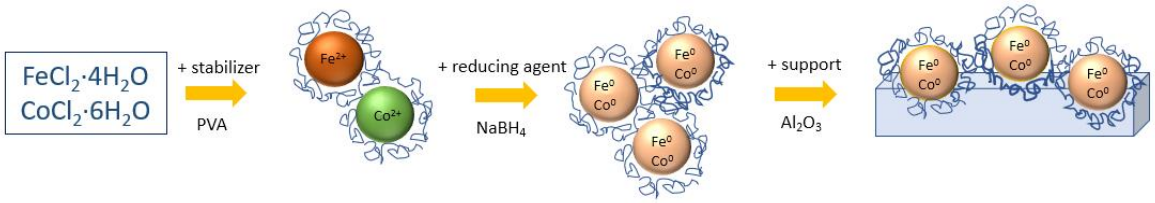

Figure 2.1. Schematic representation of the sol immobilization preparation method for a bimetallic FeCo catalyst.

For the preparation of 2 wt% Fe_1Co_1/Al_2O_3, a 10 mg/mL solution of $FeCl_2 \cdot 4H_2O$ and another of $CoCl_2 \cdot 6H_2O$ were prepared using Milli-Q water. 1.76 mL of the Fe solution and 2.07 mL of the Co solution were put in a beaker containing 150 mL of Milli-Q water. Subsequently, 0.5 ml of PVA solution (0.1 g in 10 mL), previously prepared making sure that the PVA was completely

dissolved, and 3.48 mL of $NaBH_4$ 0.5 M solution were added to reduce the metallic precursors. After the reduction of the precursors, the solution turned black and was kept under stirring for 30 minutes. Then, 0.5 g of Al_2O_3 and 1 drop of concentrated H_2SO_4 were added to promote the deposition of metallic nanoparticles on the catalyst surface. After 1 hour, the solution was filtered with a Buchner funnel, and the obtained solid was washed three times with Milli-Q water. The catalyst was then dried in an 80°C oven for approximately 6 hours and recovered. The resulting powder showed a greyish/pink colour.

To prepare the 2 wt% Fe/Al_2O_3 catalyst, a 5 mg/mL solution of Fe precursor was prepared weighing 0.399 g of $FeCl_2{\cdot}4H_2O$ into 10 mL of MilliQ water. Then, 2 mL of Fe(II) solution (pale yellow colour) were added into a beaker containing 150 mL of Milli-Q H2O under stirring at RT. Then, 1 mL of a polyvinyl alcohol (PVA, 0.1 g in 10 mL) solution was added to the beaker and left stirring for 5 minutes. At this point, a solution of $NaBH_4$ 0.1M in MilliQ water was prepared and 6 mL (In order to obtain the desired ratio between the metal precursor and excess $NaBH_4$ of 1:5) were added to the beaker within 2 minutes from its preparation. The solution turned dark yellow. It was left under stirring at RT for 30 minutes. Then, 0.5 g of Al_2O_3 and 1 drop of concentrated H_2SO_4 were added to promote the deposition of metal nanoparticles on the surface of the catalyst. After 1 hour, the solution was filtered with a double Buchner filter, washing the obtained solid 3 times with Milli-Q H_2O (500 mL in total). The catalyst was then dried in an oven at 80°C for about 6 hours and recovered. The obtained powder also showed a grey colour in this case.

For the preparation of 2 wt% Co/Al_2O_3, 0.399 g of $CoCl_2{\cdot}6H_2O$ were used for the preparation of the 10 mg/mL precursor solution (pale pink colour) in 10 mL of Milli-Q water, and 1 mL of that solution was added to 150 mL of Milli-Q H_2O in the first step as above. The solution turned to dark brown upon pouring the $NaBH_4$ solution, and the following steps were the same as the ones employed above.

2.1.1.2. Fe, Co and Fe_1Co_1 on γ-Al_2O_3 by inverse microemulsion

This series was prepared by the inverse microemulsion technique, with a modification of Martinez-Arias' group [3] mixed oxide preparation, which is for the preparation of

homogeneous mixed oxides. Instead, here the two metals (Fe and Co) particles are supported and not in the form of a pure mixed oxide (Figure 2.2).

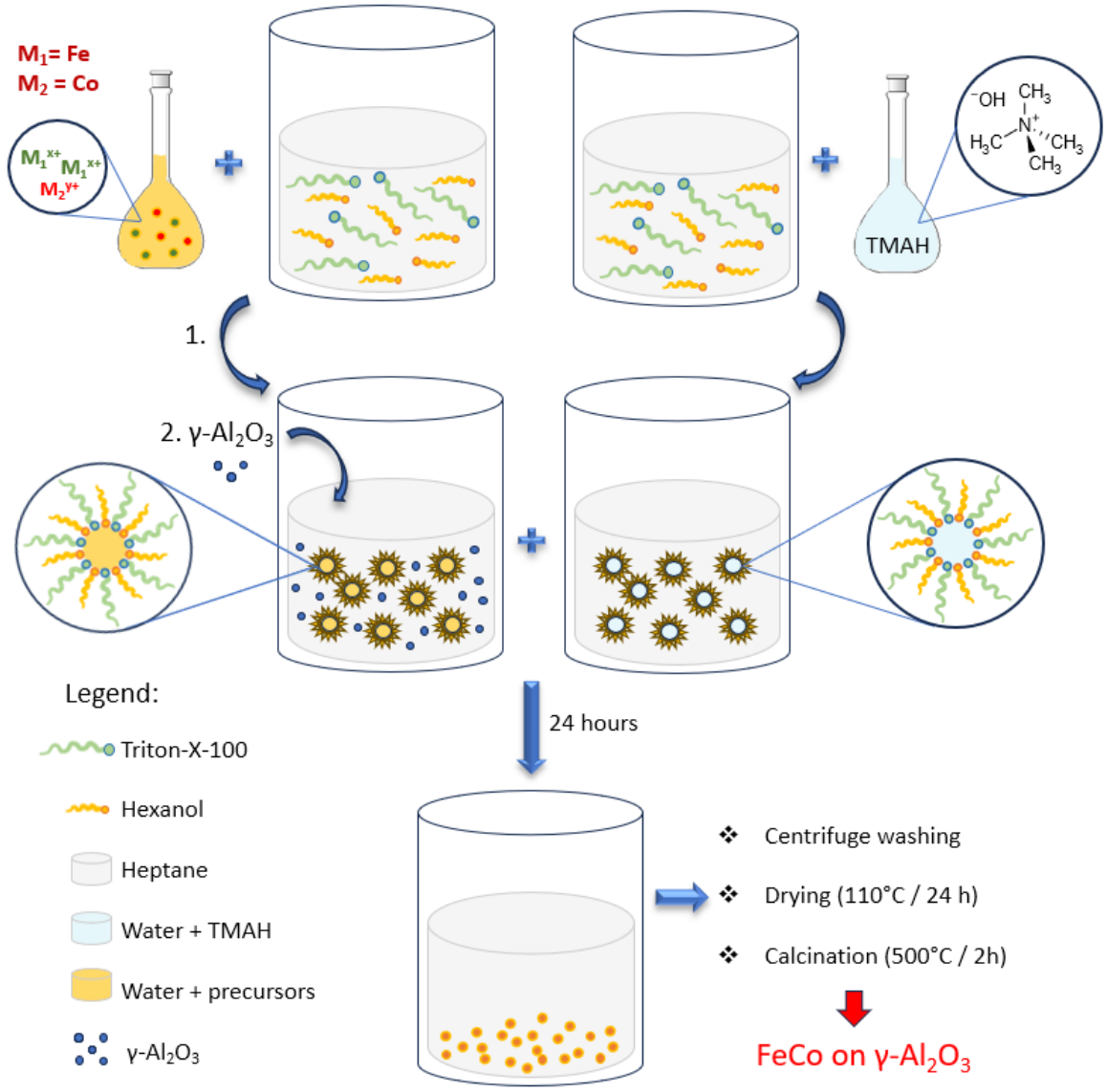

Figure 2.2. Inverse microemulsion scheme with the addition of a support, in order to obtain the Fe and Co metals supported on γ-Al_2O_3.

In this method, the reaction occurs within reverse micelles formed by dispersing an aqueous phase over an organic phase (W/O) of nanometric size. In order to prepare the 2 wt% Fe_1Co_1/γ-Al_2O_3 bimetallic system with a 1:1 ratio, 1.237 g of $Fe(NO_3)_3{\cdot}9H_2O$ and 0.873 g of $Co(NO_3)_2{\cdot}6H_2O$ were dissolved in 50 mL of milliQ water. Then, 2.803 g of the tetramethylammonium hydroxide pentahydrate base ($TMAH{\cdot}5H_2O$, $(CH_3)_4NOH{\cdot}5H_2O$) was added to another 50 mL of milliQ water. The concentration of $TMAH{\cdot}5H_2O$ was selected to ensure that there were 3 moles of the base for every mole of Fe^{3+} and 2 moles of $TMAH{\cdot}5H_2O$

for every mole of Co^{2+}. Then, to create two inverse microemulsions (water in organic), equal amounts of organic solvent (427 mL of n-heptane), non-ionic surfactant (89 mL of Triton X-100), and co-surfactant (93 mL of 1-hexanol) were stirred in separate Erlenmeyer flasks. The aqueous solution containing the cations was added to one flask while the other flask received the TMAH·$5H_2O$ precipitating base solution. This results in the formation of two transparent inverse microemulsions, which comprise stable aqueous micelles containing Fe^{3+} and Co^{2+} metal precursors as well as the TMAH·$5H_2O$ base. In this moment, the addition of 2.803 g of γ-alumina to the Erlenmeyer containing the precursors microemulsion was carried out paying attention not let the alumina stick onto the walls. After stirring the mixture for 30 minutes, the microemulsion containing the base was poured onto the cationic microemulsion. As the resulting mixture was stirred for an additional twenty-four hours, cloudiness emerges due to the precipitation of Fe and Co on the alumina surface. When the time had passed, the suspension was then centrifuged and washed four times with methanol in order to remove the organic part. The resulting slime was put into an oven to dry at 110°C for 24 hours. Then it was recovered and mortared into a fine powder to subsequently undergo calcination at 500°C for 2 hours, in order to eliminate the nitrates and transform the remaining hydroxides into oxides, therefore obtaining the final Fe_1Co_1 bimetallic system on alumina. The final oxide was mortared again into a fine powder before storage. For a better understanding of the technique, pictures of the preparation method carried out for the creation of mixed oxides by inverse microemulsion are reported later in this section, in Chapter 2.1.3.1. $Fe_{0.1}Ce_{0.9}O_x$ (where the only difference in the methodology is the absence of the support).

For the preparation of 2 wt% Fe/Al_2O_3 and 2 wt% Co/Al_2O_3 the entire microemulsion process had to be scaled down due to different lab equipment available in Milan. Therefore, compared to the regular microemulsion optimized in Cádiz University, the amount of the organic phase, concentration of the precursors and of the base were scaled down of a ¼ factor. The precursors were further scaled down for the obtainment of 0.7 g of catalyst in the end, due to alumina shortage. The main differences in the Milan setup were using smaller lab equipment (erlenmeyer and beaker), a different centrifuge, meaning more washing steps with methanol needed, and a tubular furnace to calcine in the final step instead of a muffle furnace.

In order to obtain the 2 wt% Fe on alumina, 0.1033 g of $Fe(NO_3)_3 \cdot 9H_2O$ (0.25 mmol) were used for the preparation of the precursors solution in a 15 mL flask filled of Milli-Q water. Similarly, another 15 mL flask was prepared with 0.1401 mg of $TMAH \cdot 5H_2O$. Two separate microemulsions containing 107 mL of Heptane, 23 mL of Triton X-100 and 24 mL of hexanol were made, adding then the precursor solution to one and the base to the other. At this point, 0.686 g of γ-Al2O3 were added to the Erlenmeyer containing the precursor microemulsion. Then, the preparation methodology was carried out exactly as for the Fe_1Co_1 catalyst until the obtainment of the final oxide.

In order to obtain the 2 wt% Co on alumina, 0.0698 g of $Co(NO_3)_2 \cdot 6H_2O$ and 0.0888g of $TMAH \cdot 5H_2O$ were used, respectively, for the preparation of the precursors and base solutions in two 15 mL flasks with Milli-Q water. Then, 107 mL of Heptane, 23 mL of Triton X-100 and 24 mL of hexanol were used for the preparation of each of the two inverse microemulsions. 0.686 g of γ-Al_2O_3 were added to the Erlenmeyer containing the precursor microemulsion and the rest of the procedure was carried out exactly as for the Fe_1Co_1 catalyst, eventually obtaining the 2 wt% Co/Al_2O_3 catalyst.

2.1.1.3. Fe, Co and Fe_1Co_1 on γ-Al_2O_3 by incipient wetness

This series of catalysts was prepared by a slightly modified incipient wetness procedure. In this method, the amount of metal nitrates precursors is calculated in order to have the metallic species at 2 wt% compared to Al_2O_3. Then, for each 2 grams of catalyst, 2 mL of precursors solution is to be added in the case of Al_2O_3. Therefore, for the preparation of 2 g of 2 wt% Co/Al_2O_3, 0.198 g of $Co(NO_3)_2 \cdot 6H_2O$ should be present for each 2 mL of milliQ water. A 10 mL solution in milliQ water containing 0.988 g of $Co(NO_3)_2 \cdot 6H_2O$ was prepared and poured into a 10 mL burette. 1.996 g of γ-Al_2O_3 were put in a mortar under the burette. The solution was then poured two or three drops at a time, mortaring very carefully to a fine powder on each addition and letting it dry for some minutes, as in Figure 2.3.

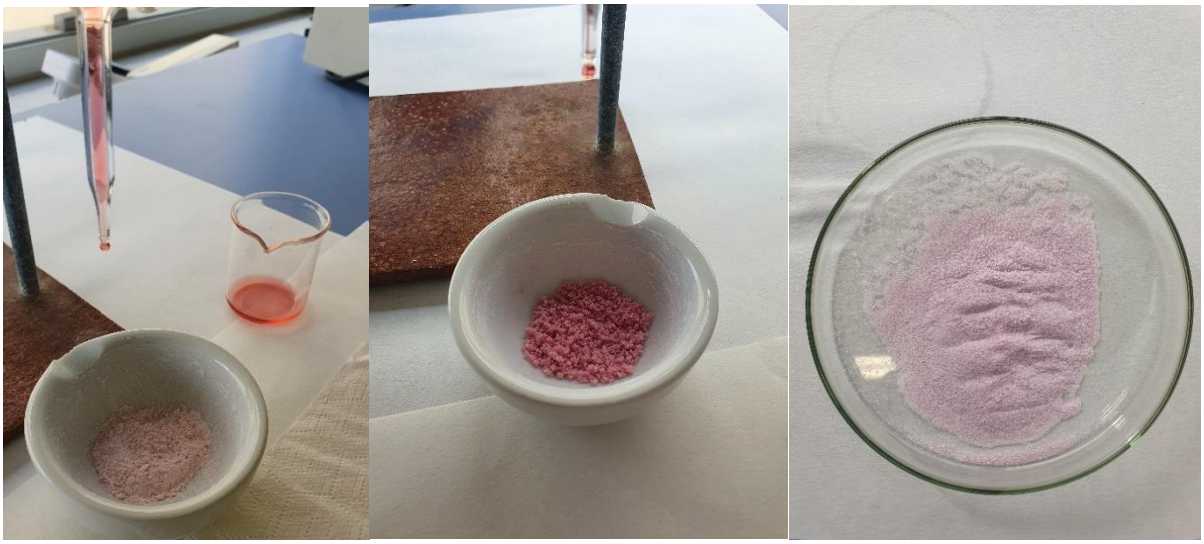

Figure 2.3. Experimental setup for the incipient wetness preparation method and resulting aspect of the cobalt precursor powder after pouring the whole solution.

When all the 2 mL of solution had been added this way, calcination at 500°C for two hours was carried out under air in a muffle furnace in order to break the nitrates of the precursors and obtain the final oxides. A change of colour from pink to dark green was observed for the Co/Al_2O_3 catalyst after calcination.

For the preparation of 2 g of 2 wt% Fe/Al_2O_3, 0.289 g of $Fe(NO_3)_3{\cdot}9H_2O$ were calculated to be necessary for each 2 mL of Milli-Q water in the burette. A solution containing 1.477g of $Fe(NO_3)_3{\cdot}9H_2O$ was prepared and utilised for the incipient wetness method preparation following the procedure of the 2 wt% Co/Al_2O_3 explained above. Almost no change in colour was observed for the 2 wt% Fe/Al_2O_3 catalyst after calcination, passing from orange to a slightly darker tone of orange.

Eventually, the same exact procedure was followed for the preparation of the bimetallic 2 wt% Fe_1Co_1/Al_2O_3. The amount of $Fe(NO_3)_3{\cdot}9H_2O$ and $Co(NO_3)_2{\cdot}6H_2O$ calculated to have a 1:1 Fe:Co molar ratio on 2 mL of solution was, respectively, 0.144 g and 0.103 g. In the 10 mL solution, 0.718 g of $Fe(NO_3)_3{\cdot}9H_2O$ and 0.518 g of $Co(NO_3)_2{\cdot}6H_2O$ were used. After the calcination step, the colour of the powder passed from orange to a dark green/brown colour.

2.1.2. Au-based catalysts

Two series of catalysts composed of Au nanoparticles combined with Cu and Sn, respectively, and supported on different oxides were prepared by sol immobilization and solvated metal

atom dispersion (SMAD). All the monometallic Au, Cu and Sn counterparts were prepared as well.

2.1.2.1. Au, Cu and Au_1Cu_1 supported on Al_2O_3

A 2 wt% monometallic Au/Al_2O_3 preparation was already reported in [4]. For this synthesis an aqueous Au monometallic sol was obtained by reduction of $HAuCl_4$ precursor with $NaBH_4$ in the presence of PVA used as protecting agent. Precisely, 75 mL of a solution of $NaBH_4$ (25.6 mM) was added rapidly to 685 mL of a $HAuCl_4$ (0.33 mM) and PVA (0.013 wt%) solution, under vigorous stirring. After 1 h of stirring, a proper amount of alumina support (Degussa Aluminium oxide C, 100 m^2/g) was added to have a final metal loading equal to 2 wt%. After the complete decolouration of the sol (~2h) the catalyst was filtered and dried in air at 80 °C.

A monometallic 2 wt% Cu/Al_2O_3 was then prepared with the same methodology but working in an inert environment under a N_2 flux for preventing Cu oxidation during the preparation. In this case, the Cu monometallic sol was obtained by reduction of $Cu(NO_3)_2$ precursor with $NaBH_4$ and in the presence of PVA as stabilizing agent as in the case of monometallic Au. Accordingly, 658 mL of a solution of $Cu(NO_3)_2$ (0.33 Mm) and PVA (0.013 wt%) was reduced adding 75 mL of $NaBH_4$ (25.6 mM) under continuous stirring. Alumina was added after 1 h, then after 2 h the final catalyst was filtered and dried in air at 80 °C, having a final metal loading of 2 wt%.

The same method [5] was used to synthesize the bimetallic catalyst 2 wt% Au_1Cu_1/Al_2O_3 with an Au/Cu molar ratio of 1. To prepare the bimetallic sample, an aqueous Au-Cu bimetallic sol was created using a 1:1 molar ratio of Au/Cu. This was achieved by co-reducing $HAuCl_4$ and $Cu(NO_3)_2$ precursors with $NaBH_4$ as the reducing agent and PVA as the protecting agent. The precursor solution amounts and concentrations used were the same as those used in preparing the monometallic sols. The final bimetallic catalyst was obtained by adding a suitable amount of alumina to achieve a final metal loading of 2 wt%. A schematic representation of the procedure is indicated in Figure 2.4. The resulting solid was filtered after the sol had completely lost its colour (after approximately 2 hours) and then dried in air at 80°C.

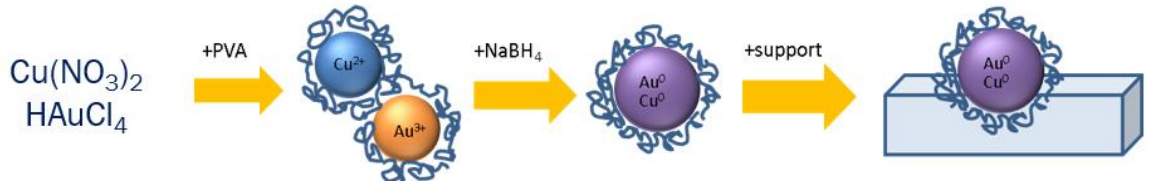

Figure 2.4. Representation of the procedure for the preparation of 2 wt% Au_1Cu_1/Al_2O_3 bimetallic catalyst.

2.1.2.2. Au, Sn and Au_1Sn_2 supported on Al_2O_3 and TiO_2

This series was prepared by the SMAD technique. The synthesis of Au and Sn mono- and AuSn bimetallic catalysts was carried out in a previous work, following the solvated metal atoms dispersion method (SMAD) [6]. Monometallic Au catalysts were prepared by condensation of Au (100 mg, beads) vapour with acetone vapours (100 mL). The resulting Au-Acetone solvated metal atoms (SMA) (96 mL) containing 0.70 mg/mL Au (measured by ICP-OES analysis) was divided into two portions (48 mL) that were impregnated on 1.0 g of Al_2O_3 and TiO_2 support, respectively. The mixtures were stirred for 12 h at room temperature. The supernatant solutions were then removed and the red-brown solid was washed with n-pentane (3 x 50 mL) and dried under reduced pressure. Similarly, Sn monometallic catalysts were prepared. A schematic representation of the procedure for obtaining a general bimetallic AuSn system is reported below in Figure 2.5.

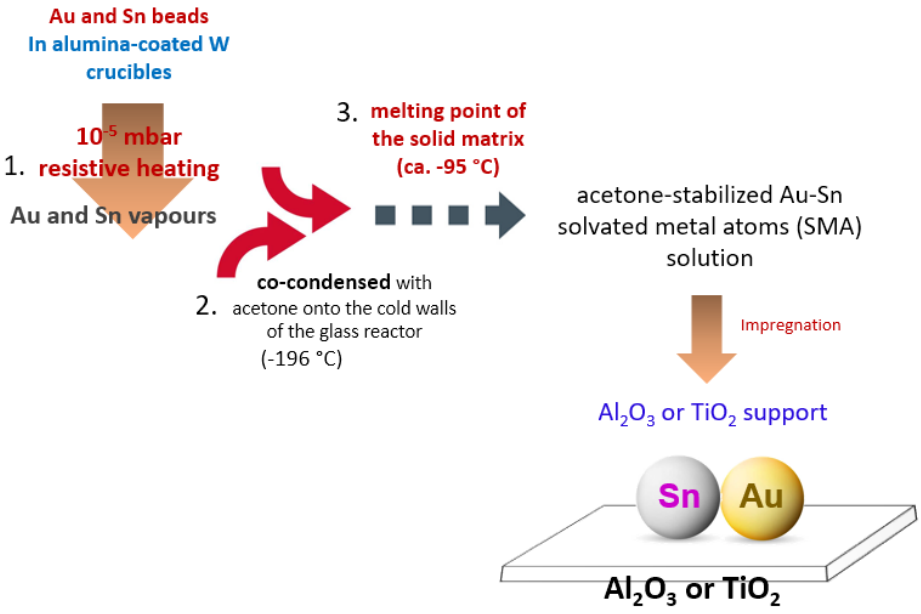

Figure 2.5. Schematic representation of the solvated metal atom dispersion method for the preparation of a AuSn bimetallic catalyst on Al_2O_3 or TiO_2.

For the preparation of 3 wt% bimetallic Au_1Sn_2 catalysts supported on Al_2O_3 or TiO_2, Au and Sn vapours generated at 10^{-5} mbar by resistive heating of two different alumina-coated tungsten crucibles (filled with 100 mg of Au beads and 12 mg Sn shot) were co-condensed simultaneously with acetone (100 mL) onto the cold walls of the glass reactor maintained at liquid nitrogen temperature (-196 °C) for 1 h. The reactor chamber was heated to the melting point of the solid matrix (ca. -95 °C) and the resulting acetone-stabilized Au-Sn solvated metal atoms (SMA) solution (96.0 mL) was kept under argon atmosphere in a Schlenk tube at -80 °C. The resulting Au-Sn/Acetone solvated metal atoms (SMA) (96 mL) containing 0.65 mg/mL of Au and 0.11 mg/mL of Sn was divided into two portions (48 mL) that were added to an acetone suspension of 1.0 g of Al_2O_3 and TiO_2 support, respectively. The mixtures were stirred for 12 h at room temperature. The supernatant solutions were then removed and the red-brown solid was washed with n-pentane (3 x 50 mL) and dried under reduced pressure. A similar procedure was used to prepare the Au-Sn catalysts containing a different Au/Sn molar ratio, using 96 mL of Au-Sn/acetone SMA, containing 0.78 mg/mL of Au and 0.62 mg/mL of Sn, and 1.7 g of Al_2O_3 and TiO_2 support, respectively.

2.1.3. CeZr series: Cu and Fe containing Ce- and Zr-based mixed oxides

This CeZr series is composed of four mixed oxides, specifically four Ce- or Zr-based mixed oxides containing either Cu or Fe at 10% molar (1:9 molar ratio between Cu or Fe and Ce or Zr). CeO_2 and ZrO_2 oxides were also prepared by inverse microemulsion in order to compare the monometallic counterparts.

2.1.3.1. $Fe_{0.1}Ce_{0.9}O_x$

First, the FeCe (1:9) mixed oxide was prepared. The method used was that of inverse microemulsion (Figure 2.6), which has already been previously used in the bibliography [3,7,8], with a modification of the amount of the metals in order to have them in a 1:9 ratio.

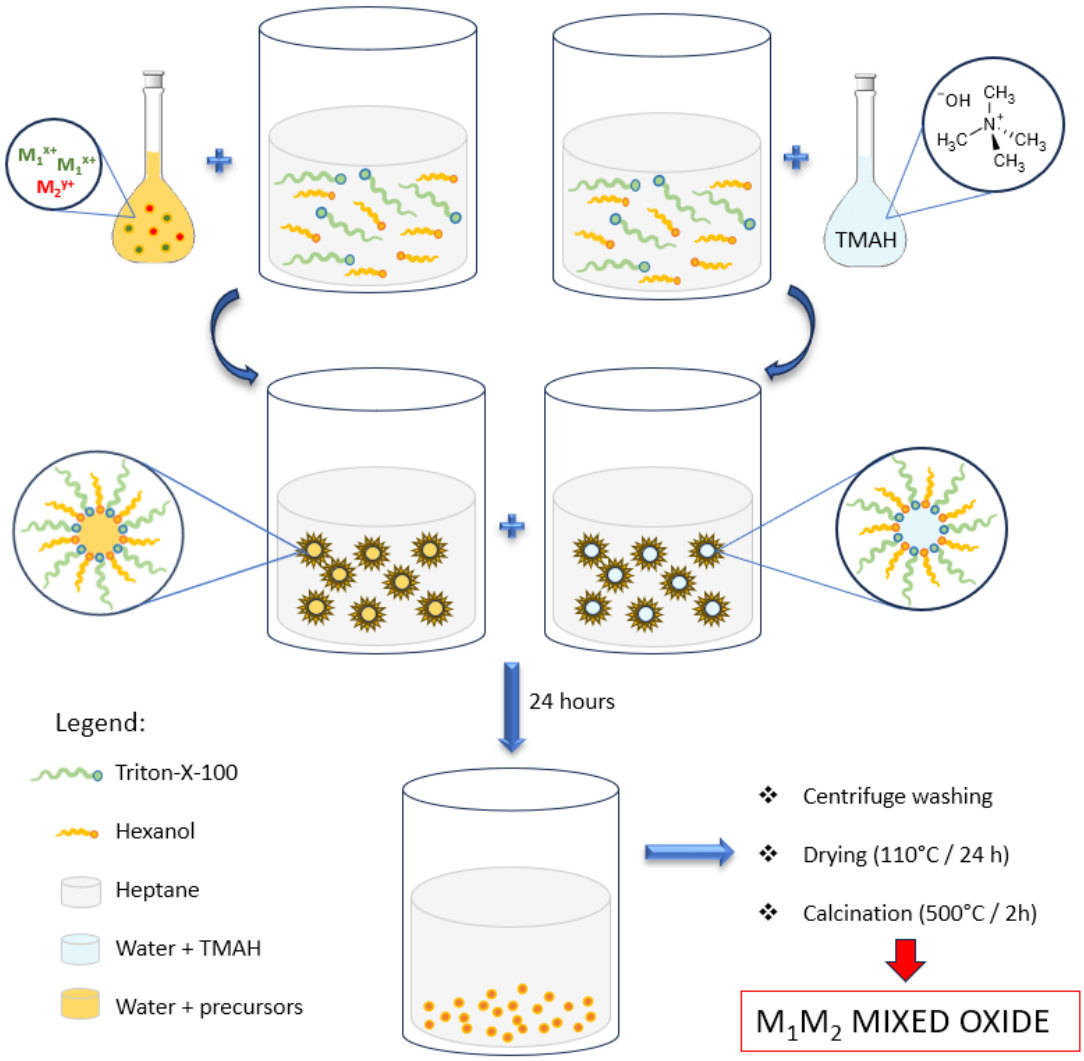

Figure 2.6. Schematic representation of a M_1M_2 mixed oxide preparation by inverse microemulsion.

To achieve a 1:9 precipitated oxide, an aqueous solution must be prepared with the correct quantities of Fe^{3+} and Ce^{3+} cations. To do this, 1.031 g of nonahydrate iron (III) nitrate ($Fe(NO_3)_3 \cdot 9H_2O$) and 9.770 g of hexahydrate cerium (III) nitrate ($Ce(NO_3)_3 \cdot 6H_2O$) precursors are dissolved in a 50 mL 0.25 M solution. Additionally, a 50 mL solution of 14.013 g of tetramethylammonium hydroxide pentahydrate ($TMAH \cdot 5H_2O$, $(CH_3)_4NOH \cdot 5H_2O$) is prepared as the base. The concentration of $TMAH \cdot 5H_2O$ is selected to ensure that there are 3 moles of the base for every mole of Ce^{3+} and 3 moles of $TMAH \cdot 5H_2O$ for every mole of Fe^{3+}.

Then, two different Erlenmeyer flasks were used to stir the same amount of each of the components. These include the organic solvent (427 mL of n-heptane), the non-ionic surfactant (89 mL of Triton X-100), and the co-surfactant (93 mL of 1-hexanol). When an aqueous solution containing the cations is added to one Erlenmeyer and the $TMAH \cdot 5H_2O$

precipitating base solution is added to the other, two inverse microemulsions (water in organic) are formed, (Figure 2.7). This process creates two types of stable aqueous micelles that contain both Ce^{3+} and Zr^{4+} metal precursors and the $TMAH{\cdot}5H_2O$ base. The micelles are formed by a monolayer of the surfactant (Triton X-100) and co-surfactant (1-hexanol) present in a majority of organic phase (n-heptane).

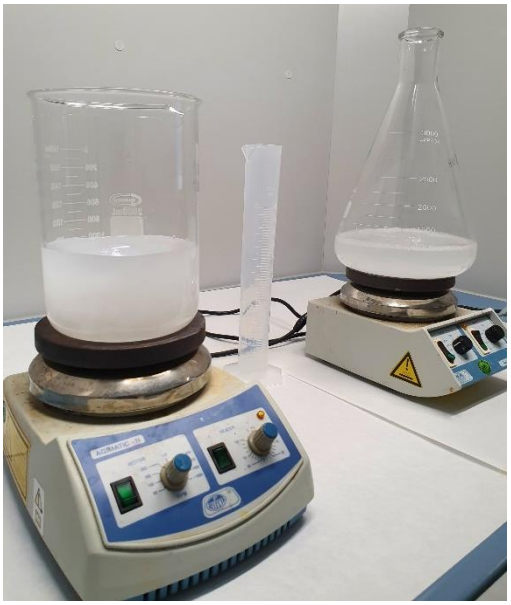

Figure 2.7. The two separates inverse microemulsions containing the precursors and the base, respectively.

The mixture is stirred for thirty minutes before pouring the microemulsion containing the base onto the cationic microemulsion. When the two solutions are combined, the base prompts precipitation in the form of hydroxides or oxides of nanometric size, due to the drops in the microemulsion acting as microreactors during collision (Figure 2.8). The resulting mixture is stirred for an additional twenty-four hours, during which a cloudiness appears as a result of Fe-Ce oxide precipitation.

Figure 2.8. Addition of the solution containing the base to the microemulsion containing the precursors.

During the 24 hours of mixing, it can be noticed that the colour of the suspension changes and becomes clearer along with the coming in contact of the droplets containing the base with the droplets containing the precursors [3,7–10] (Figure 2.9).

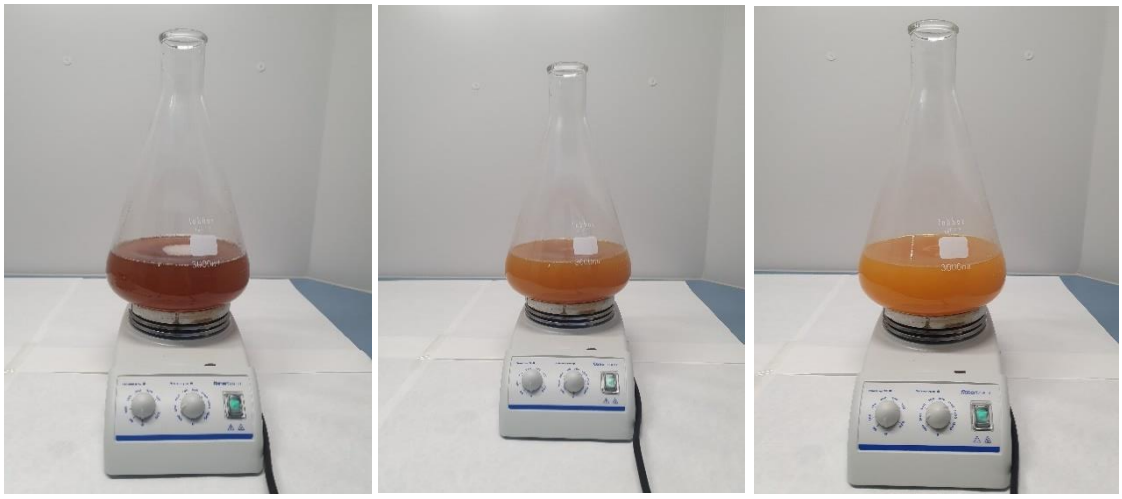

Figure 2.9. Formation of the corresponding hydroxides and oxides of nanometric size during time.

Following the designated duration, the suspension is centrifuged (Torval ST16 ThermoScientific® centrifuge) and the supernatant liquid is decanted. The resultant precipitate is washed three times with methanol, leading to the formation of an orange-coloured gelatinous solid (Figure 2.10).

Figure 2.10. Centrifugation of the solution washed several times with methanol.

Subsequently, the solid is subjected to a short period of air-drying, followed by an extended period of 24 hours of drying inside an oven maintained at a temperature of 110°C. The resulting sample is then ground as finely as possible using an agate mortar, eventually yielding an ochre-coloured powder (Figure 2.11).

Figure 2.11. Dried orange slime after the oven treatment (110°C), crushed into a fine powder.

To complete the process, the sample is calcined inside a muffle furnace under air, and the temperature is maintained at 500°C for 2 hours (with a temperature ramp of 2°C/min). By doing this, the nitrates that are still present are eliminated and the remaining hydroxides are converted into oxides.

2.1.3.2. $Cu_{0.1}Ce_{0.9}O_x$

For the preparation of the $Cu_{0.1}Ce_{0.9}O_x$ the same method as in 2.1.3.1. ($Fe_{0.1}Ce_{0.9}O_x$) was employed but changing the ratio between the two metals. In fact, a solution of 0.604g of $Cu(NO_3)_2{\cdot}3H_2O$ and 9.770 g of $Ce(NO_3)_3 \cdot 6H_2O$ in 50 mL of milliQ water was prepared as the precursor solution, in order to obtain a molar ratio of 1:9 between Cu and Ce. As for the base, 13.136 g of $TMAH{\cdot}5H_2O$ were dissolved in other 50 mL of milliQ water. The concentration of $TMAH{\cdot}5H_2O$ was chosen in order to ensure there were 3 moles of the base for each mole of Ce^{3+} and 2 moles for each Cu^{2+}. Then the preparation and mixing of the two microemulsions, the stirring, washing with methanol, drying and calcination were carried out exactly as in as in 2.1.3.1., obtaining the final mixed oxide.

2.1.3.3. $Fe_{0.1}Zr_{0.9}O_x$

The preparation of $Cu_{0.1}Zr_{0.9}O_x$ to achieve a mixed oxide with a molar ratio of 1:9 Cu:Zr followed the same procedure as in 2.1.3.1. ($Fe_{0.1}Ce_{0.9}O_x$). To accomplish this, a precursor solution was created by dissolving 1.031 g of $Fe(NO_3)_3{\cdot}9H_2O$ and 5.202 g of $ZrO(NO_3)_2{\cdot}xH_2O$ in 50 mL of milliQ water. In a separate solution, 16.815 g of $TMAH{\cdot}5H_2O$ were dissolved in another 50 mL of milliQ water as the base solution. The concentration of $TMAH{\cdot}5H_2O$ was chosen in order to ensure there were 3 moles of the base for each mole of Fe^{3+} and 4 moles for each Zr^{4+}. The remaining steps were then performed in the same manner as outlined in 2.1.3.1., resulting in the final mixed oxide product.

2.1.3.4. $Cu_{0.1}Zr_{0.9}O_x$

To obtain a mixed oxide with a molar ratio of 1:9 Cu:Zr, the same procedure as in 2.1.3.1. ($Fe_{0.1}Ce_{0.9}O_x$) was followed for the preparation of $Cu_{0.1}Zr_{0.9}O_x$. This involved dissolving 0.604 g of $Cu(NO_3)_2{\cdot}3H_2O$ and 5.202 g of $ZrO(NO_3)_2{\cdot}xH_2O$ in 50 mL of milliQ water as the precursor solution, and separately dissolving 16.815 g of $TMAH{\cdot}5H_2O$ in another 50 mL of milliQ water as the base solution. The concentration of $TMAH{\cdot}5H_2O$ was chosen in order to ensure there were 4 moles of the base for each mole of Zr^{4+} and 2 moles for each Cu^{2+}. The remaining steps were carried out as described in 2.1.3.1., resulting in the final mixed oxide product.

2.1.3.5. CeO_2

The preparation of the CeO_2 oxide by inverse microemulsion was carried out in Milan with a slightly different setup, and for this reason the amount of the organic phase, concentration of the precursors and of the base were scaled down of a ¼ factor. In this preparation, 2.714 g of $Ce(NO_3)_3 \cdot 6H_2O$ (6.25 mmol corresponding to ¼ of the usual 25 mmol of precursor) were dissolved in a 15 mL flask of Milli-Q water. Another 15 mL flask was prepared containing 3.503 g of the base $TMAH \cdot 5H_2O$ in Milli-Q water. Two separate microemulsions using 107 mL of heptane, 23 mL of Triton X-100 and 24 mL of hexanol as co-surfactant were prepared and stabilized for 45 minutes, one containing the precursor and the other the base. Then, the same procedure employed in 2.1.3.1. ($Fe_{0.1}Ce_{0.9}O_x$) was carried out in order to obtain the final oxide.

2.1.3.6. ZrO_2

The preparation of the ZrO_2 oxide by inverse microemulsion was carried out in Milan as in 2.1.3.5., by using a different setup and amounts of precursors compared to the traditional microemulsion learnt in Cádiz. Here, 1.445 g of $ZrO(NO_3)_2 \cdot xH_2O$ were dissolved in a 15 mL flask brought to volume with MilliQ water to prepare the precursors solution. Another 15 mL flask was prepared containing 4.530 g of the base $TMAH \cdot 5H_2O$ in Milli-Q water (4 mol of TMAH for each mole of Zr). Then, the procedure was carried out precisely as in 2.1.3.5 (CeO_2) until the obtainment of the final ZrO_2 oxide.

2.1.4. Reduction of the Ce-/Zr-based mixed oxides

The as-prepared mixed oxides were reduced with a procedure modified from [11], in which it was carried out on TiO_2. In order to do so, each mixed oxide was mortared together with $NaBH_4$ in a 3:1 ratio, until the obtainment of a homogeneous mixture. Then, the reduction was carried out at 300°C for 50 minutes, with a controlled ramp of 10°C/min under a flow of Ar. The reduced oxides were recovered and washed with 250 mL of boiling water in order to remove the residuals deriving from $NaBH_4$. They were then put into the oven to dry at 80°C for the whole night. The preparation system for the reduction process is reported in Figure 2.12.

Figure 2.12. Preparation system for the reduction of the mixed oxides.

2.2. Characterization setup

This chapter is divided into two main parts containing the experimental setups utilized for the 1) characterization of the catalysts and 2) analysis of the products.

2.2.1. Catalysts characterization

The characterization of the catalysts was carried out using various solid-state analytical technique including high resolution transmission electron microscopy (HRTEM), scanning transmission electron microscopy (STEM) coupled with energy disperse X-ray analysis (EDX), X-ray photoelectron spectroscopy (XPS), X-ray diffraction of powders (PXRD, or simplified XRD) and BET surface analysis. For a better characterization, also Inductively Coupled Plasma (ICP) analyses were carried out in order to detect actual loading of the supported metals or metal leaching in some cases. Mössbauer spectroscopy was used only for the identification of the chemical state of Sn samples in the AuSn series.

2.2.1.1. Electron microscopy (HRTEM and STEM/EDX)

The samples were analysed mainly in Cádiz University using two different electron microscopes, namely the FEI TALOS F200X and the FEI Titan^3 Themis 60-300. The FEI TALOS

F200X is an uncorrected microscope used for structural and analytical characterization studies on the angstrom-scale, operated at 200 kV with a high-brightness X-FEG electron. In contrast, the FEI Titan^3 Themis 60-300 is a double Cs aberration-corrected scanning transmission electron microscope that is equipped with a gun monochromator combined with an X-FEG gun and ultra-high stability HT tank. Both microscopes have four STEM detectors, including a Bright-Field detector, two Dark Field Detectors (DF2, DF4), and a High Angle Annular Dark Field detector (HAADF)). Additionally, they are equipped with a Super-X detector for energy dispersive X-ray analysis, which has four-windowless detectors that can be used independently.

The structural characteristics of the samples were analyzed by high-resolution transmission electron microscopy (HRTEM) and scanning transmission electron microscopy (STEM),. The composition of the samples was analyzed by energy-dispersive X-ray spectroscopy (EDX) to obtain elemental maps. The Velox® software v. 2.13.0.1138 was used for processing of the STEM/EDX maps, while Digital Micrograph® software v. 3.50.3584.0 was used for the High-Resolution TEM images processing. Fast Fourier transform (FFT) patterns were indexed using the EjeZ software, which was used for the interpretation of the digital diffraction patterns (DDP) of the images.

The preparation the samples varied depending on the material that was to be analysed. Normally, for samples not containing copper, a Cu grid with lacey carbon film was utilized. In the case of Cu-containing samples, an Au or Ni grid with a lacey carbon film was employed. In the case of the Ni grid, special care was put in the handling by using non-magnetic tweezers.

In Eindhoven, the Netherlands, STEM/EDX composition measurements and spectrum imaging were performed on the supported Au-based series samples and on the parent sols drop-dried on molybdenum microgrids. The measurements were conducted using a FEI Titan Themis 200kV Cs-corrected TEM transmission electron microscope with 0.09 nm HRTEM and 0.16 nm STEM resolution equipped with 4 Thermofischer EDX detectors. The obtained data were analyzed, and elemental maps were generated using the Velox software. EDX spectra recorded in 80-500 scans of a selected area were cumulated, depending on the stability of the particles during the measurements. The background-corrected and fit Au-L and Cu-K intensities were applied for Au and Cu elemental maps, respectively. The Au/Cu atomic ratio was calculated

for various particles on an area localized on HAADF image that was measured simultaneously with the STEM/EDX measurements.

2.2.1.2. XPS

Surface chemical composition and oxidation state of the samples were analyzed through XPS measurements carried out on a Kratos Axis Ultra DLD spectrophotometer with multi-technique capabilities, installed at IMEYMAT (Institute of Electron Microscopy and Materials) at Cádiz University. This equipment features a vacuum system consisting of a turbomolecular pump (250 L/s) coupled with an ion pump (220 L/s), allowing for vacuum levels of around 5-10^{-10} torr. The X-ray emission source employed provides a continuous, stable, and monochromatic signal corresponding to the characteristic value of Al Kα (1486.8 eV). The installed monochromator is a Rowland circle type with a diameter of 500 mm, 450 kW power, and provides a fixed spot size of 1x2 mm, enabling a resolution of less than 0.48 eV (FWHM Ag $3d_{5/2}$).

The spectrum acquisition chamber is made of stainless steel with a double Mu-metal shielding coating. The equipment includes a 165 mm radius semi-spherical analyser with 128 simultaneous detection channels, an electron and ion detector based on a Multi-Channel Plate (MCP) electron multiplier system, and a delay-line detector (DLD). The measurements were operated in constant energy mode (CAE, Constant Energy Analyzer) with a 20 eV energy pass during data acquisition.

The samples were prepared as self-supported pellets by pressing the powder samples, which were then affixed to a double-sided adhesive conducting polymer tape. The Kratos coaxial neutralization system was used to compensate for surface charging effects. The BE scale was calibrated with respect to the C 1s signal at 284.8 eV.

2.2.1.3. XRD

Powder X-ray experiments were carried out on a Bruker D8 Advance diffractometer, using Cu K_α radiation (λ = 1.54 Å) as the radiation source. X-ray diffractograms were collected at room temperature over the 2 Theta range from 20 to 80°, with a step size increment of 0.05° and a step time (or acquisition time) of 3 s at every angle. The anode current and voltage were 40

mA and 40 kV, respectively. After the data collection, the XRD pattern analyses of all samples were identified in accordance with the reference patterns recorded in the ICDD database. Scherrer and Bragg equations (see Introduction - chapter 1.3.3.5. XRD) were used to estimate the crystallite size and lattice parameters by using the PowderCell software v. 2.3.

2.2.1.4. BET

The Brunauer–Emmett–Teller (BET) surface areas of the samples were determined by N_2 physisorption at −196 °C on a Micromeritics ASAP 2020 instrument. In order to carry out the analysis, the reactor was weighed together with the glass bar and the lid. Then the sample was inserted and weighed again before putting it in a heating coat (Figure 2.13) and connecting it to the instrument.

Figure 2.13. BET reactor wrapped in a heating coat and containing the sample.

The software values were introduced, and the sample was degassed in the degassing section of the instrument for 2 hours at 200°C with a ramp of 10°C/min. Once degassed, the reactor was weighed, and the weight was recorded to note any changes. Then, a reactor cover was placed on it, and the reactor was inserted into the measurement section of the instrument, with the thermocouple on the side above the dewar containing liquid N_2. The N_2 level was monitored to ensure it was sufficient, and the new weight of the sample was recorded before starting the analysis, which lasted approximately 5 hours.

2.2.1.5. ICP

An ICP Perkin Elmer optical emission spectrometer Optima 8000ICP-OES was used to evaluate the actual metal loading of each catalyst. For the AuCu samples, they were dissolved using a CEM MARS One Microwave Digester and the digestion was performed at 180 °C using an acidic solution of HCl (37%) and H_2SO_4 (98%) (2:3 molar ratio). Similar digestion was performed for the FeCo series leaching determination. For AuSn samples the digestion was performed at 200 °C using a mixture of HCl (37%), H_2SO_4 (95%) and HNO_3 (65%) with a ratio of 1:3:1.

2.2.1.6. Mössbauer Spectroscopy

A KFKI spectrometer was used, operating in constant acceleration mode, in transmission geometry at 78 K and 298 K using an in situ cell [12] with a 555 MBq $Ca^{119m}SnO_3$ source. The velocity scale was calibrated with α-Fe measurements, while the isomer shifts were given relative to SnO_2. The accuracy of the positional parameters was ±0.03 mm s^{-1}. The recorded spectra were evaluated by least-square fitting of the lines using the MossWinn code [13]. A Lorentzian line shape was used for the decomposition; no parameters were constrained.

2.2.2. Products characterization

The characterization of the products in this reaction was very complex as explained in the Introduction - Chapter 1.3.4. Concerns on products analysis, due to the high volatility of cyclohexane, the thermal stability of some products (such as CyOOH) and the solubility of the products when cooling down the autoclave. Nevertheless, taking these concerns into account, a thorough study of the reaction products, ramp of analysis and choice of the best standard was carried out during the PhD using different techniques such as gas chromatography (GC), GC coupled with mass spectroscopy (GC-MS) and high-performance liquid chromatography (HPLC).

2.2.2.1. Gas Chromatography

Gas chromatography was the main technique employed for the analysis of the organic phases and the determination of the reaction products, essential for the calculations of selectivity to

KA oil and KA oil productivity. The analysis of the reaction products was carried out with a Thermo Scientific TRACE 1300 gas chromatograph equipped with an Agilent® TG-5MS apolar column (similar to HP-5). This column separates the products for boiling point. The temperature ramp chosen to analyse the products was modified in order to last around 11 minutes and to have a good separation of the product mixture (Figure 2.14).

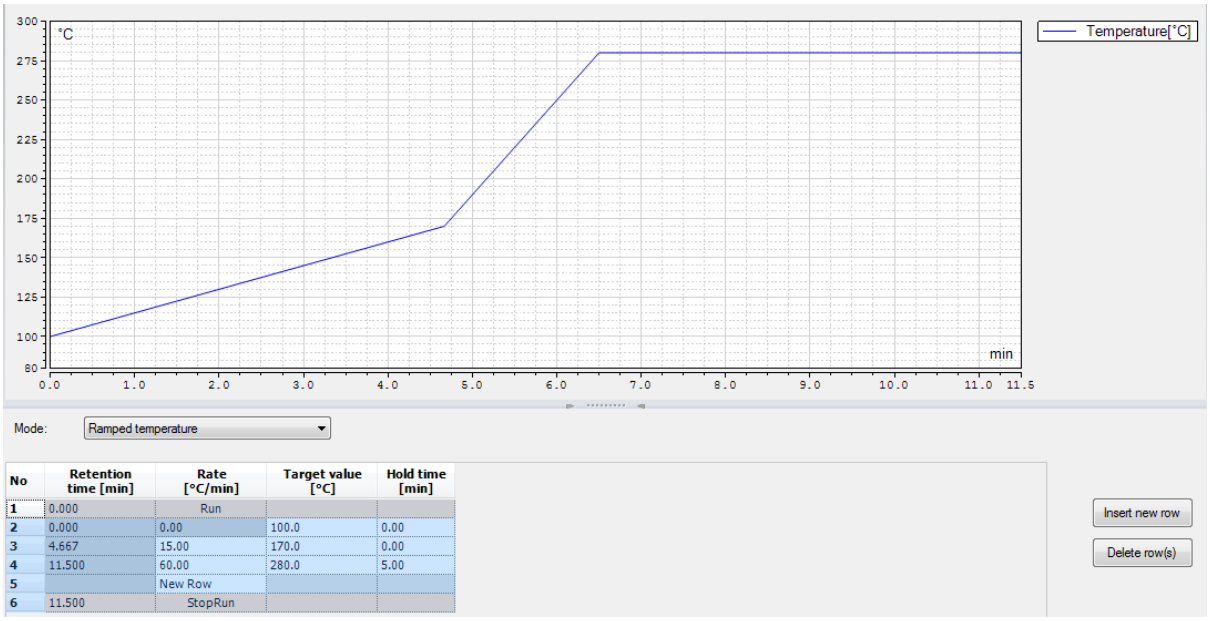

No	Retention time [min]	Rate [°C/min]	Target value [°C]	Hold time [min]
1	0.000	Run		
2	0.000	0.00	100.0	0.00
3	4.667	15.00	170.0	0.00
4	11.500	60.00	280.0	5.00
5		New Row		
6	11.500	StopRun		

Figure 2.14. Temperature ramp of the gas chromatograph method chosen for optimized separation of the reaction products.

Products analysis of this reaction is complicated by a multitude of factors (see Introduction 1.3.4. – Concerns on products analysis). Nevertheless, the products that underwent calibration were cyclohexane (when determining the mass return), cyclohexanol, cyclohexanone, adipic acid, benzaldehyde (used as radical initiator), benzoic acid and benzyl alcohol. Some products injected for the identification of unknown peaks included caprolactone, 1,2-, 1,3- and 1,4-cyclohexane diol. The calibration was carried out selecting a range of three concentrations for each substance within the range expected to be obtained from the reaction. A fixed amount of standard was put in each of the three flasks, and they were injected using the method and temperature ramp described above. From the resulting chromatographs, the response factor (f_r) of the substance was calculated with the following formula (Equation 2.1):

$$fr = \frac{Cx}{Cstd} * \frac{Astd}{Ax}$$

Equation 2.1. Calculation of the response factor for a substance X given the concentrations and GC areas of the substance and the reference standard.

With Equation 2.1 it is possible to obtain three response factors from the three analyses at the three different concentrations, which should be as close to the same number as possible. After checking the R^2 acceptability of the line having for $y=A_{std}/A_x$, $x=C_{std}/C_x$ and f_r as angular coefficient, an average between the three factors was calculated in order to give the f_r of each specific substance.

Different standards have been selected for the quantification of the reaction products. Both internal and external standard methods were employed during the choice of the most suitable standard for the reaction. It was found out that chlorobenzene is a suitable internal standard for this reaction and does not react or interfere with the complex mechanism, inspired by its previous successful employment by Graham et al. [14]. Therefore, it was utilized for the study of the FeCo series of catalysts. As external standard, dodecanol was used for the Au-based catalysts test. Then, biphenyl was used as internal standard following the works of other research groups [15,16]. For the experiments on the CeZr series, undecane was used as external standard as dodecanol was found to be harder to deal with due to its tendency to solidify at low ambient temperatures.

The preparation of the reaction sample in the case of an external standard was carried out by withdrawing 150 μL of the centrifuged reaction mixture and mixing it in an Eppendorf vial with 150 μL of the STD solution at known concentration. In the case of an internal standard, the centrifuged reaction sample was the one directly injected. The injection of the reaction products was executed by using a 10 μL syringe, withdrawing and injecting 1 μL of the prepared sample.

2.2.2.2. GC-MS

One product present in the final reaction mixture has proven difficult to identify, as its response factor in GC analyses was not corresponding to any of the products and by-products injected as commercial reagents. Although several hypotheses were considered to complete

the identification of the unknown product, from a practical point of view, the task was rather complex since a product had to be identified from a reaction solution, which therefore contained a large quantity of products and by-products, making it impossible to use, e.g., NMR. The only way that was easily possible turned out to be GC-MS. In fact, using this technique, it is possible to first separate the product mixture and then carry out mass spectroscopy. The source was an EI with energy at 70 KeV. GC-MS spectroscopy was therefore extremely helpful for the determination of what eventually we attributed to unreacted cyclohexyl hydroperoxide, using the Xcalibur software v. 4.0.27.10 for the determination. The m/z fragments of the product are reported in Figure 2.15.

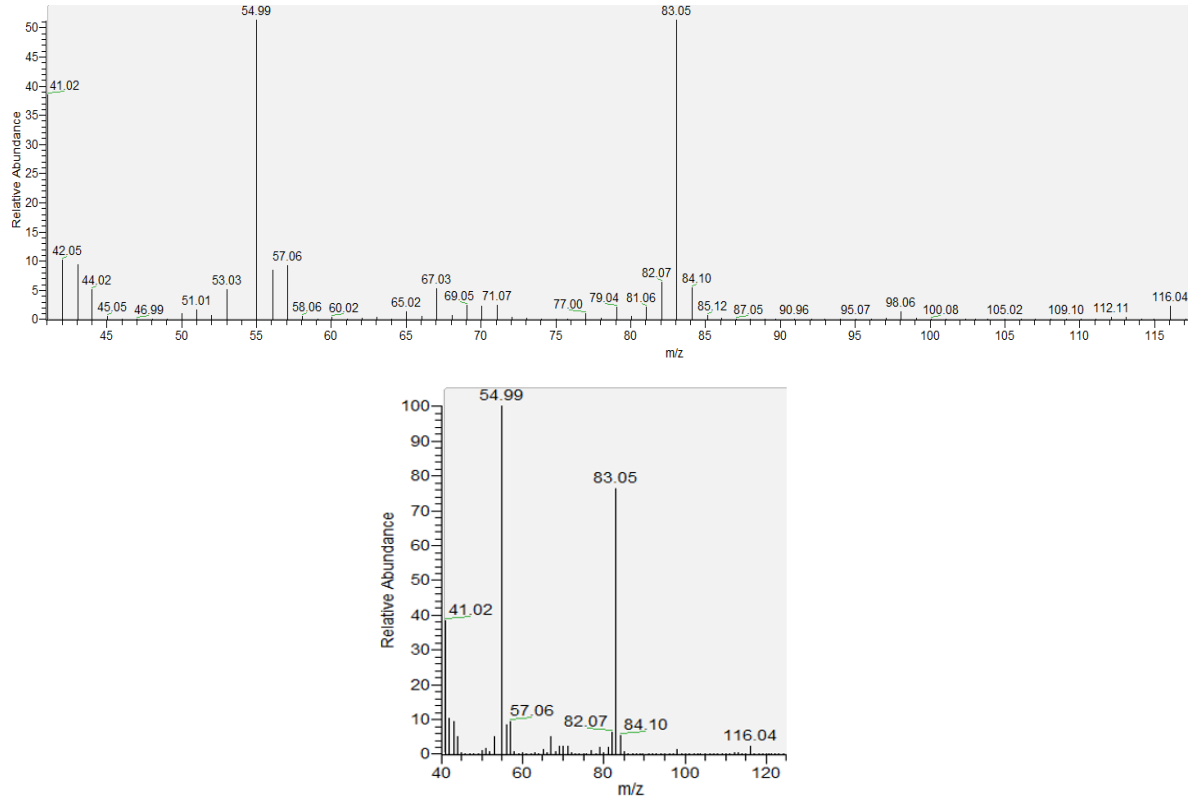

Figure 2.15. Mass spectrum of the unknown product present in the mixture after reaction.

The analysis led to the understanding that the product formed is a derivative of cyclohexane, as the characteristic fragment with a mass-to-charge ratio (m/z) of 83 is observed. This fragment is also visible in the presence of cyclohexanol and cyclohexanone, and it represents the $C_6H_{11}^{\bullet}$ fragment. At m/z 55, there is a base peak corresponding to $C_4H_7^{\bullet}$, obtained through the ring opening of the cyclohexane. Another fragment with m/z 41 is attributable to $C_3H_5^{\bullet}$. These two fragments, which are also visible in the presence of cyclohexanol and cyclohexanone, help confirm that it is indeed a cyclohexane derivative.

The molecular ion had an m/z of 116, which led to the hypothesis that the product could be either a cyclohexane diol isomer or alternatively cyclohexyl hydroperoxide. The possibilities of 1,2-cyclohexanediol, 1,3-cyclohexanediol, and 1,4-cyclohexanediol were eventually discarded since they were all injected and their retention time was not matching our product's. Therefore, we attributed the product being unreacted cyclohexyl hydroperoxide, which is a highly formed species in the radical mechanism of cyclohexane oxidation [16–18].

2.2.2.3. High Pressure Liquid Chromatography

HPLC was used for the for the determination of adipic acid content. In fact, since adipic acid is a white solid which is insoluble in cyclohexane but partially soluble in cyclohexanol and cyclohexanone [19], a methodology was necessary for an actual quantitative determination. After 5 hours of reaction, 10 mL of ethanol, which is miscible in cyclohexane, were poured in the autoclave to dissolve all the adipic acid. The mixture was put in a 100 mL round bottom flask where cyclohexane and ethanol were evaporated using the rotavapor. Mainly adipic acid, cyclohexanol and cyclohexanone remained at this point in the flask. The products were dissolved using 15 mL of MilliQ water transferring the content into a 15 mL flask and bringing to volume. The obtained solution was then injected into the HPLC, equipped with an ultra-visible (UV) detector and a Rezex ROA-Organic Acid H+ (8%) column. The solvent utilized was H_2SO_4 0.005 M. The column temperature was set at 60°C and the flow rate at 0.5 mL/min. The determination of the adipic acid content was carried out by analysing the area coming from the UV detector at λ = 210 nm.

2.3. Oxidation of cyclohexane

The oxidation of cyclohexane was carried out in a small artisanal autoclave (batch reactor) featuring a 100 mL volume capacity and stainless-steel walls. The autoclave was inserted into a heating bell placed on a heating plate with the auxilium of a thermocouple for temperature control. The whole system is reported in Figure 2.16.

Figure 2.16. The autoclave used for the reactions, inserted in the heating bell with a thermocouple on the rear side, placed on the heating plate.

A set of reactions with Au-based catalysts was experimented on 10 mL of reaction volume. The other tests of this thesis work were carried out using 15 mL of reaction volume, as 20 mL were found to be an excessive volume for constraints related to autoclave capacity and head space at our conditions. The amount of benzaldehyde put into the initial mixture as radical initiator was 10 µL, with the exception of the studies on the influence of the initial [benzaldehyde] (in the Au-based series), where that amount was varied accordingly.

In order to withdraw the samples, each time the autoclave was first cooled down in an ice bath and the remaining gas was emptied before opening. The sampling of the products occurred at t = 0, 1 h, 3 h, 4 h and 5 h of reaction, each time refilling the autoclave with O_2.

2.4. References

[1] L. Prati, A. Villa, Catalysts 2 (2011) 24–37.

[2] A. Villa, D. Wang, D.S. Su, L. Prati, ChemCatChem 1 (2009) 510–514.

[3] A. Martínez-Arias, M. Fernández-García, V. Ballesteros, L.N. Salamanca, J.C. Conesa, C. Otero, J. Soria, Langmuir 15 (1999) 4796–4802.

[4] G. Nagy, A. Beck, G. Sáfrán, Z. Schay, S. Liu, T. Li, B. Qiao, J. Wang, K. Lázár, (n.d.).

[5] M. Stucchi, S. Capelli, S. Cardaci, S. Cattaneo, A. Jouve, A. Beck, G. Sáfrán, C. Evangelisti, A. Villa, L. Prati, Catalysts 10 (2020).

[6] E. Pitzalis, R. Psaro, C. Evangelisti, Inorganica Chim. Acta 533 (2022) 120782.

[7] M. Fernández-García, A. Martínez-Arias, A. Iglesias-Juez, C. Belver, A.B. Hungría, J.C. Conesa, J. Soria, J. Catal. 194 (2000) 385–392.

[8] F. Basile, R. Mafessanti, A. Fasolini, G. Fornasari, E. Lombardi, A. Vaccari, J. Eur. Ceram. Soc. 39 (2019) 41–52.

[9] T. Masui, K. Fujiwara, Y. Peng, T. Sakata, K.I. Machida, H. Mori, G.Y. Adachi, J. Alloys Compd. 269 (1998) 116–122.

[10] M. Sanchez-Dominguez, C. Aubery, C. Solans, Smart Nanoparticles Technol. (2012).

[11] M. Pradenas, J. Yáñez, S. Ranganathan, D. Contreras, P. Santander, H.D. Mansilla, Water Environ. Res. 91 (2019) 157–164.

[12] K. Lázár, K. Matusek, J. Mink, S. Dobos, L. Guczi, A. Vizi-Orosz, L. Markó, W.M. Reiff, J. Catal. 87 (1984) 163–178.

[13] Z. Klencsár, E. Kuzmann, A. Vértes, J. Radioanal. Nucl. Chem. 210 (1996) 105–118.

[14] M. Conte, X. Liu, D.M. Murphy, K. Whiston, G.J. Hutchings, Phys. Chem. Chem. Phys. 14 (2012) 16279–16285.

[15] B.P.C. Hereijgers, B.M. Weckhuysen, J. Catal. 270 (2010) 16–25.

[16] A. Ramanathan, M.S. Hamdy, R. Parton, T. Maschmeyer, J.C. Jansen, U. Hanefeld, Appl. Catal. A Gen. 355 (2009) 78–82.

[17] P. Wu, P. Bai, K.P. Loh, X.S. Zhao, Catal. Today 158 (2010) 220–227.

[18] M. Sadiq, M. Ali, R. Iqbal, K. Saeed, A. Khan, M.N. Umar, H.U. Rashid, J. Chem. Sci. 127 (2015) 1167–1172.

[19] X. Yu, Z. Shen, Q. Sun, N. Qian, C. Zhou, J. Chen, J. Chem. Eng. Data 61 (2016) 1236–1245.

3. Results and Discussion

3.1. Activation of the C-H bond in cyclohexane

The radical activation of the C-H bond in cyclohexane is at the basis of the initiation of the radical mechanism in cyclohexane oxidation. Usually, in heterogeneous catalysis, a radical initiator is necessary for this purpose [1–5]. In this first part of my work, the C-H activation was dealt with the idea of finding a cheaper, less toxic, and easier to handle radical initiator compared to the most commonly employed one in heterogeneous catalysis: tert-butyl hydroperoxide (TBHP, see Introduction, Chapter 1.2.5. TBHP and H_2O_2 as oxidants). A suitable initiator also had to efficiently activate cyclohexane at the relatively mild reaction conditions selected to be employed (120°C, 4 bar O_2), milder than the ones employed in the classic industrial process (150-180°C, 10-15 bar of air).

A first series of tests were made using cumene hydroperoxide, a classical initiator derived from cumene, which can produce radicals by homolytic cleavage of the RO-OH bond. However, cumene was not able to activate cyclohexane under our conditions (Scheme 3.1, see also Introduction - Chapter 1.2.3. Autoxidation and reaction mechanism).

$$1)\quad Cy - H + X\ (peroxide, superoxide, unsaturated\ metal\ centre) \rightarrow Cy\bullet + XH$$

Scheme 3.1. Radical initiator-mediated activation of cyclohexane.

Therefore, the focus of my studies shifted on benzaldehyde autoxidation, a long-studied reaction in the Milan group, which is known to proceed via radical mechanism.

3.1.1. Benzaldehyde oxidation

Cyclohexane oxidation was investigated by adding benzaldehyde in the reaction solution, in order to probe if the radical mechanism of benzaldehyde autoxidation to benzoic acid [6–8] could aid the initiation of the radical mechanism of cyclohexane oxidation. Indeed, the spontaneous aerobic oxidation of benzaldehyde to yield benzoic acid takes place even under very mild conditions e.g. upon exposure to air at ambient temperature (approximately 293 K) [9].

Studies at different benzaldehyde concentrations have been performed to highlight the impact on the oxidation rate and formation of the desired KA oil products. As all radical mechanisms, the reaction should be independent on the initial concentration of the radical initiator, yet only a minimum amount of benzaldehyde to initiate the mechanism forming the peroxy- species (Scheme 3.2) should be necessary. Thus, it was tried performing the reaction in the absence of catalyst and investigated different initial benzaldehyde concentration. Reaction results expressed in terms of KA oil productivity are summarised in Figure 3.1 showing the independence (Figure 3.1) of productivity (around 2.5 mmol) with respect to benzaldehyde concentration thus confirming the radical mechanism.

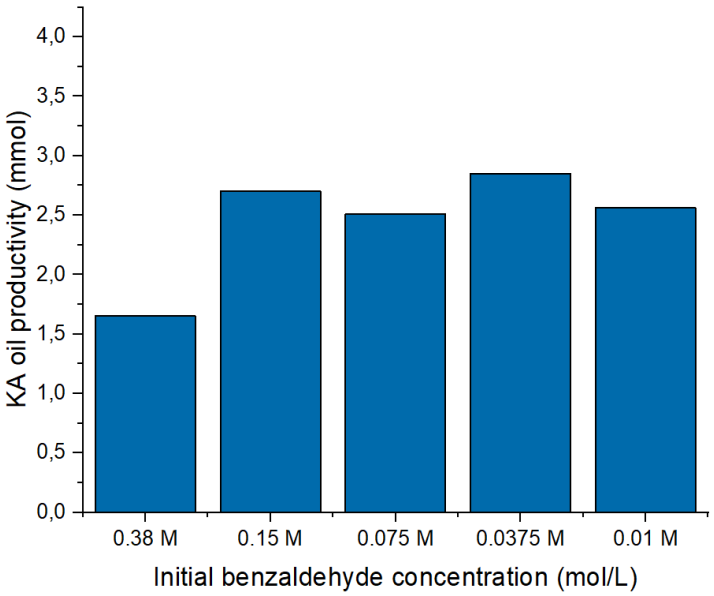

Figure 3.1. Benzaldehyde oxidation tests (at 120°C, 4 bar O_2, 5 hours), varying the initial concentration of benzaldehyde in cyclohexane.

Benzaldehyde oxidation to benzoic acid occurred in the first hour of reaction, forming benzoic acid and a certain amount (4-5%) of benzyl alcohol, which is assumed to be formed by the disproportion of two molecules of hydroxybenzyl radicals [8]. In this regard, Hutchings et al. [8] found that even under extreme conditions of high temperature and high O_2 pressure, the presence of a very small amount of benzyl alcohol or other alcohols with an active C-H group for hydrogen atom transfer hinders the oxidation of benzaldehyde to benzoic acid. To further confirm the hypothesis of the presence of free $^{\bullet}OH$ radicals, octanol was used as radical scavenger. The addition of octanol in the initial solution was able to completely shut down the reaction, even preventing benzaldehyde conversion into benzoic acid.

As shown in Figure 3.1, at the highest tested concentration of benzaldehyde (~ 0.4 M) a lower productivity was observed, that was attributed to an increased concentration of benzyl alcohol, which can act as octanol as radical scavenger quenching the radical mechanism of cyclohexane oxidation. To be noted that benzoic acid as well can have a detrimental effect on the reaction due to its precipitation thus deposition on catalyst surface.

An important parameter to be mentioned in the context of cyclohexane oxidation is the K/A ratio, which indicates the amount of ketone and alcohol present in the reaction mixture at the end of the reaction. The importance of K/A ratio rely on the definition of the possible role of catalyst in the initiation of the reaction (Scheme 3.2 - step 1a vs 1b).

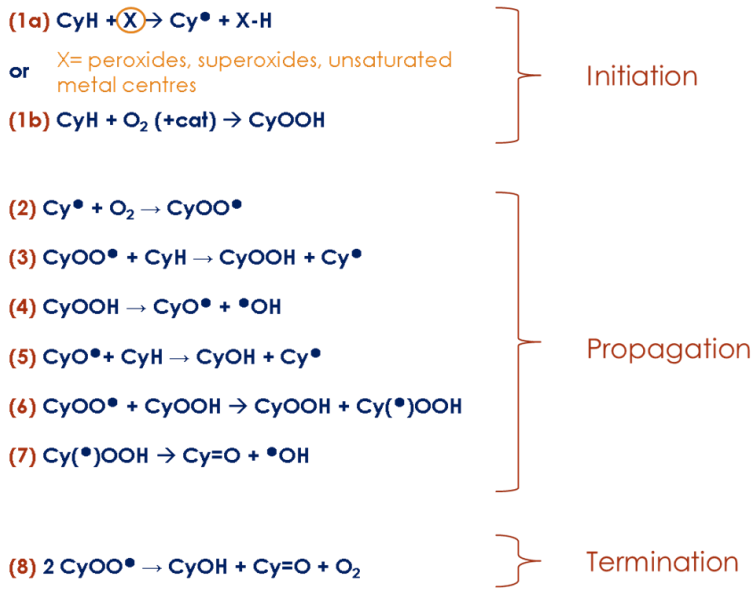

Scheme 3.2. Radical-chain mechanism for the oxidation of cyclohexane.

The pure radical mechanism has been established to result in a high K/A, and different research groups also suggest that a K/A ratio greater than 1.5 would be due to a pathway not involving a mediation from a catalyst surface [10,11]. In my work, this was experimentally confirmed by the experimental result in the presence of the initiator-only. The K/A ratio here introduced is a parameter of paramount importance because it varies in the presence of a catalyst, as it will be shown in later catalytic tests.

In conclusion, not only benzaldehyde was found to effectively initiate the free-radical pathway of cyclohexane oxidation even in the absence of a catalyst, but it also represented advantages over state-of-the-art radical initiators. Among the advantages, it is much less expensive than

the most commonly employed radical initiator tert-butyl hydroperoxide (20.00 € for 250 mL of benzaldehyde Reagentplus >99% pure vs 96.60 € for just 25 mL of TBHP 0.5-0.6 M in decane). Moreover, benzaldehyde is available in the pure form, whereas TBHP is sold in solution (decane or water) which can add additional problems of compatibility with the actual reaction conditions (solventless). Benzaldehyde is also less toxic than TBHP. The study and the use of benzaldehyde as radical initiator was then carried on for all catalysed reactions, until the end of the Ph.D. final year.

3.1.2. Tests on the industrial catalyst

In the classic industrial process developed by Du Pont in the early 1940s [12], many homogeneous catalysts have been patented for the oxidation of cyclohexane, being all based on transition metals salts. The most employed up to our days consists in Co(II) naphthenate salts. In the classic process, a high temperature of 150-180°C is necessary, and a high pressure of 10-15 bar using air or O_2. In order to verify the ability of the industrial catalyst of working at our milder reaction conditions, I tested an amount of Co(II) naphthenate solution equal to the corresponding amount of heterogeneous catalyst's active species that I would have put in the heterogeneous conditions, for maintaining a molar ratio of ~1:2500 met:cyclohexane. The catalyst was tested using 120°C, 4 bar O_2 and 10 mL of cyclohexane as solvent-reagent. Even after 5 hours of reaction, the catalyst was not able to convert cyclohexane. Then, I performed the reaction in the presence of benzaldehyde with an initial concentration of $[benzaldehyde]_i$ = 0.15 M. However, even in this case, no cyclohexane conversion was observed. This time, the catalyst also exerted a quenching effect on the autoxidation of benzaldehyde which remained unreacted. This was a first important result, as it was proved that the industrial catalyst could not convert cyclohexane under our reaction conditions.

3.2. FeCo bimetallic systems supported on γ-Al_2O_3

Many efforts have been put in the past years to improve the classic industrial process based on the homogeneous Co(II) naphthenate catalyst by replacing it with a heterogeneous catalyst. Indeed, the use of a heterogeneous catalyst is more advantageous in terms of separation, recyclability and disposal, and it also represents an interesting way to implement a continuous process. As it was stated in the Introduction section (see Introduction- Chapter 1.2.2. Heterogeneous catalysis), among the heterogeneous systems proposed for the oxidation of cyclohexane, recent research in a 2022 review [13] has highlighted the effectiveness of metal and metal oxide catalysts. The current focus revolves around discovering cost-effective systems that utilize abundant metals, exhibiting excellent stability under varying temperature and pressure conditions (high T and P stability), and possessing intriguing redox properties that can aid in facilitating the intricate single electron exchanges inherent to the radical reaction mechanism. In this context, our attention began shifting to the metal used for the homogeneous process, cobalt. In this context, we deeply explored the catalytic potential of Fe as modifier of classical Co oxide, thus creating a new category of supported oxides featuring Co and Fe on Al_2O_3. The choice of alumina as support is related to its non-reducible oxide classification, high surface area and high thermal stability.

Co systems have attracted numerous researchers in the past decades due to its extended use over the years in the industrial homogeneous process, paired with its inexpensiveness and peculiar oxidation-reduction abilities. In fact, in addition to its elemental form, cobalt can exist in Co^{2+} and Co^{3+} oxidation states, which enhance its ability to create composites by combining with other elements or supports, and it also shows exceptional catalytic activity due to its partially filled d orbital (3d7) [14]. Cobalt has been used in different forms with different supports (MCM-41, SBA-15, ZSM-5, TiO_2, mesoporous molecular sieves such as TUD-1), as nano oxides and even as mixed oxides or spinels [15]. Among the remarkable results, solvent-free cyclohexane oxidation performed with Mn-Co-TUD-1 allowed to obtain a 12.3% conversion after 8 hours with a high selectivity of 90.4% at 70°C, with the use of TBHP as radical initiator [16]. 2% Co/SBA-15 exhibited 9.6% conversion of cyclohexane and 81.1% selectivity to KA oil at 135°C and 6 bars of O_2 pressure [17]. In addition, cobalt is usually capable of forming alloys and interaction with a variety of metals [18] and one of the most

interesting combinations is with Fe. Indeed, Fe is the fourth most common element present on the planet crust and iron (hydr)oxides are widely employed in the aerobic oxidation of organic compounds to produce fine chemicals among many other applications [19], also due to its divalent and trivalent states and the inherently nanocrystalline forms in which it is found in nature. Iron oxides are also used as heterogeneous catalysts for Fenton oxidation system because of their abundance, easy separation and lower cost [20]. The original Fenton reaction is an homogeneous process that generates highly reactive hydroxyl radicals by decomposition of hydrogen peroxide using ferrous ions, where Fe(II) passes to Fe(III) [21]. Many Fenton catalysts have been developed as pure iron oxides (magnetite, hematite, ferrites, pyrite and ferrihydrite) or mixed with other transition metals, and it was reported of spinel ferrites with AB_2O_4 formula, where B is Fe and A is generally Co or Mn [22]. The oxidation of cyclohexane was little studied in Fenton-like reactions with heterogeneous systems and H_2O_2 as radical initiator although with some remarkable examples [23]. However, the ability of Fe(II) to decompose hydroperoxides along with its oxidation-reduction properties brought us to the consideration it could help the homolytic cleavage of the cyclohexyl hydroperoxide intermediate.

Therefore, both Fe and Co are attractive systems because of their properties of electron exchange with external species, the existence in different oxidation states and their ability to donate or withdraw electrons [14]. In particular, at 1.6 MPa of O_2 and 145-150°C studies on cobalt ferrite ($CoFe_2O_4$) alone [24] obtained up to 16.4% conversion and 90.3 % selectivity to KA oil at harsh conditions, while SiO_2 supported (5 wt%) cobalt ferrite [25] allowed to obtain a selectivity to KA oil of 95.4% at 7.4% conversion. Sonochemistry-prepared 1:1 Fe:Co amorphous oxide supported on TiO_2 was also tested in cyclohexane oxidation [26], but it resulted in only 60% selectivity to KA oil, much lower than that of the monometallic counterparts. In the light of these considerations, in this work it has been investigated the behaviour of Fe, Co and FeCo (1:1) catalytic systems supported on γ-Al_2O_3 and prepared by three different techniques, namely sol immobilization, inverse microemulsion and incipient wetness, to be tested in the aerobic oxidation of cyclohexane at our relatively mild reaction conditions (120°C, 4 bar O_2).

3.2.1. The FeCo series

Three series of catalysts were prepared with three different methods: sol immobilization, inverse microemulsion and incipient wetness. Each series is composed of three catalysts monometallic Fe, Co and the bimetallic Fe_1Co_1. The aim of this series was to make bimetallic Fe_1Co_1. The monometallic catalysts were prepared for comparison. All the catalysts were prepared at 2 wt% total metal loading on γ-Al_2O_3. The samples divided by preparation method are labelled as follows (Table 3.1):

Sol immobilization	Inverse microemulsion	Incipient wetness
2 wt% Fe/γ-Al_2O_3-SOL	2 wt% Fe/γ-Al_2O_3-ME	2 wt% Fe/γ-Al_2O_3-IW
2 wt% Co/γ-Al_2O_3-SOL	2 wt% Co/γ-Al_2O_3-ME	2 wt% Co/γ-Al_2O_3-IW
2 wt% Fe_1Co_1/γ-Al_2O_3-SOL	2 wt% Fe_1Co_1/γ-Al_2O_3-ME	2 wt% Fe_1Co_1/γ-Al_2O_3-IW

Table 3.1. The whole FeCo series, featuring the monometallic Fe and Co and the bimetallic FeCo systems all supported on γ-Al_2O_3, obtained by the three different preparation methods.

Considering the variety of these systems, being prepared by different methodologies and particularly in the case of the three bimetallic Fe_1Co_1/Al_2O_3 catalysts, it was decided to explore these systems starting by electron microscopy to better understand the morphology, combination and distribution of the Fe and Co species on Al_2O_3. The metal particles composition was evaluated employing high-angle annular dark-field (HAADF) scanning transmission electron microscopy (STEM) and energy-dispersive X-ray spectroscopy (EDX). Then, powder XRD was carried out for phase detection.

3.2.1.1. STEM/EDX characterization

The STEM/EDX images of the monometallic 2 wt% Fe/γ-Al_2O_3-SOL, 2 wt% Co/γ-Al_2O_3-SOL and 2 wt% Fe_1Co_1/γ-Al_2O_3-SOL prepared by sol immobilization are reported in Figure 3.2a,b,c, with the related EDX spectra.

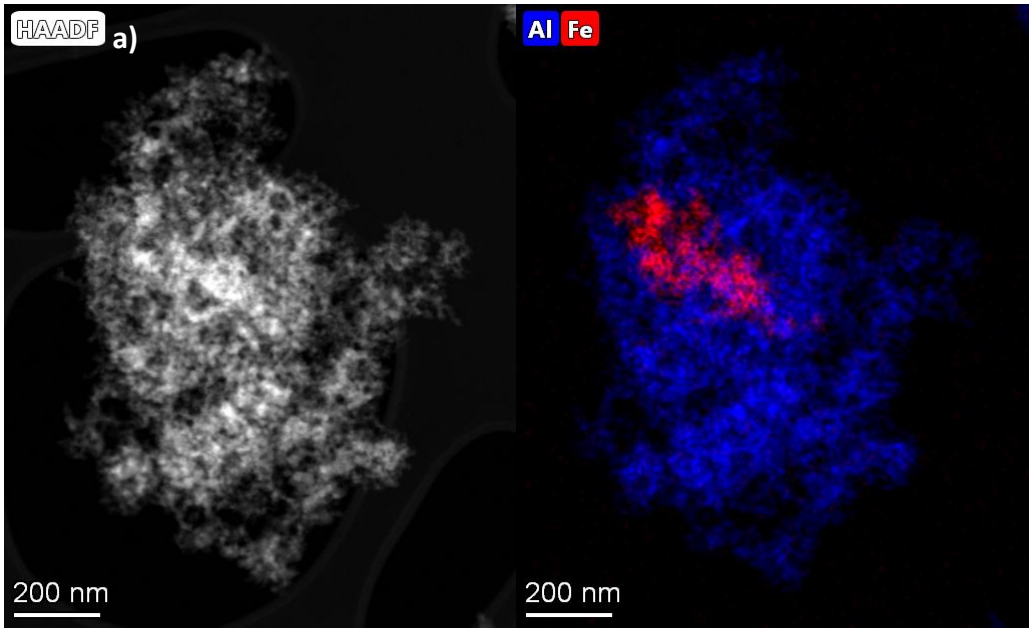
HAADF
a)
200 nm
Al
Fe
200 nm

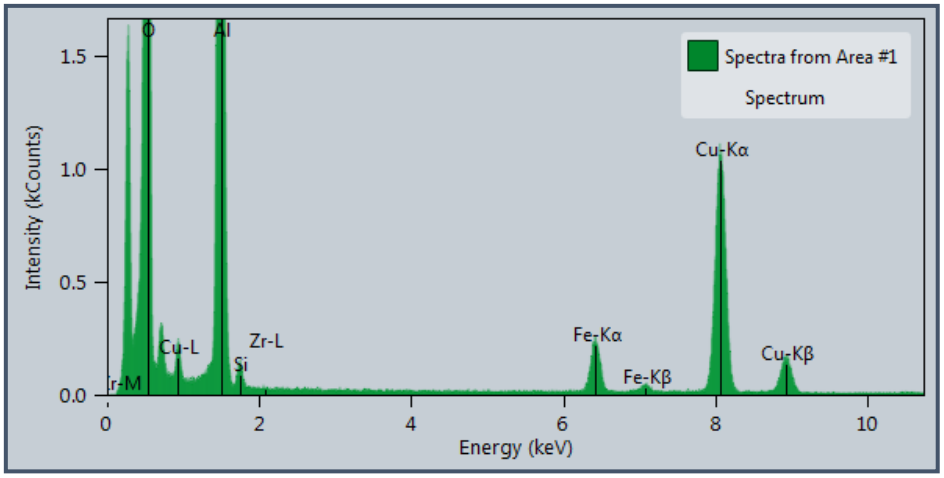
O
Al
Spectra from Area #1
Spectrum
Cu-Kα
Intensity (kCounts)
1.5
1.0
0.5
0.0
Cu-L
Zr-L
Si
Fe-Kα
Fe-Kβ
Cu-Kβ
0
2
4
6
8
10
Energy (keV)

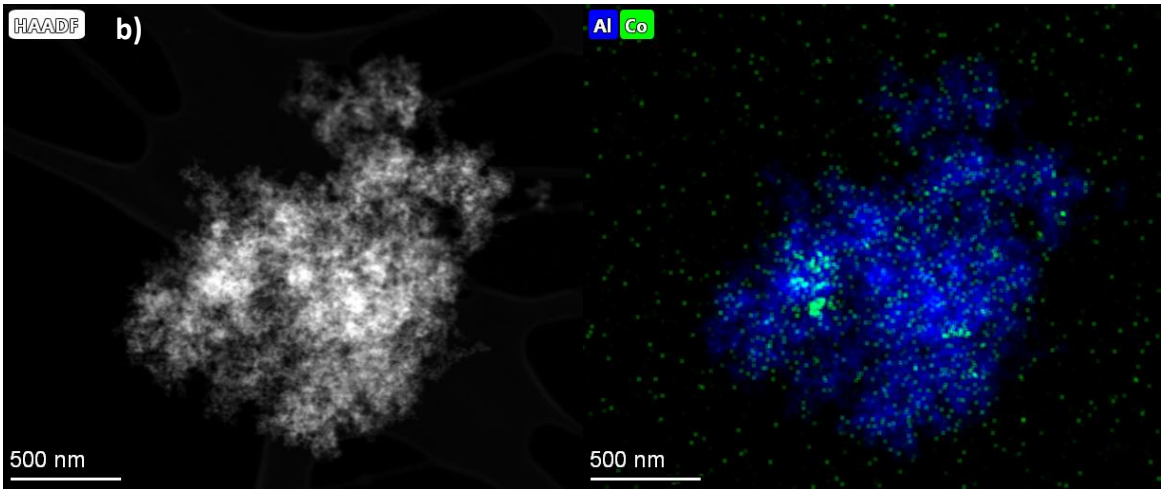
HAADF
b)
500 nm
Al
Co
500 nm

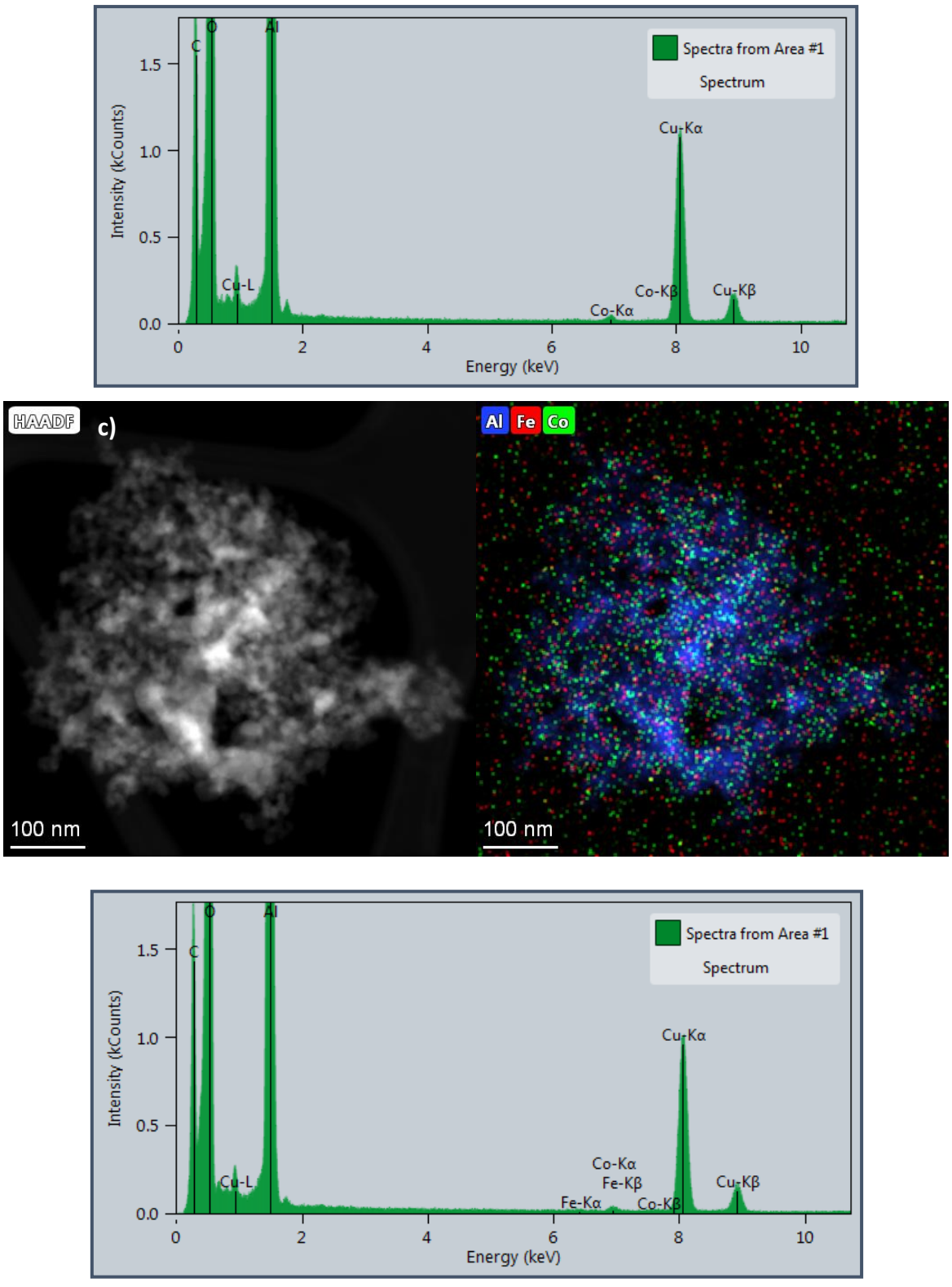

Figure 3.2. STEM mode HAADF image, EDX elemental map and element spectra of (a) 2 wt% Fe/γ-Al_2O_3-SOL,, (b) 2 wt% Co/γ-Al_2O_3-SOL and (c) 2 wt% Fe_1Co_1/γ-Al_2O_3-SOL.

As it can be noticed from Figure 3.2a and b, the monometallic sols were highly heterogeneous in composition. In particular, 2 wt% Fe/γ-Al_2O_3-SOL featured big agglomerates of 200 nm

particles in some regions, whilst most of the sample was characterized by the absence of Fe. For 2 wt% Co/γ-Al_2O_3-SOL, smaller agglomerates of 20-100 nanometres were observed, whereas in some areas it was completely absent. In the case of 2 wt% Fe_1Co_1/γ-Al_2O_3-SOL, a very small amount of Fe and Co was detected on the studied areas. It was impossible to encounter any aggregates in any of the multiple area analysed. No contamination was observed in the elemental spectra of the SOL catalysts, where the Cu signal derives from the support grid. The average atomic ratio between Fe and Co was determined to be 35/65, with a higher abundance of Co. The STEM/EDX images of the samples prepared by inverse microemulsion are reported in Figure 3.3a,b,c.

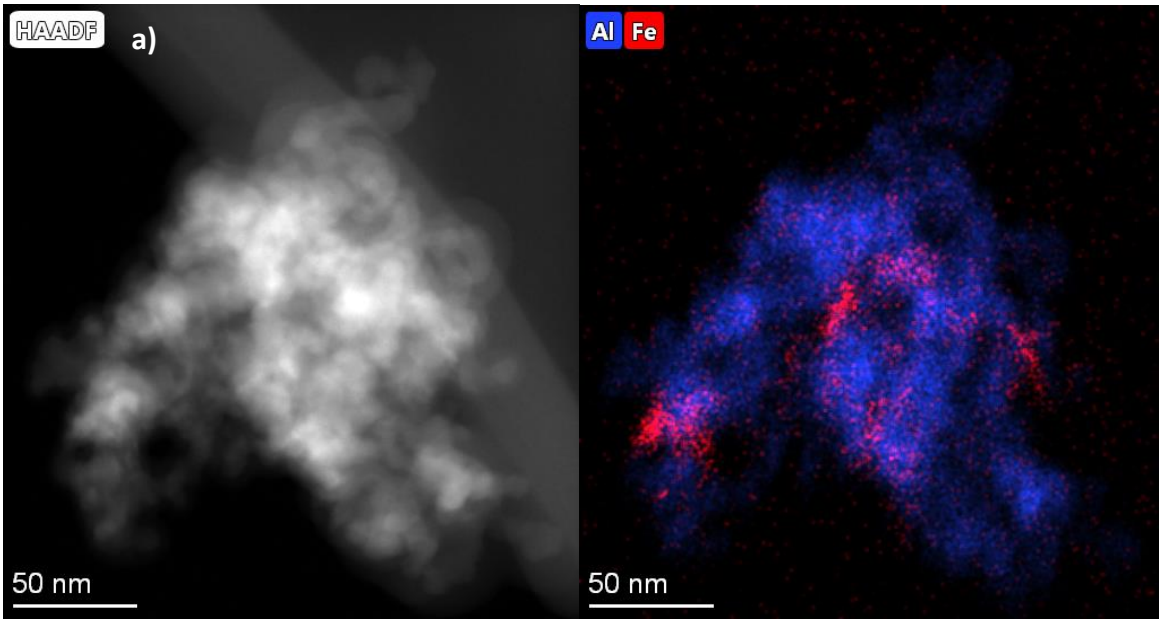

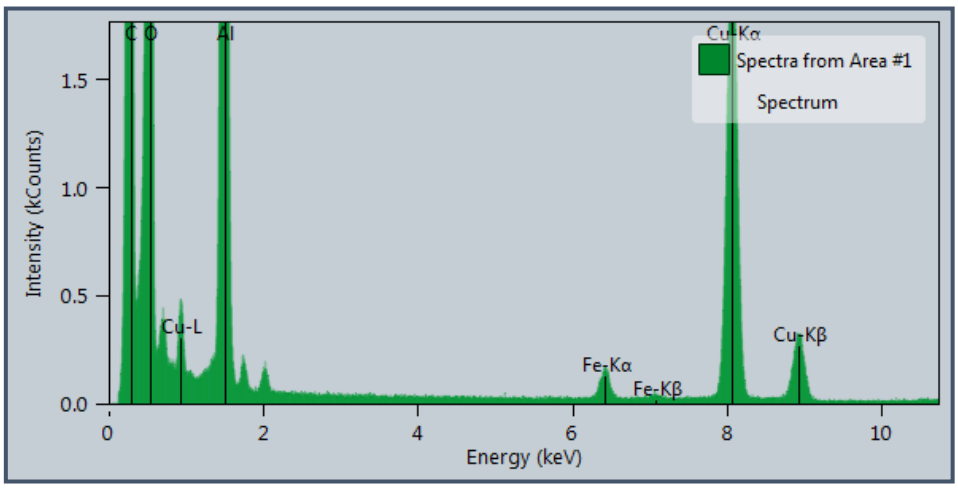

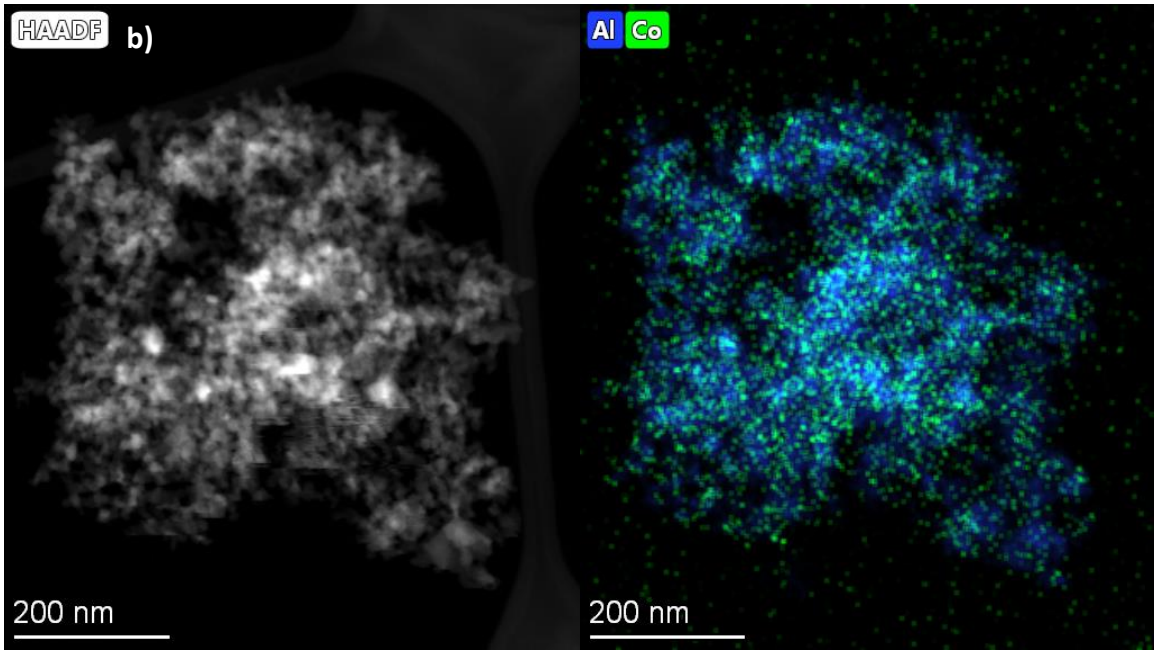
HAADF
b)
Al
Co
200 nm
200 nm

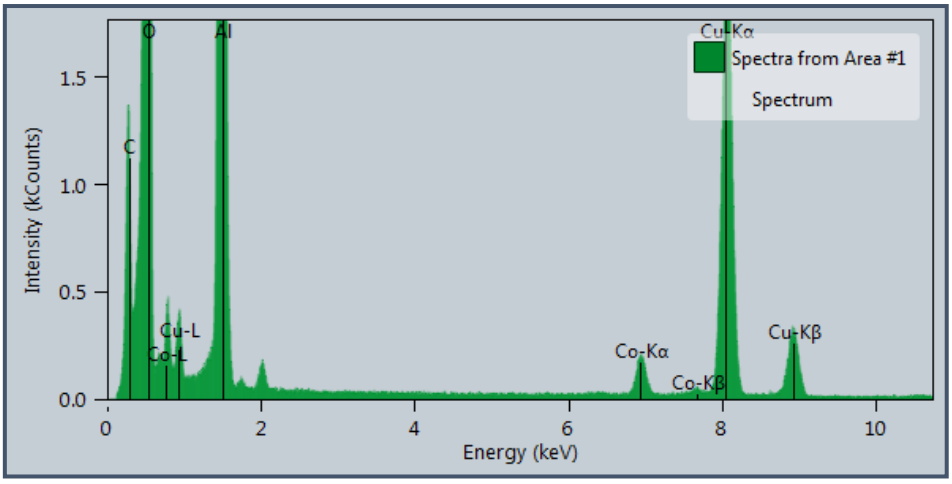
O
Al
Cu-Kα
Spectra from Area #1
Spectrum
C
Cu-L
Co-L
Co-Kα
Co-Kβ
Cu-Kβ
Intensity (kCounts)
Energy (keV)
0.0
0.5
1.0
1.5
0
2
4
6
8
10

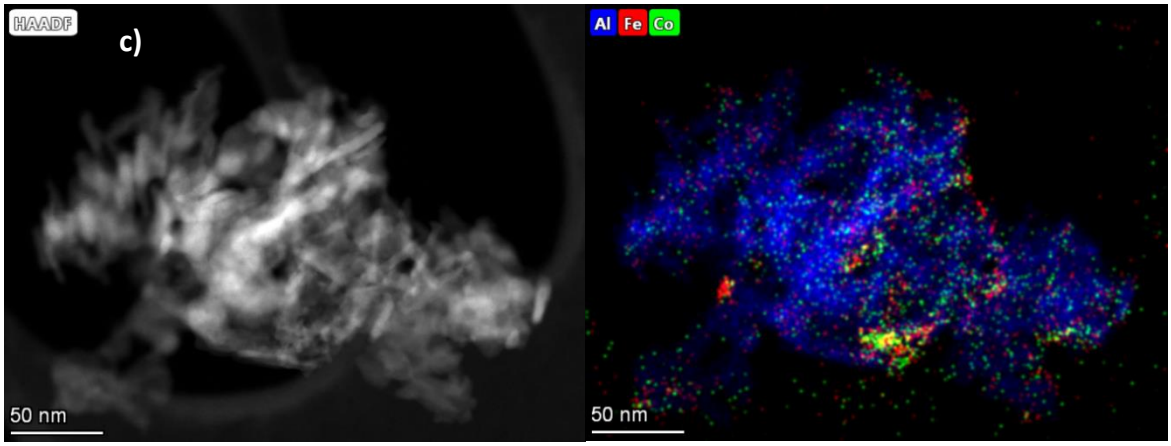
HAADF
c)
Al
Fe
Co
50 nm
50 nm

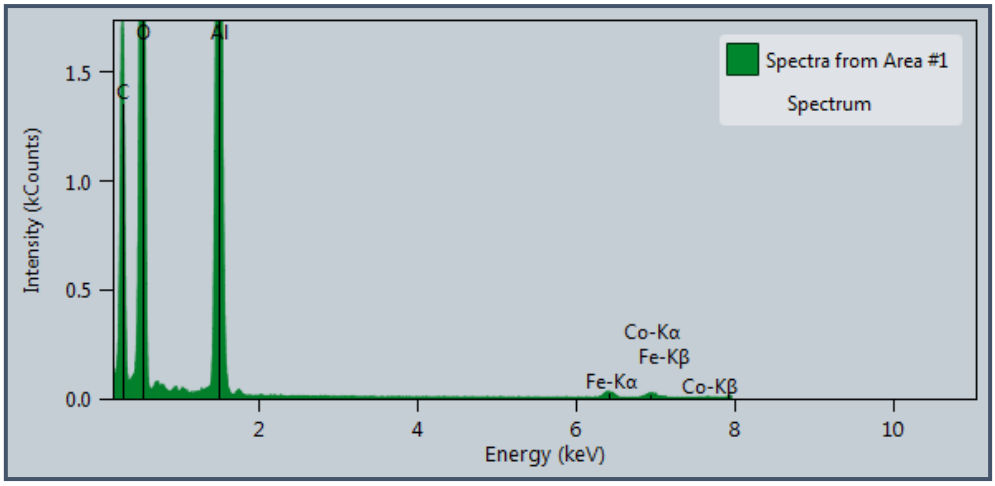

Figure 3.3. STEM mode HAADF image, EDX elemental map and element spectra of (a) 2 wt% Fe/γ-Al_2O_3-ME, (b) 2 wt% Co/γ-Al_2O_3-ME and (c) 2 wt% Fe_1Co_1/γ-Al_2O_3-ME.

Even in the case of 2 wt% Fe/Al_2O_3-ME, the sample presented big agglomerates (~30 nm) of Fe all over the alumina in the crystallites observed, unevenly distributed on the surface. On the contrary, 2 wt% Co/Al_2O_3-ME showed great homogeneity of Co distribution, in the form of small (5-15 nm) particles. The sample of 2 wt% Fe_1Co_1/γ-Al_2O_3-ME exhibited small to medium-sized (5 to 20 nm) agglomerates of Fe and Co on the alumina support, primarily in very intimate contact. The dispersion of these agglomerates on the alumina surface showed heterogeneity. The average atomic ratio between Fe and Co was determined to be 60/40, with a slightly higher abundance of Fe.

The samples prepared by incipient wetness were also observed through STEM/EDX microscopy (Figure 3.4a, b and c).

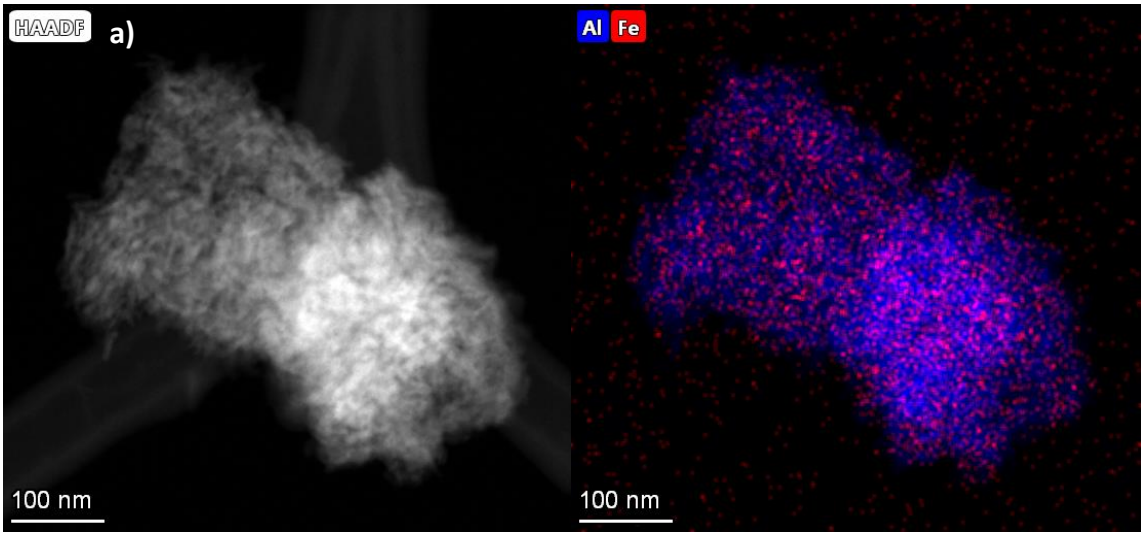

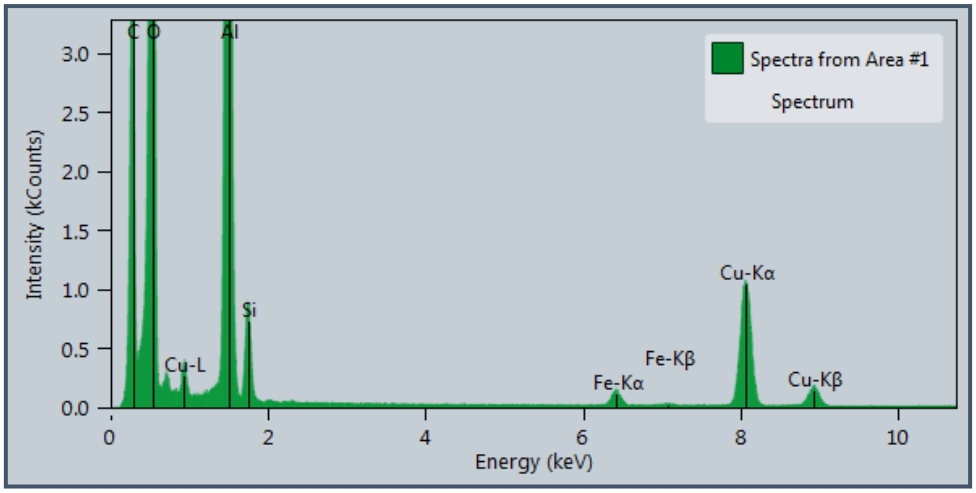
C
O
Al
Si
Cu-L
Fe-Kα
Fe-Kβ
Cu-Kα
Cu-Kβ
Spectra from Area #1
Spectrum
Intensity (kCounts)
Energy (keV)
0.0
0.5
1.0
1.5
2.0
2.5
3.0
0
2
4
6
8
10

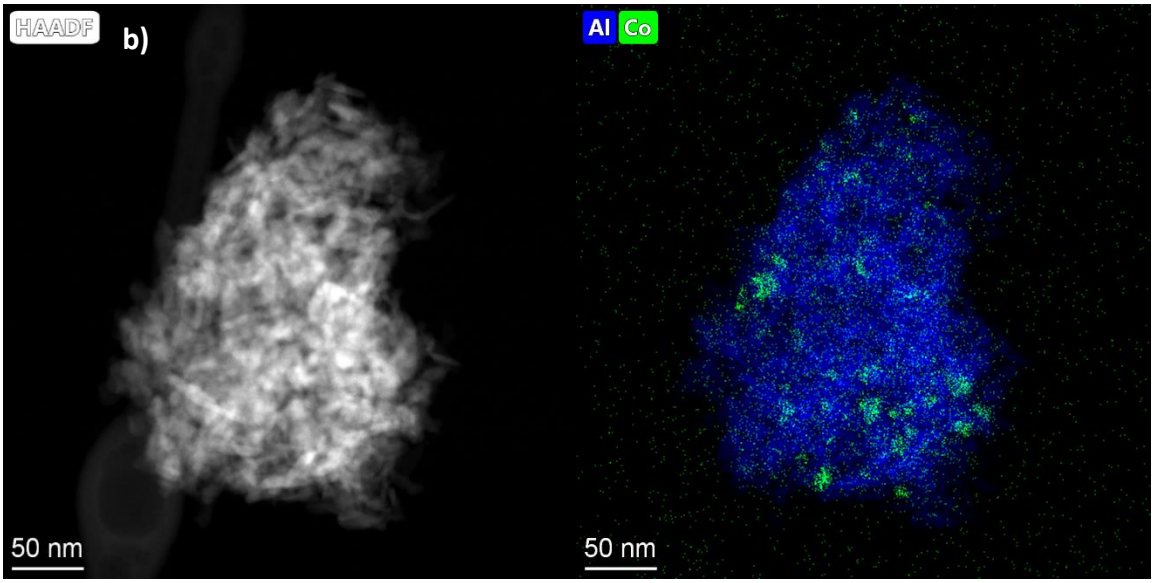
HAADF
b)
Al
Co
50 nm
50 nm

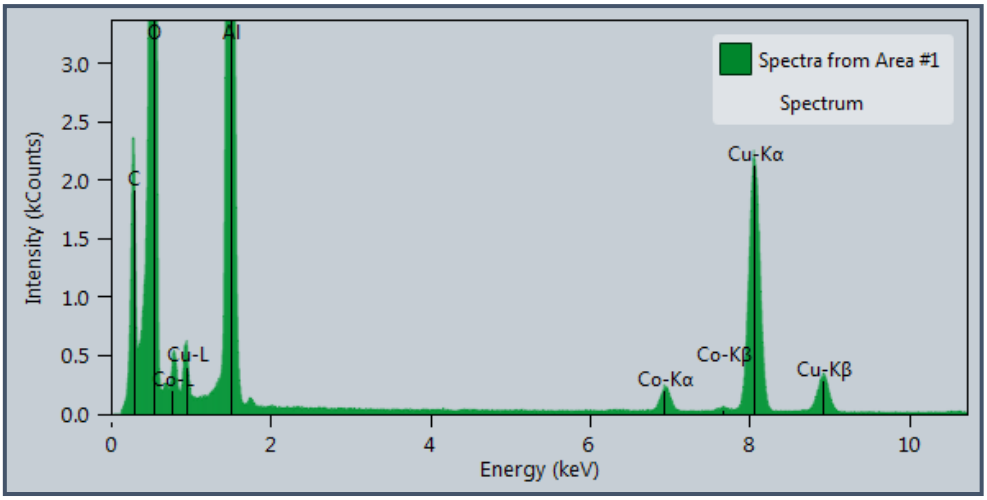
O
Al
C
Cu-L
Co-L
Co-Kα
Co-Kβ
Cu-Kα
Cu-Kβ
Spectra from Area #1
Spectrum
Intensity (kCounts)
Energy (keV)
0.0
0.5
1.0
1.5
2.0
2.5
3.0
0
2
4
6
8
10

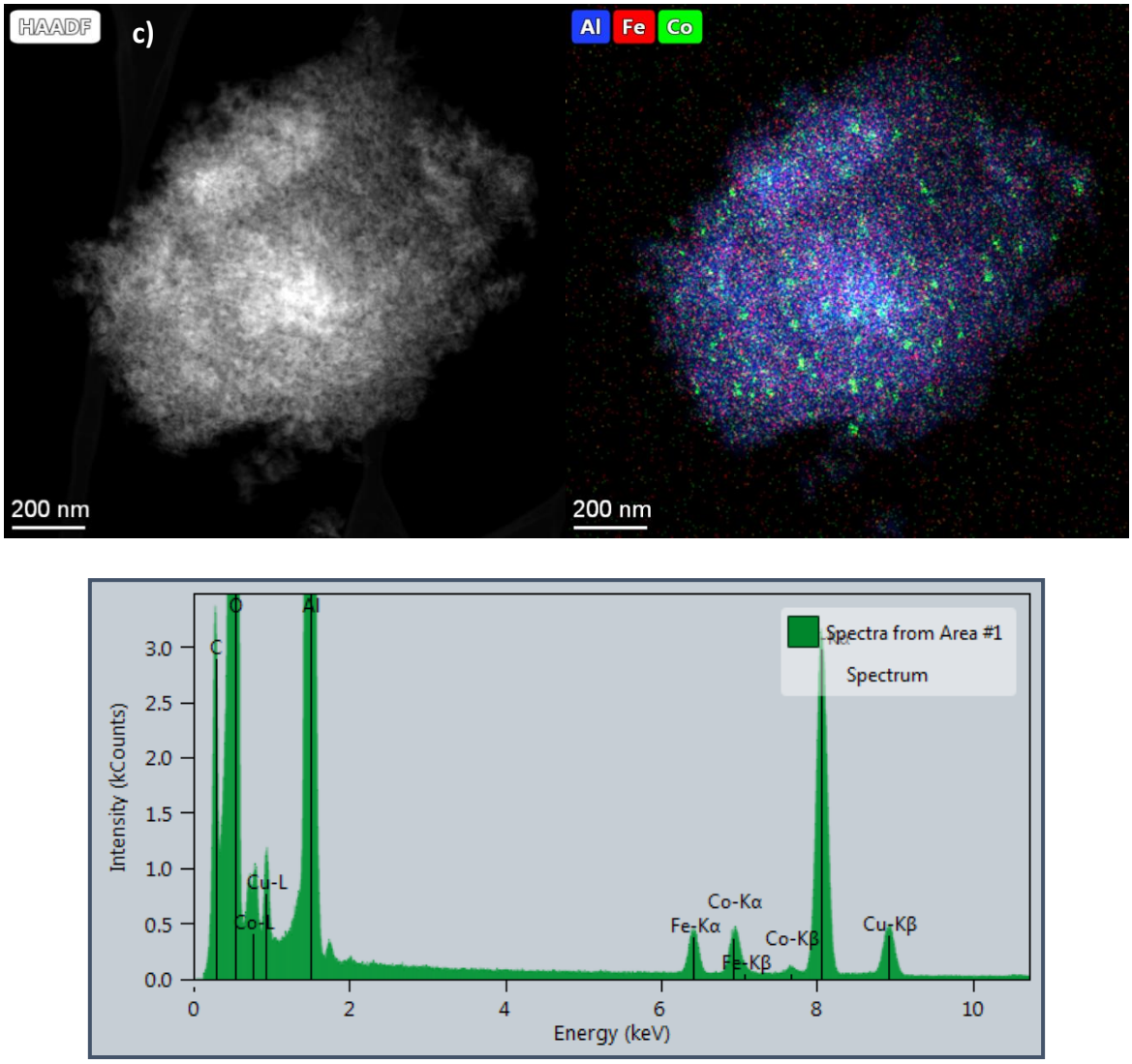

Figure 3.4. STEM mode HAADF image, EDX elemental map and element spectra of (a) 2 wt% Fe/γ-Al_2O_3-IW, (b) 2 wt% Co/γ-Al_2O_3-IW and (c) 2 wt% Fe_1Co_1/γ-Al_2O_3-IW.

In the case of 2 wt% Fe/γ-Al_2O_3-IW, the metal was very well dispersed on the surface of Al_2O_3 throughout the whole sample, forming small agglomerates of 5-10 nm size. Contrarily, the elemental map performed on 2 wt% Co/γ-Al_2O_3-IW presented clusters of Co ranging from 15-25 nanometres and with a good dispersion on the alumina surface. Interestingly, the bimetallic 2 wt% Fe_1Co_1/γ-Al_2O_3-IW reported to possess both characteristics. In fact, from the EDX maps, Co is more present in the form of small-to-medium size nanoparticles, while Fe is mainly dispersed on the surface. From the spectrum of the area measured on different particles, the presence of both Fe and Co in a 50:50 ratio was confirmed, in agreement with the theoretical calculations of the preparation. The intimate contact of Fe and Co particles is evident, and there are areas where it is possible to observe them in the same spot as bimetallic particles.

3.2.1.2. XRD analyses

XRD analyses were carried out in order to possibly detect metallic NPs and bulk phases present in the samples in the range of 2θ = 20-80° (Figure 3.5, Figure 3.6 and Figure 3.7).

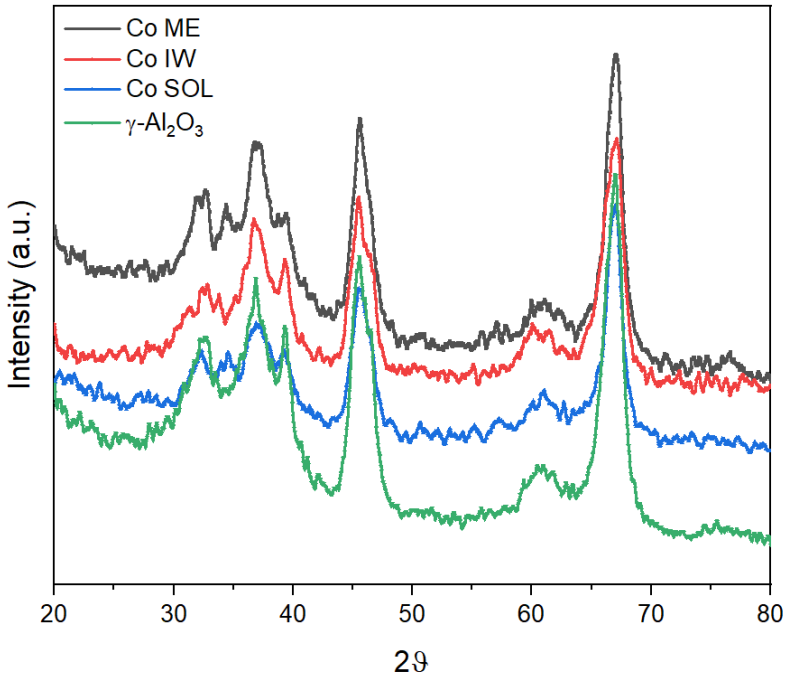

Figure 3.5. XRD diffraction patterns of 2 wt% Co/Al_2O_3-ME, 2 wt% Co/Al_2O_3-IW and 2 wt% Co/Al_2O_3-SOL in the range 20° < 2ϑ < 80°, compared with γ-alumina.

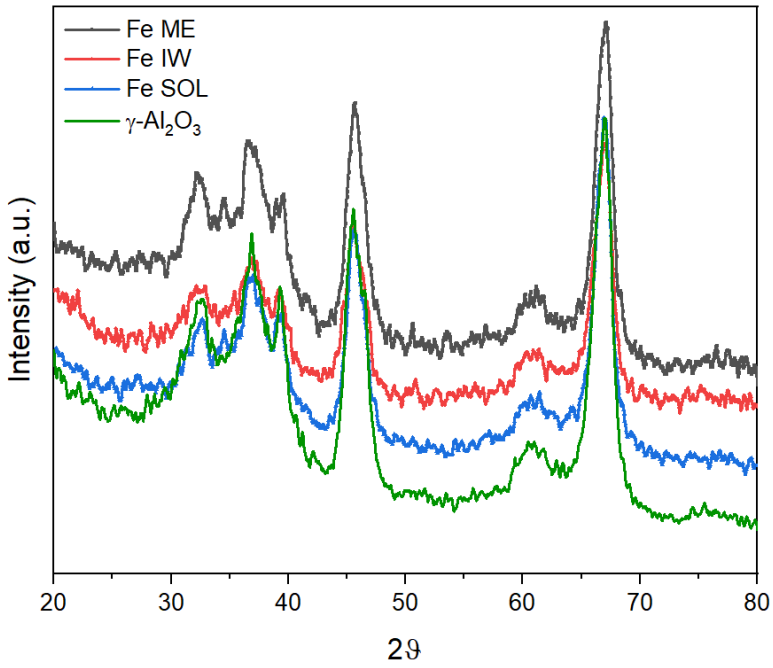

Figure 3.6. XRD diffraction patterns and phase identification for 2 wt% Fe/Al_2O_3-ME, 2 wt% Fe/Al_2O_3-IW and 2 wt% Fe/Al_2O_3-SOL in the range 20° < 2ϑ < 80°, compared with γ-alumina.

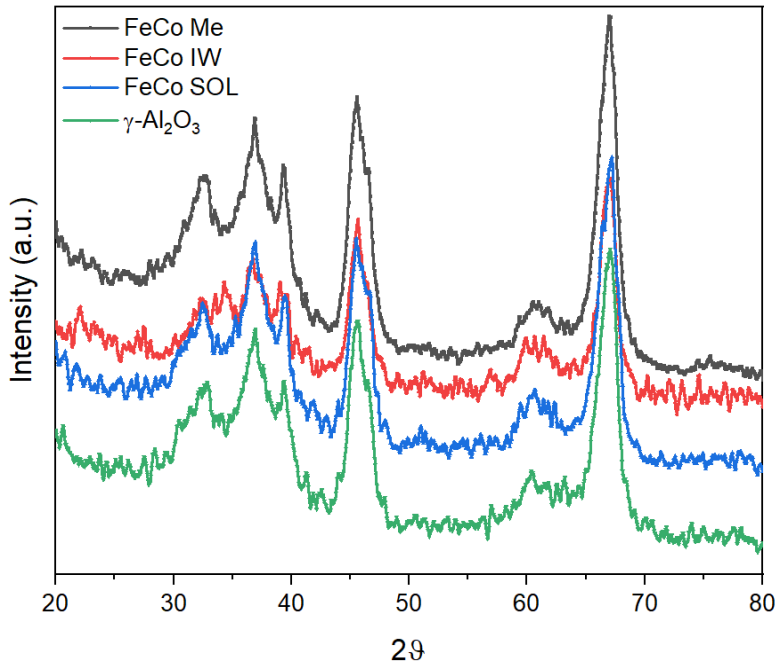

Figure 3.7. XRD diffraction patterns and phase identification for 2 wt% Fe_1Co_1/Al_2O_3-ME, 2 wt% Fe_1Co_1/Al_2O_3-IW and 2 wt% Fe_1Co_1/Al_2O_3-SOL in the range 20° < 2ϑ < 80°.

All the samples showed the diffraction pattern of only γ-alumina. The absence of both Fe or Co peaks was ascribed to the low total loading (2 wt%) and the small size of nanoparticles. The small peak appearing in some of the diffraction patterns at 2θ ~ 34° was attributed to minor contamination of γ-Al_2O_3.

3.2.2. Oxidation of cyclohexane with the FeCo series

The oxidation of cyclohexane was carried out at the same relatively mild reaction conditions used for the tests on benzaldehyde and on the industrial catalyst (120°C, 4 bar O_2), employing 15 mL of cyclohexane and 10 µL of benzaldehyde as radical initiator. 20 mg of catalysts were used for each reaction tests. A graphical representation and table with the results of the whole FeCo series are reported (Figure 3.8 and Table 3.2), with abbreviated catalysts labels for the sake of clarity. For each of the three preparation methods, a physical mixture of the Fe and Co monometallic catalysts was also tested in the same reaction conditions. The physical mixture was prepared weighing and mixing the two monometallic catalysts so that the molar amount of Fe and Co contained in 20 mg of mixture would be equal to the amount found in the corresponding bimetallic Fe_1Co_1 catalyst. This kind of test was made in order to verify the catalytic effectiveness of the bimetallic system compared to the contribution of the single

metals combined together. Below and in the following sections of this manuscript, the catalytic performance is described based on KA oil productivity and selectivity only. The conversion of cyclohexane is not reported due to the difficulty of a correct estimation derived from using cyclohexane as highly volatile solvent-reagent, and the consequent complex mass balance. The uncertainty error calculated on repeatability tests was estimated being between 5 and 10% for the productivity, and ±2% for the selectivity to KA oil.

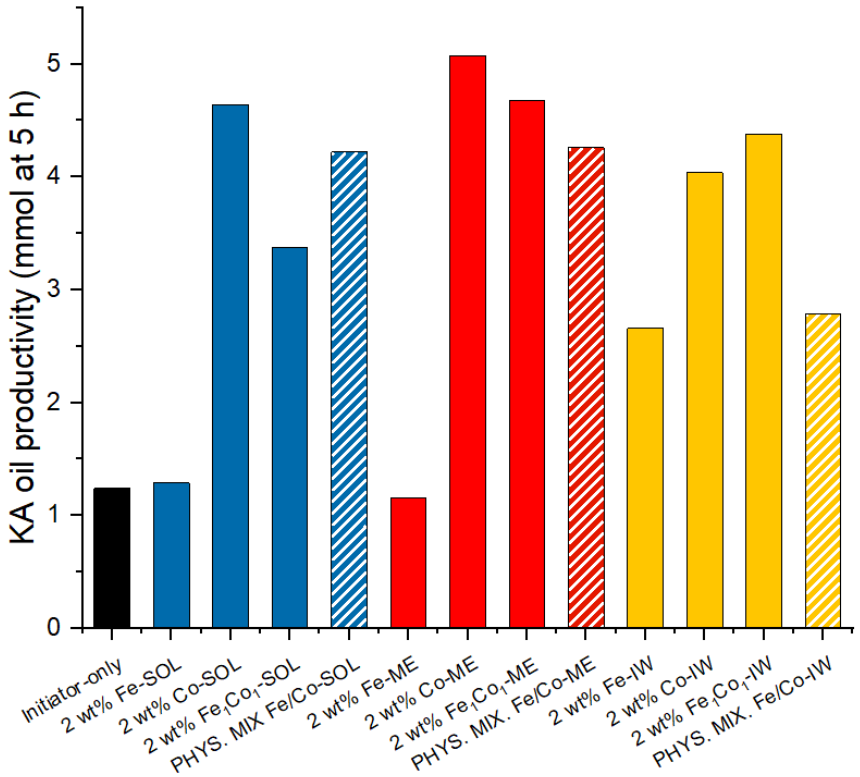

Figure 3.8. Graphical representation of KA oil productivity for the whole FeCo series after 5 h of reaction, compared to the non-catalysed initiator-only reaction and the physical mixture of the monometallic oxides.

Catalyst	Productivity of KA oil (mmol at 5 h)	Productivity of AA (mmol at 5h)	K/A ratio	Selectivity to KA %
Initiator-only	1.24	NO AA	2.65	94.2
2 wt% Fe/γ-Al_2O_3-SOL	1.29	0.01	1.95	85.6
2 wt% Co/γ-Al_2O_3-SOL	4.64	0.04	0.78	98.7
2 wt% Fe_1Co_1/γ-Al_2O_3-SOL	3.37	0.04	0.78	98.8
PHYS. MIX. Fe/Co-SOL	4.22	0.03	0.86	99.0
2 wt% Fe/γ-Al_2O_3-ME	1.16	0.01	2.30	88.2
2 wt% Co/γ-Al_2O_3-ME	5.07	0.02	0.93	96.0
2 wt% Fe_1Co_1/γ-Al_2O_3-ME	4.68	0.03	0.96	98.8
PHYS. MIX. Fe/Co-ME	4.26	0.05	0.87	98.9

2 wt% Fe/γ-Al_2O_3-IW	2.66	0.03	1.03	90.6
2 wt% Co/γ-Al_2O_3-IW	4.04	0.05	0.86	97.6
2 wt% Fe_1Co_1/γ-Al_2O_3-IW	4.38	0.04	0.99	98.4
PHYS. MIX. Fe/Co-IW	2.79	0.01	0.93	94.8

Table 3.2. KA oil (KA) and adipic acid (AA) productivities, K/A ratio and selectivity % to KA oil of the FeCo series after 5 h of reaction, compared to the initiator-only reaction and to the physical mixture of the monometallic catalysts.

All the cobalt-containing (both mono- and bimetallic) supported catalysts resulted in very high productivity, whereas monometallic Fe systems produced only a low amount of KA oil. Monometallic Fe interestingly produced a K/A ratio >1 whereas in all the other case K/A is always <1. It was already discussed about the importance of K/A ratio in determining the role of catalyst on the different steps of radical mechanism (See Chapter 3.1.1. Benzaldehyde oxidation). In the presence of a catalyst, the K/A ratio is altered [27] normally decreased compared the value obtained with a non-catalysed process. The different behaviour of Co-based catalysts with respect of monometallic Fe could be attributed to the ability of Co to perform the homolytic cleavage of the CyO-OH bond at higher rates leading to a higher production of cyclohexanol in the final mixture. Notably, the ketone can be considered the most valuable product in the KA oil mixture. 2 wt% Fe/γ-Al_2O_3-IW is the only one Fe catalyst performing better than non-catalysed reaction, and this could be attributed to the good metallic dispersion revealed. However, unfortunately the overall selectivity decreased from the 94.2% in the non-catalysed process to 90.6%.

On the other hand, the productivity of KA oil was very high throughout the whole series for the monometallic Co and bimetallic Fe_1Co_1 samples. In the case of ME preparations productivity was up to 5.07 mmol of KA oil in 5 hours for the 2 wt% Co/γ-Al_2O_3-ME and 4.68 mmol for the 2 wt% Fe_1Co_1/γ-Al_2O_3-ME. In the case of the 2 wt% Fe_1Co_1/γ-Al_2O_3-ME catalyst the high performance could be attributed to the presence of bimetallic Fe_1Co_1 nanoparticles as observed by electron microscopy. The great performance of the monometallic 2 wt% Co/γ-Al_2O_3-ME was instead attributed to the presence of small particles homogeneously distributed on the alumina support as it was observed by STEM/EDX analyses. 2 wt% Fe_1Co_1/γ-Al_2O_3-ME was also the most selective, exhibiting a very high selectivity of 98.8%. Among the SOL catalysts, 2 wt% Co/γ-Al_2O_3-SOL was the most productive (4.64 mmol) probably due to the small particles observed. The bimetallic sample 2%wt Fe_1Co_1/γ-Al_2O_3-SOL showed a lower

productivity but this was attributed to the low metal dispersion. Both catalysts however presented very high selectivity (98.7% for monometallic Co and 98.8% for the bimetallic) highlighting the beneficial role of Co behaviour. Among the IW series, mono- and bimetallic Fe_1Co_1-IW presented high productivity (4.04 mmol and 4.38 mmol respectively) attributed to the well dispersed Fe and Co particles observed. In particular the bimetallic sample showed a very high selectivity of 98.4%.

To be noted, monometallic Co-IW presented a selectivity to KA oil of 97,6% but among to by-product it was observed adipic acid (AA) (0.05 mmol) in the highest amount. Interestingly, all the FeCo series allowed for the direct production of adipic acid, in particular the bimetallic samples. As adipic acid represents the most interesting by-product for this reaction, being it the following target of KA oil transformation in industry for the final obtainment of nylon-6,6, its direct obtainment is very desirable. The mechanistic route for the obtainment of adipic acid is therefore discussed and still uncertain due to the complex reaction mechanism. The major cause of adipic acid production was demonstrated to be formed through cyclohexanone and then 2-hydroxycyclohexanone oxidation, even at low conversion values of cyclohexane. Considering this route, adipic acid is considered more as a final product of cyclohexane oxidation rather than an intermediate, and most of its formation (86-95%) proceeds via cyclohexanone [28]. Since adipic acid is a white solid insoluble in cyclohexane and only slightly soluble in some of the reaction products, a procedure for its separation and analysis with HPLC was developed (see Experimental section – Chapter 2.2.2.3. HPLC). The production of AA in the whole series seems to be related to the presence of Co in the systems, which enhances the catalytic activity enough to shift the reaction equilibrium towards a partial overoxidation of KA oil. Moreover, the only by-product found other than adipic acid was attributed to cyclohexyl hydroperoxide (CHHP) from GC-MS analyses. It is well established that product analysis for this reaction is complicated due to different reasons such as a) the solubility of the products after cooling down the reactor, b) the thermal stability of some products such as CyOOH, c) gas-phases products that could evaporate while opening and refilling the autoclave and d) evaporation of cyclohexane itself [29]. Taking this into account, the rest of the by-products, mainly 6-hexanoic, n-butyric, n-valeric, n-succinic and glutaric acids [30] or those that could derive mainly from ring cleavage of cyclohexanone according to [9], were not present or detectable by GC and could be present in small traces (<1%).

The test on the physical mixture of the monometallic counterparts, taken in the corresponding amount to the metals species present in the bimetallic Fe_1Co_1, gave some unexpected results. In fact, calculating the theoretical KA oil productivity of the physical mixture of the monometallic Fe and Co for each preparation method, it was obtained that the experimental productivity is higher than the theoretical (Table 3.3), in the SOL and ME cases. Only in the case of IW preparation, the expected value is comparable to the actually found. These results were ascribed to the intrinsic instability of the systems where during the reaction a reconstruction of the catalyst itself occurred. Unfortunately, we are not yet able to perform a full characterisation of the used physical mixture, which would clarify this point. Among the possible explanations, dissolution and redeposition of one species on top of the other creating intimate contact between Fe and Co, or dissolution of the species in the reaction mixture acting in the homogeneous conditions (just as Co in the industrial process) are valid hypotheses.

System	Theoretical KA oil prod. physical mix.	Experimental KA oil prod. physical mix.	Bimetallic catalyst productivity
Fe_1Co_1 - SOL	3.01	4.22	3.37
Fe_1Co_1 - ME	3.17	4.26	4.68
Fe_1Co_1 - IW	3.37	2.79	4.38

Table 3.3. Comparison between the physical mixture theoretical and experimental KA oil productivity, and the bimetallic catalyst productivity for each preparation method.

3.2.2.1. ICP analyses for leaching detection

The ICP analyses allowed to uncover the possible presence of leaching of the supported metal species in the reaction solution. This gave us a first indication of the stability of the catalysts. For an actual determination of the active species in solution, which would be important as the industrial process is carried out with cobalt salts in the homogeneous phase, hot filtration of the catalyst should have been carried out. However, due to difficulties related to 1) dangerous handling of cyclohexane at high temperature and 2) consistent evaporations observed, this experiment was not carried out. Graphical representation of the leakage of Co and Fe after reaction is reported (Figure 3.9a,b).

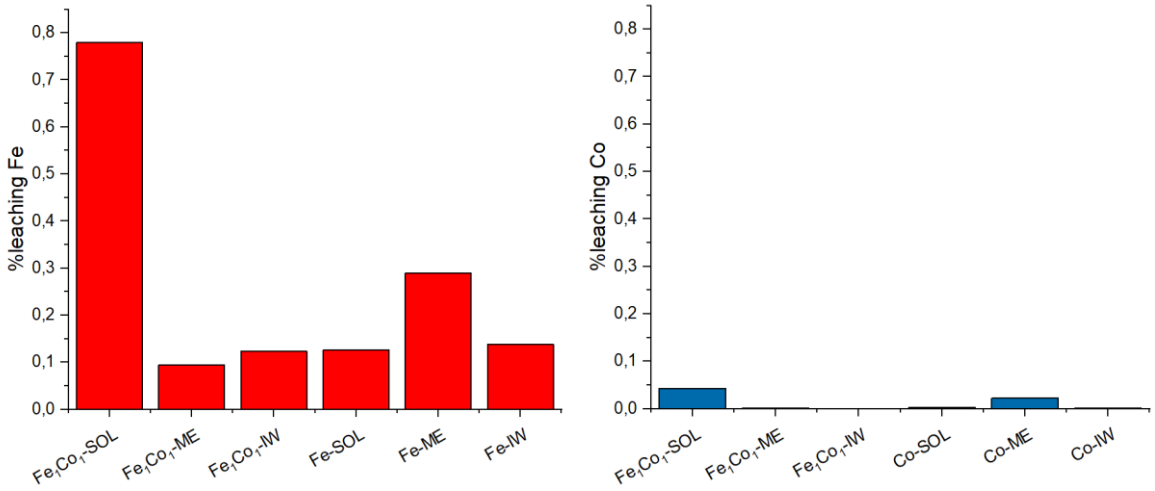

Figure 3.9. Fe% and Co% percentage of leached metal after 5 hours of reaction at 120°C/4 bar O_2.

Fe was found to be leaching more than Co in all the analysed catalysts. The highest leaching % for both Fe and Co happened for 2 wt% $Fe_1Co_1/\gamma\text{-}Al_2O_3$-SOL, being it 0.77% and 0.04%, respectively on the basis of total metal. The high percentage of leached Fe and Co in the SOL means that the two metals were not firmly anchored to the support thus limiting the long use of the catalyst. The leaching of both metals in ME and IW was reduced or not even present.

3.2.3. Conclusions on the FeCo series

The FeCo series of catalysts allowed for the preparation, by different methodologies, Fe and/or Co systems supported on Al_2O_3. The sol immobilization procedure resulted in the least homogeneous catalysts and showed atomically dispersed Fe and some areas with Co small agglomerates. The microemulsion technique resulted in very homogeneously dispersed monometallic cobalt on alumina and Co being intimately in contact with Fe in the bimetallic Fe_1Co_1. With the incipient wetness technique, the best control on the morphology was achieved, since finely dispersed small iron particles (5-10 nm) on alumina and bigger (15-25 nm) well dispersed particles of Co in both the monometallic and bimetallic catalysts were obtained.

According to our previous studies on benzaldehyde as radical initiator, even in the presence of a catalyst the introduction of catalytic amount of benzaldehyde ($7 \cdot 10^{-4}$ M) allowed for the initiation of the oxidation mechanism. The oxidation of cyclohexane was carried out at the relatively mild reaction conditions of 120°C and 4 bar of O_2. In terms of productivity of KA oil,

it was high throughout the whole series for the Co-containing catalysts (mono- and bimetallic Fe_1Co_1), around 4.5-5 mmol of KA after 5 hours. The beneficial effect of Co is also evident if the selectivity is considered, which was always higher than 96% for Co-containing catalysts and reached a maximum of 98.8% for the 2 wt% $Fe_1Co_1/\gamma\text{-}Al_2O_3$-ME. Selectivity is in fact the most important parameter from an industrial point of view. Moreover, among the by-products obtained, one is adipic acid, which is the most interesting by-product obtainable (due to its use in direct nylon-6,6 production) and it is easily separable from the reaction mixture.

The Fe could have a role in enhancing the K/A ratio favouring the ketone production and, notably, in bimetallic samples its presence increases the selectivity especially in the case of ME series. Indeed, Fe_1Co_1 system prepared via IW showed the best results in terms of productivity (4.38), selectivity (98.4%) and approximate K/A to 1. Nevertheless, the results of the tests performed on the physical mixture of the monometallic catalysts evidenced a probable instability of catalytic systems which lowered the attractiveness of these systems.

The prolonged use of catalytic system is one of the outmost requirements for a scaling-up of the process and it was then decided investigating the preparation of more stable systems. Au-based catalysts represented good candidates as they already have shown good stability in several reactions [31–34].

3.3. Au-based catalysts

Among the heterogeneous catalysts researched for cyclohexane oxidation, gold resulted one of the most studied despite the elevated cost, particularly due to its great performance in selective oxidation reactions [35,36] and considering its efficiency in activating the C-H bond [37]. It has already been discussed that the use of a heterogeneous catalyst for cyclohexane oxidation requires the presence of a radical initiator that is often tert-butyl hydroperoxide (TBHP), which is often employed even if the very high price makes it unattractive for industry [38]. In combination with TBHP as initiator, Au-based catalysts have been reported as active and very selective toward K/A oil formation [3,39–41]. However, a study reported by Weckhuysen et al. [29] showed that results on gold-based catalysts are often masked by the difficult product analysis. In particular, they investigated the activity and selectivity of Au/Al_2O_3, Au/TiO_2 and Au/SBA-15 catalysts taking into account the product analysis of both the gas and the liquid phases. Considering the actual formation of by-products, which included also adipic acid, the combined selectivity toward cyclohexanone and cyclohexanol decreased, thus concluding that Au catalysts performed poorly compared to the autoxidation in terms of selectivity and in initiating the reaction.

This fact is fundamental to understand the actual performance of some literature-proposed catalysts for cyclohexane oxidation. Many recent papers which reported good results in cyclohexane oxidation to KA oil, using metal-based catalysts including some gold-based, did not in fact really perform a precise and complete by-product analysis. For example, one of the best claimed achievements recently reported by Luo et al. [42], showed the possibility to reach 50% of cyclohexane conversion with a selectivity toward cyclohexanol and cyclohexanone higher than 90% using Ag clusters supported on graphene oxide and TBHP as radical initiator. However, in this case as in others it is not clear how conversion and selectivity have been calculated. There are in fact difficulties and quite often lacking quantitative mass balance in the analysis of by-products.

Considering the potential of gold-based catalysts, and the strong expertise of the Milan group in Au-based catalysts preparation, this section reports a study on the productivity of monometallic and bimetallic Au supported catalysts in cyclohexane oxidation at relatively mild reaction conditions. In particular, the possibility to overcome the limits of Au (low selectivity

and high cost) was explored coupling it with metals such as Cu (transition metal) and Sn (post transition metal). In fact, these latter metals were found interesting as capable of favouring single-electron oxidation, thus positively influencing the reaction rate. These Au-based catalysts have been supported on two different supports (Al_2O_3 and TiO_2) in order to evaluate the impact of metal-support interaction. All these systems were then tested at the usual relatively mild reaction conditions (120°C, 4 bar O_2), using biphenyl as internal standard in order to obtain more precise quantitative analysis of the products.

3.3.1. The AuCu series

Cu is a transition metal widely used in oxidation reactions, and can easily switch between its 0, I and II oxidation states. In this series, it was paired with Au in order to investigate the potential of a bimetallic Au-Cu catalyst, enhancing the electronic properties of the system and lowering the amount of precious metal. The monometallic 2 wt% Au/Al_2O_3, 2 wt% Cu/Al_2O_3 and the corresponding bimetallic 2 wt% Au_1Cu_1/Al_2O_3 were prepared and characterized accordingly to our previous research [43], employing the sol immobilization method. The specific Au:Cu ratio of 1:1 was chosen on the basis of previous study showing this ratio was the best for obtaining intimate contact between the two metals compared to other Au/Cu ratios [43]. The metal precursors here are added together and undergo simultaneous co-reduction during the preparation, forming the bimetallic NPs (see also Experimental section, Chapter 2.1.2.1. Au, Cu and Au_1Cu_1 supported on Al_2O_3).

ICP measurements of the filtrate, confirmed an actual metal loading of 1.8 wt% for the monometallic Au catalyst, 2.0 wt% for the Cu/Al_2O_3 and of 1.82 wt% for the bimetallic one. In the bimetallic catalyst the Au/Cu molar ratio was 0.9. For the sake of simplicity, the catalysts will be still referred as 2 wt% even if the correct metal loading will be considered.

The TEM characterizations of the monometallic catalyst 2 wt% Au/Al_2O_3 and of the bimetallic 2 wt% Au_1Cu_1/Al_2O_3 are reported in Figure 3.10 and Figure 3.11. The monometallic sample showed very well dispersed Au nanoparticles with narrow particle size distribution and NPs average diameter of 2.5 nm (Figure 3.10), as well as a high metal dispersion with narrow particle size distribution (avg. diameter of 1.9 nm) was observed in the case of the bimetallic sample (Figure 3.11).

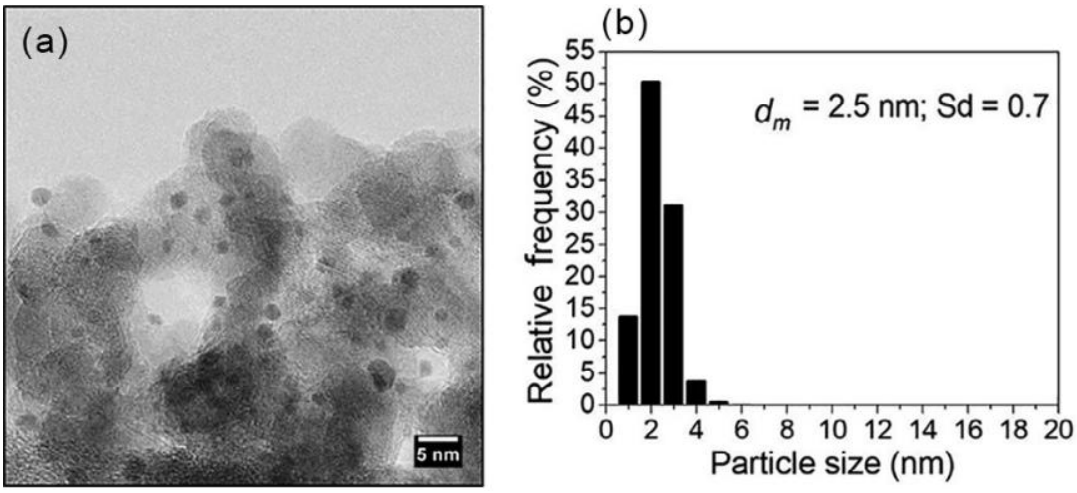

Figure 3.10. (a) TEM micrograph and (b) particle size distribution for 2 wt% Au/Al_2O_3.

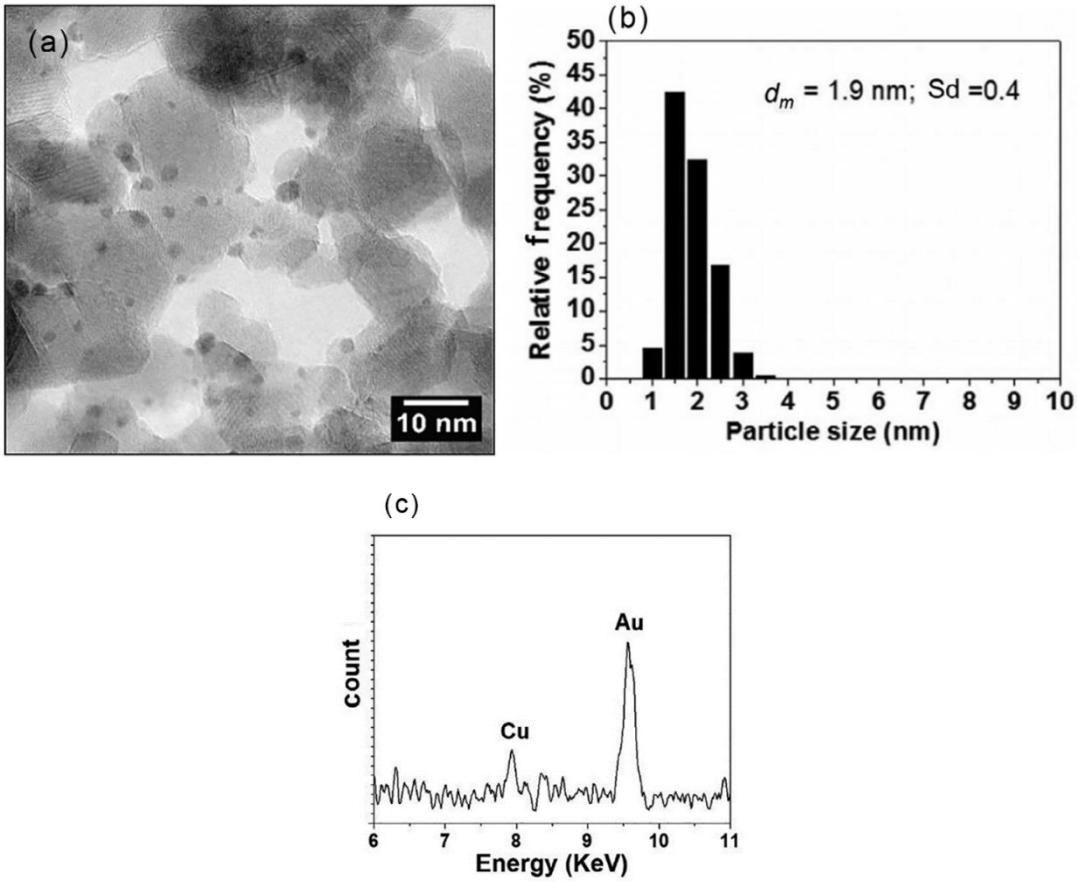

Figure 3.11. (a) TEM micrograph; (b) particle size distribution of 2 wt% Au_1Cu_1/Al_2O_3 and (c) example of EDX analyses on single particle.

STEM/EDX analyses on single particles for the bimetallic 2 wt% Au_1Cu_1/Al_2O_3 catalyst (Figure 3.12) revealed the bimetallic nature of nanoparticle even of variable composition. The Au and Cu elemental maps showed the coexistence of the two metals in single particles, with an Au/Cu atomic ratio between 44/66 and 61/39 (EDX spectra collected on nine particles) [43].

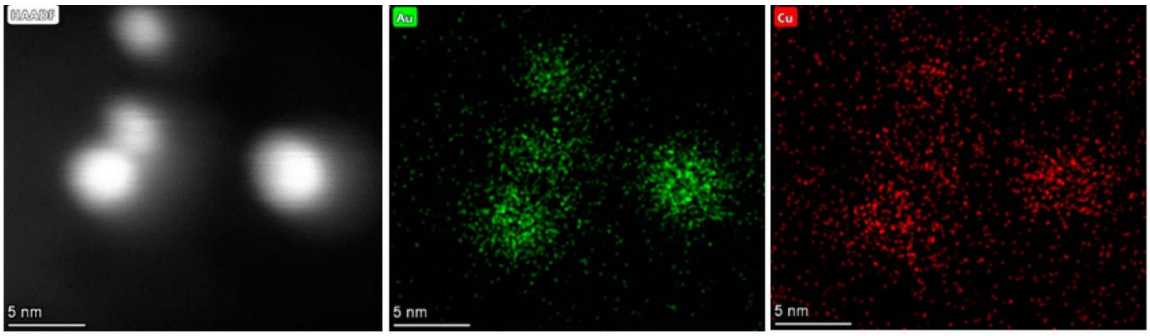

Figure 3.12. STEM/EDX images of the 2 wt% Au_1Cu_1/Al_2O_3 catalyst including the elemental maps of Au and Cu.

XPS analysis (Table 3.4) resulted in an Au/Cu ratio equal to 0.76, thus showing that Cu species are prevalent on the surface compared to the bulk composition observed (0.9 by ICP). From the high-resolution spectra of $Au(4f)_{7/2}$, as expected, the presence of two different species of Au was identified, i.e. Au^0 (83.5–84.4 eV) and $Au^{\delta+}$ (85.4–86.1 eV), showing relative amount of 83% and 17%, respectively. In the case of Cu $(2p)_{3/2}$ the presence of both Cu^0/Cu^+ and Cu^{2+} species was observed, with an amount of 61% and 39%, respectively.

Sample ($2wt\% Au_1Cu_1/Al_2O_3$)	**Survey**	**High Resolution (HR)**			
Orbital	-	$Au(4f)_{7/2}$		$Cu(2p)_{3/2}$	
Species	-	Au^0	$Au^{\delta+}$	Cu^0-Cu^+	Cu^{2+}
B.E. (eV)	0-1300	83.5	86.1	932.9	935.6
% At.	0.76 (Au/Cu ratio)	83 %	17 %	61 %	39 %

Table 3.4. XPS survey and high-resolution spectra information on the 2 wt% Au_1Cu_1/Al_2O_3 catalyst.

3.3.2. Oxidation of cyclohexane with the AuCu series

The oxidation of cyclohexane (10 mL) was carried out in a stainless-steel autoclave, at 120 °C and 4 bars of oxygen pressure using biphenyl as internal standard (0.2 M) and 20 mg of catalyst. As in the case of uncatalyzed reaction, a study on the influence of the initial concentration of benzaldehyde in the reaction mixture was carried out in the presence of 2 wt% Au_1Cu_1/Al_2O_3 catalyst (see Chapter 3.1.1. Benzaldehyde oxidation). Here as well, the

concentration of benzaldehyde ([benzaldehyde]$_i$) was varied ranging from 0.01 M to 0.4 M (Table 3.5 and Figure 3.13).

[benzaldehyde]$_i$	KA oil productivity (mmol at 5 h)
0.36 M	2.41
0.2 M	3.61
0.15 M	4.50
0.1 M	3.17
0.01 M	2.63

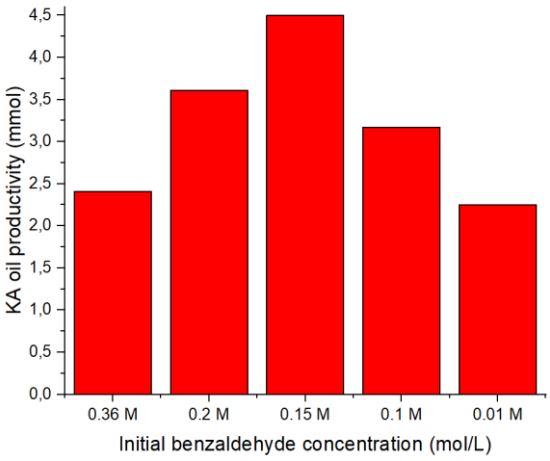

Table 3.5. Values of KA oil productivity obtained varying the initial concentration of benzaldehyde in the presence of 2 wt% Au_1Cu_1/Al_2O_3 catalyst.

Figure 3.13. Graphical representation of KA oil productivity of 2 wt% Au_1Cu_1/Al_2O_3 varying with respect to the initial benzaldehyde concentration.

The obtained volcano-shaped trend of KA oil productivity is very different from the trend obtained in the non-catalysed reaction (see Chapter 3.1.1. Benzaldehyde oxidation) and indicates that there is an optimal amount of benzaldehyde to start the reaction with. In fact, the mechanism appeared to be influenced by the presence of catalyst, but the presence of benzaldehyde could be detrimental by poisoning the catalyst with the formation of large amounts of benzoic acid, which crystallise in the autoclave and decrease KA oil productivity over a long reaction time. Moreover, benzoic acid is known as a very strong inhibitor of gold catalysts [44,45]. In addition, the small amount of benzyl alcohol produced during the autoxidation of benzaldehyde has been already attributed being a radical scavenger for the reaction [8] (see Chapter 3.1.1. Benzaldehyde oxidation). Therefore, the initial amount of benzaldehyde must be carefully checked, balancing the enhanced rate due to the increase of radical concentration in the presence of a catalyst and the detrimental effect of benzaldehyde's oxidation products which act as radical scavengers or catalyst poison.

The whole AuCu series (monometallic Au, Cu and bimetallic Au_1Cu_1) was then tested on cyclohexane oxidation at [benzaldehyde]$_i$ = 0.15 M, and the catalytic results are reported in Figure 3.14 and Table 3.6. By using the monometallic 2 wt% Cu/Al_2O_3 (Figure 3.14b) the

amount of KA oil formed at the end of the reaction decreased compared to the non-catalysed reaction (Figure 3.14a), down to 1.32 mmol, whereas the K/A ratio (0.70) overturns, having in this case a higher amount of cyclohexanol compared to cyclohexanone. As it was seen in the FeCo series, when the catalyst is present and it takes part into the oxidation mechanism, the K/A ratio is expected to decrease [27]. Compared to Cu/Al_2O_3 and also compared to the non-catalysed reaction, the monometallic Au/Al_2O_3 (Figure 3.14c) led to a higher productivity of KA oil, which increased to 4.03 mmol at 5 h and even here the K/A ratio of 0.62 confirmed the active role of the catalyst in favouring the formation of cyclohexanol. In the presence of the bimetallic 2 wt% Au_1Cu_1/Al_2O_3 catalyst (Figure 3.14d), the productivity of KA oil grew up to 4.50 mmol. A test with the physical mixture of monometallic catalyst mimicking the content of Au and Cu into the bimetallic sample, confirmed the synergistic effect between the two metals. Considering the actual molar content of Au and Cu in the bimetallic catalyst, the productivity calculated for a simple physical mixture of the 2 wt% Au/Al_2O_3 and 2 wt% Cu/Al_2O_3 catalysts in the corresponding amount should have been 3.01 mmol, value that compared to 4.5 mmol obtained with the bimetallic sample clearly indicates a synergistic effect of the bimetallic system. The K/A ratio in the case of the bimetallic Au_1Cu_1 raised to 0.91, higher value with respect to both monometallic counterparts.

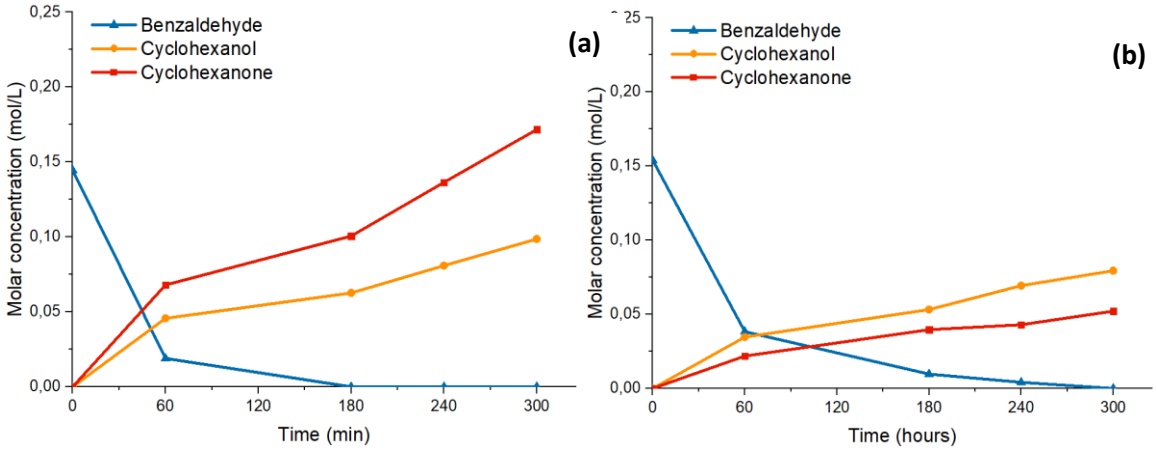

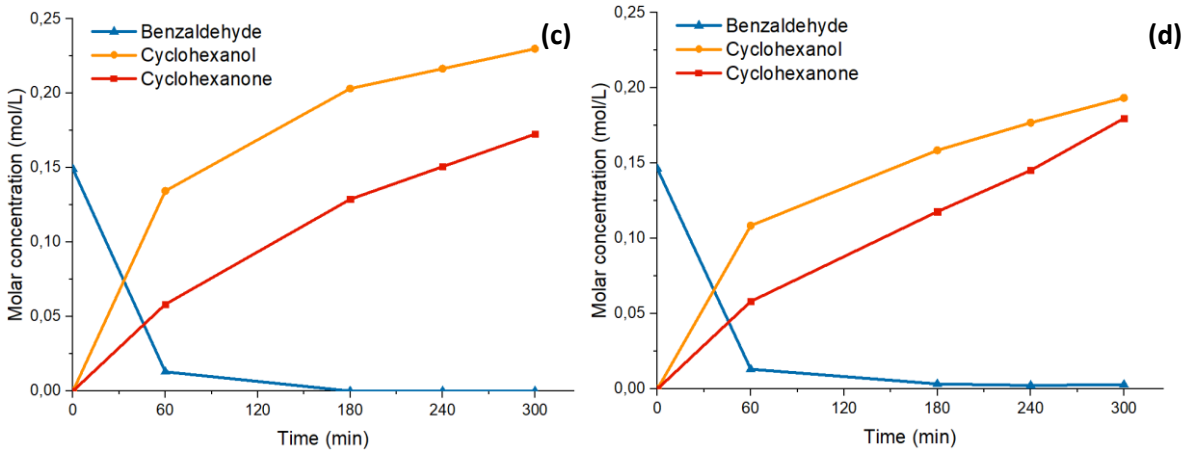

Figure 3.14. Cyclohexane oxidation in the presence of benzaldehyde (0.15 M) at 120 °C and 4 bar of O_2. Reaction performed without a catalyst (a), in the presence of 20 mg of 2 wt% Cu/Al_2O_3 (b), 20 mg of 2 wt% Au/Al_2O_3 (c) and 20 mg of 2 wt% Au_1Cu_1/Al_2O_3 (d).

Catalyst	KA oil prod. (mmol at 5h)	K/A ratio	Sel. to KA oil %
Initiator-only	2.70	1.74	94.2%
2 wt% Cu/Al_2O_3	1.32	0.70	88.6%
2 wt% Au/Al_2O_3	4.03	0.62	92.2%
2 wt% Au_1Cu_1/Al_2O_3	4.50	0.91	94.4%

Table 3.6. KA oil productivity, K/A ratio and selectivity after 5 hours of reaction for the whole AuCu series.

In addition, the catalysed reaction with 2 wt% Au_1Cu_1/Al_2O_3 is highly selective towards KA oil (up to 94.4%) where the only by-products detected were attributed to be unreacted cyclohexyl hydroperoxide (CHHP), adipic acid and traces of other by-products (~1%). This was another important result as the selectivity of the monometallic counterparts and of the benzaldehyde-only reaction was outperformed.

3.3.3. The AuSn series

In parallel with the tests on the AuCu series, it was decided to couple gold with a post transition metal possessing redox capabilities, and Sn was chosen as a bio-relevant and earth-abundant metal that can easily switch between its oxidation states. Tin is also poorly investigated as an active component of heterogeneous catalysts, as it has been studied more intensively in the field of electrocatalysis. In this work, Au, Sn and AuSn-supported catalysts were synthesized using Au and Sn metal powders as precursors by the solvated metal atom dispersion (SMAD) method [46,47], carried out by Dr. Claudio Evangelisti at the CNR-ICCOM

institute of Pisa. The method was employed because the sol immobilization preparation failed for supporting Sn on both Al_2O_3 and TiO_2, producing very low metal dispersion, possibly due to the low melting point of Sn. Moreover, the SMAD method allowed for great control on the mixing of the two metals and dispersion onto the two different supports. Therefore, acetone-stabilized Au- and Sn-solvated metal atoms (SMAs) were used to obtain Au-, Sn- and AuSn-supported catalysts by impregnation on a reducible (TiO_2) and a non-reducible (Al_2O_3) metal oxide. These two kinds of supports were chosen to shed light on the influence of metal-support interaction. The series prepared consisted in two catalysts at 3 wt%, with Au and Sn in 1:2 molar ratio as indicated in Table 3.7, and all the monometallic counterparts on both supports prepared for comparison.

Catalyst name	Au/Sn ratio
3 wt% Au_1Sn_2/Al_2O_3	0.5
3 wt% Au_1Sn_2/TiO_2	0.5

Table 3.7. Bimetallic catalysts labels for the AuSn series.

The choice of having a specific ratio between the Au and Sn metals was taken on the basis of previous findings, whereby it is possible to obtain stable AuSn bimetallic systems [48]. The choice of the 3% metal loading instead of 2% was done to simplify the SMAD preparation.

The actual metal loading of each catalyst was determined by ICP while TEM measurements were used to calculate the mean diameter of Au-containing particles measuring more than 260 particles. A FEI Titan Themis 200 kV spherical aberration (Cs)-corrected TEM equipped with EDX detectors was employed to investigate the morphology and composition of the AuSn bimetallic samples drop-dried from aqueous suspensions onto Cu grids. The composition of the samples was determined by STEM-EDX along with recording HAADF-STEM images on selected areas. The actual Au/Sn molar ratio, metal loading (wt%) and mean particle diameter are reported in Table 3.8.

Catalyst name	Au/Sn ratio	Metal loading (wt%)	Mean Particle Diameter
3 wt% Au_1Sn_2/Al_2O_3	0.54	3.26	6.28 ± 3.11 nm
3 wt% Au_1Sn_2/TiO_2	0.50	3.35	7.24 ± 3.56 nm

Table 3.8. Actual Au/Sn ratio, metal loading (wt%) calculated by ICP and mean particle size calculated by TEM.

TEM images of both bimetallic samples are reported in Figure 3.15.

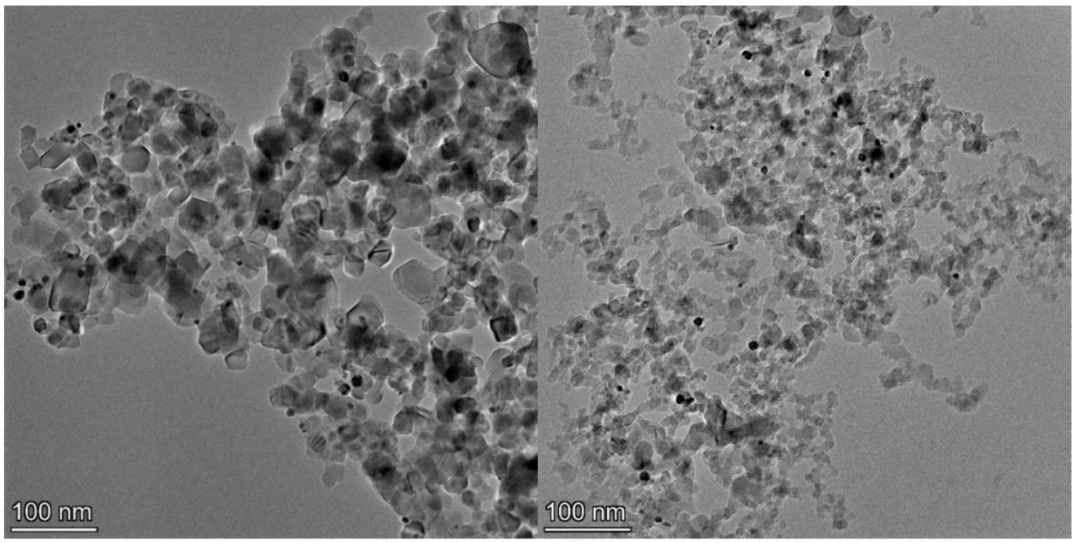

Figure 3.15. Representative HRTEM images of a) Au_1Sn_2/TiO_2 and b) Au_1Sn_2/Al_2O_3 samples.

The interaction and morphology of the active components were investigated by STEM/EDX and visualized on Au and Sn elemental maps (Figure 3.16).

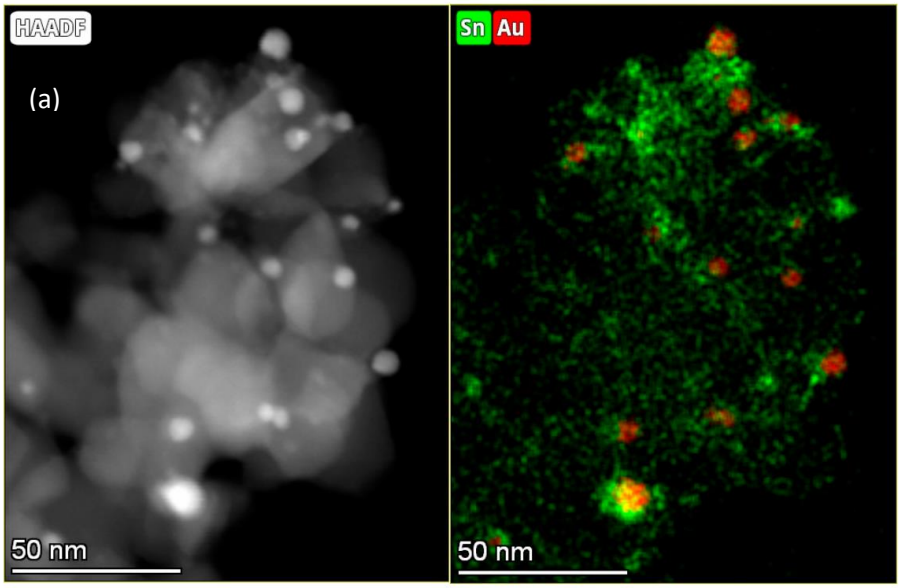

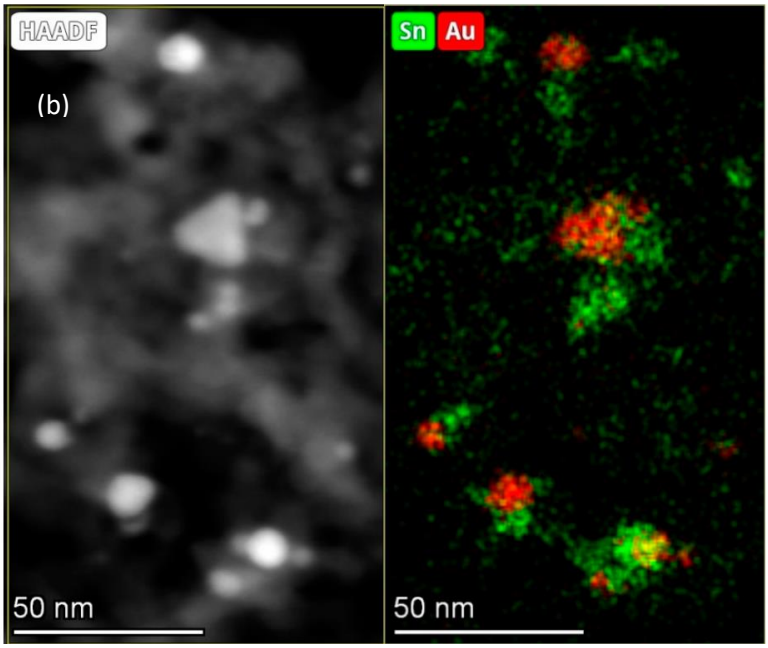

Figure 3.16. HAADF STEM/EDX image and elemental map of a) Au_1Sn_2/TiO_2 and b) Au_1Sn_2/Al_2O_3.

While gold is concentrated in particles, Sn is more dispersed in both bimetallic catalysts. The combined Au and Sn maps show that Au particles are typically surrounded by Sn-containing phases, and the joint appearance of Sn and Au signals at single particles likely indicates the presence of Au-Sn bimetallic systems. The Au particles are typically decorated, surrounded by SnO_2, possibly diminishing the concentration of the accessible surface Au sites. Another significant part of Sn-oxide is located on the support, separated from gold.

Due to the problematics related to the interpretation of XPS spectra for Sn species (SnO and SnO_2 have very close binding energies, and difficult deconvolution), ^{119}Sn-Mössbauer spectra were recorded to establish the chemical state of the Sn species. A total of 298 and 78 K of the ^{119} Sn-Mössbauer spectra were collected from the tin-rich Au_1Sn_2/Al_2O_3 and Au_1Sn_2/TiO_2 samples (Figure 3.17). The probability of having the Mössbauer effect depends on the temperature of the measurement and it is more expressed for zerovalent tin (and bimetallic Sn-containing) components than for Sn(IV). In this context, the isomer shift in the Mössbauer spectra is the most interesting parameter, as it can give an indication on the oxidation state of the Sn species. The characteristic isomer shift (IS) values for Sn(IV) are around 0.0 mm s^{-1}. The isomer shift of Au-Sn bimetallic particles depends inversely on the composition; it is 2.56 mm s^{-1} for the metallic β-Sn and, ca., 2.0 mm s^{-1} for the gold-rich bimetallic AuSn [49]. Tin usually prefers to spread over the oxide supports, and indeed dedicated methods should be used to

obtain true bimetallic AuSn particles [50]. The data obtained from the deconvolution of the spectra are reported in Table 3.9.

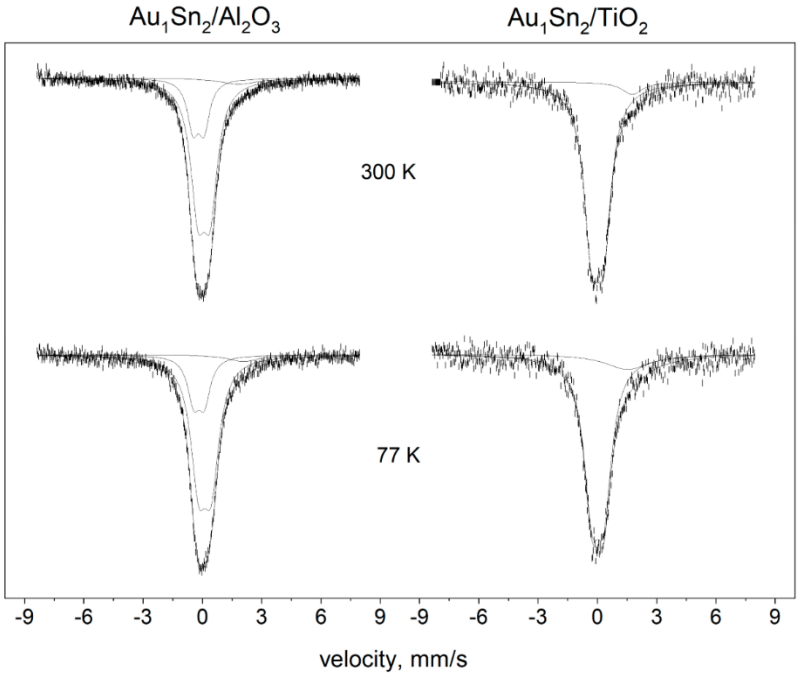

Figure 3.17. ^{119}Sn-Mössbauer spectra of the Au_1Sn_2/Al_2O_3 and Au_1Sn_2/TiO_2 samples.

Temperature		300 K				77 K			
Support	**Component**	**δ[a]**	**Δ[b]**	**FWHM[c]**	**Rel. Int.[d]**	**δ[a]**	**Δ[b]**	**FWHM[c]**	**Rel. Int.[d]**
		(mm s^{-1})			(%)	(mm s^{-1})			(%)
Al_2O_3	**Sn(IV)-(1)**	-0.20	0.56	0.69	22.4	-0.17	0.54	0.75	21.9
	Sn(IV)-(2)	0.08	0.62	0.90	72.5	0.12	0.65	0.97	73.7
	Singlet	1.84	-	2.35	5.1	2.08	-	1.91	4.4
TiO_2	**Sn(IV)**	0.00	0.60	0.93	94.3	0.02	0.61	0.98	86.2
	Singlet	1.76	-	1.28	5.7	1.56	-	2.72	13.8

δa isomer shift, Δb quadrupole splitting, FWHMc full line width at half maximum, Rel. Int.d spectral contribution.

Table 3.9. ^{119}Sn-Mössbauer parameters of the spectra presented in Figure 3.17.

Based on these structural investigations of both Au_1Sn_2 catalysts, only low amounts of metallic Sn in interaction with gold could be detected, while the largest part of tin, 95% on Al_2O_3 and 86% on TiO_2, is present as Sn(IV), likely as SnO_2. This observation is in good correspondence with the affinity of tin to oxygen especially in well-dispersed form. It should be noted that the metallic tin oxidizes, during storage in air, if it is not well stabilized in bimetallic systems. A broad additional singlet contribution is also present in each sample with low intensity. The isomer shift of this component is definitely below 2.0 mm s^{-1}: the starting value characterizing

the AuSn bimetallic particles with low tin content. The line width of this component is broad, probably indicating that different types of local tin species are buried beneath. Most probably, this component can be attributed to the tin in Au particles decorated with SnO_2, as observed by STEM/EDX microscopy.

3.3.4. Oxidation of cyclohexane with the AuSn series

As previously discussed, cyclohexane oxidation in the presence of benzaldehyde formed ketone in excess with respect to the alcohol (K/A ratio = 1.7 at $[benzaldehyde]_i$ = 0.15 M) [10,51]. Here, the reaction was carried out on each catalyst by using 10 mL of cyclohexane as solvent-reagent, 20 mg of catalyst, 120°C/4 bar O_2 as T and P, and benzaldehyde 0.15 M as radical initiator. Figure 3.18a,b and c reports the comparison between the non-catalysed reaction versus the bare Al_2O_3 and TiO_2 supports. At the bottom of this paragraph, Table 3.10 resumes all the results of the reactions performed in this series.

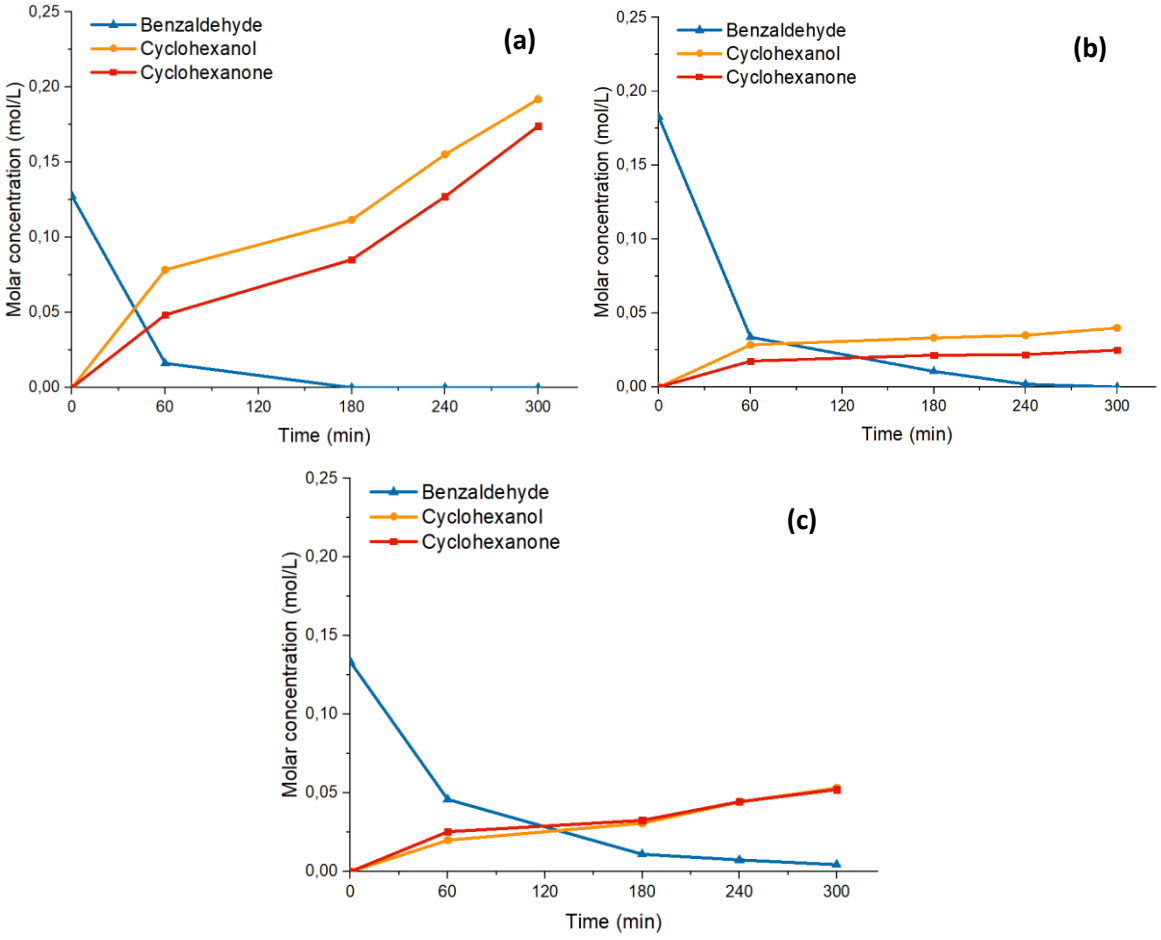

Figure 3.18. Cyclohexane (10 mL) oxidation in the presence of benzaldehyde (0.15 M) at 120 °C and 4 bars of O_2. Reaction performed without a catalyst (a), in the presence of 20 mg of Al_2O_3 (b) and 20 mg of TiO_2 (c).

Rather surprisingly, the addition of the bare supports, Al_2O_3 (Figure 3.18b) and TiO_2 (Figure 3.18c), seems to slow down the formation of the oxidation products with respect to the reaction without catalysts, possibly influencing the radical formation. This latter hypothesis is in fact supported by some studies, which described the possible role of Al_2O_3 as a radical scavenger [52,53]. For example, Fukuzumi et al. [53] reported the effects of Al^{3+} on the scavenging of a 2,2-diphenyl-1-picrylhydrazyl radical ($DPPH^{\bullet}$), which is frequently used as a reactivity model of peroxyl radicals' behaviour. In that case, the study proved that Al^{3+}, as a strong Lewis acid, can act as a radical-scavenger by stabilising the one-electron-reduced species of the radical. Even more recently, Jabbari et al. [54] described the adsorption of the free radical TEMPO ($C_9H_{18}NO$) on Al_2O_3 nanoparticles in different solvents, evaluating the radical scavenging activity. It was proven that Al_2O_3 nanoparticles have efficient radical scavenging activity (RSA) in the range of 50–72% as well as a large adsorption energy associated with the adsorption over the Lewis acidic sites of Al_2O_3 [55]. The explanation of the role of the bare TiO_2 on the radical mechanism of the reaction seems to be more difficult. Indeed, TiO_2 is usually considered to be able to produce reactive radical species (e.g., radical $^{\bullet}OH$, $O_2^{\bullet-}$), which are generated at its surface. However, this happens only under UV irradiation [49,56]. On the other hand, both the Lewis and Brønsted acid sites have been recognized on the surface of TiO_2-based materials by the adsorption of organic dyes or 4-carboxy TEMPO [50]. From these data, considering the proved adsorption of radical species on the Lewis acid sites of Al_2O_3, a similar behaviour on the Lewis acid sites of TiO_2 is supposed, which can be the reason for the reduced reaction rate of the KA oil formation in the presence of TiO_2 compared to the non-catalysed reaction.

Considering the Au-based catalysts, the addition of Au nanoparticles on the supports' surface increased the productivity (Figure 3.19). The KA oil productivity (mmol) increased from 2.70 mmol of the non-catalysed reaction to 3.18 mmol in the presence of 3% Au/TiO_2 and to 3.66 mmol with 3% Au/Al_2O_3 (Table 3.10). Moreover, the effect of the catalyst was evident, considering the selectivity to the alcohol or the ketone formation: in all of the catalysed reactions, the K/A ratio is lower than 1, indicating once again a major involvement of the catalytic-mediated contribution in the radical mechanism.

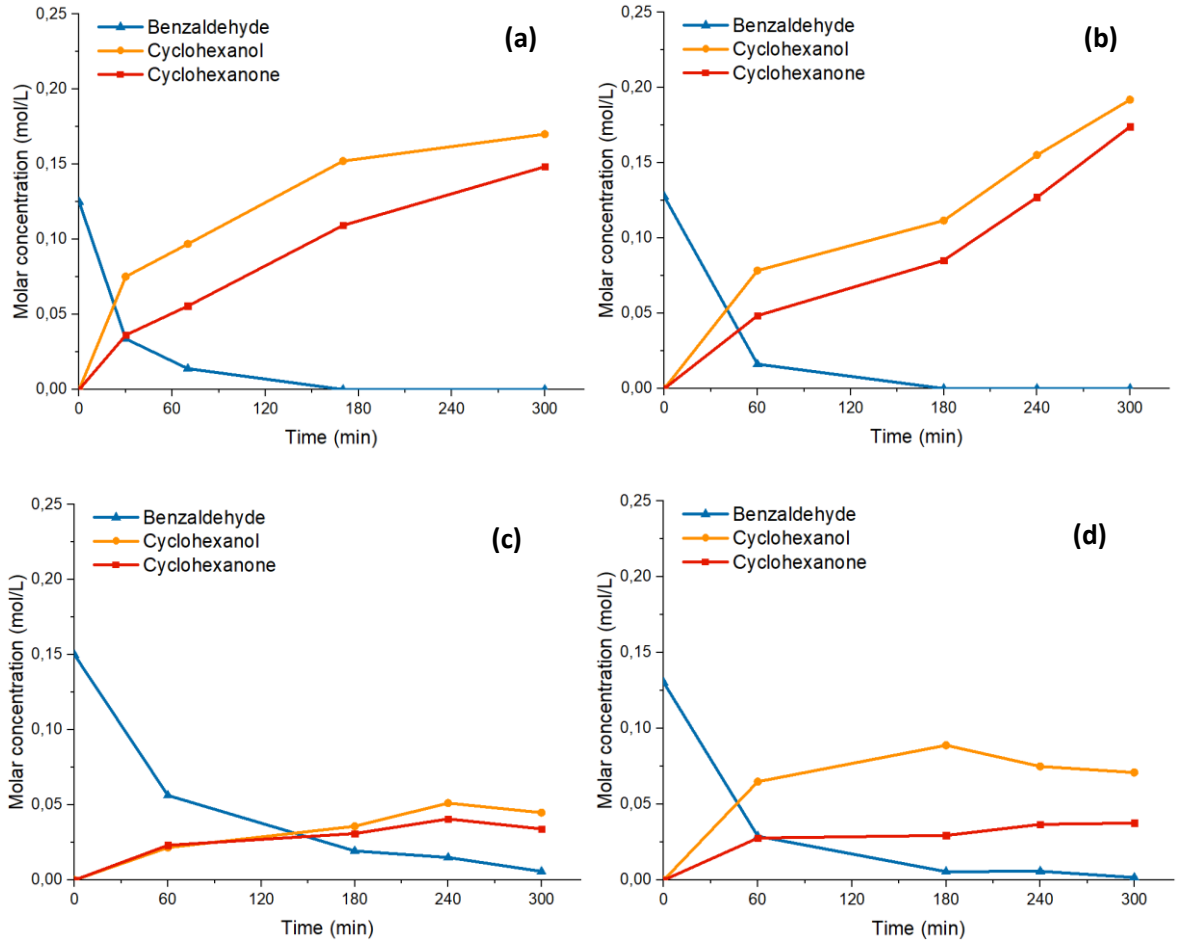

Figure 3.19. Cyclohexane (10 mL) oxidation in the presence of benzaldehyde (0.15 M) at 120 °C, 4 bars of O_2 with 20 mg of catalyst: 3 wt% Au/TiO_2 (a), 3 wt% Au/Al_2O_3 (b), 3 wt% Sn/TiO_2 (c) and 3 wt% Sn/Al_2O_3 (d).

The presence of Au active sites in the reaction reversed the K/A ratio (0.87–0.90), increasing the formation of the alcohol. However, this behaviour seems to be independent from the support since the K/A ratio values obtained with TiO_2 or Al_2O_3 are very similar (Table 3.10). In addition, it is possible to notice a slight difference in the reaction profiles, where the Au/Al_2O_3 catalyst did not show deactivation, differently from Au/TiO_2 where the reaction profile seems to go toward a plateau. This aspect will be better discussed later, together with the results obtained with the Au_1Sn_2 bimetallic catalysts. In monometallic Sn catalysts, the presence of Sn did not change the catalytic behaviour of the bare supports a lot, compared to which showed, in fact, a similar productivity and K/A ratio. Overall, the KA oil productivity obtained with the monometallic Sn catalysts was lower than that obtained with the corresponding Au catalysts.

When in the presence of bimetallic Au_1Sn_2 systems, a variation of the catalytic behaviour is observed. The reaction profiles are reported in Figure 3.20.

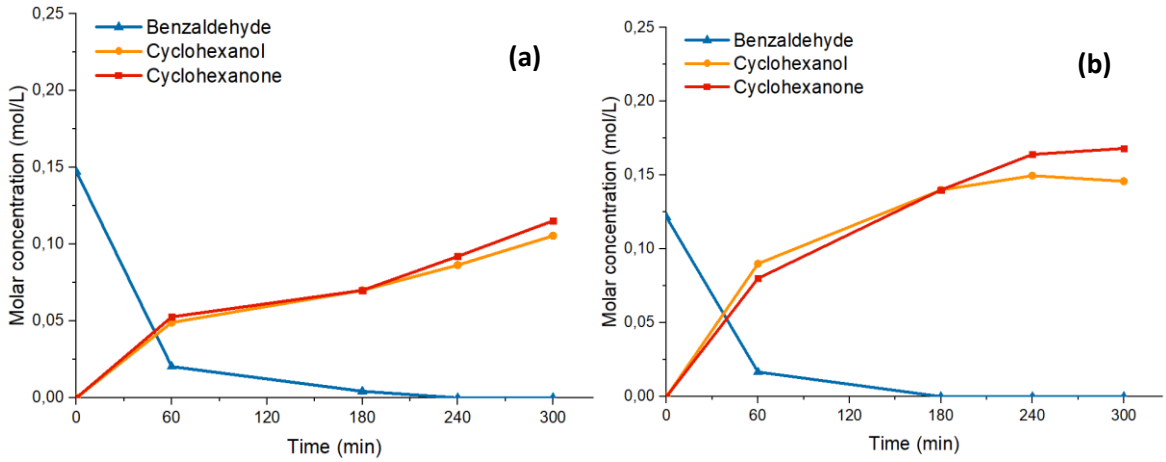

Figure 3.20. Reaction profiles of cyclohexane oxidation (benzaldehyde 0.15 M, 120°C, 4 bar O_2 and 20 mg cat.) in the presence of bimetallic Au_1Sn_2 catalysts (a) Au_1Sn_2/Al_2O_3, and (b) Au_1Sn_2/TiO_2.

When Sn was present and in intimate contact with Au (bimetallic catalysts), the productivity of KA oil increased with respect to the monometallic Sn catalysts, while it slightly decreased with respect to the monometallic Au catalysts (see Table 3.10). However, it has to be noted that the amount of Au, which was the most active species, in the bimetallic catalysts is much lower compared to monometallic. In addition, another effect of the bimetallic Au_1Sn_2 catalysts is mostly marked, regarding the formation of the alcohol or the ketone (Figure 3.20). It is in fact immediately clear from the reaction profiles that the K/A ratio is always slightly higher than 1 (Figure 3.20 and Table 3.10, last column), differently from all the other cases.

This behaviour was attributed to the copresence of Au and Sn, in intimate contact, which influences the radical mechanism and the relative rate of formation of radical species. A recent study [57] can explain this phenomenon through the formation of superoxides ($O_2^{\bullet -}$) species, which are created upon O_2 adsorption on the surface of SnO_2 when this latter is e^--enriched by, in this case, the Au species which are in intimate contact with it. These superoxide species could then contribute to the enhancement of the radical mechanism, enhancing the pure radical pathway due to their nature, thus increasing the final K/A ratio.

Looking at the reaction profiles of the bimetallic samples (Figure 3.20a,b), it can be noted that in each case where Al_2O_3 is the support, the reaction profiles exhibited no deactivation; on the contrary, the curves of those where TiO_2 is the support go towards a plateau, which can indicate that the catalyst is gradually decreasing its activity and blocking the radical chain. Nevertheless, TiO_2-supported catalysts showed a considerably higher productivity than the

Al_2O_3-supported ones. Being TiO_2 a reducible support, the higher KA oil productivity was attributed to the enhanced e^- exchange modulation exerted by metal-support interaction. Further explanations could be ascribed to the better distribution of SnO_2 for TiO_2-supported bimetallic catalysts observed by electron microscopy. Therefore, a "combined effect" was supposed, depending both on the support and the bimetallic species, considering that this difference was not present in the bare supports (see Figure 3.18). For comparison with the bimetallic catalysts, a reaction was performed in the presence of a physical mixture of Au/Al_2O_3 and Sn/Al_2O_3, and another one with Au/TiO_2 and Sn/TiO_2 (Figure 3.21), taken into account the corresponding molar amount of Au and Sn which are contained in the bimetallic Au_1Sn_2 catalysts.

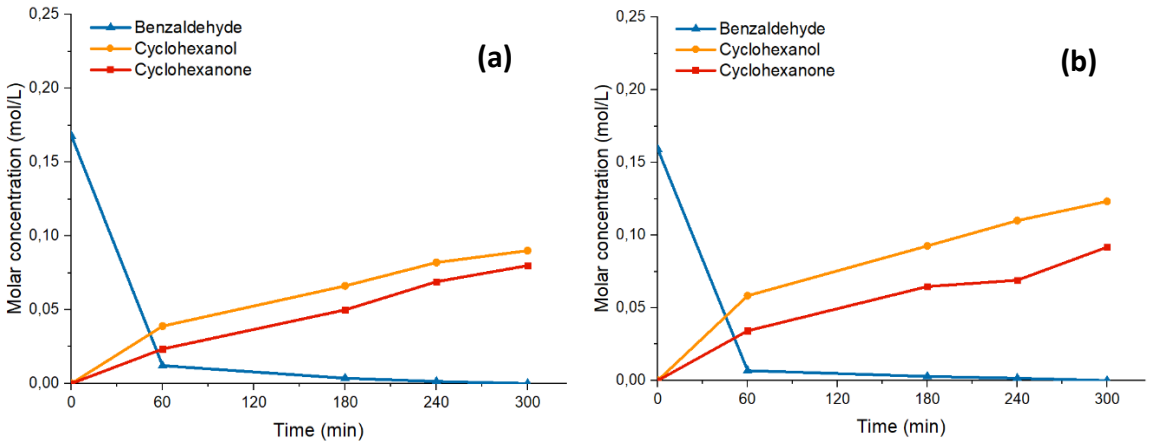

Figure 3.21. Cyclohexane (10 mL) oxidation in the presence of benzaldehyde (0.15 M) at 120 °C and 4 bar of O_2. Reaction performed in the presence of a physical mixture of (a) 3 wt% Au/Al_2O_3 and Sn/Al_2O_3 and (b) 3 wt% Au/TiO_2 and Sn/TiO_2.

Looking at KA oil productivity at the end of the reaction (Table 3.10) by using a physical mixture of Au and Sn on both alumina and titania, it was lower than the productivity obtained by the corresponding bimetallic Au_1Sn_2/Al_2O_3 and Au_1Sn_2/TiO_2, thus confirming the synergistic effect between gold and tin. Moreover, the K/A ratio is severely different, changing from 1.09 in the case of the bimetallic catalyst on Al_2O_3 to 0.89 using the physical mixture of the monometallic samples, and from 1.15 to 0.74 in the case of the TiO_2-supported systems, highlighting a profound difference in the nature of the active sites in the two cases.

Table 3.10 is reported below, resuming all the catalytic results reported in this paragraph.

Catalyst	KA oil prod. (mmol at 5h)	K/A ratio
Initiator-only	2.70	1.74
TiO_2	1.05	0.98
Au/TiO_2	3.18	0.87
Sn/TiO_2	0.79	0.76
Au_1Sn_2/TiO_2	3.14	1.15
Physical mixture (Au/TiO_2 + Sn/TiO_2)	2.15	0.74
Al_2O_3	0.65	0.63
Au/Al_2O_3	3.66	0.90
Sn/Al_2O_3	1.08	0.54
Au_1Sn_2/Al_2O_3	2.21	1.09
Physical mixture (Au/Al_2O_3 + Sn/Al_2O_3)	1.70	0.89

Table 3.10. Catalytic results of KA oil productivity (mmol at 5 h of reaction) and K/A ratio for the whole AuSn series.

3.3.5. Conclusions on the Au-based series

In this series, a variety of Au-based catalysts coupled with different transition metals and supported on different supports (reducible and non-reducible oxides) have been prepared and demonstrated great ability to produce the desired KA oil mixture. The characterization of the AuCu series (monometallic Au, Cu and bimetallic Au_1Cu_1) prepared by sol immobilization on Al_2O_3 as support, revealed very well dispersed nanoparticles with narrow particle size distribution and small average particle size. Moreover, the presence of bimetallic Au-Cu particles was assessed by STEM/EDX analyses in the case of Au_1Cu_1.

Carrying out tests on the 2 wt% Au_1Cu_1/Al_2O_3 catalyst, KA oil productivity was studied as a function of the variation of the concentration of benzaldehyde in the initial reaction mixture. These experiments highlighted that in the case of a catalysed reaction, an optimal initial amount of benzaldehyde exists as a result of the radical scavenging properties of benzyl alcohol and of benzoic acid poisoning effect. Testing the whole AuCu series on cyclohexane oxidation, the best results were obtained in the case of the bimetallic Au_1Cu_1 catalyst, where a remarkable KA oil productivity was obtained, as high as 4.50 mmol after 5 hours of reaction, with a high selectivity to KA oil of 94.4% (the rest being mainly CHHP, and traces of adipic acid

and other by-products <1%). The bimetallic catalyst outperformed the monometallic Au and Cu on Al_2O_3 and their physical mixture in both KA oil productivity and selectivity, highlighting the advantage of having the two metals in the form of bimetallic particles.

The study on the AuSn series on Al_2O_3 and TiO_2 prepared by SMAD allowed to better understand the role of Sn by comparing the monometallic Au- and Sn-based catalysts with the bimetallic Au_1Sn_2 systems. Monometallic Au was found to be much more active than Sn on both Al_2O_3 and TiO_2 supports. Despite Au being the most active metal, the bimetallic Au_1Sn_2 effectively improved the productivity of KA oil (up to 3.14 mmol at 5 hours for 3 wt% Au_1Sn_2/TiO_2) even with a low amount of Au (1:2 to Sn) and, most importantly, acted on the K/A ratio and therefore influenced the radical chain mechanism. The pure radical mechanism resulted in a K/A ratio of 1.74, while the presence of Au active sites reversed the ratio to 0.87–0.90; differently, the addition of Sn in the form of bimetallic Au_1Sn_2 made the ratio slightly higher than 1. Considering that this happened only when Au and Sn were in intimate contact, these results were ascribed to the possible enhancement of the radical pathway related to the presence of SnO_2, revealed by the analyses of the ^{119}Sn-Mössbauer spectra: indeed, SnO_2 has cations with empty orbitals and charges deficient anions, which could favour the electrons exchange to form radicals. Further explanation was attributed to a particular interaction between SnO_2 and oxygen from which superoxide (O_2^-) ions, singly (O^-) and doubly (O^{2-}) ionized atomic oxygen or also peroxide (O_2^{2-}) ions can be formed, and such interaction occurs only in the co-presence of Au (as an e^- rich metal) and Sn (as oxide). These species could then participate and improve the pure radical mechanism, thus enhancing the K/A ratio. The dependency of catalytic behaviour from the type of support was also considered, as the systems on TiO_2 showed higher productivity. This phenomenon was ascribed to TiO_2 being a reducible support able to modulate the e^- exchange within the bimetallic interaction.

3.4. CeZr mixed oxides

Bi or tri-metal oxides received large interest in some recent studies [13] due to their peculiar properties and enhanced stability. Coupled with our previous results in cyclohexane oxidation where a beneficial effect was obtained by using a reducible oxide, this pushed us to investigate mixed oxides, particularly Ce and Zr systems.

Ce oxide is renowned for its ability to take or release oxygen, known as its oxygen storage capacity (OSC), without changing its cationic structure upon the oxidation-reduction process from Ce^{3+} to Ce^{4+} [58]. A recent study from Yuan et Al. [59] insisted on how Ce is widely applied in oxidation reactions and can promote the mobility and storage of O_2 due to the Ce^{3+}/Ce^{4+} redox pairs creating oxygen vacancies. Their group efficiently obtained a conversion and selectivity to KA oil of 12.8% and 95.5% respectively, with a Ce-Ni modified Co_3O_4 derived from impregnation on ZIF-67 MoF used as template, in a solvent-free oxidation of cyclohexane at 130°C and 8 atm of O_2 pressure. In general, Zr oxide is known for its redox and textural properties, and its stability at elevated temperatures. The use of ZrO_2 for this reaction was found to be surprisingly rare, mostly used in combination with other transition metals such as Ti, Co and Ni [60,61]. With $Ti_{70}Zr_{10}Co_{20}$ alloy it has been possible to reach up to 6.8% conversion and 90.4% selectivity to KA oil [61].

In this context, transition metals such as Cu and Fe were thought to be effectively used to modify Ce and Zr oxides. These metals are available at low cost and widely used in a variety of oxidation reactions. Most importantly they are also renowned for the easiness of switching between their oxidation states. This could be helpful for the propagation of radical mechanism in cyclohexane oxidation, similarly to what happens to Co(II) in the Haber-Weiss mechanism for the homogeneous process [62].

3.4.1. The CeZr series

A series of Ce or Zr mixed oxides modified by the inclusion of Cu or Fe have been prepared. This series is composed of monometallic CeO_2 and ZrO_2, and of four 1:9 molar Cu:Ce, Fe:Ce, Cu:Zr and Fe:Zr mixed oxides all prepared by inverse microemulsion. The ratio between the included metal (Cu or Fe) and the main oxide (Ce or Zr) was set to 1:9 in order to avoid

structural modification of the CeO_2 and ZrO_2 structures. With the inverse microemulsion technique it is possible to obtain oxides or very homogeneous mixed oxides (see Introduction - Chapter 1.3.2.2. Inverse microemulsion), and these preparations have been carried out in Cádiz during my stay under the supervision of Prof. Ana Hungría. The idea behind the procedure is preparing two inverse microemulsions (water in organic), one containing the metal precursors, the other a precipitating agent. Upon mixing the two microemulsions under stirring, the slow and controlled formation and precipitation of the precursor(s) hydroxides happens. Later steps are made to remove any organic phase or template and oxidize (calcination) the species to obtain the final mixed oxides.

The bare oxides were tested in the selective oxidation of cyclohexane under the usual reaction conditions of 120°C and 4 bar of O_2, with 10 µL of benzaldehyde as radical initiator. With the idea of introducing structural and O defects and possibly obtaining the metals in different oxidation states, the four Cu and Fe-containing mixed oxides were also reduced adapting a procedure from [63], where it was originally carried out on TiO_2. Table 3.11 reports the whole list of catalysts prepared.

Sample label	Reduced sample label
CeO_2	-
$Cu_{0.1}Ce_{0.9}O_x$	$Cu_{0.1}Ce_{0.9}O_x$RED
$Fe_{0.1}Ce_{0.9}O_x$	$Fe_{0.1}Ce_{0.9}O_x$RED
$Cu_{0.1}Zr_{0.9}O_x$	$Cu_{0.1}Zr_{0.9}O_x$RED
$Fe_{0.1}Zr_{0.9}O_x$	$Fe_{0.1}Zr_{0.9}O_x$RED
ZrO_2	-

Table 3.11. The whole CeZr series prepared, mixed oxides bare and reduced.

The $Cu_{0.1}Ce_{0.9}O_x$, $Fe_{0.1}Ce_{0.9}O_x$, $Cu_{0.1}Zr_{0.9}O_x$ and $Fe_{0.1}Zr_{0.9}O_x$ mixed oxides prepared by the inverse microemulsion method previously reported in [64] were characterized by many solid-state analytical techniques: electron microscopy in both STEM/EDX and HRTEM modes, BET surface area analysis and XPS analyses. STEM/EDX, HRTEM and BET analyses were carried out personally as a part of the training received at Cádiz University.

3.4.1.1. Electron microscopy (STEM/EDX and HRTEM)

The two monometallic CeO_2 and ZrO_2 were characterized solely by STEM/EDX and HRTEM to verify the homogeneous composition and size of the agglomerates and the phases present (Figure 3.22 and Figure 3.23).

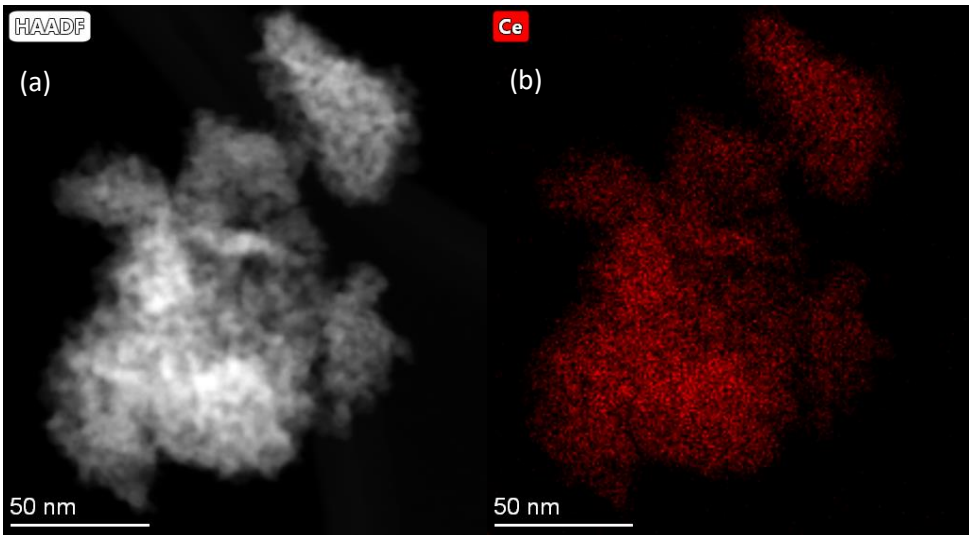

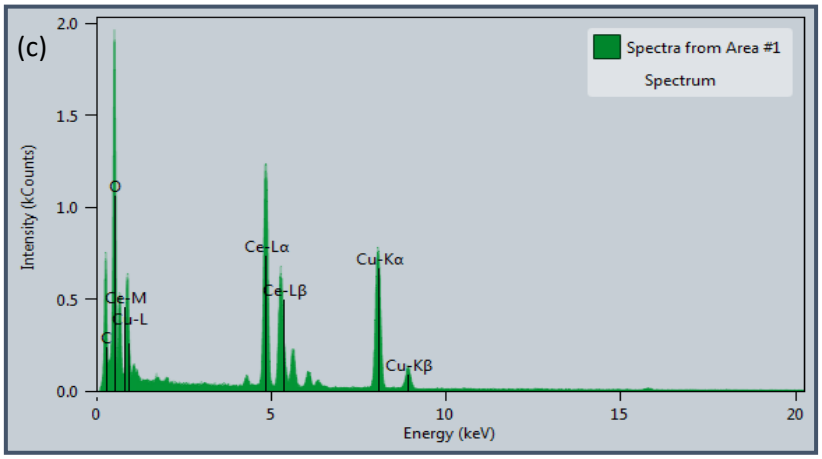

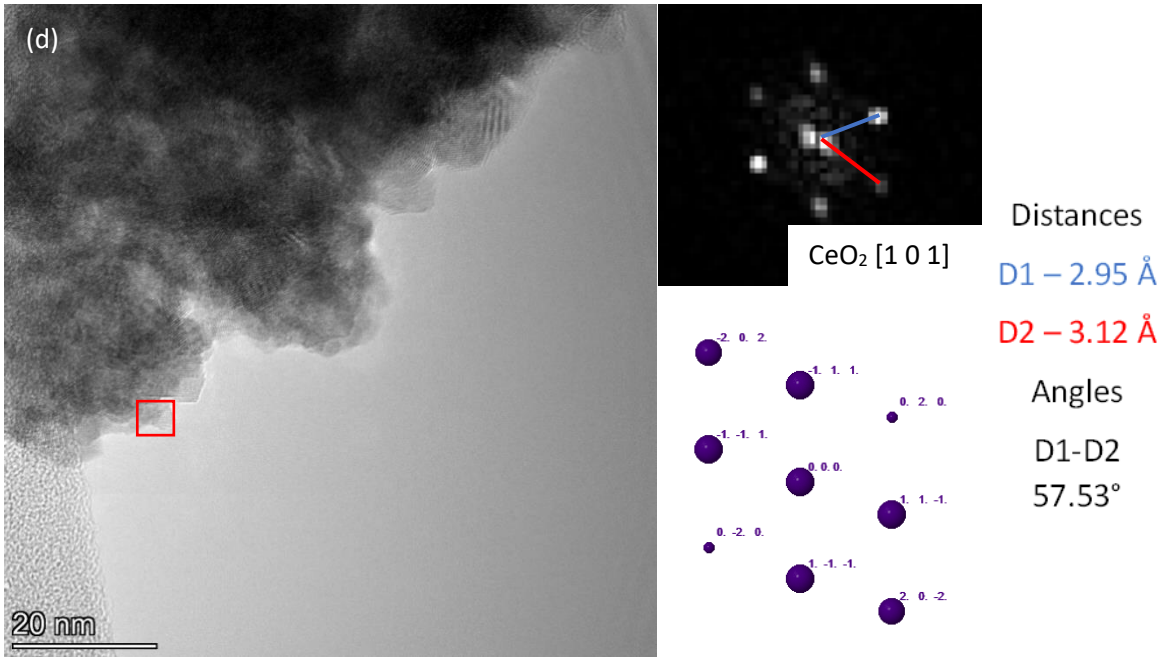

Figure 3.22 (a) HAADF image, (b) EDX elemental map, (c) Elements spectrum and (d) HRTEM image and digital diffraction pattern of CeO_2.

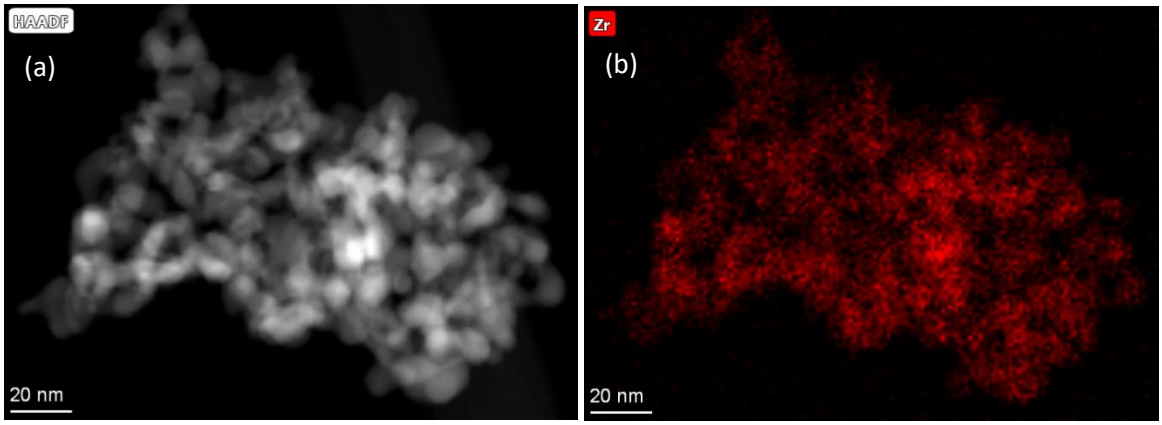

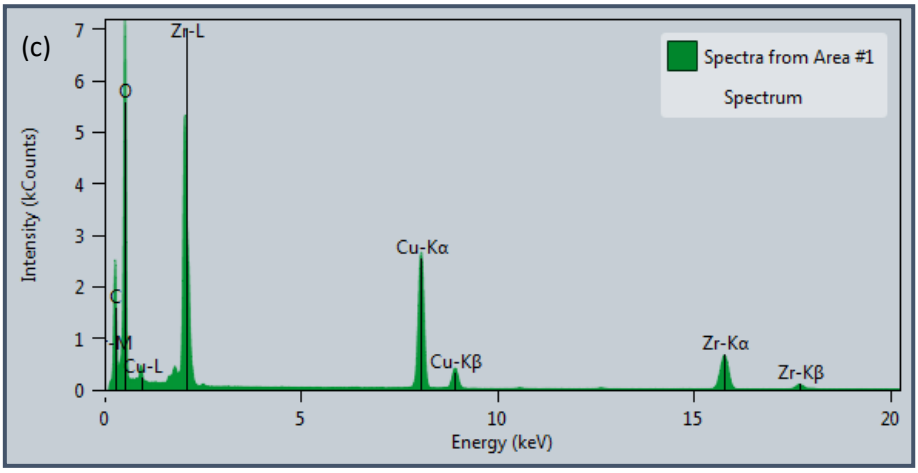

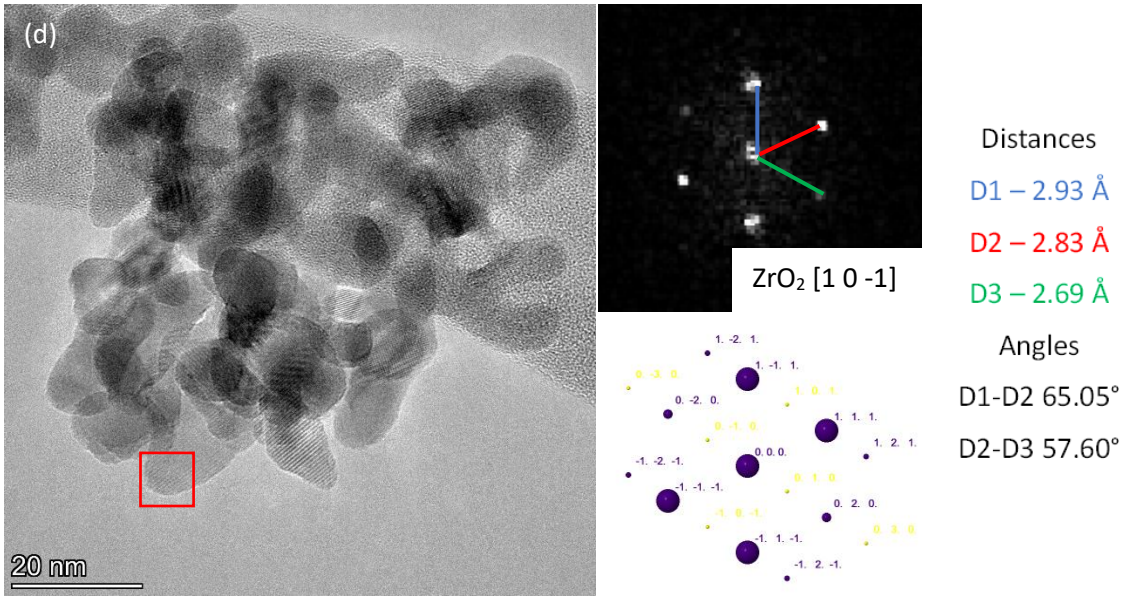

Figure 3.23. (a) HAADF image, (b) EDX elemental map, (c) Elements spectrum and (d) HRTEM image and digital diffraction pattern of ZrO_2.

In both CeO_2 and ZrO_2 samples, from EDX elemental analysis no contamination was observed in the spectrum, and each oxide possesses a homogeneous distribution of Ce and Zr all over the crystallites. The elements spectrum taken on the whole region (Figure 3.22c and Figure 3.23c) showcased only peaks related to Ce and Zr, respectively, and the signal of the Cu grid. From HRTEM images of the particles, the digital diffraction pattern (DDP) of the selected areas in the red squares allowed to identify the fluorite phase for the CeO_2 sample, and the tetragonal baddeleyite phase for ZrO_2, as expected.

It is with the analyses of the four 10% Cu or Fe-containing mixed oxides that the analysis became more complex due to the intimate mixing of the two phases within each sample. The most representative STEM/EDX and HRTEM images of the four mixed oxides characterization are reported (Figure 3.24 - Figure 3.28).

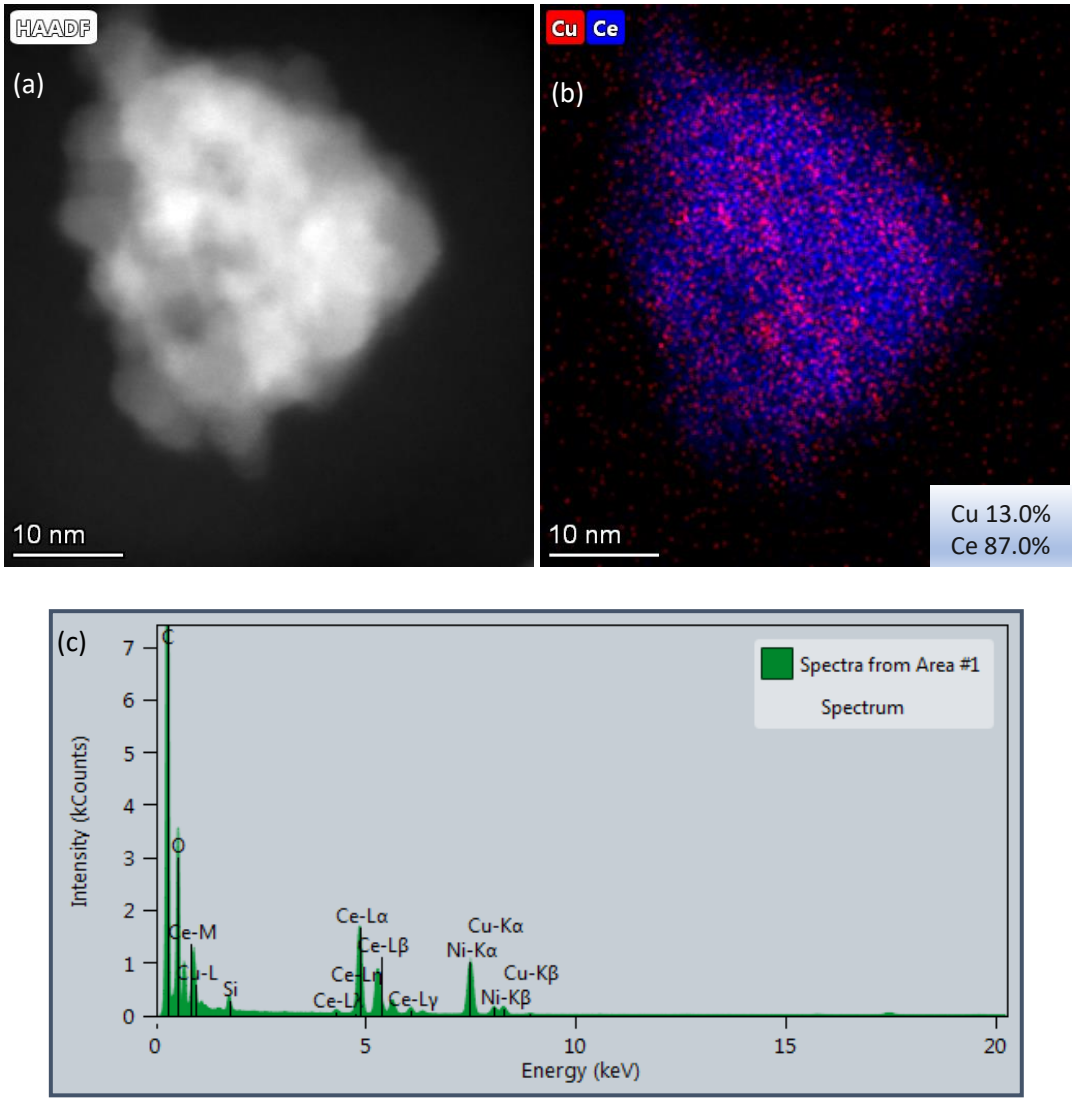

Figure 3.24. (a) HAADF image, (b) EDX elemental map, (c) Elements spectrum and (d) HRTEM image and digital diffraction pattern of $Cu_{0.1}Ce_{0.9}O_x$.

In $Cu_{0.1}Ce_{0.9}O_x$ (Figure 3.24), the mixed Cu/Ce composition observed from the STEM/EDX images is homogeneous although some areas richer in Cu can be identified as agglomerates (Figure 3.24b), differently from the other mixed oxides. The theoretical composition of Cu:Ce 1:9 is respected, as by the elemental maps an atomic Cu% and Ce% of, respectively, 13.0% and 87.0% was obtained. From the elemental spectrum the Ce and Cu peaks are evidenced, and no contamination was detected, whereas the Ni signal came from the grid. Analysis of the DDP obtained from the HRTEM images allowed to find mainly the fluorite phase, seen from the CeO_2 [1 0 1] zone axis in the particular case reported (Figure 3.24d). Indeed, being the presence of Cu and Fe in the four mixed oxides limited to a theoretical 10% compared to Ce and Zr, in general it was almost impossible to encounter those phases in a suitable position for HRTEM analysis, but for extreme luck during the acquisition. For example, in the sample below reported, the paramelaconite phase related to Cu_3O_4 (from zone axis [1 0 1]) was attributed to a crystallite (Figure 3.25).

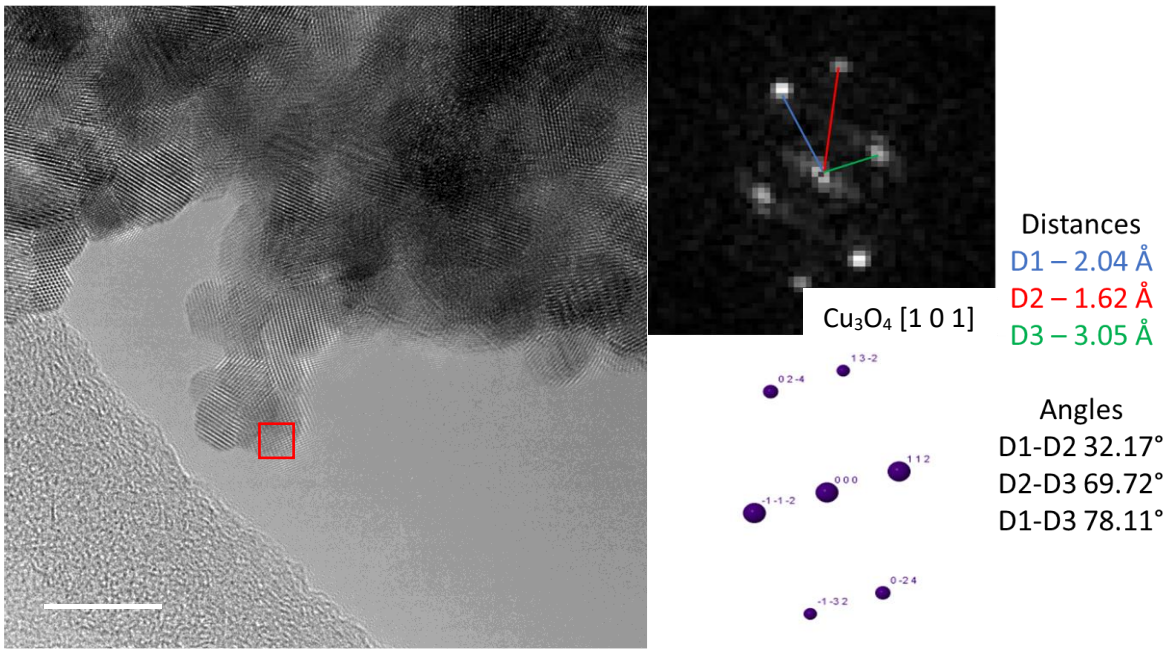

Figure 3.25. HRTEM image and DDP interpretation of another area of $Cu_{0.1}Ce_{0.9}O_x$.

STEM/EDX and HRTEM of $Cu_{0.1}Zr_{0.9}O_x$ mixed oxide are shown in Figure 3.26.

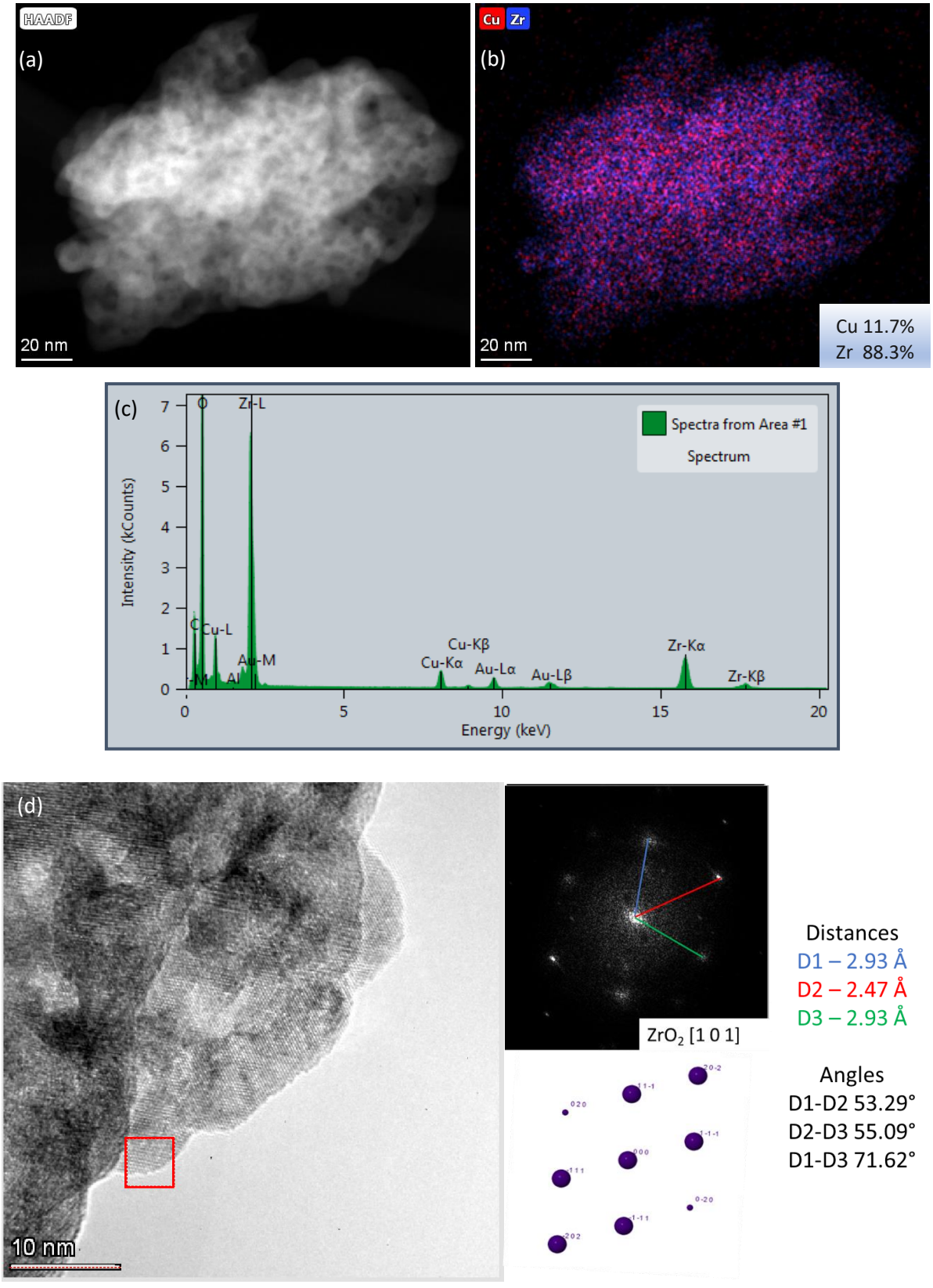

Figure 3.26. (a) HAADF image, (b) EDX elemental map, (c) Elements spectrum and (d) HRTEM image and digital diffraction pattern of $Cu_{0.1}Zr_{0.9}O_x$.

From EDX elemental maps, this sample showed a great homogeneity in the distribution of the Cu and Zr phases. The actual loading was very close to the theoretical loading of 1:9, being Cu% and Zr% equal to 11.7% and 88.3%, respectively. In the elements spectra the peaks corresponding to Cu and Zr are well visible, together with the Au signals coming from the grid used for this analysis. From the acquired HRTEM images, the interpretation of the DDP in the area selected in Figure 3.26d led to the finding of the cubic zirconia phase for ZrO_2 seen from the [1 0 1] zone axis. In fact, despite supposedly being monoclinic zirconia the most stable ZrO_2 phase, in the literature it was researched that the introduction of up to a 10% in weight of another metal such as Fe (and in this case also Cu) in the ZrO_2 structure can actually stabilize the cubic phase even at these temperatures [65].

STEM/EDX and HRTEM analyses of $Fe_{0.1}Ce_{0.9}O_x$ are reported (Figure 3.27).

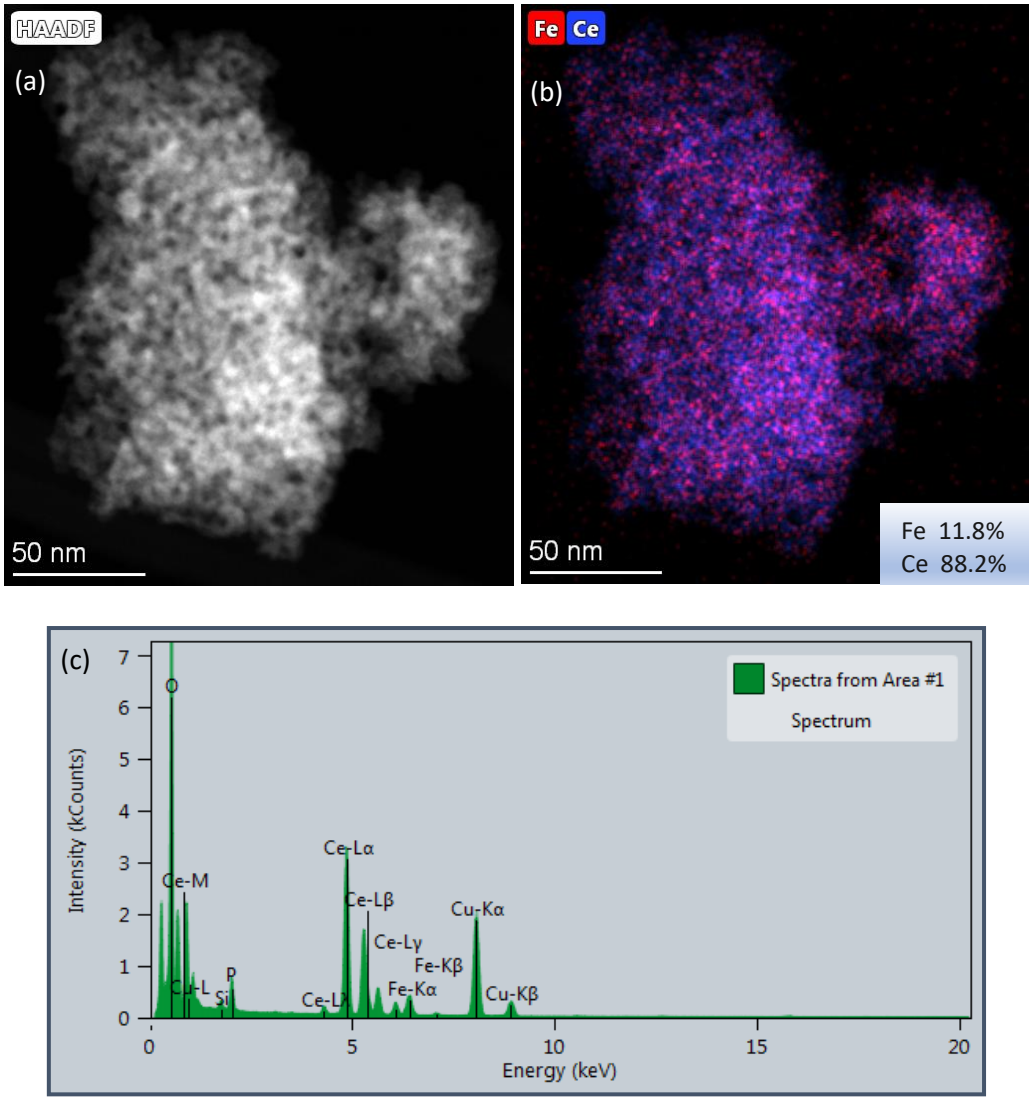

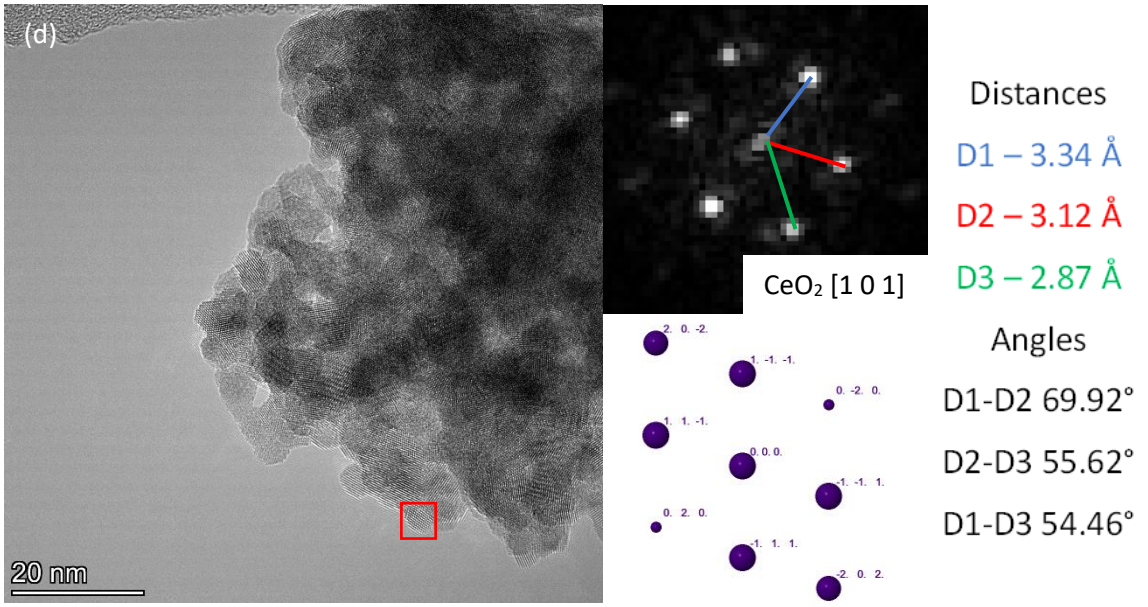

Figure 3.27. (a) HAADF image, (b) EDX elemental map, (c) Elements spectrum and (d) HRTEM image and digital diffraction pattern of $Fe_{0.1}Ce_{0.9}O_x$.

This mixed oxide features very well homogeneously mixed Fe and Ce maintaining once again an average composition close to the theoretical one, as the %Fe and %Ce were calculated to be respectively 11.8% and 88.2%. From the element spectra it was found that there was no contamination and only the corresponding lines of Fe and Ce are visible, together with those of the Cu grid. The DDP analysis of the area in the HRTEM image reported allowed to confirm the presence of the fluorite phase of Ce, whereas a phase corresponding to Fe could not be encountered.

The analysis on $Fe_{0.1}Zr_{0.9}O_x$ is reported (Figure 3.28).

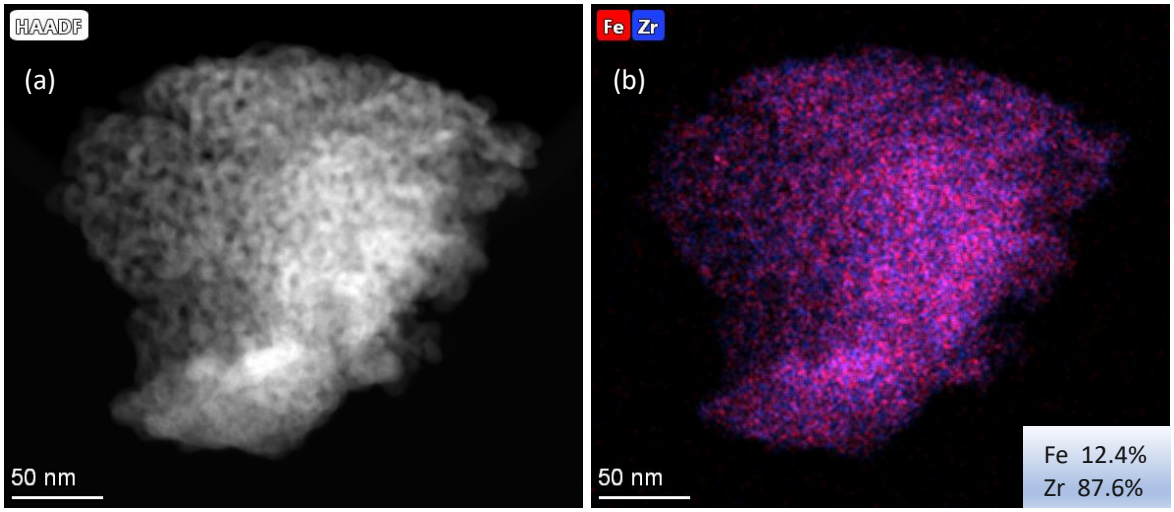

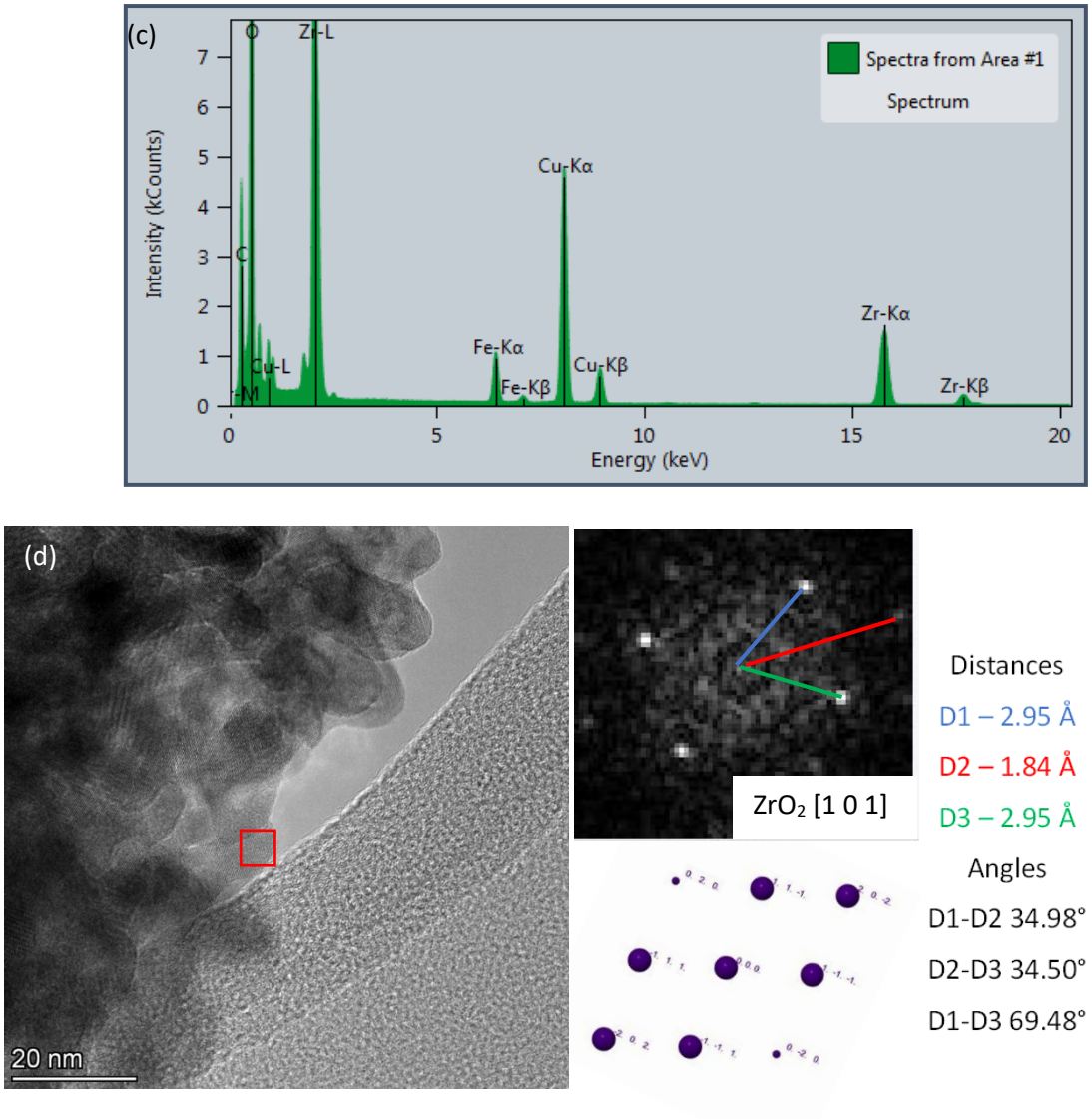

Figure 3.28. a) HAADF image, (b) EDX elemental map, (c) Elements spectrum and (d) HRTEM image and digital diffraction pattern of $Fe_{0.1}Zr_{0.9}O_x$.

The sample is once again very homogeneous in the mixing of the two metals as observed by the EDX elemental map reported, with a composition of 12.5% Fe and 87.5% Zr. On the elements spectra the peaks corresponding to Fe and Zr are well visible, together with Cu peaks deriving from the grid. No contamination was observed in this sample. From the analysis of the DDP of the area selected in the HRTEM image, the phase corresponding to the stabilized cubic zirconia was found due to the presence of Fe inclusion, just as in the case of the $Cu_{0.1}Zr_{0.9}O_x$ sample.

Summing up, the metals in each mixed oxide were found to be homogeneously mixed, especially for the Zr-based ones, whereas slight heterogeneity was encountered in the distribution of Cu in the $Cu_{0.1}Ce_{0.9}O_x$ sample (Figure 3.24b). In general, Cu-containing oxides were found to be less homogeneous than the Fe-containing ones. Moreover, from EDX

quantification of distinct regions of each sample, all the as-prepared oxides presented a very precise stoichiometric control on the average composition of the two metals. For each mixed oxide, the actual composition observed was very similar to the theoretical composition of 10:90%.

3.4.1.2. XRD analyses

As anticipated in Chapter 3.4.1. - The CeZr series, all the mixed oxides were subjected to a reduction treatment for the introduction of defects. XRD analyses were carried out on both the as-prepared and reduced oxides and showed that the Ce and Zr phases were the only detectable phases by the intrinsic sensitivity of the XRD technique, due to the modest content of Cu and Fe (10%), voluntarily introduced in order not to modify the main oxides structures. For clear evidence, Figure 3.29a reports the diffraction patterns of the Ce-based mixed oxides, as-prepared and reduced, in comparison with the cubic fluorite phase of CeO_2. Figure 3.29b reports the diffraction patterns of Zr-based mixed oxides, as-prepared and reduced, in comparison with the monoclinic and cubic ZrO_2 phases.

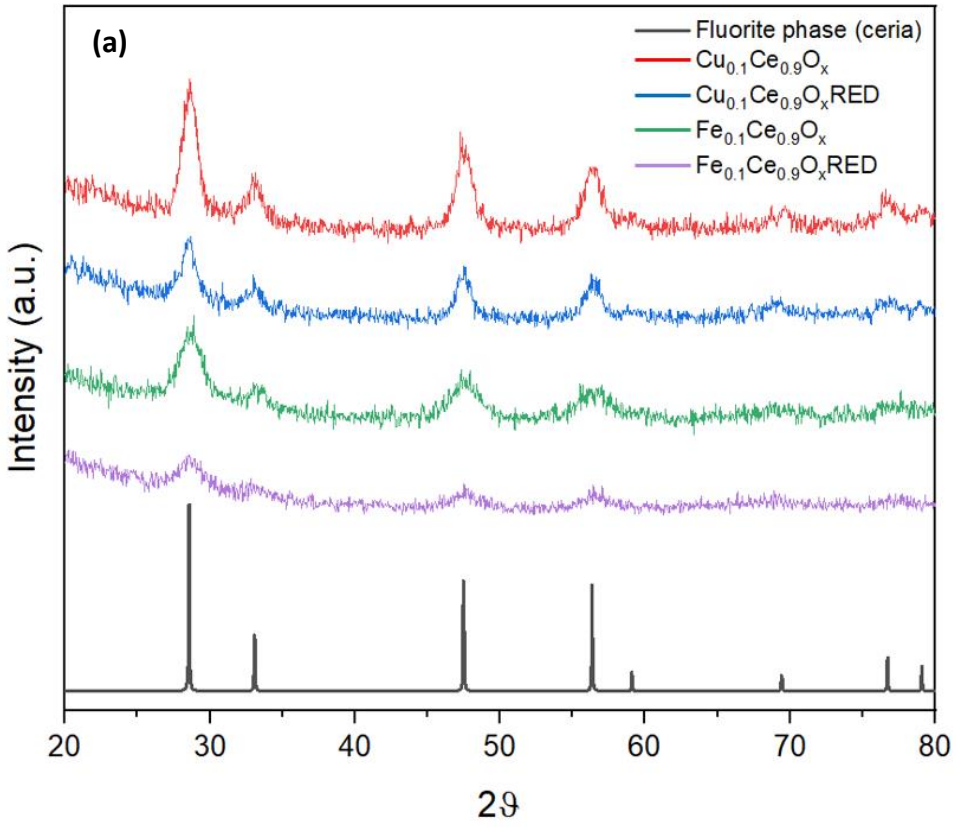

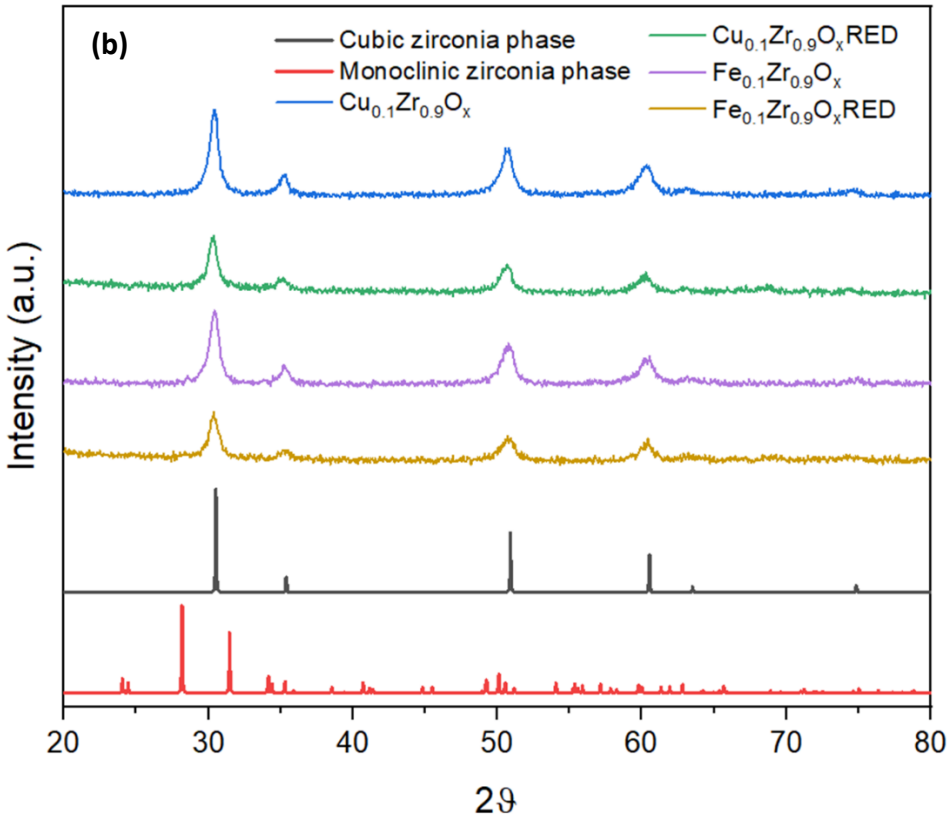

Figure 3.29. Comparison between XRD diffraction patterns of (a) Ce-based mixed oxides (as-prepared and reduced) and cubic fluorite phase and (b) Zr-based mixed oxides (as-prepared and reduced), monoclinic and cubic zirconia phases.

In the case of Ce-based samples, only the fluorite phase of CeO_2 was detectable. In the case of Zr-based mixed oxides, the diffraction patterns confirmed the presence of a stabilized cubic zirconia phase instead of the more stable monoclinic ZrO_2 due to the addiction of the second metal in a small percentage, in agreement with literature findings [65]. This had already been observed by the HRTEM analyses of the DDP found for $Cu_{0.1}Zr_{0.9}O_x$ and $Fe_{0.1}Zr_{0.9}O_x$ that were identifying the cubic zirconia phase (Figure 3.26d).

In addition, variation of the lattice parameters and average particle size (calculated by Scherrer Equation) were observed as a consequence of the treatment. In the case of $Cu_{0.1}Ce_{0.9}O_x$, the lattice parameter slightly decreased (5.415 to 5.408 Å) while the mean average crystallite size grew of about 2 nm (from 11 to 13 nm). On the other hand, $Fe_{0.1}Ce_{0.9}O_x$ exhibited a smaller mean average crystallite size of 8 nm ca. and lowered its lattice parameter (5.428 to 5.405 Å) as well. In the case of $Cu_{0.1}Zr_{0.9}O_x$ the lattice parameter of the cubic phase grew up from 5.087 to 5.093 Å maintaining the same crystallite size (13 nm), whereas the

lattice parameter of $Fe_{0.1}Zr_{0.9}O_x$ decreased from 5.082 to 5.074 Å together with its mean crystallite sized, from 12 to 10 nm ca.

3.4.1.3. BET surface area analyses

BET surface area characterization of the as-prepared mixed oxides resulted in medium surface areas of around 80 m^2/g for each mixed oxide, excluding $Fe_{0.1}Ce_{0.9}O_x$ which resulted in a higher area of 120 m^2/g ca. In this case, the smaller size of the crystallites observed by XRD could account for the higher surface area. The adsorption and desorption isotherms are reported in Figure 3.30, and the isotherms of type IV indicate the mesoporous nature of the materials.

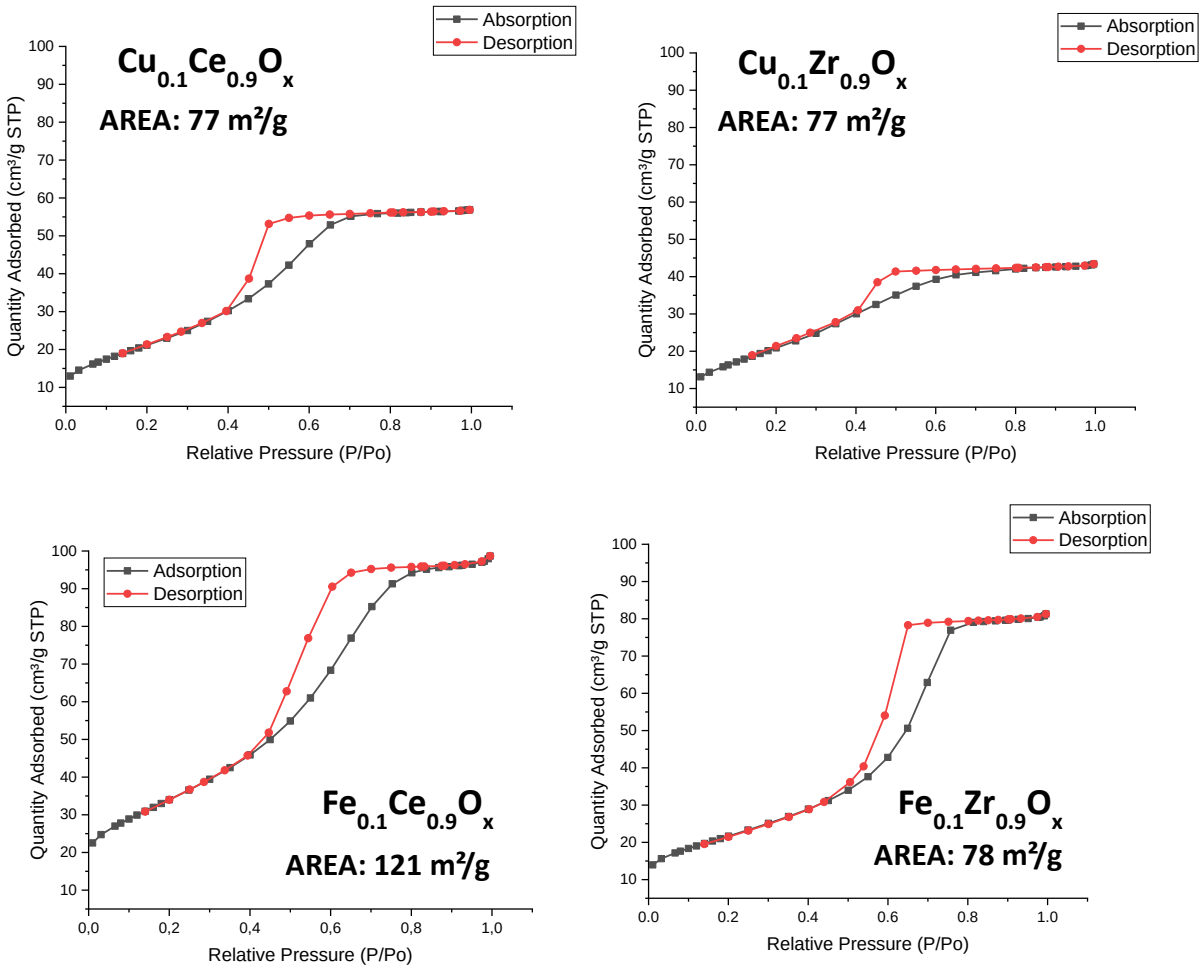

Figure 3.30. BET surface area characterization of the as-prepared mixed oxides: $Cu_{0.1}Ce_{0.9}O_x$, $Cu_{0.1}Zr_{0.9}O_x$, $Fe_{0.1}Ce_{0.9}O_x$ and $Fe_{0.1}Zr_{0.9}O_x$.

3.4.1.4. The CeZr series: reduction treatment

Since cyclohexane oxidation is ruled by a radical mechanism, and this latter can be favoured by the presence of unsaturated metal centres and structural and/or O_2 defects, the Cu and Fe-containing mixed oxides were reduced at 300°C for 50 minutes with 1:3 (w/w) $NaBH_4$:oxide by adapting a method indicated in [63], where it was specifically used for the introduction superficial defects on the particles. Following, the characterization carried out on the reduced mixed oxides through STEM/EDX analyses and XPS is reported.

As for electron microscopy, the reduced mixed oxides were characterized solely by STEM/EDX analyses, as this technique could give the most interesting information on the composition after reduction, and also given that HRTEM was found being limited to the observation of the Ce and Zr phases only. The acquired HAADF images and EDX elemental maps are reported (Figure 3.31a-d).

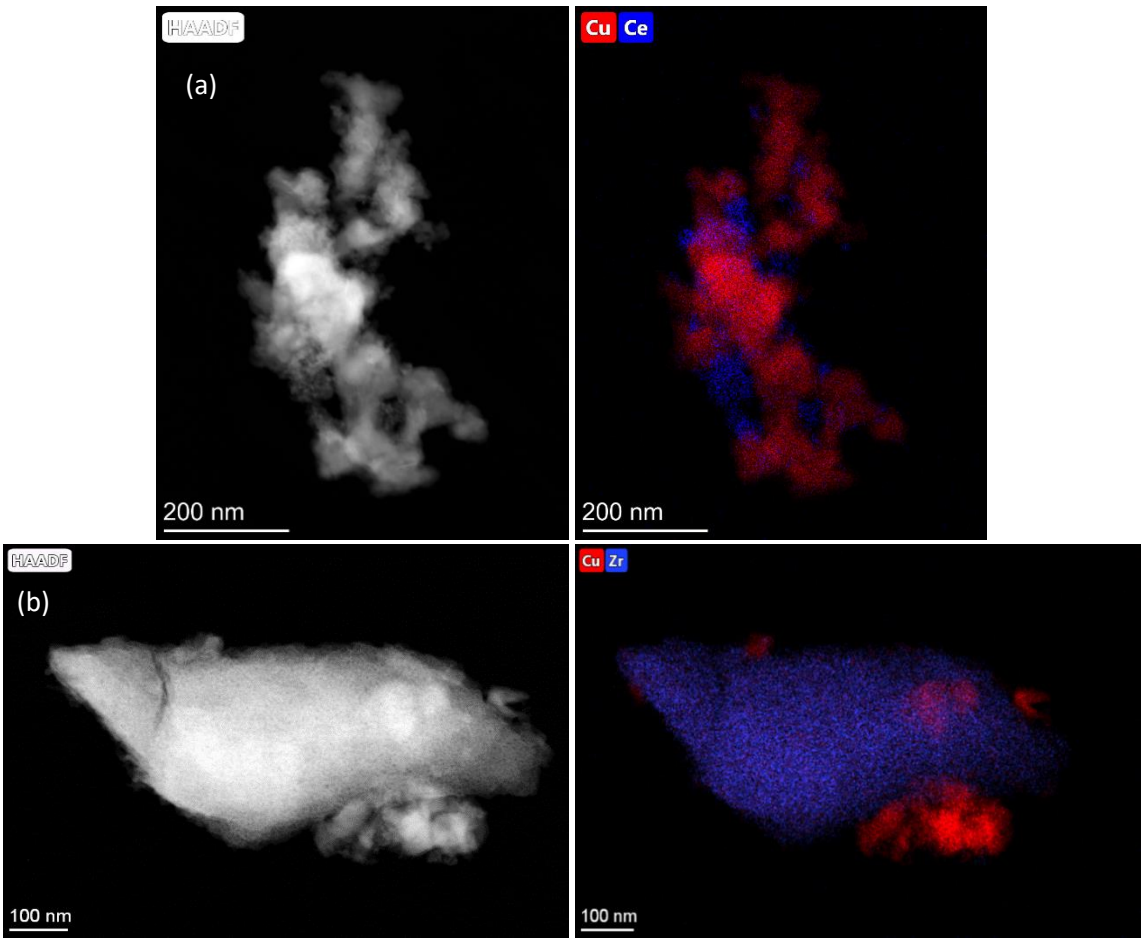

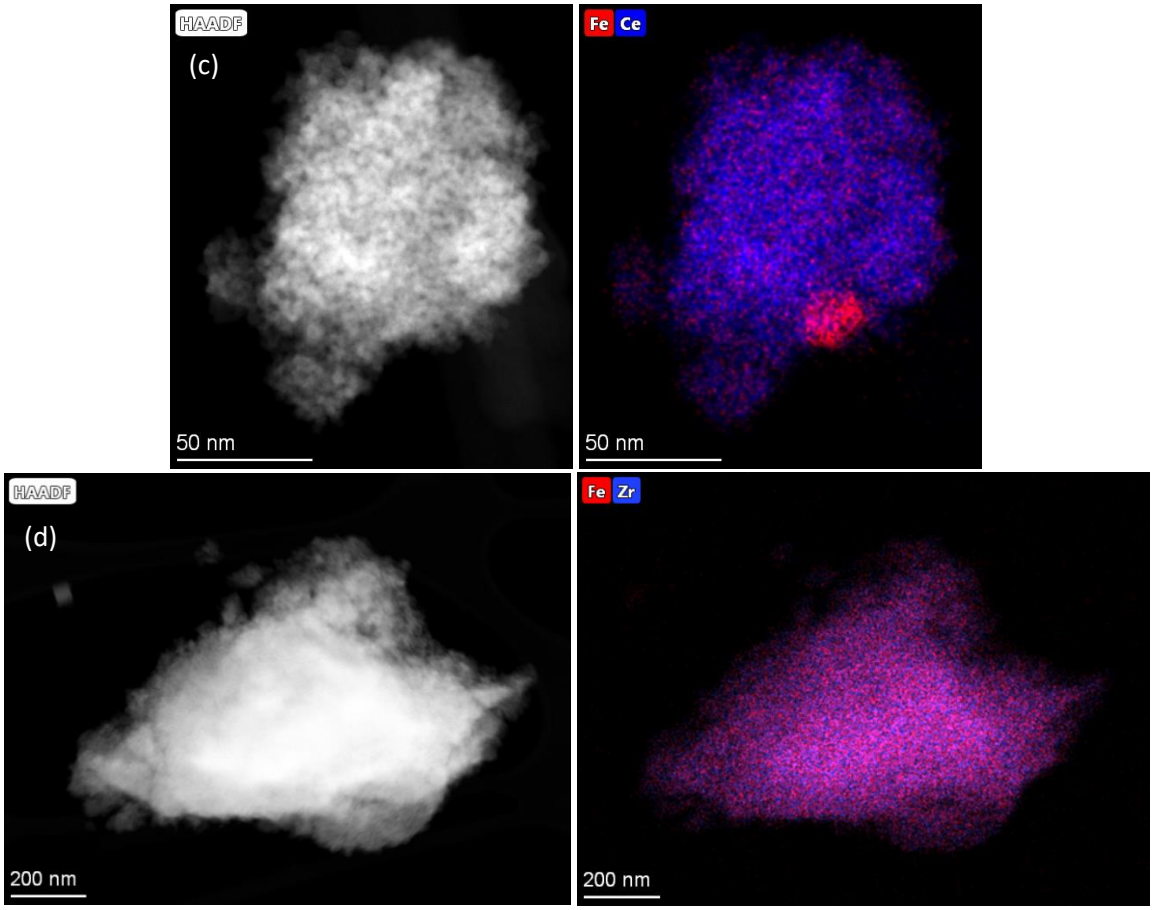

Figure 3.31. HAADF (left) and EDX elemental map (right) images of (a) $Cu_{0.1}Ce_{0.9}O_xRED$, (b) $Cu_{0.1}Zr_{0.9}O_xRED$, (c) $Fe_{0.1}Ce_{0.9}O_xRED$ and (d) $Fe_{0.1}Zr_{0.9}O_xRED$ samples.

The reduced samples exhibited heterogeneity, and the included metal (Cu or Fe) segregated from the mixed oxide structure in all cases apart from $Fe_{0.1}Zr_{0.9}O_x$, which instead demonstrated to preserve its homogeneity upon treatment. The formation of agglomerates of the Fe and Cu species was observed. Upon treatment, reconstruction of the oxides took place, creating surface defects and varying the contact between the two metals. In the case of Cu-containing oxides, Cu resulted being in a partially reduced state. This was confirmed by drawing an EDX intensity profile (quantification of the elements crossed by the yellow arrow) and by EDX quantification of O in both Cu-rich and Ce-/Zr-rich areas for the Cu-containing reduced samples (Figure 3.32 and Figure 3.33).

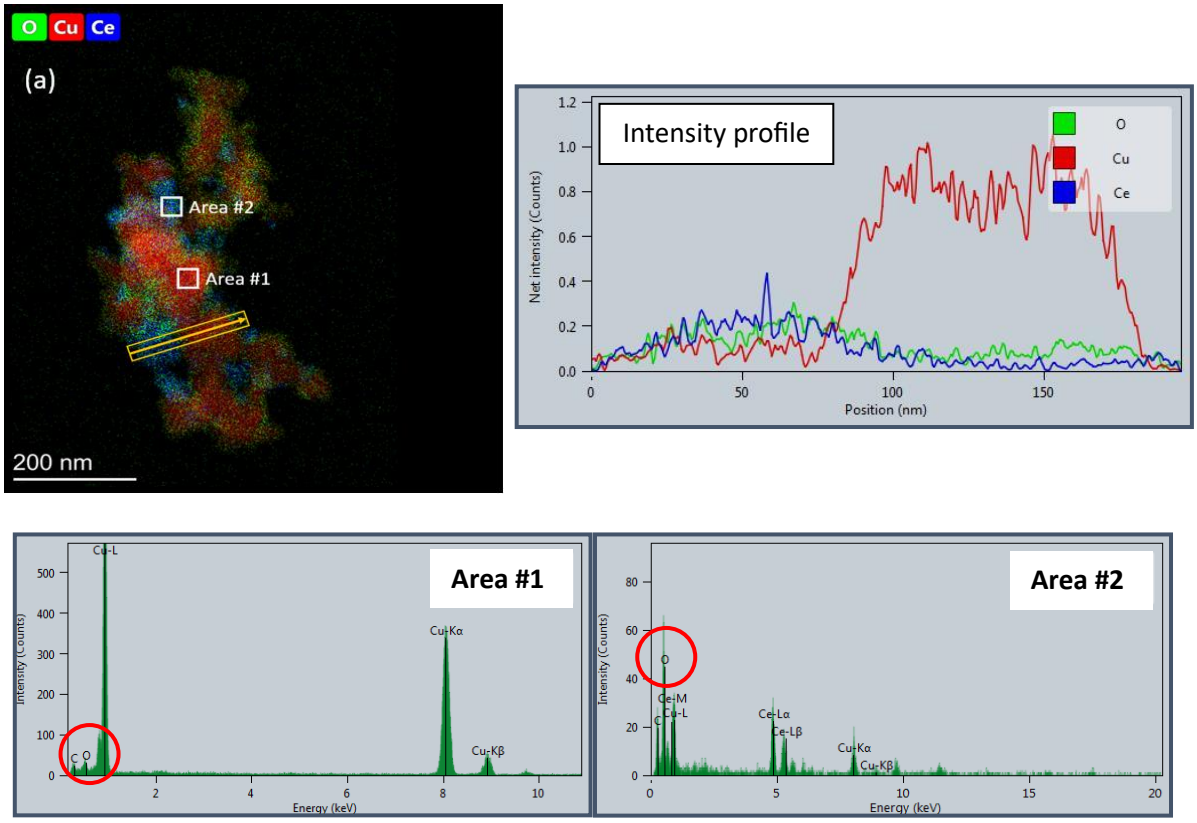

Figure 3.32. STEM/EDX elemental map of $Cu_{0.1}Ce_{0.9}O_x$RED, intensity profile and EDX quantification of O in the two areas.

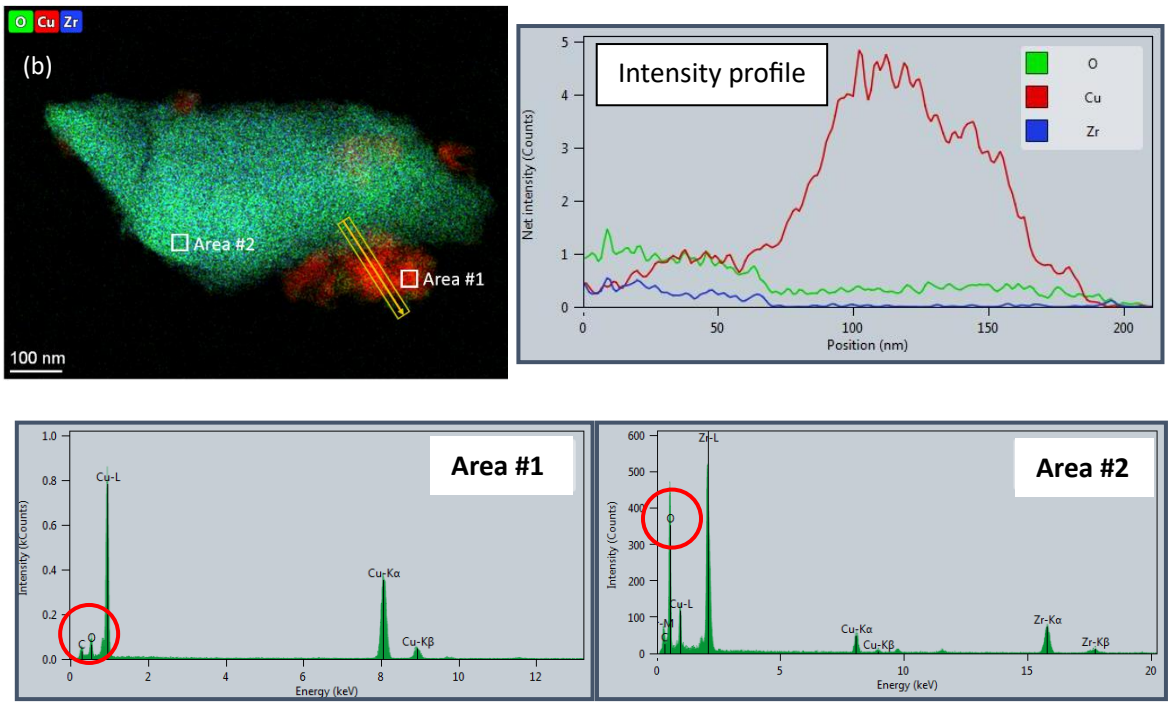

Figure 3.33. STEM/EDX elemental map of $Cu_{0.1}Zr_{0.9}O_x$RED, intensity profile and EDX quantification of O in the two areas.

In these images, oxygen (in green) is observable in the areas corresponding to Ce and Zr, whereas is mostly absent where Cu is found. The EDX intensity profile line (in yellow) further confirmed a great presence of Cu and negligible presence of O in the Cu-rich areas crossed by

the line. Another confirmation came from the EDX mapping of the two squared areas for each sample. In Figure 3.32, related to $Cu_{0.1}Ce_{0.9}O_x$RED, the Cu-rich area (Area #1) presents a very low-intensity signal for O, whereas the Ce-rich area (Area #2) exhibits an intense O signal. The same behaviour was observed in Figure 3.33 for $Cu_{0.1}Zr_{0.9}O_x$RED.

On the other hand, Fe-containing oxides exhibited a homogeneous distribution of O all over the sample, highlighting the stability of Fe to the reduction treatment.

3.4.1.5. XPS analyses

XPS survey analyses were finally conducted on both the as-prepared and reduced oxides, and evidenced some differences in the surface metal composition, occurring upon the reduction treatment (Table 3.12).

Catalyst (M1M2Ox)	% At M1 (Cu or Fe)	%At M2 (Ce or Zr)
$Fe_{0.1}Ce_{0.9}O_x$	5.5	94.5
$Fe_{0.1}Ce_{0.9}O_x$ RED	10.7	89.3
$Fe_{0.1}Zr_{0.9}O_x$	9.7	90.4
$Fe_{0.1}Zr_{0.9}O_x$ RED	7.6	92.4
$Cu_{0.1}Ce_{0.9}O_x$	15.0	85.0
$Cu_{0.1}Ce_{0.9}O_x$ RED	19.1	80.9
$Cu_{0.1}Zr_{0.9}O_x$	5.1	94.9
$Cu_{0.1}Zr_{0.9}O_x$ RED	9.9	90.1

Table 3.12. XPS survey analysis table of all the as-prepared and reduced mixed oxides.

Following the treatment, the amount of the included metal (Cu or Fe) on the surface of the oxides increased as a consequence of their migration occurring upon segregation, resulting in about a 5% increment. The observed segregation with subsequent migration of the included metal was indeed an exsolution phenomenon, where the system passed from a mixed oxide structure towards a kind of supported system. This is true for all the mixed oxides apart from the $Fe_{0.1}Zr_{0.9}O_x$ one for which the segregation did not occur, in accordance with the STEM/EDX characterization, for which the surface composition remains very similar to the original one. It can be noticed that CuCe oxides (both as-prepared and reduced) are deviating from the 10:90 theoretical atomic ratio to a 20:80 ratio on the surface of the materials. This consideration could be again paired with the more pronounced heterogeneity observed in

$Cu_{0.1}Ce_{0.9}O_x$ with STEM/EDX analyses, compared to the other oxides, resulting in a more marked reconstruction of the catalyst. For the attribution of the presence of O defects in the mixed oxides created upon treatment, a shoulder peak at BE=531-532 eV in the O1s spectra can be related to oxygen vacancies [66,67]. However, this claim has been discredited by a recent paper [68], in which it is stated that ex-situ measurements cannot reveal the presence of O vacancies, discarding regular XPS analyses from the viable techniques for that purpose. In general, ex-situ measurements are not the most suitable for the detection of the O defects, and in-situ measurements could be the topic of a future study on these materials. Raman spectroscopy could be the solution to the determination of O vacancies presence, as it was successfully utilized for their determination on modified Ce oxide [69].

3.4.2. Oxidation of cyclohexane with the CeZr series

Using the same reaction conditions employed for the previous series of catalysts, the oxidation of cyclohexane was carried out at 120°C and 4 bars of O_2 pressure, which are relatively milder reaction conditions than what is reported for the industrial practice and in many state-of-the-art heterogeneous processes. Benzaldehyde was put in the initial reaction mixture to serve as radical initiator.

In the tests the productivity of the monometallic counterparts, CeO_2 and ZrO_2 prepared by inverse microemulsion, was compared to the four mixed oxides as-prepared and reduced. The purpose was to disclose the many effects of 1) the main oxide, comparing the role of Ce and Zr due to their different properties, 2) the inclusion of Fe and Cu in the mixed oxides structures, exerting different effects and 3) the effect of the reduction treatment, and in particular how the exsolution phenomenon observed with STEM/EDX characterization could affect the final productivity. A graphical representation of the catalytic results regarding the as-prepared and reduced mixed oxides are reported (Figure 3.34 and Table 3.13). The colours used differentiate the Zr- and Ce-based blocks from each other and from the non-catalysed reaction.

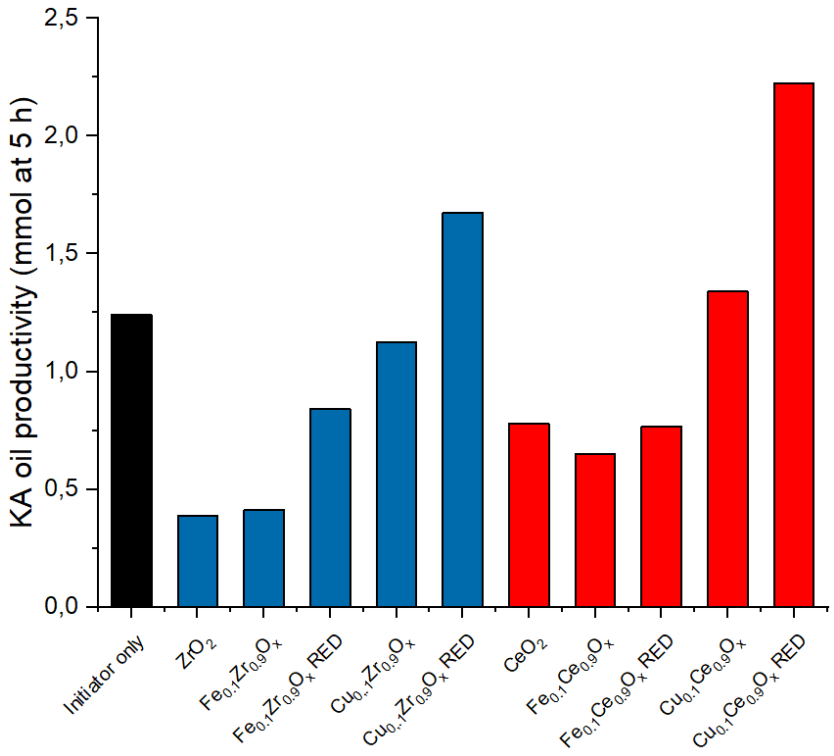

Figure 3.34. Graphical representation of KA oil productivity for the whole series of mixed oxides after 5 h of reaction, compared to the non-catalysed initiator-only reaction.

Catalyst	Prod. KA oil (mmol at 5 h)	K/A ratio	Selectivity to KA (%)
Initiator only	1.24	2.65	94.2
ZrO_2	0.39	1.29	79.1
$Fe_{0.1}Zr_{0.9}O_x$	0.41	1.85	72.0
$Fe_{0.1}Zr_{0.9}O_x$ RED	0.84	3.11	90.3
$Cu_{0.1}Zr_{0.9}O_x$	1.12	2.82	92.9
$Cu_{0.1}Zr_{0.9}O_x$ RED	1.67	2.83	95.6
CeO_2	0.78	1.08	86.5
$Fe_{0.1}Ce_{0.9}O_x$	0.65	0.71	70.0
$Fe_{0.1}Ce_{0.9}O_x$ RED	0.76	0.70	69.7
$Cu_{0.1}Ce_{0.9}O_x$	1.34	2.26	91.9
$Cu_{0.1}Ce_{0.9}O_x$ RED	2.22	2.58	93.2

Table 3.13. Productivity (mmol KA), K/A ratio and selectivity % to KA oil of the whole series of mixed oxides after 5 h of reaction, compared to the non-catalysed initiator-only reaction.

The nature of the main oxide, whether Ce or Zr, significantly influenced catalyst performance. Ce-based catalysts outperform Zr-based ones in all compositions, likely due to ceria's superior oxygen exchange capacity and the presence of numerous Ce^{3+}/Ce^{4+} redox pairs. However, both

the monometallic oxides (CeO_2 and ZrO_2) appear to inhibit the reaction compared to the benzaldehyde-only test. This behaviour was attributed to the already discussed presence of the Lewis acidic sites within the oxides, which can act as radical scavengers [55] (See Chapter 3.3.2.2. Oxidation of cyclohexane with AuSn catalysts). With both supports, despite resulting in poor productivity of KA oil, the K/A ratio is <1, meaning these species interfere with the pure radical pathway of the non-catalysed reaction (K/A=2.65).

Different behaviour can be observed when including Cu or Fe in the ceria and zirconia structures. The productivity of KA oil with the Cu-containing as-prepared mixed oxides was higher than that of Fe-containing ones, both with Ce and Zr, and it overperformed the non-catalysed reaction in the case of $Cu_{0.1}Ce_{0.9}O_x$ (1.34 mmol). On the contrary, Fe-containing as-prepared mixed oxides seemed to inhibit the productivity of KA oil (all lower than 1 mmol at 5 h). However, a noteworthy effect occurred on the ability of the mixed oxides to obtain KA oil upon the reduction treatment, as in all cases the reduction treatment brought to an increase in the productivity. This behaviour was ascribed to the exsolution of the Cu and Fe species, meaning their segregation with subsequent migration to the surface of the catalysts, which created new and different active sites for the oxidation mechanism to occur, and the presence of unsaturated metal centres which could act as an initiator of the cyclohexane oxidation mechanism [10]. The partial reduction of Cu species, observed by STEM/EDX O-containing maps (Figure 3.32 and Figure 3.33), could explain the productivity boost observed for $Cu_{0.1}Zr_{0.9}O_x$RED and $Cu_{0.1}Ce_{0.9}O_x$RED, producing up to 2.22 mmol of KA oil. It can be observed that at the conditions employed for the reduction treatment, Cu is more easily reduced than Fe and partially reduced Cu in the form of mixed phases/redox pairs would give additional explanation for the higher productivity. As future improvement for this series, further tests at higher T of reduction under a flux of H_2 would confirm the high KA oil productivity of wholly reduced Fe as well. The higher productivity of $Cu_{0.1}Zr_{0.9}O_x$ RED could be also attributed to the enhancement in the lattice parameter seen by XRD after the reduction treatment, which could lead to higher oxygen exchange internal to the lattice. Fe catalysts, both as-prepared and reduced, all resulted in low productivity of KA oil probably also following a different reaction pathway, as indicated by their K/A ratios opposite to those observed for Cu-containing oxides.

Similarly to what was observed in the FeCo series between Fe and Co-containing systems, different K/A ratios were observed depending on the included metals (Cu or Fe), but also on the main oxide (Ce or Zr). According to Table 3.13, FeCe catalysts presented a K/A<1. As it was seen in the previous FeCo and Au-based series, when the alcohol is the favoured product (low K/A), this is possibly attributed to a perturbation of the pure radical pathway due to the enhancement catalyst surface-mediated homolytic cleavage of the CyO-OH bond. The test on pure CeO_2 gave a K/A of 1.08, indicating that ceria possesses a lower ability to perform that cleavage alone, or that it can enhance the pure radical mechanism more, than when it is doped with Fe. On the other hand, the test on pure ZrO_2 resulted in a higher K/A of 1.29. Cu-containing catalysts consistently exhibited high K/A ratios exceeding 2. One of the routes for the formation of a high amount of cyclohexanone can derive from unstable [70] alpha-hydroperoxyalkyl radicals ($Cy^{\bullet}OOH$), formed by alpha-abstraction from cyclohexyl hydroperoxide (CyOOH), which rapidly dissociate into $OH^{\bullet}$ and Cy=O [62,71] (see Introduction section - Chapter 1.2.3. Autoxidation and reaction mechanism). Moreover, it was found that Cu catalysts can increase ketone amount by dehydrogenating the cyclohexanol to cyclohexanone [72]. To be noted that cyclohexanone also represents the most interesting product for the industry in order to make ε-caprolactam [29,73] as feedstock for nylon-6,6 production. Therefore, the production of a high amount of cyclohexanone compared to cyclohexanol while maintaining high selectivity to the KA mixture is highly desirable.

The K/A ratio in this series is strictly connected to the selectivity to KA oil. The selectivity to KA oil at our mild conditions is still very high throughout the whole series, as the only by-product observed was attributed to be cyclohexyl hydroperoxide (CHHP), as suggested by GC mass analyses of the reaction mixture. In the Initiator-only reaction, a high selectivity of 94.2% was obtained, value which decreased drastically by about ~10-15% when performing the same reaction with the monometallic CeO_2 or ZrO_2. Similarly, Fe-containing oxides all exhibited diminished selectivity to KA oil reaching around 70%, being the rest identified as CHHP and traces of other by-products. On the contrary, Cu-containing oxides with both Ce and Zr possessed the highest selectivity in the series and all above 90%, reaching a maximum of 95.6% in the case of $Cu_{0.1}Zr_{0.9}O_x$RED, higher than in the non-catalysed reaction. In addition, in both cases (with Ce and Zr) the selectivity for the Cu-containing oxides was boosted upon reduction.

Moreover, looking at the reaction profiles for the most interesting catalysts, namely the reduced $Cu_{0.1}Ce_{0.9}O_xRED$ and $Cu_{0.1}Zr_{0.9}O_xRED$, no deactivation can be observed (Figure 3.35).

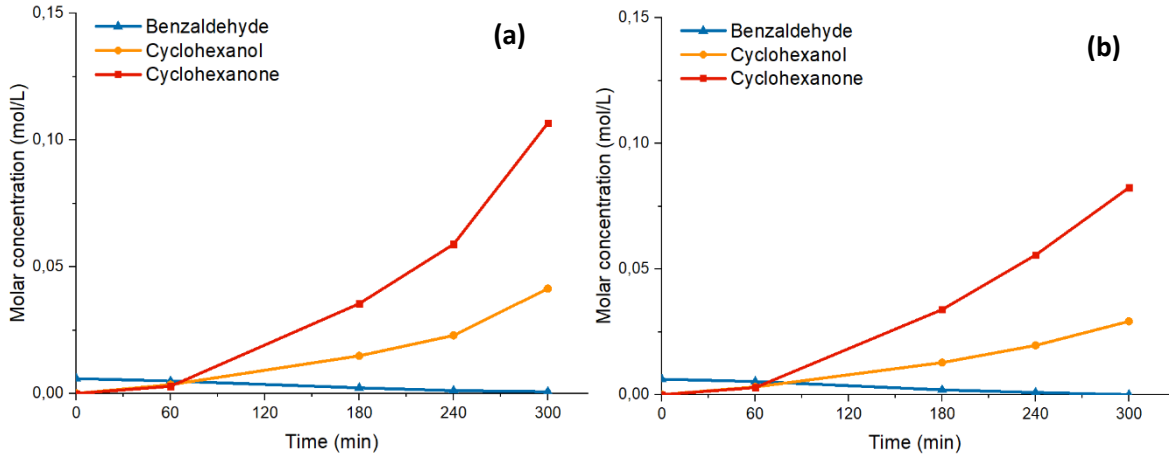

Figure 3.35. Reaction profiles of (a) $Cu_{0.1}Ce_{0.9}O_xRED$ and (b) $Cu_{0.1}Zr_{0.9}O_xRED$.

From this observation, it can be concluded that carrying out a long catalytic run (e.g. 24 hours) of the two catalysts would represent an interesting future study to for the production of KA oil at mild conditions with a very low amount of initiator and of catalyst.

Considering the interesting performance of the as-prepared and reduced Cu-containing mixed oxides, it was decided to test commercial CuO, as-commercialized and then after submitting it to a reduction treatment based on the expertise of the Cádiz group to reduce the crystallite size of the Cu species.

3.4.3. Tests on commercial CuO

Pure commercial CuO from Sigma Aldrich has been tested as-supplied and after being submitted to a reduction treatment at 300°C for 50 minutes under a H_2 flow and, subsequently, air-reoxidized. The samples were labelled as in Table 3.14. Other than for comparison, the intent of reduction here was also decreasing the particle size as well. In fact, this procedure is derived from recent studies of the Cádiz group, and yet unpublished at the time of writing, which allow for the decrease of the crystallites size in CuO-containing samples.

Catalyst	Description
CuO	Commercial CuO
CuO-RED	CuO reduced at 300°C for 50 min with H_2
CuO-REOX	CuO after reduction treatment and reoxidation in air

Table 3.14. Commercial CuO and derived catalysts after reduction treatment: labels and description.

After reduction was carried out, the colour of the powder changed entirely from black to the typical red-orange characteristic of metallic Cu. The bare and reduced CuO were characterized by SEM in order to verify a variation in the morphology upon the reduction treatment (Figure 3.36 and Figure 3.37).

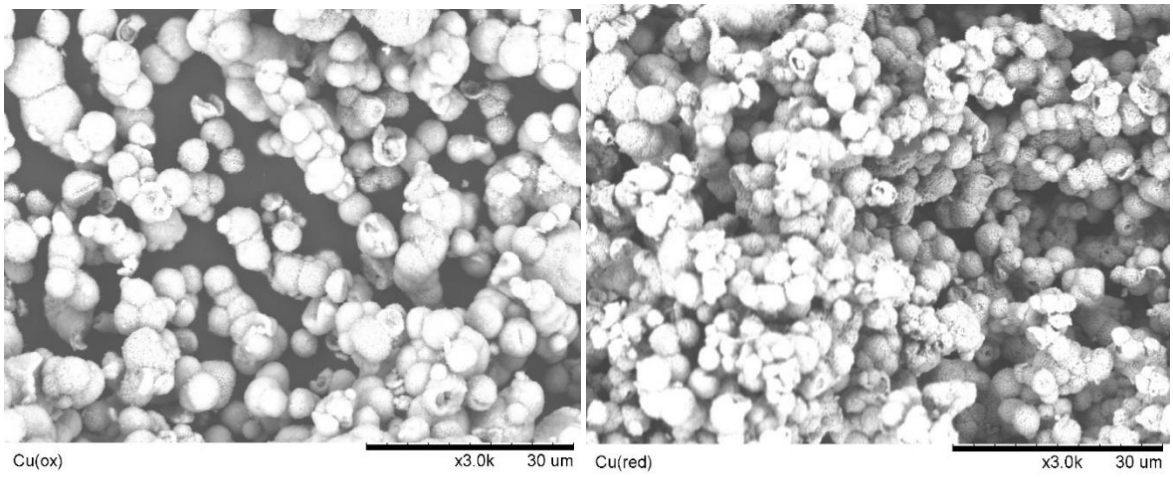

Figure 3.36. SEM characterization of CuO and CuO-RED at 3.0k x magnification.

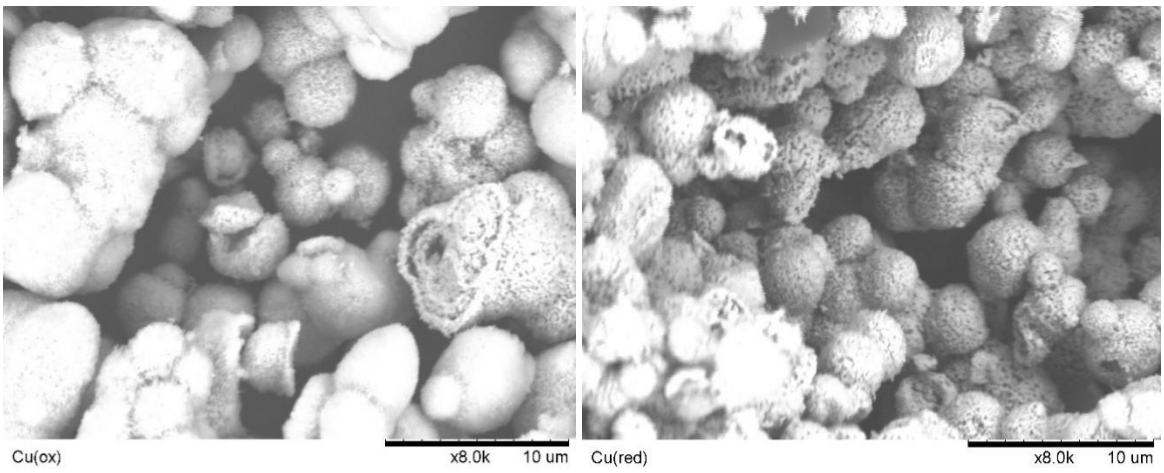

Figure 3.37. SEM characterization of reduced CuO and CuO-RED at 8.0k x magnification.

The morphology of the sample did not change upon reduction and the particles maintained a rounded shape with visible pores. From the comparison it was also noticed that the reduced sample, at all the magnifications observed, presented smaller particles than as-supplied CuO,

as expected. Part of the reduced catalyst was let reoxidize in open air for a week. A change in colour was observed due to reoxidation, as the powder turned to a darker orange.

XRD characterization was performed on the commercial CuO and on the reoxidized CuO-REOX to reveal any bulk phase change induced by reduction. Comparing the experimental diffraction patterns of the samples with all the possible Cu phases (metallic Cu, CuO, Cu_2O, Cu_3O_4), it resulted clear that that the diffraction peaks of the two samples corresponded only with CuO (tenorite) and metallic Cu, as it is clearly visible in Figure 3.38.

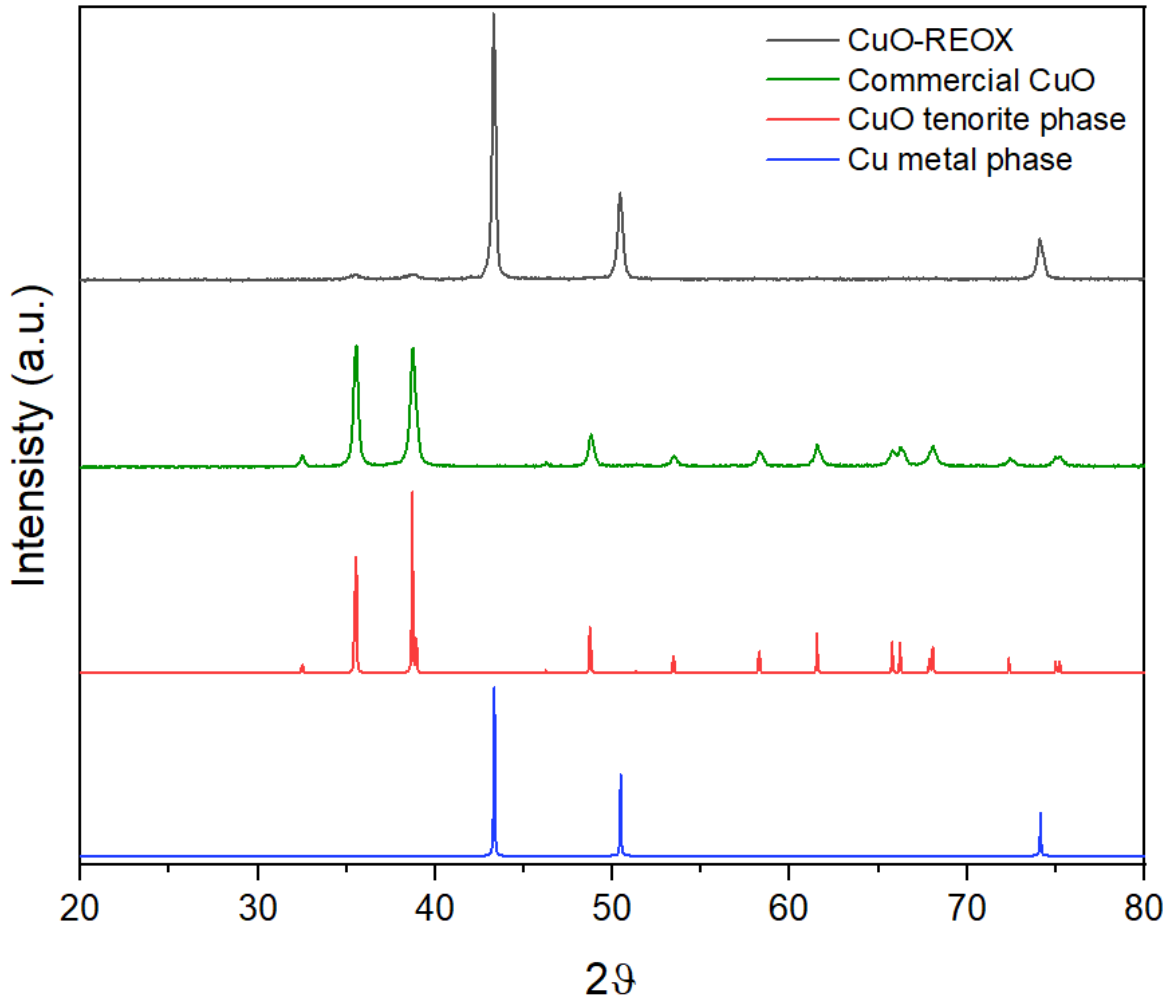

Figure 3.38. Diffraction patterns of commercial CuO and reoxidized CuO (CuO-REOX), in comparison with CuO (tenorite) and metallic Cu patterns.

The commercial CuO diffraction pattern was matching perfectly with the CuO tenorite phase. On the other hand, CuO-REOX exhibited peaks corresponding mainly to metallic Cu, but for two small diffraction peaks also matching the tenorite phase (at 2θ between 35 and 40), thus suggesting the presence of some mixed phase. This clear effect of the reduction treatment

was further confirmed by the fitting of the phases performed by using the PowderCell software (Figure 3.39a and b). The software confirmed 100% tenorite phase correspondence for the commercial CuO sample. In the case of CuO-REOX, the fitting indicated the presence of a mixed phase corresponding to 81.5% metallic Cu and 18.5% CuO tenorite phase.

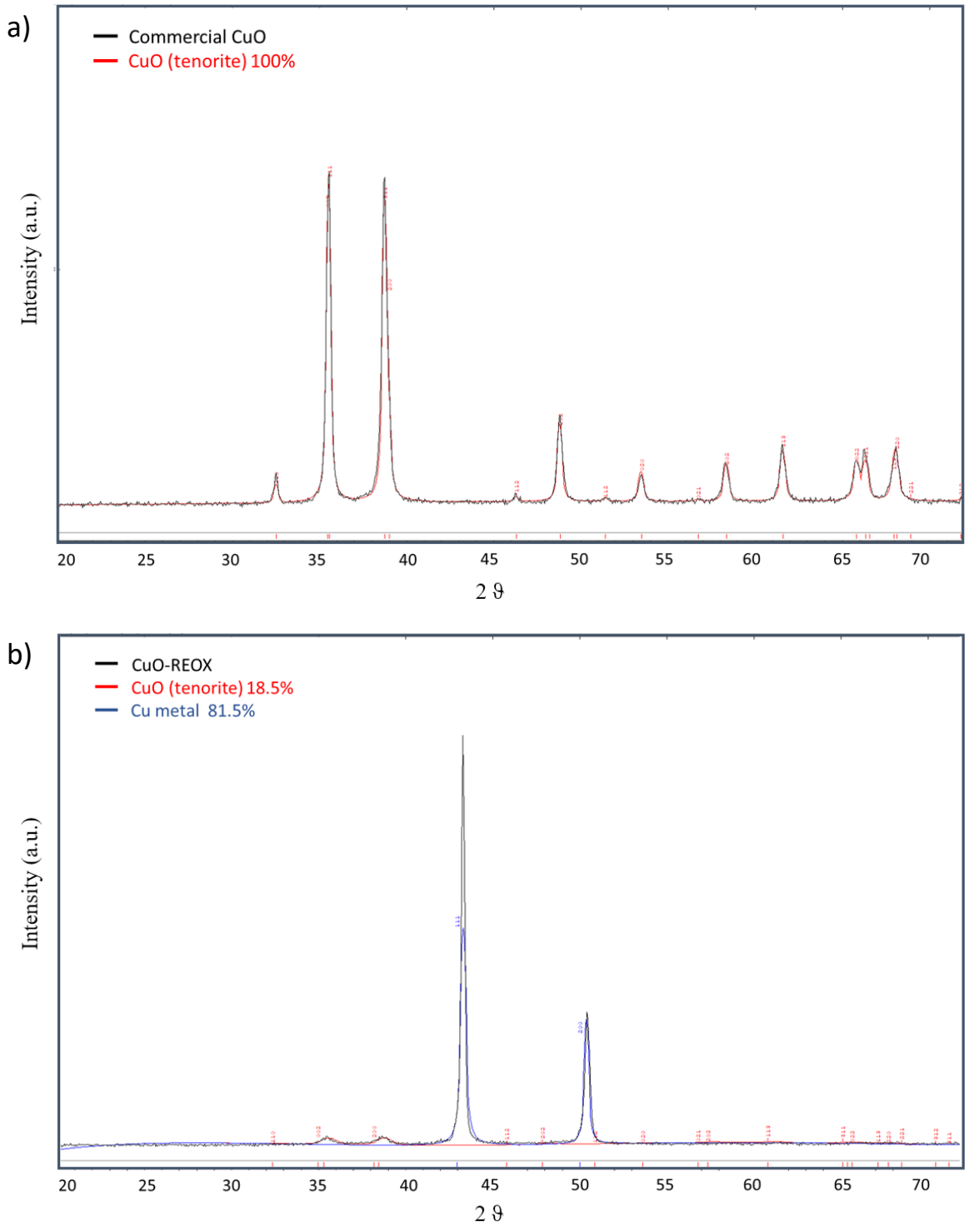

Figure 3.39. Phase identification by PowderCell software fitting for (a) commercial CuO and (b) CuO-REOX.

Moreover, from the calculations performed using Scherrer equation, a decrease was obtained in the average crystallites size from the 38.2 nm of the commercial CuO down to 18.8 nm in the case of CuO-REOX. Smaller particles in the reoxidized system are observable also by HAADF-STEM characterization of the two samples (Figure 3.40).

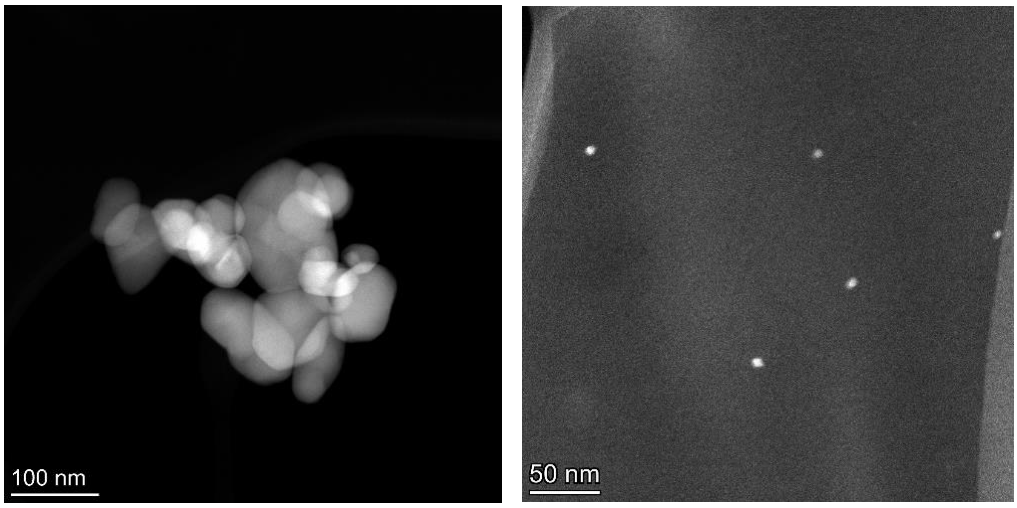

Figure 3.40. HAADF-STEM images of (a) Commercial CuO and (b) CuO-REOX samples.

From the STEM images big particles could only be detected in the case of the commercial CuO sample and small isolated 10-20 nm particles for the reoxidized sample. The huge decrease in particle size can also be responsible for the much better performance observed for the reoxidized sample. In fact, the catalysts were all tested in the oxidation of cyclohexane at the same reaction conditions as it was done for the CeZr series (120°C, 4 bar O_2, 10 uL benzaldeyde). In the following Figure and Table the catalytic results are compared with the CeZr series (Figure 3.41 and Table 3.15).

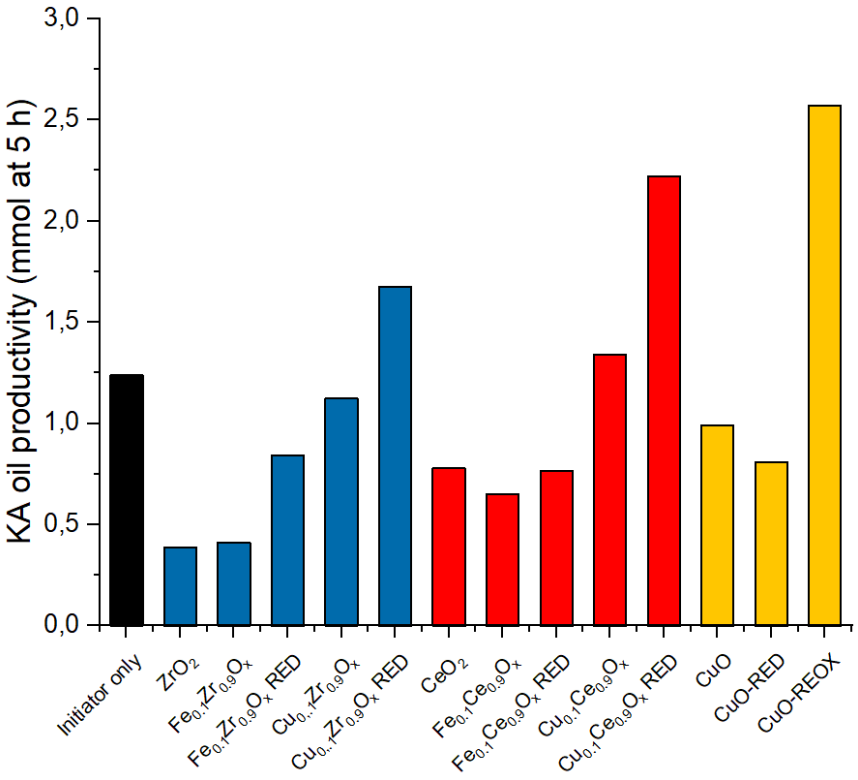

Figure 3.41. Graphical representation of KA oil productivity for the whole series of CeZr mixed oxides after 5 h of reaction, now including the tests on commercial CuO bare, reduced and reoxidized.

Catalyst	Prod. KA oil (mmol at 5 h)	K/A ratio	Selectivity to KA (%)
Initiator only	1.24	2.65	94.2
CuO	0.99	2.39	87.2
CuO-RED	0.81	2.64	87.4
CuO-REOX	2.57	1.98	98.8

Table 3.15. Productivity (mmol KA), K/A ratio and selectivity % to KA oil of commercial CuO, reduced CuO and reoxidized CuO after 5 h of reaction, compared to the non-catalysed initiator-only reaction.

Commercial CuO and CuO-RED did not perform well in the oxidation, as they inhibited the reaction also obtaining lower KA oil productivity even compared to the initiator-only reaction. The selectivity to KA oil of these two catalysts was lower too. The K/A ratio was very high (>2) in both cases, confirming the trend for Cu-containing catalysts. On the contrary, the reoxidized CuO-REOX catalyst gave very good result of 2.57 mmol of KA oil produced after five hours. Most interestingly, the selectivity of CuO-REOX was the highest obtained until now, being it extremely high at 98.8%, making it the most attractive catalyst of this thesis work if paired with the low cost of the material and of its preparation. The K/A ratio for CuO-REOX was also

very high (~2), confirming the presence of the supposed Cu-mediated mechanism leading to high K/A ratios compared to other metals. This further increases the industrial attractiveness of the system, as it was already discussed that cyclohexanone is the most interesting product of the KA oil mixture for the industrial production of nylon-6,6. The overperformance of CuO-REOX over the commercial CuO and the just-reduced CuO-RED catalysts was attributed to the copresence of Cu^0/Cu^{II} mixed phases and of smaller crystallites. In our opinion these two effects are the reason of the outstanding results, and why the reoxidized catalyst overperformed even the best catalyst of the CeZr series ($Cu_{0.1}Ce_{0.9}O_x$RED).

3.4.4. Conclusions on the CeZr series and CuO

The production of up to 2.22 mmol of KA oil with a 93.2% selectivity was obtained after 5 hours with the $Cu_{0.1}Ce_{0.9}O_x$RED mixed oxide at 120°C and 4 bar of O_2 pressure. The preparation of the mixed oxides by the inverse microemulsion technique allowed to obtain very homogeneous mixing between the metal species and a precise control on the stoichiometry of the two metals oxides. The Cu-containing oxides all performed better than the Fe-containing ones in terms of productivity of KA oil, and a 10% molar inclusion of Cu in the CeO_2 and ZrO_2 structure allowed for a 3x and 2x increased productivity compared to their monometallic counterparts. On the other hand, the Fe-containing systems proved to inhibit the radical mechanism, giving a low productivity and resulting in a low K/A ratio compared to the non-catalysed and Cu-catalysed reactions. Indeed, the differences in the K/A ratio, associated with the different reaction rates in the propagation step of the reaction mechanism, highlighted profound difference in the behaviour of Fe and Cu oxides. Cu oxides resulted in a high (>2) K/A ratio, which could potentially represent an advantage as cyclohexanone is considered the most valuable product of the mixture. Selectivity to KA oil for this series was very high when concerning the Cu-containing oxides (up to 95.6% for $Cu_{0.1}Zr_{0.9}O_x$RED). Indeed, the K/A ratio was found being linked to the selectivity, as a mirroring of a different reaction pathway occurring in the two cases (high selectivity-high K/A ratio and vice versa). The reduction treatment carried out on the mixed oxides allowed for the improvement of the catalytic performances of the whole series, attributed to the synergistic effect of the segregation and migration to the surface of the included metal species (restructuring), and therefore the creation of surface defects and altered contact between the

metal species. This was linked to have consequences on the rates of initiation and propagation of the radical mechanism.

To expand on the better performance of Cu-containing oxides, studies on commercial CuO, which was also reduced and reoxidized in air, revealed how important to the productivity of KA oil are a) the average crystallites size of the mixed oxide in the catalytic performance and b) the presence of coexisting mixed Cu^0 and Cu^{II} phases. Indeed, while the commercial CuO and the reduced CuO-RED did result in low KA oil productivity, the decreased crystallite size in conjunction with the mixed Cu^0/Cu^{II} phases of CuO-REOX resulted in great productivity of up to 2.57 mmol with extremely high selectivity (98.8%) after 5 hours, maintaining a high K/A of 1.98. Such high selectivity represents and enormous advantage from an industrial point of view, which coupled with the maintenance of a high K/A and no deactivation observed in the reaction profile, represents the most applicable result obtained among the three years. The use of non-noble metals systems together with the mild conditions employed, the high stability transition metals mixed oxides [74] and the preservation of high selectivity to the desired products make these novel catalytic systems attractive for the application on cyclohexane oxidation, to be further studied in longer reaction runs due to the lack of catalysts deactivation.

3.5. References

[1] L. Wang, S. Zhao, C. Liu, C. Li, X. Li, H. Li, Y. Wang, C. Ma, Z. Li, J. Zeng, Nano Lett. 15 (2015) 2875–2880.

[2] N.A. Milas, D.M. Surgenor, J. Am. Chem. Soc. 68 (1946) 205–208.

[3] Y.J. Xu, P. Landon, D. Enache, A.F. Carley, M.W. Roberts, G.J. Hutchings, Catal. Letters 101 (2005) 175–179.

[4] T.G. Traylor, S. Tsuchiya, Y. Byun, C. Kim, (1993) 2775–2781.

[5] B. Puértolas, A.K. Hill, T. García, B. Solsona, L. Torrente-Murciano, Catal. Today 248 (2015) 115–127.

[6] H.L.J. Bäckström, J. Am. Chem. Soc. 49 (1927) 1460–1472.

[7] M.F.R. Mulcahy, I.C. Watt, Nature 168 (1951) 123–124.

[8] M. Sankar, E. Nowicka, E. Carter, D.M. Murphy, D.W. Knight, D. Bethell, G.J. Hutchings, Nat. Commun. 5 (2014) 1–6.

[9] R.A. SHELDON, J.K. KOCHI, Met. Oxidations Org. Compd. (1981) 120–151.

[10] X. Liu, M. Conte, Q. He, D.W. Knight, D.M. Murphy, S.H. Taylor, K. Whiston, C.J. Kiely, G.J. Hutchings, Chem. - A Eur. J. 23 (2017) 11834–11842.

[11] I. Hermans, J. Peeters, P.A. Jacobs, Top. Catal. 50 (2008) 124–132.

[12] Donald J. Loder - E.I. Du Pont de Nemours & Co., Production of Cyclic Alcohols and Ketones, 2,223,494, 1940.

[13] A. Abutaleb, M.A. Ali, Rev. Chem. Eng. 38 (2022) 769–797.

[14] S. Gupta, R. Fernandes, R. Patel, M. Spreitzer, N. Patel, Appl. Catal. A Gen. 661 (2023).

[15] A.P. Unnarkat, T. Sridhar, H. Wang, S. Mahajani, A.K. Suresh, Z. Qiao, Z. Wang, C. Zhang, S. Yuan, Y. Zhu, J. Wang, AIChE J. 62 (2016) 4384–4402.

[16] A.A. Alshehri, A.M. Alhanash, M. Eissa, M.S. Hamdy, Appl. Catal. A Gen. 554 (2018) 71–79.

[17] J. Jian, D. Kuang, X. Wang, H. Zhou, H. Gao, W. Sun, Z. Yuan, J. Zeng, K. You, H. Luo, Mater. Chem. Phys. 246 (2020) 122814.

[18] D. Klarstrom, P. Crook, A.B.T.-R.M. in M.S. and M.E. Sharif, in: Elsevier, 2017.

[19] M.C. Pereira, L.C.A. Oliveira, E. Murad, Clay Miner. 47 (2012) 285–302.

[20] S. Rahim Pouran, A.A. Abdul Raman, W.M.A. Wan Daud, J. Clean. Prod. 64 (2014) 24–35.

[21] X. Xue, K. Hanna, N. Deng, J. Hazard. Mater. 166 (2009) 407–414.

[22] S.T. Mkhondwane, V.S.R. Pullabhotla, (2022).

[23] R. Goyal, B. Sarkar, S. Sameer, A. Bag, A. Bordoloi, ACS Appl. Nano Mater. 2 (2019) 5989–5999.

[24] X. Tan, X. Wang, Q. Liu, J. Zhou, P. Zhang, S. Zheng, S. Miao, Int. J. Hydrogen Energy 42 (2017) 19001–19009.

[25] J. Tong, L. Bo, X. Cai, H. Wang, Q. Zhang, L. Su, Ind. Eng. Chem. Res. 53 (2014) 10294–10300.

[26] N. Perkas, Y. Koltypin, O. Palchik, A. Gedanken, S. Chandrasekaran, Appl. Catal. A Gen. 209 (2001) 125–130.

[27] M. Conte, X. Liu, D.M. Murphy, K. Whiston, G.J. Hutchings, Phys. Chem. Chem. Phys. 14 (2012) 16279–16285.

[28] E.F.J. Duynstee, J.L.J.P. Hennekens, Recl. Des Trav. Chim. Des Pays-Bas 89 (1970) 769–780.

[29] B.P.C. Hereijgers, B.M. Weckhuysen, J. Catal. 270 (2010) 16–25.

[30] U. Schuchardt, W.A. Carvalho, E.V. Spinacé, Synlett 1993 (1993) 713–718.

[31] N. Kapil, T. Weissenberger, F. Cardinale, P. Trogadas, T.A. Nijhuis, M.M. Nigra, M. Coppens, Angew. Chemie 133 (2021) 18333–18341.

[32] K. Jiang, Z. Li, Z. Zhang, J. Li, X. Qi, J. Zhou, X. Wang, H. Wei, H. Chu, Inorg. Chem. (2023).

[33] X.-Q. Cao, J. Zhou, S. Li, G.-W. Qin, Rare Met. 39 (2020) 113–130.

[34] K. Yu, Z. Wu, Q. Zhao, B. Li, Y. Xie, J. Phys. Chem. C 112 (2008) 2244–2247.

[35] A. Stephen, K. Hashmi, G.J. Hutchings, A.S.K. Hashmi, G.J. Hutchings, (n.d.).

[36] C. Della Pina, E. Falletta, L. Prati, M. Rossi, (2008).

[37] C. Della Pina, E. Falletta, M. Rossi, Chem. Soc. Rev. 41 (2012) 350–369.

[38] U. Schuchardt, D. Cardoso, R. Sercheli, R. Pereira, R.S. da Cruz, M.C. Guerreiro, D. Mandelli, E. V Spinacé, E.L. Pires, Appl. Catal. A Gen. 211 (2001) 1–17.

[39] L.X. Xu, C.H. He, M.Q. Zhu, S. Fang, Catal. Letters 114 (2007) 202–205.

[40] M. Wu, Y. Fu, W. Zhan, Y. Guo, Y. Guo, Y. Wang, G. Lu, Catalysts 7 (2017).

[41] J. Büker, B. Alkan, Q. Fu, W. Xia, J. Schulwitz, D. Waffel, T. Falk, C. Schulz, H. Wiggers, M. Muhler, B. Peng, Catal. Sci. Technol. 10 (2020) 5196–5206.

[42] R. Anumula, C. Cui, M. Yang, J. Li, Z. Luo, J. Phys. Chem. C 123 (2019) 21504–21512.

[43] M. Stucchi, S. Capelli, S. Cardaci, S. Cattaneo, A. Jouve, A. Beck, G. Sáfrán, C. Evangelisti, A. Villa, L. Prati, Catalysts 10 (2020).

[44] E. Skupien, R.J. Berger, V.P. Santos, J. Gascon, M. Makkee, M.T. Kreutzer, P.J. Kooyman, J.A. Moulijn, F. Kapteijn, Catalysts 4 (2014) 89–115.

[45] N. Dimitratos, J.A. Lopez-Sanchez, D. Morgan, A. Carley, L. Prati, G.J. Hutchings, Catal.

Today 122 (2007) 317–324.

[46] E. Pitzalis, R. Psaro, C. Evangelisti, Inorganica Chim. Acta 533 (2022) 120782.

[47] G.B. Sergeev, K.J. Klabunde, Nanochemistry (2013) 55–73.

[48] H.M. Maltanava, O.N. Vrublevskaya, T.N. Vorobyova, Met. Finish. 111 (2013) 28–34.

[49] C. Tao, Q. Jia, B. Han, Z. Ma, Chem. Eng. Sci. 214 (2020) 115438.

[50] Y. Harima, T. Fujita, Y. Kano, I. Imae, K. Komaguchi, Y. Ooyama, J. Ohshita, J. Phys. Chem. C 117 (2013) 16364–16370.

[51] A. Vomeri, M. Stucchi, A. Villa, C. Evangelisti, A. Beck, L. Prati, J. Energy Chem. 70 (2022) 45–51.

[52] S. Parham, S. Chandren, D.H.B. Wicaksono, S. Bagherbaigi, S.L. Lee, L.S. Yuan, H. Nur, RSC Adv. 6 (2016) 8188–8197.

[53] I. Nakanishi, K. Ohkubo, Y. Ogawa, K. Matsumoto, T. Ozawa, S. Fukuzumi, Org. Biomol. Chem. 14 (2016) 7956–7961.

[54] S. Alidoust, M. Zamani, M. Jabbari, Free Radic. Res. 55 (2021) 937–949.

[55] M. Zamani, A.M. Delfani, M. Jabbari, Spectrochim. Acta Part A Mol. Biomol. Spectrosc. 201 (2018) 288–299.

[56] J. Low, J. Yu, M. Jaroniec, S. Wageh, A.A. Al-Ghamdi, Adv. Mater. 29 (2017) 1601694.

[57] K. V. Sopiha, O.I. Malyi, C. Persson, P. Wu, ACS Appl. Mater. Interfaces 13 (2021) 33664–33676.

[58] S.Y. Christou, A.M. Efstathiou, Top. Catal. 56 (2013) 232–238.

[59] E. Yuan, M. Gu, P. Jian, Korean J. Chem. Eng. 37 (2020) 1137–1148.

[60] J. Hao, H. Cheng, H. Wang, S. Cai, F. Zhao, J. Mol. Catal. A Chem. 271 (2007) 42–45.

[61] J. Hao, J. Wang, Q. Wang, Y. Yu, S. Cai, F. Zhao, Appl. Catal. A Gen. 368 (2009) 29–34.

[62] I. Hermans, P.A. Jacobs, J. Peeters, Chem. - A Eur. J. 12 (2006) 4229–4240.

[63] M. Pradenas, J. Yáñez, S. Ranganathan, D. Contreras, P. Santander, H.D. Mansilla, Water Environ. Res. 91 (2019) 157–164.

[64] A. Martínez-Arias, M. Fernández-García, V. Ballesteros, L.N. Salamanca, J.C. Conesa, C. Otero, J. Soria, Langmuir 15 (1999) 4796–4802.

[65] N. Doufar, M. Benamira, H. Lahmar, M. Trari, I. Avramova, M.T. Caldes, J. Photochem. Photobiol. A Chem. 386 (2020).

[66] A. Ahmed, M. Naseem Siddique, U. Alam, T. Ali, P. Tripathi, Appl. Surf. Sci. 463 (2019) 976–985.

[67] S. Shi, D. Gao, Q. Xu, Z. Yang, D. Xue, RSC Adv. 4 (2014) 45467–45472.

[68] H. Idriss, Surf. Sci. 712 (2021) 121894.

[69] E. Sartoretti, C. Novara, M.C. Paganini, M. Chiesa, M. Castellino, F. Giorgis, M. Piumetti, S. Bensaid, D. Fino, N. Russo, Catal. Today 420 (2023) 114037.

[70] L. Vereecken, T.L. Nguyen, I. Hermans, J. Peeters, Chem. Phys. Lett. 393 (2004) 432–436.

[71] S. Rautiainen, O. Simakova, H. Guo, A.R. Leino, K. Kordás, D. Murzin, M. Leskelä, T. Repo, Appl. Catal. A Gen. 485 (2014) 202–206.

[72] K. Teramura, T. Tanaka, M. Kani, T. Hosokawa, T. Funabiki, J. Mol. Catal. A Chem. 208 (2004) 299–305.

[73] M.G. Clerici, M. Ricci, G. Strukul, Metal-Catalysis in Industrial Organic Processes, Chapter 2. Formation of C–O Bonds by Oxidation, 2007.

[74] T.P. Mabate, N.P. Maqunga, S. Ntshibongo, M. Maumela, N. Bingwa, SN Appl. Sci. 5 (2023).

4. Conclusions and possible improvements

For improving the state-of-the-art of heterogeneous catalysts in cyclohexane oxidation, by the preparation of the reported catalysts during the three years of my Ph.D. course I went through a process of optimization of the materials, obtaining performing catalysts at relatively mild reaction conditions while maintaining high productivity and selectivity to the KA oil mixture. First, the FeCo series studied the behaviour of the metal used in the industrial process, Co, in a heterogeneous system supported on Al_2O_3. The non-reducible support was chosen for reducing any interference derived from metal-support interaction thus analysing better the contribute of the metal species. In addition, the study employed three different preparation methods to disclose the effect of catalyst design. Very different morphologies were obtained, and particular focus was put on structure-activity correlation. Due to the instability problems revealed from experiments on the FeCo series, the Au-based series allowed obtaining more stable systems. Au was also the most employed noble metal for cyclohexane oxidation in heterogeneous catalysis. The catalytic performance of Au and its enhancement when paired with a transition metal possessing redox properties were explored, benefiting also from lowering the precious metal content and thus the cost of the systems. In particular, the AuCu series was also exploited for the understanding the effect of Cu modulating Au properties in a bimetallic system, and the Au_1Cu_1 catalyst was also used to study the influence of the initial [benzaldehyde] in the presence of a catalyst. Instead, the AuSn series highlighted the importance of the support role on the modulation of the electronic exchange properties of SnO_2 when in intimate contact with Au. This intimate contact also demonstrated to exert a beneficial effect on the productivity of KA oil and to influence the K/A ratio, attributed to the formation of reactive superoxide ($O_2^{\bullet-}$) species. Moving on to noble metal-free systems possessing high stability, transition metals mixed oxides were researched. The CeZr series allowed for the study of mixed oxides systems with reducible metals, disclosing the influence of Fe and Cu inclusion in the ordered structure of CeO_2 and ZrO_2 and the effect of their structural reconstruction upon a reduction treatment. The promising catalytic performance of Cu was further investigated in the studies on commercial CuO, where its reduction and reoxidation were key to boost the productivity and obtaining extremely high selectivity to KA oil by reducing the particle size and creating Cu^0/Cu^{II} pairs. In Table 4.1, the results of the best

catalytic systems of each series are reported in comparison with the benchmark benzaldehyde-only, non-catalysed reaction.

Catalyst	Prod. KA oil (mmol at 5 h)	K/A ratio	Selectivity to KA (%)
Initiator-only	1.24	2.65	94.2
2 wt% $Fe_1Co_1/\gamma\text{-}Al_2O_3$-ME	4.68	0.96	98.8
2 wt% Au_1Cu_1/Al_2O_3	4.50	0.91	94.4
$Cu_{0.1}Ce_{0.9}O_x$RED	2.22	2.58	93.2
CuO-REOX	2.57	1.98	98.8

Table 4.1. Comparison of the best catalytic results among the three series of catalysts of this thesis work, at the same reaction conditions of T and P (120°C, 4 bar O_2).

The initiator-only reaction gave a high selectivity to KA oil of 94.2% with a high K/A ratio, intended as the value for the pure radical mechanism. Despite the low productivity, none of the catalysts could convert cyclohexane without the radical initiation from benzaldehyde. This is in accordance with the majority of the state-of-the-art works requiring an initiator.

The FeCo series prepared by different methodologies allowed to obtain extremely efficient and selective catalysts. In particular 2 wt% $Fe_1Co_1/\gamma\text{-}Al_2O_3$-ME gave the high productivity of 4.68 mmol of KA oil and extremely high selectivity of 98.8%. However, the SOL and ME systems were found to be unstable at our reaction conditions. Future studies on this series should focus on obtaining stable systems, possibly starting by exploring different intermetallic ratios between Fe and Co and the influence of different supports. The 2 wt% Au_1Cu_1 catalyst supported on alumina was one of the most productive catalysts of this thesis work (4.5 mmol of KA oil), reaching also high selectivity to KA oil (94.4%) and overperforming the monometallic counterparts while lowering the amount of precious metal. Avoiding completely the use of noble metals, $Cu_{0.1}Ce_{0.9}O_x$RED resulted in lower productivity with respect to the other series but allowed for the obtainment of a very high K/A ratio, with high selectivity and no deactivation observable the reaction profile. Being cyclohexanone the most interesting product of the mixture, selectively obtaining it even at lower hourly productivity is very desirable. Further studies should focus on running the reaction for longer time (i.e. overnight) to check catalyst life. The work on commercial CuO demonstrated how reducing and reoxidizing CuO can be highly beneficial to the catalytic performance due to the reduction of the crystallites size and the creation of Cu^0/Cu^{II} mixed phases. This way, extremely high

selectivity (98.8%) was obtained while maintaining a high K/A, making the catalyst the most interesting of this thesis work in the mindset of industrial applicability. Future looks could focus on reducing even more the particle size or supporting Cu onto other supports and exploring their interaction. Eventually, the roles between Cu^{0} and Cu^{II} in enhancing the catalytic performance should be looked out too.

In conclusion, the systems investigated during these three years offered an interesting alternative and new insights for the obtainment of KA oil from cyclohexane at high selectivity. Combined with the employment of relatively mild reaction conditions, the low cost of the materials and the ease of preparation of the catalysts, they could meet industrial interest.

5. Publications

In this section, I report a list of the scientific papers published during these three years regarding cyclohexane oxidation, which feature me as author or co-author.

- **Vomeri A**.; Stucchi, M.; Villa, A.; Evangelisti, C.; Beck, A.; Prati, L. *New insights for the catalytic oxidation of cyclohexane to K-A oil*, J. Energy Chem. 2022,70, 45–51.
- M. Stucchi, **A. Vomeri**, S. Stichleutner, K. Lázár, E. Pitzalis, C. Evangelisti, L. Prati, *Exploring the Effect of Sn Addition to Supported Au Nanoparticles on Reducible/Non-Reducible Metal Oxides Supports for Alkane Oxidation*, Chemistry, 2023, 5, 3, 1560-1576.
- In preparation (2023): "**Vomeri, A.**; Stucchi, M; Calvino, J.; Hungría A.B.; Prati, L., *Cu and Fe modified Cerium and Zirconium mixed oxides for the Oxidation of cyclohexane to KA oil*".

Other papers published as collaborator and co-author:

- Stucchi, M.; Vasile, F.; Cattaneo, S.; **Vomeri, A.**; Hungría, A.B.; Prati, L. *Pt-WOx/C catalysts for α, β- unsaturated aldehydes hydrogenation: a NMR study of the effect of the reactant adsorption on activity and selectivity*, European J. Org. Chem., 2022.
- Zanella, E.; Secundo, L.; Bellomi, S.; **Vomeri, A.**; Villa, A.; Pirola, C. *Bio-Adipic Acid Production from Muconic Acid Hydrogenation on Palladium-Transition Metal (Ni and Zn) Bimetallic Catalysts*, Catalysts 2023, 13, 486.